Dissertation

submitted to the

Combined Faculties of the Natural Sciences and Mathematics

of the Ruperto-Carola-University of Heidelberg, Germany

for the degree of

Doctor of Natural Sciences

Put forward by

*Jolanta Zjupa*

*born in: Radom (Poland)*

*Oral examination: 26.10.2018*

# The impact of feedback

# on galactic and extra-galactic scales

Referees: Prof. Dr. Volker Springel

Prof. Dr. Björn Malte Schäfer

‘Where shall I begin?’ asked the White Rabbit.
‘Begin at the beginning, and go on till you come to the end: then stop.’

Alice’s Adventures in Wonderland
*Lewis Carroll* (adapted)

# Abstract

Recent cosmological hydrodynamical simulations were for the first time able to produce galaxy populations with realistic sizes and morphologies. This success can be attributed to the inclusion of subgrid models for supernovae winds and active galactic nuclei (AGN) feedback. In this thesis, we investigate the impact of feedback driven galactic outflows. First, the expulsion of gas proves to be crucial for the rotational support of haloes hosting realistic galaxies. We employ the state-of-the-art hydrodynamical simulation suites Illustris and IllustrisTNG to characterise the amount of specific angular momentum in the baryonic component of haloes. We find the baryonic spin at $z = 0$ to be a factor of $\sim 2$ higher than the dark matter spin, which is due to the transfer of a constant cumulative spin of $\Delta\lambda = 0.0013$ by $z = 0$ from dark matter to the gas during mergers, and to the preferential expulsion of low angular momentum gas by mostly AGN feedback. Second, galactic outflows impact the state of the diffuse gas on large scales. We employ the Lyman-$\alpha$ forest to examine the feedback induced changes in the inter-galactic medium (IGM) that serves as gas reservoir for accretion onto galaxies. For a clean comparison, we have run a suite of simulations with both galaxy formation physics and with the Quick Lyman-$\alpha$ (QLA) technique yielding an unperturbed IGM. We find the Lyman-$\alpha$ flux power spectrum to exhibit increasingly more power at large scales and correspondingly less power at small scales in the presence of outflows, as well as the IGM to be generally hotter. Employing IllustrisTNG we investigate the excess Lyman-$\alpha$ absorption as a function of impact parameter for haloes exhibiting strong and weak feedback and find significant differences that can largely be explained by the higher temperature of the perturbed gas.

# Zusammenfassung

Neuste kosmologische hydrodynamische Simulationen haben zum ersten Mal Populationen von Galaxien mit realistischen Größen und Morphologien produziert. Dieser Erfolg ist der Verwendung von Subgridmodellen für Supernovaewinde und der Rückkopplung von Aktiven Galaktischen Kernen (AGN) zu verdanken. In dieser Arbeit untersuchen wir den Einfluss von rückkopplungsprozessgetriebenen galaktischen Ausflüssen. Der Ausstoß von Gas aus realistischen Galaxien stellt sich als essentiell für den Drehimpuls von den sie beherbergenden Halos heraus. Wir verwenden die neuste Generation hydrodynamischer Simulationen Illustris und IllustrisTNG, um den spezifischen Drehimpuls der baryonischen Halokomponente zu charakterisieren. Hierbei zeigt sich, dass der spezifische Drehimpuls der Baryonen bei $z = 0$ etwa um einen Faktor $\sim 2$ größer ist als der spezifische Drehimpuls Dunkler Materie. Dies kann man auf einen konstanten Übertrag von einem kumulativen spezifischen Drehimpuls von $\Delta\lambda = 0.0013$ bis $z = 0$ von Dunkler Materie auf das Gas im Zuge von Akkretionsprozessen auf den Halo zurückfüren, sowie dem bevorzugten Ausstoß von Gas mit geringem spezifischen Drehimpuls aus Galaxien und ihren Halos durch AGN-Rückkopplungsprozesse. Desweiteren beeinflussen galaktische Ausflüsse den Zustand des diffusen Gases auf großen Skalen. Wir verwenden den Lyman-$\alpha$-Wald, um die rückkopplungsinduzierten Veränderungen im intergalaktischen Medium (IGM) zu untersuchen, welches als Gasreservoir für Akkretion auf Galaxien dient. Für einen sauberen Vergleich haben wir eine Simulationsreihe mit sowohl Galaxienphysik als auch der Quick-Lyman-$\alpha$-Technik (QLA), die ein ungestörtes IGM liefert, durchgeführt. Dabei zeigt das Lyman-$\alpha$-Fluss Power-Spektrum zunehmend mehr Power auf großen Skalen und entsprechend weniger Power auf kleinen Skalen in der Gegenwart von Ausflüssen. Zudem weist das IGM in Gegenwart von galaktischen Ausflüssen eine allgemein höhere Temperatur auf. Unter Verwendung von IllustrisTNG untersuchen wir die Lyman-$\alpha$-Überschussabsorption als Funktion des Abstandes vom Zentrum von Halos, die starke und schwache Rückkopplungsprozesse aufweisen, und finden signifikante Unterschiede, die weitgehend von der höheren Temperatur des gestörten Gases erklärt werden können.

# Table of contents

# Chapter 1

# Introduction

## 1.1 Overview

Structures in the universe emerge through growth of primordial density perturbations enlarged by inflation, first forming small dark matter haloes which then hierarchically merge into bigger structures (Blumenthal et al., 1984, Davis et al., 1985). The cosmic gas collapses onto the potential wells provided by dark matter forming galaxies at the centres of dark matter haloes through subsequent cooling and star formation (White and Rees, 1978). Throughout their evolution stars produce metals and return part of their metal-enriched mass in form of stellar winds and supernovae driven galactic winds to the surrounding gas that is heated as a consequence (Mo et al., 2010). Furthermore, with ongoing galaxy evolution a black hole forms at the halo centre and given sufficient gas influx turns into an active galactic nucleus (AGN) that drives large-scale outflows of hot gas (Mo et al., 2010). Both supernovae driven winds and AGN feedback driven outflows establish a baryon cycle in the circum-galactic gas (CGM). Galactic outflows furthermore partially reach and perturb the inter-galactic gas (IGM) changing the properties of the gas reservoir for accretion onto galaxies. In this thesis, we investigate two major aspects in the context of galaxy formation that are regulated by feedback driven outflows. First, the expulsion of gas proves to be crucial for galactic dynamics, and in particular for the rotational support of galaxies and their haloes. Second, the expelled gas changes the thermal state of the CGM and IGM and introduces additional matter on large scales impacting the Lyman-$\alpha$ absorption properties of the cosmic gas.

We structure the remained of the introduction as follows. We first give an overview of $\Lambda$CDM cosmology in Section 1.2 providing the framework for structure and galaxy formation in the universe, which we expand on in Section 1.3. In Section 1.4 we give a brief introduction into the two aspects of galaxy and structure formation on galactic and extra-galactic scales regulated by feedback driven outflows, which will be covered in the individual chapters

of this thesis in excruciating detail. We present the major hydrodynamical cosmological simulation suites of galaxy formation used in this thesis in Section 1.5, and in Section 1.6 we give a broad overview of simulation techniques used in computational astrophysics in order to put our approach in perspective. We discuss in detail the most relevant feedback mechanisms and their implementation in form of subgrid models for hydrodynamical simulations of galaxy formation in Section 1.7.

We structure the main part of this thesis as follows. In Chapter 2, we employ state-of-the-art cosmological hydrodynamical simulations to characterise the specific angular momentum of haloes hosting a realistic galaxy population and provide a first attempt to disentangle the mechanisms contributing to significantly more specific angular momentum in the gas component compared to dark matter necessary for realistic galaxies to form at halo centres. In Chapter 3, we expand on our first study by augmenting our analysis with results from cosmological hydrodynamical simulations with different models for galactic feedback physics allowing us to refine the understanding of the mechanisms crucial to establish an observed baryonic specific angular momentum in a model-independent way. The key mechanism turns out to be supernovae and AGN feedback driven outflows expelling a significant fraction of halo gas beyond the virial radius. In Chapter 4, we investigate the role of haloes with different properties in driving these outflows as well as their extend and impact on the state of the cosmic gas. In order to make a comparison between the properties of the inter-galactic medium (IGM) with and without the impact of feedback driven outflows in the most clean way, we run a suite cosmological hydrodynamical simulations with the up-to-date most complete galaxy evolution and feedback physics and with an unperturbed IGM which we employ for a statistical comparison of the state of the IGM probed by the Lyman-$\alpha$ forest. We conclude in Chapter 5.

## 1.2 $\Lambda$CDM Cosmology

Galaxies as well as all other astrophysical objects of interest are embedded in the large-scale structure (LSS) of the universe that forms within an evolving space-time. Therefore, to understand structure and galaxy formation, first a description of the properties and the evolution of the universe as a whole is necessary. The subfield of astrophysics dealing with these questions is called cosmology.

At the heart of the cosmological framework lies the *Copernican* or also called *cosmological principle* (e.g. Carroll, 2004) which is the notion that our position in the universe is not special with respect to any other possible position. Furthermore, the observed universe is isotropic which combined with the cosmological principle can be rephrased to the universe

being *homogeneous* and *isotropic*, whereas homogeneity is invariance under translations and isotropy invariance under rotations. However, due to ongoing structure formation, homogeneity and isotropy are always only valid above a certain scale that grows with time due to the increasing clustering of matter.

Out of the four fundamental interaction (strong, weak, electromagnetic, and gravitational), the only force relevant for cosmological structure formation is gravity, because of its infinite range and the non-existence of negative mass that could shield the effect from 'normal' mass. A description of gravity is given in the framework of general relativity (GR) where gravity is expressed as the curvature of spacetime. The mathematical description of a curved spacetime is given by a manifold with a distance measure given by a metric $g_{\mu\nu}$ (e.g. Carroll, 2004, Bartelmann, 2009). The entries of the metric can be determined when considering the invariant line element $ds$ with

$$\begin{aligned} ds^2 &= g_{\mu\nu} dx^\mu dx^\nu \\ &= g_{00} c^2 dt^2 + g_{0j} c dt dx^j + g_{i0} dx^i c dt + g_{ij} dx^i dx^j. \end{aligned} \tag{1.1}$$

where $dx^\mu$ and $dx^\nu$ $(\mu, \nu = 0, 1, 2, 3)$ are four-dimensional infinitesimal coordinate displacements, and $dx^0 = cdt$ with $c$ being the constant speed of light. Integrated out, the invariant line element provides the distance between two points in spacetime given by the four-vectors $x^\mu$ and $x^\nu$. The line element is called invariant as it neither depends on whether the distance is calculated between $x^\mu$ and $x^\nu$ or between $x^\nu$ and $x^\mu$ nor on the chosen coordinate system, which are necessary requirements for a distance measurement.

Starting out from Eq. 1.1 the entries of the metric $g_{\mu\nu}$ can be derived. For a point in its own rest frame the spatial components $dx^i$ and $dx^j$ $(i, j = 1, 2, 3)$ of its four-vector become zero, such that the line separation becomes by definition a pure time separation,

$$ds^2 = g_{00} c^2 dt^2. \tag{1.2}$$

The time that elapses in the restframe of a point is called *eigentime* $\tau$ of this point, defined by

$$ds^2 = -c^2 d\tau^2. \tag{1.3}$$

In the given configuration the system time $t$ and the points eigentime $\tau$ are the same, $dt = d\tau$, such that we can conclude $g_{00} = -1$. The $g_{i0}$ and $g_{0j}$ components vanish, $g_{i0} = 0 = g_{0j}$, as a coupling of a spatial component with the time component singles out a preferred direction by imposing an evolution of this spatial component that is different from the other spatial components, violating isotropy. Those constraints reduce the line element to

$$ds^2 = -c^2dt^2 + g_{ij}dx^i dx^j. \tag{1.4}$$

Furthermore, the same argument enforces that all connections between two spatial components scale with the same *scale factor* $a(t)$ that is a function of time $t$ only. The spatial part $g_{ij}$ of the metric can therefore be written as

$$g_{ij} = a^2(t)h_{ij}, \tag{1.5}$$

where $h_{ij}$ is a time independent metric. In spherical coordinates, with the most general expression for $h_{ij}$ obeying homogeneity and isotropy, the line element reads

$$ds^2 = -c^2dt^2 + a^2(t)\left(\frac{dr^2}{1-kr^2} + r^2d\Omega^2\right), \tag{1.6}$$

where $k$ is the so called *curvature constant*. The corresponding metric in spherical coordinates

$$g_{\mu\nu} = diag\left(-1,\ \frac{a^2(t)}{1-kr^2},\ a^2(t)r^2,\ a^2(t)r^2sin^2(\theta)\right), \tag{1.7}$$

is called *Friedmann–Lemaitre–Robertson–Walker* (FLRW) metric. The FLRW metric is symmetric, which is a necessary condition for the distance measurement to be commutative, as discussed above.

*Einstein field equations* given by

$$G_{\mu\nu} + g_{\mu\nu}\Lambda = \frac{8\pi G}{c^4}T_{\mu\nu}, \tag{1.8}$$

describe how curvature representing gravity contained in the *Einstein tensor* $G_{\mu\nu}$ couples to its sources, mass and energy, that are contained in the *energy-momentum tensor* $T_{\mu\nu}$. In Eq. 1.8, $G$ is the gravitational constant, and $\Lambda$ the so called *cosmological constant* that accounts for the expansion of spacetime. Assuming that the different components of the universe behave as an ideal fluid on large scales, the stress-energy tensor of an ideal fluid given by

$$T_{\mu\nu} = \left(\rho + \frac{P}{c^2}\right)v_\mu v_\nu + Pg_{\mu\nu}, \tag{1.9}$$

can be adopted as the cosmological energy-momentum tensor. Thereby, $P$ denote the pressure of the fluid, $\rho$ the density, and $v$ the fluid velocity. $P$ and $\rho$ are functions of time only, as otherwise would violate homogeneity.

Solving Einsteins equations with the FLRW metric yields the *Friedmann equations*

$$\left(\frac{\dot{a}}{a}\right)^2 = \frac{8\pi G}{3}\rho - \frac{kc^2}{a^2} + \frac{\Lambda c^2}{3}, \tag{1.10}$$

$$\left(\frac{\ddot{a}}{a}\right) = -\frac{4\pi G}{3}\left(\rho + \frac{3p}{c^2}\right) + \frac{\Lambda c^2}{3}, \tag{1.11}$$

which are two differential equations for the scale factor $a(t)$. Following conventions and setting $a(\text{today}) = 1$ uniquely determines the scale factor at all times. Based on the scale factor the *Hubble parameter* is defined as

$$H(t) := \frac{\dot{a}}{a} \tag{1.12}$$

and the *Hubble constant* as

$$H_0 := H(\text{today}) \tag{1.13}$$

Both have units of km/(sMpc). For convenient use especially in the field of numerical cosmological simulations the Hubble constant is often expressed in terms of the *dimensionless Hubble parameter h* defined through

$$H = 100h\frac{km}{sMpc}. \tag{1.14}$$

The Hubble constant appears as proportionality constant in *Hubble's Law*,

$$cz = H_0 d, \tag{1.15}$$

which relates the linear distance $d$ of an object from us to its redshift $z$. The light we receive from a distant object is always redshifted due to the expansion of spacetime and is related to the scale factor by

$$a(t) = \frac{1}{1+z}. \tag{1.16}$$

The observed redshift is however always the measured Dopplershift of an object that is contaminated by the objects proper motion. The error introduced into the distance measurement due to this contamination gets progressively smaller with distance, and is negligible compared to measurement errors for large distances. Due to the constant speed of light, the redshift $z$ can also be used as time coordinate.

In a static ($\Lambda = 0$) and spatially flat ($k = 0$) universe the first Friedmann equation yields the so called *critical density*

$$\rho_{crit}(t) := \frac{3H^2(t)}{8\pi G}, \tag{1.17}$$

that provides a threshold value for the geometry of spacetime (e.g. Ryden, 2002). If the mean density $\rho_{mean}(t)$ in the universe is above the critical density, spacetime exhibits a closed geometry and positive curvature $k > 0$, if the mean density is below the critical density, spacetime has an open geometry and negative $k < 0$. Objects with higher average density than the mean density eventually decouple from the expansion of the universe and collapse to form gravitationally self-bound structures called *haloes* which host galaxies. These haloes then settle in dynamical and thermal equilibrium (e.g. Binney and Tremaine, 2008). They can be viewed as closed systems, and given they have a Newtonian gravitational potential, which is homogeneous of degree $-1$, yielding a gravitational potential energy

$$E_{grav} = \int_0^{\text{object boundaries}} \rho(\mathbf{r})\Phi(\mathbf{r})\, dV \tag{1.18}$$

that is also homogeneous of degree $-1$, haloes obey the *virial theorem*

$$E_{kin} = -\frac{1}{2}E_{grav}. \tag{1.19}$$

The boundaries of a halo are typically defined following the top-hat collapse model, which derives the mean density of a virialised system to be slightly below 200 times the critical density, assuming a spherical halo. Following this idea, the boundaries of a so called 'spherical overdensity' halo are given by the surface of a sphere enclosing matter with mean density equal to 200 times the critical density, $\rho_{200} = 200 \cdot \rho_{crit}$. For practical applications, the centre of the sphere is either set to the densest point or to the minimum of the gravitational potential, which however does not affect the outcome significantly. In observations those centres are identified by the luminosity peak or through e.g. weak gravitational lensing, respectively. Following the above convention, the radius of such a sphere is denoted by $r_{200}$ and its mass by $M_{200}$. Further quantities of a spherical overdensity halo can be derived from these basic properties, and are denoted by the subscript '200' or 'vir'.

The first Friedmann equation can be expressed in a further way. Solving the equation of state for an ideal baryonic gas,

$$PV = Nk_BT \tag{1.20}$$

for $P$, and inserting the equipartition theorem for relativistic matter, $E_{therm} = 3k_BT$, results in

$$P = \frac{N}{V}k_BT = \frac{n}{3}E_{therm} = \frac{n}{3}E_{kin} = \frac{n}{3}Pc = \frac{1}{3}\rho vc, \tag{1.21}$$

where $n = N/V$. For photons traveling at the speed of light $c$ this yields

$$P = \frac{1}{3}\rho c^2. \tag{1.22}$$

Compared to the radiation field of the photons the pressure exerted by non-relativistic matter is negligible, $P \approx 0$. Both cases can be combined to

$$P = w_{r/m}\rho c^2 \begin{cases} w_r = \frac{1}{3}, & \text{radiation} \\ w_m = 0, & \text{matter.} \end{cases} \tag{1.23}$$

This general equation of state for ideal gas can be used to combine the Friedmann equations Eq. 1.10 and 1.11 into the *adiabatic equation*,

$$\frac{d}{dt}(a^3\rho c^2) = -P\frac{d}{dt}(a^3). \tag{1.24}$$

Solving the adiabatic equation for the density making use of the general equation of state yields

$$\rho_{r/m}(t) = \rho_{r/m0}a^{-3(1+w_{r/m})}. \tag{1.25}$$

Inserting this in the first Friedmann equation results in

$$\begin{aligned} H^2(a) &= \frac{8\pi G}{3}(\rho_{r0}a^{-4} + \rho_{m0}a^{-3}) + \frac{\Lambda}{3} - \frac{kc^2}{a^2} \\ &= H_0^2\left(\Omega_{r0}a^{-4} + \Omega_{m0}a^{-3} + \Omega_{\Lambda 0} + \Omega_{k0}a^{-2}\right), \end{aligned} \tag{1.26}$$

which makes use of the present day values of the *density parameters* for radiation, matter, the cosmological constant $\Lambda$ and the curvature parameter $k$ defined as

$$\Omega_r(t) := \frac{\rho_r(t)}{\rho_{crit}(t)}, \tag{1.27}$$

$$\Omega_m(t) := \frac{\rho_m(t)}{\rho_{crit}(t)}, \tag{1.28}$$

$$\Omega_\Lambda(t) := \frac{\Lambda}{3H^2(t)}, \tag{1.29}$$

$$\Omega_k(t) := -\frac{kc^2}{H_0^2}, \tag{1.30}$$

whereas the present day values ($a = 1$) fulfil $1 = \Omega_{r0} + \Omega_{m0} + \Omega_{\Lambda 0} + \Omega_{k0}$ in order for Eq. 1.26 to hold. The latest and most precise values for the cosmological parameters where obtained by the Planck Collaboration et al. (2016b) from the cosmic microwave background (CMB), and are $H_0 = 67.8 \pm 0.9$ s$^{-1}$ Mpc$^{-1}$ km, $\Omega_{m0} = 0.308 \pm 0.012$ and $\Omega_{\Lambda 0} = 0.692 \pm 0.012$, whereas both $\Omega_{r0}$ and $\Omega_{k0}$ are close to zero. This corresponds to a spatially flat universe that today is dominated by the cosmological constant $\Lambda$ that causes an accelerated expansion of the universe. $\Lambda$ drives the expansion of the universe, as expressing $\Omega_\Lambda$ in analogy to $\Omega_m$ or $\Omega_r$ as a density fraction and describing the time evolution for $\rho_\Lambda(t)$ by Eq. 1.25 yields $w_\Lambda = -1$ and thus a negative pressure according to the general equation of state Eq. 1.23. Due to its effect $\Lambda$ is often also referred to as *dark energy*, and its significant impact on the evolution of the universe leads to it being the first letter in the term $\Lambda$CDM cosmology. The last three letters stand for *cold dark matter*, which is a yet undetected particle that interacts only gravitationally. According to the latest measurements by the Planck Collaboration et al. (2016b), dark matter amounts to 84.2% of all ordinary (non-relativistic) matter, and only 15.8% is in baryonic form. Despite their small mass fraction, the baryons exhibit the most complex interactions and are the critical ingredient in the universe that accounts for the variety of astronomical phenomena. Therefore, it will be effects of baryonic physics that we will focus on in this thesis.

## 1.3 Structure and galaxy formation

Structures within the otherwise homogeneously expanding space-time form from initial density perturbations that have been enlarged by inflation (e.g. Peebles, 1993, Peacock, 1999). Gravitational attraction leads to the formation of a filamentary large-scale structure, as well as of gravitationally self-bound objects referred to as *haloes* typically at locations that attract matter from at least two different spatial directions. The growth of the large-scale structure is often described employing not the real space density field $\delta(x)$ but its decomposition into Fourier modes $\hat{\delta}(k)$. In the early radiation-dominated era of the universe sub-horizon modes grow as $ln(a)$, and super-horizon modes as $a^2$, whereas the horizon at any time $t$ is defined as the distance a photon with velocity $c$ can travel from the big bang until $t$. In the subsequent matter-dominated era all modes grow as $a$. However, baryonic sub-horizon modes are strongly suppressed due to radiation pressure from photons which prevent baryons from a free gravitational collapse (Puchwein, 2013). At a redshift of $z \approx 1100$ the universe has cooled sufficiently for recombination of the primordial plasma to take place (Ryden, 2002). This reduces the scattering rate of photons below the expansion rate of the universe $H$, leading to a decoupling of the baryons from photons. The last scattering surface produced

by this process is observed as the cosmic microwave background (CMB), and marks the beginning of the collapse of cosmic gas into already existing dark matter haloes which largely determine the gravitational potential of the whole future system (Rubin and Ford, 1970). Subsequent accretion and cooling of gas, and at later times dust, onto the centre of the system (White and Rees, 1978) ultimately leads to star formation and the formation of a central galaxy (Rees and Ostriker, 1977).

However, galaxy formation is not a one-way process. First non-radiative simulations incorporating only cooling and star formation have encountered two major problems yielding unrealistic galaxies. In non-radiative simulations gas was loosing energy a too high rate (Cole, 1991) resulting in a runaway collapse during which the gas turns its thermal energy into radiation loosing pressure support of the baryonic component. The uninhibited cooling led to excessive star formation ultimately resulting in galaxies that are too dense and have to a too high stellar mass (Balogh et al., 2001), commonly known as the *overcooling problem*. Furthermore, the such obtained galaxies had to little rotational support and thus were too small compared to real galaxies (Navarro and Steinmetz, 2000), an issue known as the *angular momentum* problem.

The key missing ingredient turned out to be feedback from supernovae (SN) and from active galactic nuclei (AGNs) which introduce heat into the galactic but also extra-galactic gas, balancing the undergoing cooling processes. Depending on their initial mass and metallicity, many stars end their lives as supernovae, whereas most relevant for galaxy evolution are supernovae of type Ia and core collapse supernovae (e.g. Binney and Merrifield, 1998). During these explosions most of the stellar mass is returned to the surrounding gas in a hot and metal-enriched form balancing cooling especially in galaxies less massive than the Milky Way. Furthermore, galaxies typically host a supermassive black hole (SMBH) at their centre (Kormendy and Richstone, 1995) which gravitationally attracts and accretes gas from the galaxy. Friction in the accretion disc liberates radiative energy which leaves the halo and makes the central SMBH appear very luminous, leading to the term *active galactic nucleus* (AGN). Furthermore, magnetic fields can wind up and collimate the radiative energy into narrow opposite oriented relativistic jets. Ultimately the state of the AGN and the form of its feedback depend on the strength of the accretion onto the black hole which determines the amount of liberated energy. AGN feedback is especially relevant for the energy balance of galaxies more massive than the Milky Way, as well as groups and clusters.

These processes governing galaxy evolution cover a wide range of scales and interplay in a highly non-linear way, making numerical simulations a unique tool to study this problem. Due to their high complexity, these physical feedback processes could be incorporated into sophisticated subgrid models for numerical simulations, which produce realistic galaxies

with observed properties, only recently. Later in this chapter, we will give a brief overview of the simulation techniques used in the field to simulate the baryonic component, as well as of the subgrid models for the fundamental physical process outlined above that are necessary to produce realistic galaxies. We want to note that there is other physics that is likely to play a significant role in galaxy formation, like magnetic fields, cosmic rays, or other missing processes. In this thesis we however focus on the feedback processes, their relevance for galaxy evolution, and their interaction with the cosmic gas reservoir.

## 1.4 Relevance of feedback physics

The key ingredient that enabled the latest generation of hydrodynamical simulations to produce galaxies with realistic sizes and morphologies is supernovae and AGN feedback. Feedback introduces hot, metal-enriched gas into a galaxy and its surrounding and expels a large fraction of gas from galaxies through large-scale outflows, solving the overcooling problem and the angular momentum problem in galaxy formation. The expelled gas penetrates the circum-galactic medium (CGM) and the IGM changing the properties of the gas reservoir for galaxy formation on the largest scales of the universe. In this thesis we will employ state-of-the-art cosmological simulation suites Illustris and IllustrisTNG alongside with our own simulations to investigate the impact of feedback processes on the gas content and properties both inside haloes hosting realistic galaxies as well as in the inter-galactic medium (IGM) and the implications arising from it.

### 1.4.1 The rotational support of galaxies and their haloes

First, we investigate the role that feedback processes play in shaping realistic galaxies by solving the angular momentum problem. The basic property that is characteristic for the size of a galaxy and therefore also crucial for the emerging galaxy morphology, is the specific angular momentum (angular momentum per unit mass) of a galaxy or its halo. Initially, both dark matter and baryons gain the same specific angular momentum from torques from the surrounding gravitational tidal field. At early times, when haloes are still small fluctuations of the density field, it is possible to calculate the torque on a halo applying perturbation theory (Peebles, 1969). After collapse, haloes can be approximated as point masses which generate a tidal field that interacts with the mass distribution inside a halo approximated by its quadrupole moment (Hoyle, 1949), and again calculate the torque experienced by a halo. The total torque generating the '$initital$' angular momentum of haloes can be obtained interpolating between these two approximations. The origin of an initial angular momentum

due to above processes is known as *tidal torque theory*. Amongst others it predicts a linear growth of angular momentum with time that was confirmed by N-body simulations for the early phase of structure formation (Barnes and Efstathiou, 1987), contributing to the success of the theory. The key prediction from the tidal torque theory is that both dark matter and the baryons inside gravitationally self-bound haloes have identical specific angular momentum, as they are equally subject to the purely gravitational forces generating the spin through tidal torques. However, non-radiative simulations have shown that conservation of the initial angular momentum (to good approximation) results in the angular momentum problem producing galaxies too small in size compared to observed galaxies. Therefore, in Chapter 2 and 3 of this thesis we aim to first characterise the amount of specific angular momentum in haloes hosting realistic galaxies, and second to identify the role of feedback in regulating the baryonic angular momentum through large-scale outflows leading to the formation of galaxies with realistic sizes and morphologies inside haloes.

### 1.4.2 The state of the diffuse gas and the observed Lyman-$\alpha$ absorption

Galaxies lose a large fraction of their gas due to feedback driven outflows which penetrate the CGM and IGM. Nonetheless, up to this day it has been a common assumption in theoretical studies of the IGM that it is unperturbed by galactic outflows (see Lukić et al., 2015, for the most recent in depth study, and references therein). In Chapter 4 of this thesis we therefore aim at characterising the impact of feedback driven outflows on the statistical properties of the IGM. The state of the diffuse cosmic gas is of significant importance for galaxy formation as it provides the large-scale gas reservoir for accretion onto haloes and for galaxy formation within those. Altered properties of the accreted gas impact how and at which rate gas settles in and forms a central galaxy. In our study, we employ the Lyman-$\alpha$ forest to probe the state of the IGM.

The Lyman-$\alpha$ forest is a large set of absorption lines in the spectra of quasi-stellar objects (QSO's or quasars). The absorption arises due to neutral hydrogen embedded in the large-scale structure of the universe that is intervening the line of sight towards the quasar (e.g. Rauch et al., 1997). Whenever the light emitted by the background quasar passes through neutral hydrogen a fraction (depending on the density of the neutral hydrogen) of the emitted photons are used to excite an electron in the hydrogen atom from its ground state to the first excited state. This electron transition is known as Lyman-$\alpha$ transition that has a restframe wavelength of $\lambda_{\mathrm{Ly}\alpha} = 1215.67$ Å and an associated frequency and temperature of

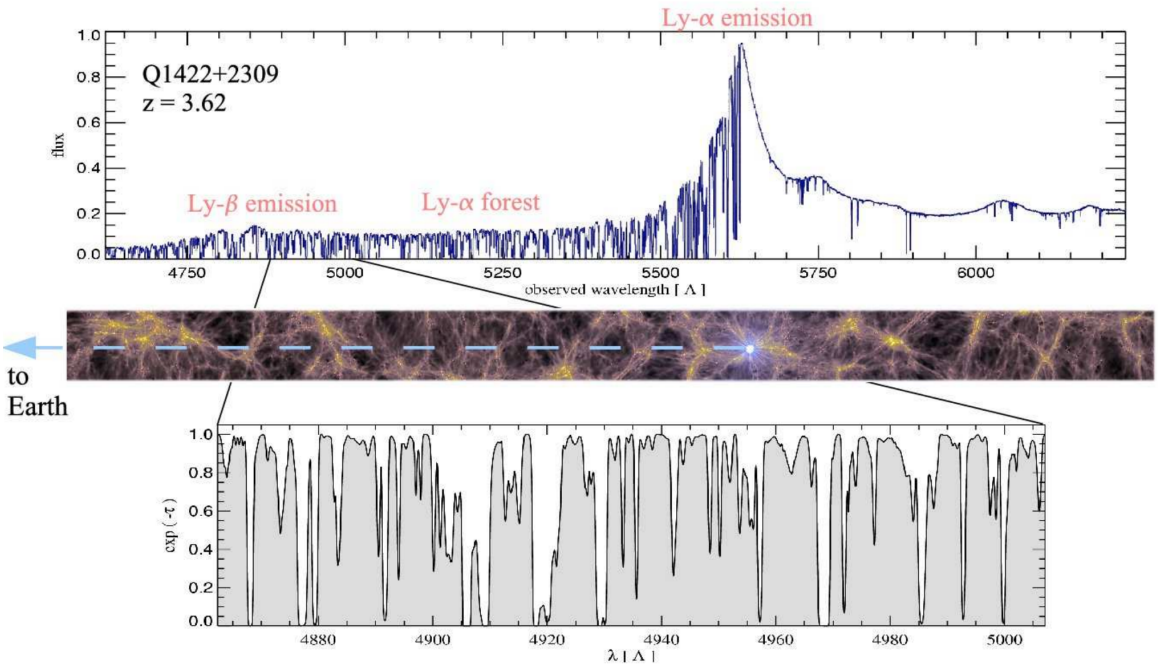


Figure 1.1: Schematic representation of the Lyman-$\alpha$ forest as a probe of the large scale structure of the universe (taken from Springel et al. (2006)). *Top panel* : shows a typical QSO absorption spectrum at $z = 3.62$. Bluewards (left) of the Lyman-$\alpha$ absorption line *Middle panel* : visualisation of the large scale gas distribution as it arises in a state-of-the-art cosmological simulation based on a $\Lambda$CDM cosmology. *Bottom panel* : a chunk of the full Lyman-$\alpha$ absorption spectrum as it is obtained from a simulation output at a constant redshift of $z = 3$.

$$\nu_{\mathrm{Ly}\alpha} = 2.47 \cdot 10^{15} \ \ [Hz], \tag{1.31}$$

$$T_{\mathrm{Ly}\alpha} = \frac{h_{\mathrm{p}} \nu_{\mathrm{Ly}\alpha}}{k_{\mathrm{B}}} = 1.18 \cdot 10^{5} \ \ [K], \tag{1.32}$$

respectively (Mo et al., 2010), where $h_{\mathrm{p}}$ is the Planck constant, and $k_{\mathrm{B}}$ the Boltzmann constant. A more detailed discussion of Lyman-$\alpha$ absorption as well as of the statistical properties of the Lyman-$\alpha$ forest will be given Chapter 4 of this thesis. In Fig. 1.1 we show a schematic representation of the Lyman-$\alpha$ forest, as it is seen in observational data of a typical QSO absorption spectrum at $z = 3.62$ (top panel) compared to its counterpart derived from simulation output (bottom panel).

The outflow induced changes in the density distribution of the inter-galactic gas change amongst others the theoretically predicted auto-correlation of the Lyman-$\alpha$ forest compared to

previously derived results from an unperturbed IGM. This also impacts the cross-correlation of the Lyman-$\alpha$ forest with other tracers of the large-scale structure (LSS), and the corresponding bias parameters of those correlations with respect to the underlaying dark matter density. Precise knowledge of both is necessary for surveys such as SDSS/eBOSS (Schlegel et al., 2015) to derive the baryonic acoustic oscillation (BAO) scale to the claimed precision and put constrains on the Dark Energy equation of state. The work presented in Chapter 4 of this thesis is a first step on the way to provide a profound theoretical understanding of how and to which extend Lyman-$\alpha$ forest statistics can be used as a probe for the properties of Dark Energy in a universe that is highly impacted by non-linear galaxy formation and evolution physics.

## 1.5 Cosmological simulations of galaxy formation

Provided a set of theoretical subgrid models for the above discussed galaxy evolution and feedback physics, it is possible to study galaxy formation by either employing zoom-in simulations of individual galaxies or by employing simulations of cosmological volumes containing millions of early-type, late-type and irregular galaxies covering the full spectrum of possible morphologies and colours. Zoom-in simulations are a unique tool to study individual objects at a resolution that otherwise is not affordable. The recent AURIGA project (Grand et al., 2017) employs the AREPO code to simulate isolated Milky-Way like galaxies in cosmological zoom-in runs at several resolutions levels, whereas the level 3 simulations reach a unprecedented resolution of $\sim 5 \cdot 10^4 M_\odot$ in dark matter mass and $\sim 6 \cdot 10^3 M_\odot$ in baryonic mass. At this resolution, detailed structure within individual galaxies can be resolved, enabling the study of phenomena such as spiral arms or bars within a thin stellar and gas disc (Grand et al., 2017), warps (Gómez et al., 2017), or satellites (Simpson et al., 2018). Going beyond this resolution, gas particles or cells cannot be assumed to contain a SSP anymore and more sophisticated physics models for star formation and ISM physics are required. The development of subgrid models for a resolution of less than $\sim 1000\, M_\odot$ per gas element is a major research effort today.

To establish the statistical relevance of individual processes for the emerging galaxy properties, large samples of galaxies are needed. Those can be obtained in large-scale cosmological simulations of representative volumes of the universe. As the universe is homogeneous and isotropic on large scales, a representative volume can be simply replicated in all directions beyond the actual simulation volume providing convenient periodic boundary conditions. In the following, we will employ the cosmological hydrodynamical simulation *Illustris* (Vogelsberger et al., 2013) executed with the code AREPO that encompasses a

comoving volume of $75^3$ Mpc$^3/h$ that is evolved from redshift $z = 127$ to $z = 0$. Illustris employed $1820^3$ dark matter particles and $1820^3$ initial gas cells which given a WMAP7 cosmology (Komatsu et al., 2011) corresponds to a mass resolution of $6.26 \cdot 10^6 M_\odot$ in dark matter and $\sim 1.26 \cdot 10^6 M_\odot$ in baryonic matter. Illustris reproduces diverse galaxy properties across time as well as the observed morphological mix (Genel et al., 2014, Vogelsberger et al., 2014b) which makes it a unique tool to study processes that are crucial for galaxy formation. In addition to this main Illustris simulation, the Illustris simulation suite further contains two simulations at reduced resolution by a factor of two and four per dimension, as well as dark matter only counterparts to each of the hydrodynamical simulations, and non-radiative counterparts to the two lower resolution simulations. This setup uniquely allows to study the impact of baryonic physics onto the dark matter properties, as well as to distinguish behaviour of the gas component that is due to its hydrodynamic nature from what is caused by galaxy formation physics.

However, some deficiencies in the original Illustris physics models for galaxy formation have been detected and improved upon for the Illustris 'the next generation' (TNG) project. The most significant changes include several improvements in the treatment of galactic winds (Pillepich et al., 2018), a new model for kinetic AGN feedback (Weinberger et al., 2017), and for the first time the inclusion of a model for magnetic fields (Pakmor et al., 2014). We give a in depth description of the employed subgrid models and the invoked changes in section 1.7. The IllustrisTNG project is a suite of simulations that resimulates the original Illustris volume at the three resolution levels with the new set of galaxy formation subgrid models and a Planck Collaboration et al. (2016b) cosmology, whereas the Illustris simulation counterpart is referred to as IllustrisTNG simulation or TNG100. The altered cosmology results into a resolution of $7.46 \cdot 10^6 M_\odot$ in dark matter mass and $\sim 1.39 \cdot 10^6 M_\odot$ in baryonic mass in TNG100. Furthermore, the IllustrisTNG suite contains a $\sim 300^3$ Mpc$^3$ volume at reduced resolution (TNG300) that can be uniquely used to study a statistical sample of groups and clusters, as well as a $\sim 50^3$ Mpc$^3$ volume (TNG50) at increased resolution that is particularly suitable to study satellite galaxies. We will employ simulations from both the Illustris and IllustrisTNG suites alongside with our own simulations to investigate the impact of feedback driven outflows.

## 1.6 Cosmological Hydrodynamical Codes

Before discussing how the most relevant physical processes for galaxy formation can be encompassed in effective subgrid models for numerical simulations, we provide an overview of state-of-the-art numerical methods for fluid dynamics and their coupling to gravity, on

top of which galaxy formation physics can be implemented in a second step. In the past decade numerical simulations have become an integral part of astrophysics, as a novel and independent way to study the chaotic and non-linear processes taking place during structure formation. Numerical codes that are used for galaxy formation simulations within the ΛCDM cosmology share a common structure. The collisionless dark matter is simulated with particle-based N-body methods, and is coupled to the cosmic gas that is treated as a hydrodynamic fluid. Whereas modern implementations of N-body methods yield the same results for the evolution of dark matter to high precision, larger variations exist in the outcome of the hydrodynamical interactions of the gas component. To obtain the motion of an ideal fluid, one has to solve the *Euler equations*:

$$\frac{d\rho}{dt} + \rho \nabla \mathbf{v} = 0, \tag{1.33}$$

$$\frac{d\mathbf{v}}{dt} + \frac{\nabla P}{\rho} = \mathbf{0}, \tag{1.34}$$

$$\frac{du}{dt} + \frac{P}{\rho} \nabla \mathbf{v} = 0, \tag{1.35}$$

where $P$ denotes the pressure, $\rho$ the density, $\mathbf{v}$ the velocity, and $u$ the thermal energy per unit mass of the fluid. These equations formulate mass conservation, momentum conservation and energy conservation, respectively, for an inviscid ideal fluid.

There are two fundamentally different ways of following the gas flow mainly used in astrophysical applications. Those approaches are called *Eulerian* and *Lagrangian* depending on the structure and motion of the computational elements. In a *Lagrangian* approach the mass of the computational elements is constant in time. Such an approach is automatically adaptive to complex geometries and can cover a large dynamic range, two properties that are of crucial importance in astrophysical applications. The computational elements of a Lagrangian technique can be cells of a mesh that move with the mass flow or particles that serve as interpolation points for the underlying continuous fluid properties. The most widely used Lagrangian simulation technique is *Smoothed Particle Hydrodynamics* (SPH) that adopts the latter approach. *Eulerian* techniques use a static mesh with individual cells as computational elements which exchange content through a mass flow across the cell boundaries. This approach allows to faithfully follow the mixing of the gas and all of its properties (especially metals) and to capture hydrodynamic shocks. To be able to deal with the large dynamic range of astrophysical problems, Eulerian codes are used in modern applications together with adaptive mesh refinement (AMR) techniques. In the following sections, we give a more detailed insight in the simulation techniques introduces here.

### 1.6.1 Smoothed particle hydrodynamics

The Lagrangian *Smoothed Particle Hydrodynamics* (SPH) approach uses particles of constant mass as computational elements. Besides its mass $m_i$ every particle $i$ is characterised by its position $\mathbf{r}_i$, density $\rho_i$, and specific entropy $K_i$. Every particle thus also has an associated finite volume $V_i = m_i/\rho_i$. These particles are used as interpolation points for all quantities (fields) of interest. Any field $F(\mathbf{r})$ can be approximated through a smoothed version $F_s(\mathbf{r})$ that is defined as convolution of $F(\mathbf{r})$ with a kernel $K(\mathbf{r}', h)$,

$$F_s(\mathbf{r}) = \int F(\mathbf{r}')K(\mathbf{r}-\mathbf{r}', h)d\mathbf{r}', \tag{1.36}$$

where $h$ is the characteristic width of the kernel. Modern applications typically adopt a cubic spline $K(r,h) = w(r/2h)$ with

$$w(q) = \frac{8}{\pi}\begin{cases} 1-6q^2+6q^3, & 0 \leqslant q \leqslant \frac{1}{2}, \\ 2(1-q)^3, & \frac{1}{2} < q \leqslant 1, \\ 0, & q > 1, \end{cases} \tag{1.37}$$

normalised to unity in three dimensions. The cubic spline resembles a Gaussian, but with a finite support, such that it drops to zero for $r = 2h$ and approaches the Dirac Delta $\delta$ in the limit $h \to 0$. The smoothed field is continuous and differentiable due to the differentiability of the kernel. In case of discrete sampling points, Eq. 1.36 becomes

$$F_s(\mathbf{r}) \simeq \sum_j \frac{m_j}{\rho_j} F(\mathbf{r}_j)K(\mathbf{r}-\mathbf{r}_j, h), \tag{1.38}$$

which constructs a smoothed version of a property of interest $F_s(\mathbf{r})$ at any point $\mathbf{r}$ in space. It becomes apparent that the finite support is crucial to reduce the summation to a finite number of neighbouring particles and such to limit the computational cost of the procedure.

To minimise errors in energy conservation, a constant mass inside the kernel volume is required. This is easily achieved in SPH due to the variability of the smoothing length in space and time, $h = h(\mathbf{r}, t)$, that can automatically adopt to the sampling particle density. The *gather* approach follows exactly that strategy and choses a smoothing length $h(\mathbf{r})$ for any position in space $\mathbf{r}$ such that the kernel volume around this point includes a prescribed constant number of neighbouring particles. Alternatively, all neighbouring particles $j$ can be assigned a smoothing length $h(\mathbf{r}_j)$ to cover a constant number of their neighbours. In this *scatter* approach, it is then evaluated what neighbouring particles overlap with their kernel volumes with the position $\mathbf{r}$ and the respective contribution from their kernels is added.

To obtain the time evolution of the system prescribed by the equations of motion one has to discretise the Euler equations given in Eq. 1.33-1.35. The Euler equations of an ideal inviscid gas can be derived from the Lagrangian

$$L = \int \rho \left( \frac{\mathbf{v}^2}{2} - u \right) dV \tag{1.39}$$

(Eckart, 1960). Gingold and Monaghan (1982) first proposed that it is therefore possible to first discretise Eq. 1.39 and then apply the Lagrangian formalism to the discretised Lagrangian

$$L_{discretised} = \sum_i \left( \frac{1}{2} m_i \mathbf{v}_i^2 - m_i u_i \right) \tag{1.40}$$

to obtain the desired discretised equations of motion, instead of working with the Euler equations directly. This idea was first worked out by Springel and Hernquist (2002).

The Euler equations are five equations for the six unknown variables, namely gas density $\rho$, velocity $\mathbf{v}$, pressure $P$, and internal energy $u$. Hence, to solve this system of equations (whether directly or from the Lagrangian) a closure relation is required. Such a relation can be obtained from statistical microphysics in form of a *equation of state* for the pressure of a fluid,

$$P = (\gamma - 1) \rho u, \tag{1.41}$$

where $\gamma = 5/3$ is the adiabatic index for a mono-atomic ideal gas. In discretised form the equation of state reads

$$P_i = (\gamma - 1)\ \rho_i\ u_i = K_i\ \rho_i^{\gamma}, \tag{1.42}$$

where in the second step it has been assumed that the internal energy of a gas particle $i$ can be expressed through an entropic function $K_i$ that is constant for an isentropic fluid. The thermal energy per unit mass for every particle can therefore be expressed as

$$u_i = K_i\ \frac{\rho_i^{\gamma-1}}{\gamma - 1}. \tag{1.43}$$

Applying the Lagrangian formalism to Eq. 1.40 then yields the equation of motion,

$$\frac{d\mathbf{v}_i}{dt} = -\sum_{j=1}^{N} m_j \left( f_i \frac{P_i}{\rho_i^2} \nabla_i K(\left|\mathbf{r}_i - \mathbf{r}_j\right|, h(\mathbf{r}_i)) + f_i \frac{P_j}{\rho_j^2} \nabla_i K(\left|\mathbf{r}_i - \mathbf{r}_j\right|, h(\mathbf{r}_j)) \right), \tag{1.44}$$

where $f_i$ is defined as

$$f_i = \left(1 + \frac{h_i}{3\rho_i}\frac{\partial \rho_i}{\partial h_i}\right)^{-1}. \tag{1.45}$$

As the constant mass and specific entropy of SPH particles automatically ensure mass conservation (Eq. 1.33) and energy conservation (Eq. 1.34), the discretised solution of the momentum conservation equation (Eq. 1.34) given through Eq. 1.44 fully determines the future evolution of the system. Eq. 1.44 determines for every particle the distance it is going to travel for a given timestep.

The above formulation is Galilei invariant and conserves energy (as there is no explicit time dependence of the Lagrangian), momentum (due to translational invariance of the Lagrangian), angular momentum (due to rotational invariance of the Lagrangian), mass (particles of constant mass), and entropy. However, the inherent entropy conservation is in conflict with entropy increase at shock fronts. Therefore, in order to be able to properly capture the physics of shocks and other discontinuities, artificial viscosity has to be included.

Furthermore, as the cosmic gas does not only move under the gravitational influence of an external potential provided by the dark matter, but also interacts gravitationally among itself, the Euler equations have to be coupled to *self-gravity* of the gas. This can be achieved taking into account the gravitational potential experienced by a gas particle from all other gas particles

$$\Phi(\mathbf{r}_i) = G\sum_j m_j \phi(\mathbf{r}_i - \mathbf{r}_j, \varepsilon_j), \tag{1.46}$$

where $\varepsilon_i$ is the gravitational softening length of a particle $i$. This leads to an additional term for the gravitational potential energy in the Lagrangian,

$$L_{grav} = \sum_i \left(\frac{1}{2} m_i \mathbf{v}_i^2 - m_i u_i\right) - \frac{G}{2}\sum_{ij} m_i m_j \phi(r_i - r_j, \varepsilon_j), \tag{1.47}$$

from which again the equations of motion for the velocity have to be worked out applying the Lagrangian formalism.

SPH is a very robust approach to hydrodynamics with automatically adaptive resolution and excellent conservation properties. However, this also implies that cases where the entropy of the gas actually changes (shocks and other discontinuities) have to be handled manually, introducing a source of error into the code from the choice of when artificial viscosity is triggered. Also the ability to capture shocks and other discontinuities is inhibited due to the averaging procedure. Furthermore, no mixing of gas or any of its properties can happen between SPH particles, and averages have sometimes to be done across particles with substantially different properties (especially at later times in a simulation). In such cases SPH

particles lose their original meaning of sampling points for a continuous underlaying field. Also, this and the limited number of neighbouring particles entering the kernel increases the artificial noise in the averaged properties, which limits the accuracy in real applications.

### 1.6.2 Eulerian methods with adaptive mesh refinement

Eulerian methods compute hydrodynamics on a uniform cartesian mesh and thus suffer severely from their inability to sufficiently resolve regions of high clustering that are the sites of galaxy formation. The Eulerian approach can however be made suitable for astrophysical applications when it is used together with adaptive mesh refinement (AMR) techniques. The original implementation of AMR was through a so called 'patch-based' or 'block-based' approach (Berger and Oliger, 1984, Berger and Colella, 1989) that builds a hierarchy of grids with increasing resolution covering chosen patches within the whole domain. First, the entire domain of interest is covered with a uniform Cartesian grid at low resolution, called the root grid. Regions of increased clustering of matter (or otherwise of interest) are then identified and covered as a whole by a grid with the next level higher resolution. Typically, the resolution increases by a factor of two per dimension for each level. Within those patches new patches can be identified and covered by the next grid in hierarchy, and so on. The grid hierarchy can be in principle arbitrarily deep. The mesh refinement can either be static (performed only once at the beginning of the simulation) or adaptive to the geometry of the problem by identifying patches of proper size at every time step. Modern implementations of the patched-based approach are employed for example in ATHENA (Stone et al., 2008) which has options for both static and adaptive mesh refinement, or ENZO (Bryan et al., 2014). An alternative to the 'patch-based' approach is the 'tree-based' approach (Khokhlov, 1998) which refines the grid on a cell by cell basis by dividing a parent cell into two new cells per dimension (resulting into eight new cells in three dimensions), effectively building a recursive tree structure. This approach has the advantage that refinement is done exactly, always, and only when needed, which comes at the cost of producing many more interfaces between different resolutions at which the accuracy of the hydrodynamical extrapolations is reduced. The 'tree-based' approach is for example adopted in RAMSES (Teyssier, 2002).

The computational elements of an Eulerian mesh are static, such that (in contrast to SPH particles) no movement of the cells themselves has to be calculated. What changes throughout time, are the physical properties of the individual cells through fluxes across cells interfaces. The relevant hydrodynamic quantities can be encapsulated into the so called *state vector*

$$\mathbf{U}(\mathbf{x},t) = \begin{pmatrix} \rho \\ \rho\mathbf{v} \\ \rho e \end{pmatrix}, \tag{1.48}$$

where $e = u + \mathbf{v}^2/2$ is the total energy per unit mass and $u$ the thermal energy per unit mass. Introducing the *flux function*

$$\mathbf{F}(\mathbf{U}) = \begin{pmatrix} \rho\mathbf{v} \\ \rho\mathbf{v}\mathbf{v}^T + P \\ (\rho e + P)\mathbf{v} \end{pmatrix}, \tag{1.49}$$

the Euler equations Eq. 1.33-1.35 can be written in compact form,

$$\frac{\partial \mathbf{U}}{\partial t} + \nabla \mathbf{F} = 0, \tag{1.50}$$

which is a hyperbolic conservation law. On a discretised mesh where the averaged properties for every cell $i$ with volume $V_i$ can be obtained through

$$\mathbf{U}_i = \frac{1}{V_i} \int_{\text{cell } i} \mathbf{U}(\mathbf{x})\, dV, \tag{1.51}$$

Eq. 1.50 can be brought in finite volume form and integrated out to yield a scheme for updating the cell averaged quantities

$$\mathbf{U}_i^{(n+1)} = \mathbf{U}_i^{(n)} - \frac{\Delta t}{\Delta x} \left( \hat{\mathbf{F}}_{i+1/2}^{(n+1/2)} - \hat{\mathbf{F}}_{i-1/2}^{(n+1/2)} \right), \tag{1.52}$$

where $\Delta t$ is the time between two timesteps $n$ and $n+1$, $\Delta x$ the one-dimensional length of a cubic cell, and $\hat{\mathbf{F}}^{(n+1/2)}$ the time-averaged flux, whereas the subscript $i+1/2$ denotes the flux over the right cell interface of cell $i$, and $i-1/2$ over the left cell interface, for a one-dimensional problem. The flux across a cell boundary is obtained by first interpolating the cell's primitive variables to cell interfaces. The interpolated values are then used to solve the Riemann problem at the cell interface. The solution to the Riemann problem yields the desired flux at the beginning of the timestep. This initial flux is used to predict the updated cell values mid timestep which are then used to recalculate the flux in the middle of the timestep. The updated mid timestep flux is then considered to be a fair estimate for the time-averaged flux $\hat{\mathbf{F}}^{(n+1/2)}$ and is applied across the whole timestep. Alternatively, the flux at the beginning of the timestep can be interpolate to the end of the timestep and the time-averaged flux can be obtained as an average of the flux at the beginning and at the end of the timestep. The idea of solving the Riemann problem at the cell interfaces to obtain the correct fluxes goes back to the mathematician Sergei K. Godunov, such that

Eq. 1.52 is also known as Godunov's scheme. It can be easily extended to two or three dimensions by adding fluxes across the additional cell interfaces in analogy to the last term in Eq. 1.52. Due to this structure, the three dimensional version of this equation can be written down as three independent one-dimensional equations. It is then possible to either apply all flux updates simultaneously in a so called unsplit scheme, or to treat the three dimensional problem as three independent one-dimensional problems and apply the such obtained fluxes consecutively. In this so called dimensional splitting approach, the cell values and therefore all fluxes are recalculated after each (one-dimensional) update. To ensure second order accuracy, the dimensionally split approach however requires a specific order in which the fluxes are applied (Springel, 2016).

Furthermore, to make Godunov's scheme second order accurate, it is insufficient to approximate the call values as piece-wise constant, like it is done in Eq. 1.51. Second order can be achieved by piece-wise linear reconstruction based on estimated gradients for each cell. However, it is crucial to apply slope limiting procedures to ensure that no new extrema are introduced when extrapolating the cell values to the cell interfaces, which can lead to large spurious oscillations (Springel, 2016). Alternatively, it is possible to apply higher order methods like e.g. Discontinuous Galerkin (DG) methods. Modern grid codes used for astrophysical applications all rely on Godunov's method, but differ in their approaches to calculate second order accurate fluxes, and in their choices of slope limiters.

Coupling Eulerian methods to self-gravity is achieved by adding a source term to the right hand side of the Euler equations Eq. 1.33-1.35,

$$\frac{\partial \mathbf{U}}{\partial t} + \nabla \mathbf{F} = \begin{pmatrix} 0 \\ -\rho \nabla \Phi \\ -\rho \mathbf{v} \, \nabla \Phi \end{pmatrix}, \tag{1.53}$$

where the gravitational potential $\Phi$ is given by the Poisson equation $\nabla^2 \Phi = 4\pi G \rho$. Working out an updating scheme for the cell averaged quantities $U_i$ from the modified Euler equations leads to an additional term on the right hand side of Eq. 1.52 (see Teyssier (2002) for more detail).

Grid codes faithfully follow the mixing of the gas and can successfully capture shocks and other discontinuities. Also, static cartesians meshes allow for an easier implementation of higher order methods. The most severe limitation of Eulerian approaches is their lack of manifest Galilei invariance. In presence of large bulk flows the numerical diffusivity is strongly increased. It can be quantified by means of the numerical diffusion constant $D = v\Delta x/2$ of first order schemes, where $v$ is the velocity of the flow and $\Delta x$ the cell width in one dimension. This effect can be reduced by choosing smaller mesh cells or employing

higher order schemes, but the inherent problem remains. Furthermore, both large bulk flows of velocity $v$ as well as reduced cell sizes in order to suppress numerical diffusion impact the largest timestep possible, as dictated by the Courant-Friedrichs-Levy (CFL) condition, $\Delta t_{\max} = \Delta x/(|v| + c_s)$, where $c_s$ is the local sound velocity, making the simulation ultimately slow. Also, applied to galaxy formation, grid codes cause a spurious alignment of the orientation of galaxies (defined by e.g. their spin vector) with the grid axis (Hahn et al., 2010), which comes from the fact that flux is only possible along the cartesian coordinate axes.

### 1.6.3 Arbitrary Lagrangian-Eulerian methods

The Lagrangian and Eulerian approach can also be combined into a hybrid, so-called Arbitrary Lagrangian-Eulerian (ALE) method, where the computational elements are neither fixed in space nor do they contain the same constant mass throughout the whole simulation. Those methods typically employ a mesh that follows the mass flow, adapting to the changing geometry, but also allowing for mass exchange between the cells of the mesh, combining advantages of both approaches. The name of ALE methods goes back to the fact that their mesh can be made static, turning the scheme effectively into a Eulerian method. But they can also be set up in such a way that no mass exchange between the cells is allowed, making them Lagrangian schemes.

For astrophysical applications there exists one representative of this class, which is the code AREPO that is based on an unstructured moving mesh (Springel, 2010a). AREPO employs as its mesh a *Voronoi tessellation*, which is a decomposition of space in polygons (in 2D) or polyhedra (in 3D) that constitute the cells of the mesh. The mesh geometry is changing continuously in time as the mesh is built from a moving set of mesh generating points. For astrophysical applications, AREPO is usually used in a *quasi-Lagrangian* mode, where the cell velocity $\mathbf{w}_i$ of cell $i$ is given by the fluid velocity $\mathbf{v}_i$ of that cell, without applying a small additional corrective velocity term that would make the approach fully Lagrangian. This allows for the necessary exchange of mass and other gas properties enabling mixing which is of crucial importance in astrophysical applications. Given a set of mesh generating points, a cell of the Voronoi tessellation is defined as all points in space that are closer to one mesh generating point than to any other mesh generating point. Based on this set of disjoint cells a *finite-volume* approach can be applied to solve the hydrodynamical equations.

Every cell $i$ with volume $V_i$ is characterised by five (globally) conserved quantities which are the mass $m_i$, momentum $p_i$, and energy $E_i$. Those quantities can be derived from the state vector $\mathbf{U}$ through an integral over the cell volume,

$$\mathbf{Q}_i = \begin{pmatrix} m_i \\ \mathbf{p}_i \\ E_i \end{pmatrix} = \int_{V_i} \mathbf{U} dV. \tag{1.54}$$

The conserved quantities are associated with the five primitive variables density $\rho$, velocity $\mathbf{v}$, and pressure $P$ that can be encapsulated into a vector

$$\mathbf{W}(\mathbf{x},t) = \begin{pmatrix} \rho \\ \mathbf{v} \\ P \end{pmatrix} \tag{1.55}$$

in analogy to the state vector. Applying Gauss' theorem to the total time derivative of $\mathbf{Q}_i$ and inserting the Euler equation Eq. 1.33-1.35 for $\partial_t \mathbf{U}$ yields

$$\frac{d\mathbf{Q}_i}{dt} = -\int_{\partial V_i} \left(\mathbf{F}(\mathbf{U}) - \mathbf{U}\mathbf{w}^T\right) d\mathbf{n}, \tag{1.56}$$

where $\mathbf{w}$ is the velocity, and $\mathbf{n}$ the outward normal vector of the cell interface. With $\mathbf{A}_{ij}$ being the oriented area of the interface between cell $i$ to $j$, pointing from $i$ to $j$, the averaged flux across the cell interface can be writen as

$$\mathbf{F}_{ij} = \frac{1}{A_{ij}} \int_{A_{ij}} \left(\mathbf{F}(\mathbf{U}) - \mathbf{U}\mathbf{w}^T\right) dA_{ij}. \tag{1.57}$$

This can be used to bring Eq. 1.56 in finite-volume form,

$$\frac{d\mathbf{Q}_i}{dt} = -\sum_j A_{ij}\mathbf{F}_{ij}. \tag{1.58}$$

To obtain a scheme for updating the cell averaged conserved quantities, Eq. 1.58 has to be integrated out. However, as the cell interfaces move continuously in time changing their face areas $\mathbf{A}_{ij}$, it is insufficient to estimate a time-averaged flux $\hat{\mathbf{F}}_{ij}^{(n+1/2)}$ and update $\mathbf{Q}_i$ according to

$$\mathbf{Q}_i^{(n+1)} = \mathbf{Q}_i^{(n)} - \Delta t \sum_j A_{ij}\hat{\mathbf{F}}_{ij}^{(n+1/2)}, \tag{1.59}$$

where $\Delta t$ is the time between two timesteps, as was done in the original implementation of AREPO (Springel, 2010a). Eq. 1.59 can be made second order accurate if the cell interfaces are also extrapolated half a timestep forward, $A_{ij}^{(n+1/2)}$. However, this requires an additional mesh construction mid timestep, which invokes significant additional computational cost (additional $\sim 30\%$ of the total runtime). Pakmor et al. (2016) has shown that to ensure

second order accuracy of the code it is also possible to adopt a variation of the second-order Runge-Kutta integration called Heun's method that uses an estimate for the flux at the end of each time step to estimate and apply an averaged flux for updating the conserved quantities $\mathbf{Q}_i$. In detail this is achieved the following way. First, the primitive variables for the next time step are estimated by

$$W_i^{(n+1)'} = W_i^n + \Delta t \frac{\partial \mathbf{W}}{\partial t}, \tag{1.60}$$

whereas the partial time derivative of the primitive variables $\partial_t \mathbf{W}$ can be exactly calculated from the Euler equations given the spatial gradients of these quantities in the cells. Second, for constant interface velocities $\mathbf{w}$ in each time step, the positions of the mesh-generating points for the next time step are given by

$$\mathbf{r}^{n+1} = \mathbf{r}_i^n + \Delta t \ \mathbf{w}_i^n, \tag{1.61}$$

which also determines the cell interfaces $A_{ij}^{n+1}$ for the next time step. Given this, the conserved quantities can be updated by averaging the flux at the beginning of the time step and of its estimated value at the end of the time step/ beginning of the next time step,

$$\mathbf{Q}_i^{(n+1)} = \mathbf{Q}_i^{(n)} - \frac{\Delta t}{2} \left( \sum_j A_{ij}^n \hat{\mathbf{F}}_{ij}^n(\mathbf{W}_i^n) + \sum_j A_{ij}^{n+1} \hat{\mathbf{F}}_{ij}^{(n+1)'}(\mathbf{W}_i^{(n+1)'}) \right), \tag{1.62}$$

where $\hat{\mathbf{F}}$ again denotes the flux that results from solving the Riemann problem at the cell interface. Also in analogy to grid codes, in order to ensure second order accuracy of the scheme, the states entering the Riemann problem are linear extrapolations of the averaged cell quantities $\phi$ to the cell faces,

$$\phi(\mathbf{r}) = \phi_i + \langle \nabla \phi \rangle_i \cdot (\mathbf{r} - \mathbf{s}_i), \tag{1.63}$$

where $\mathbf{s}_i$ is the centre of mass of the cell, and $\mathbf{r} \in V_i$. The gradients $\langle \nabla \phi \rangle_i$ in AREPO are obtained through a local least squares fit (Pakmor et al., 2016), that minimises the sum of the deviations between the cell averaged quantities $\phi_j$ of all neighbouring cells $j$ at their centres of mass $s_j$ and the values of these quantities that are obtained at $s_j$ through extrapolation,

$$S = \sum_j g_j (\phi_j - (\phi_i + \langle \nabla \phi \rangle_i \cdot (\mathbf{s}_j - \mathbf{s}_i)))^2. \tag{1.64}$$

Here, $g_j$ are the weights of the neighbours $j$ that are chosen to increase with the shared interface area $A_{ij}$ and decrease with the relative distance of the cells, $g_j = A_{ij}/|s_j - s_i|^2$. Solving the Riemann problem and obtaining the fluxes always in the rest frame of the cell

interfaces makes the approach implemented in AREPO inherently Galilei invariant. The coupling to self-gravity is done according to Eq. 1.53. AREPO combines the automatic adaptivity and Galilei invariance of Lagrangian approaches with mixing and excellent shock/ discontinuity capturing abilities of Eulerian schemes, making it a unique tool to study astrophysical flows.

## 1.7 Galaxy formation and evolution physics

Galaxy formation and evolution physics cannot be implemented in a simulation code from first principles due to limited resolution. Despite always higher computer performance through technological advances that allows for continuously better resolution, there will be always a limit on the best possible resolution. Therefore, at every stage of code development, physical process which (yet) cannot be resolved have to be modelled in an effective way. In this section we give a description of the subgrid models implemented in the galaxy formation module of the *Illustris* and *IllustrisTNG* simulations presented in Section 1.5, as those simulations are mainly used for the analysis presented in this thesis.

### 1.7.1 Cooling

Initially, gas and dark matter originating from the same (Lagrangian) region in space follow the same trajectories that are prescribed by the gravitational impact from the surrounding density field. However, when forming gravitationally bound structures, dark matter undergoes shell crossing and phase mixing due to its collisionless nature, whereas gas experiences hydrodynamical shocks that heat the gas by converting its kinetic energy in thermal energy.

Assuming that all kinetic energy of the infalling gas is converted into thermal energy, and that the gas is mono-atomic, the temperature increase of the gas with mass $M_{\rm gas}$ and infall velocity $v_{\rm infall}$ can be estimated by writing down energy conservation

$$\Delta E = \frac{3}{2}\, N\, k_{\rm B}\, \Delta T = \frac{1}{2}\, M_{\rm gas}\, v_{\rm infall}^2, \tag{1.65}$$

with the Boltzmann constant $k_{\rm B}$ and the particle number $N = M_{\rm gas}/(\mu\, m_{\rm p})$, where $\mu$ is the mean molecular weight and $m_{\rm p}$ the proton mass. This results into a temperature increase of

$$\Delta T = \frac{\mu\, m_{\rm p}}{N\, k_B}\, v_{\rm infall}^2. \tag{1.66}$$

Except for shock heating, the gas is furthermore heated by photoionisation from local sources as well as from the ultraviolet background (UVB) which is a volume filling ionising

radiation produced by young stars and active galactic nuclei (AGNs), observationally however typically referred to as quasi-stellar objects (QSOs). Photoionisation is the processes in which a photon is absorbed and its energy $E = h\nu$ is being used to unbind an electron

$$\gamma + \mathrm{X} \rightarrow \mathrm{X}^{+} + \mathrm{e}^{-}, \tag{1.67}$$

whereas the surplus energy $\Delta E = h\nu - h\nu_{\mathrm{X}}$ that is not used for ionisation ($E_{ion,\mathrm{X}} = h\nu_{\mathrm{X}}$) is converted into kinetic energy of the electron effectively heating the gas. For a primordial gas composition the heating rate from photoionisation is given by

$$H = n_{\mathrm{H}_0}\ \varepsilon_{\mathrm{H}_0} + n_{\mathrm{He}_0}\ \varepsilon_{\mathrm{He}_0} + n_{\mathrm{He}_+}\ \varepsilon_{\mathrm{He}_+}\ \ [erg/(s\ cm^3)], \tag{1.68}$$

where $n_{\mathrm{H}_0}$ denotes the density of neutral hydrogen $\mathrm{H}^0$, $n_{\mathrm{He}_0}$ that of neutral helium $\mathrm{He}^0$, and $n_{\mathrm{H}_+}$ that of single ionised helium $\mathrm{He}^+$, and

$$\varepsilon_{\mathrm{X}} = \int_{\nu_{\mathrm{X}}}^{\infty} \frac{4\pi J(\nu)}{h\nu}\ \sigma_{\mathrm{X}}(\nu)\ (h\nu - h\nu_{\mathrm{X}})\ d\nu\ \ [erg/s], \tag{1.69}$$

where $\nu_{\mathrm{X}}$ and $\sigma_{\mathrm{X}}(\nu)$ are the threshold frequency and cross section for photoionisation of the species X, and $J(\nu)$ is the intensity of the photoionising radiation at frequency $\nu$ that primarily consists of the UVB intensity and can be increased due to contributions from local sources or decreased in case of self-shielding of the gas.

Besides heating, several radiative processes lead to cooling of the gas component. For a primordial gas composition (at the densities typically resolved in hydrodynamical simulations of galaxy formation) the relevant cooling process are the following two-body processes:

- collisional excitation of neutral hydrogen $\mathrm{H}^0$, neutral helium $\mathrm{He}^0$, and single ionised helium $\mathrm{He}^+$:

$$\mathrm{X} + \mathrm{e}^{-} \rightarrow \mathrm{X}' + \mathrm{e}^{-} \rightarrow \mathrm{X} + \mathrm{e}^{-} + \gamma \tag{1.70}$$

- collisional ionisation of neutral hydrogen $\mathrm{H}^0$, neutral helium $\mathrm{He}^0$, and single ionised helium $\mathrm{He}^+$:

$$\mathrm{X} + \mathrm{e}^{-} \rightarrow \mathrm{X}^{+} + 2\mathrm{e}^{-} \tag{1.71}$$

- standard recombination neutral hydrogen $\mathrm{H}^0$, neutral helium $\mathrm{He}^0$, and single ionised helium $\mathrm{He}^+$:

$$\mathrm{X}^{+} + \mathrm{e}^{-} \rightarrow \mathrm{X} + \gamma \tag{1.72}$$

- dielectronic recombination of single ionised helium $\mathrm{He}^+$:

$$\mathrm{He}^{+} + 2\mathrm{e}^{-} \rightarrow \mathrm{He} + \mathrm{e}^{-} + \gamma \tag{1.73}$$

- bremsstrahlung (free-free emission):

$$\mathrm{X}^{+} + \mathrm{e}^{-} \rightarrow \mathrm{X}^{+} + \mathrm{e}^{-} + \gamma \tag{1.74}$$

In these processes energy that is previously present in kinetic form is either carried away through a photon or is used up for ionisation. The cooling rates for these processes are functions of the temperature $T$, the electron density $n_\mathrm{e}$ and the density $n_\mathrm{X}$ of the relevant species $X$. Therefore, to calculate cooling rates first the electron and species densities have to be determined. Following Katz et al. (1996), this can be done assuming the gas to be optically thin and in ionisation equilibrium with a given UVB:

$$\Gamma_{\mathrm{eH_0}}\, n_\mathrm{e}\, n_{\mathrm{H_0}} + \Gamma_{\gamma\mathrm{H_0}}\, n_{\mathrm{H_0}} = \alpha_{\mathrm{H_+}}\, n_{\mathrm{H_+}}\, n_\mathrm{e}, \tag{1.75}$$

$$\Gamma_{\mathrm{eHe_0}}\, n_\mathrm{e}\, n_{\mathrm{He_0}} + \Gamma_{\gamma\mathrm{He_0}}\, n_{\mathrm{He_0}} = (\alpha_{\mathrm{He_+}} + \alpha_\mathrm{d})\, n_{\mathrm{He_+}}\, n_\mathrm{e}, \tag{1.76}$$

$$\begin{aligned} &\Gamma_{\mathrm{eHe_+}}\, n_\mathrm{e}\, n_{\mathrm{He_+}} + \Gamma_{\gamma\mathrm{He_+}}\, n_{\mathrm{He_+}} + (\alpha_{\mathrm{He_+}} + \alpha_\mathrm{d})\, n_{\mathrm{He_+}}\, n_\mathrm{e} \\ &= \alpha_{\mathrm{He_{++}}}\, n_{\mathrm{He_{++}}}\, n_\mathrm{e} + \Gamma_{\mathrm{eHe_0}}\, n_\mathrm{e}\, n_{\mathrm{He_0}} + \Gamma_{\gamma\mathrm{He_0}}\, n_{\mathrm{He_0}}, \end{aligned} \tag{1.77}$$

$$\alpha_{\mathrm{He_{++}}}\, n_{\mathrm{He_{++}}}\, n_\mathrm{e} = \Gamma_{\mathrm{eHe_+}}\, n_\mathrm{e}\, n_{\mathrm{He_+}} + \Gamma_{\gamma\mathrm{He_+}}\, n_{\mathrm{He_+}}. \tag{1.78}$$

Eq. 1.75-1.78 formulate ionisation equilibrium conditions for $\mathrm{H}^0$, $\mathrm{He}^0$, $\mathrm{He}^+$, and $\mathrm{He}^{++}$, respectively, whereas the left hand side lists processes by which the respective species are created, the right hand side processes through which they are destroyed. Rates for collisional ionisation are denoted by $\Gamma_{\mathrm{eX}}$, rates for photoionisation by $\Gamma_{\gamma\,\mathrm{X}}$, and rates for recombination by $\alpha_\mathrm{X}$. Collisional ionisation and recombination rates are obtained through quantum-mechanical calculations and/or through experimental measurements in combination with theoretical extrapolations into regimes that cannot be realised in the laboratory. Photoionisation rates are calculated as

$$\Gamma_{\gamma\mathrm{X}} = \int_{\nu_\mathrm{X}}^{\infty} \frac{4\pi J(\nu)}{h\nu}\, \sigma_\mathrm{X}(\nu)\, d\nu \;\; [1/s]. \tag{1.79}$$

In addition to ionisation equilibrium also number conservation has to be ensured:

$$n_{\mathrm{H_+}} = n_\mathrm{H} - n_{\mathrm{H_0}}, \tag{1.80}$$

$$n_\mathrm{e} = n_{\mathrm{H_+}} + n_{\mathrm{He_+}} + 2 \cdot n_{\mathrm{H_{++}}}, \tag{1.81}$$

$$(n_{\mathrm{He_0}} + n_{\mathrm{He_+}} + n_{\mathrm{He_{++}}})/n_\mathrm{H} = f_\mathrm{He}/(4 - 4f_\mathrm{He}), \tag{1.82}$$

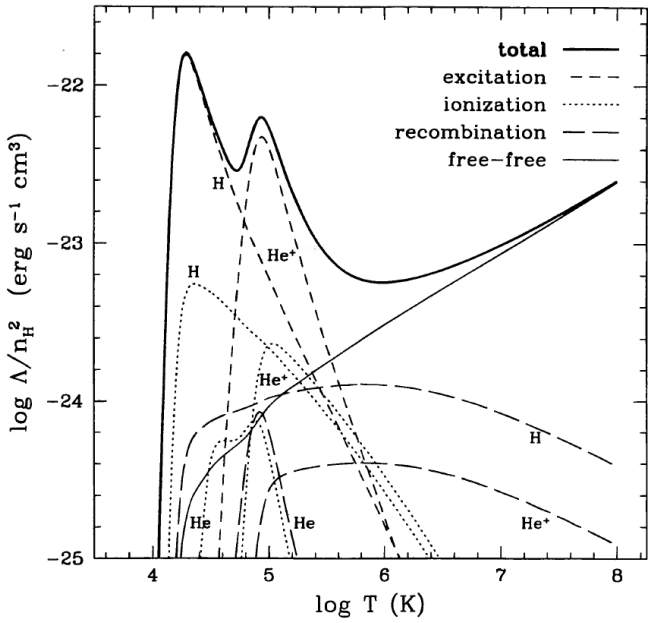


Figure 1.2: Cooling rates from Katz et al. (1996) for a primordial gas composition in ionisation equilibrium in the presence of a photoionising background. This figure shows the relevance of the different process for cooling of the gas as a function of temperature. The solid line shows the total cooling rate. Above $10^6 K$ the gas is fully ionised and the cooling function is dominated by bremsstrahlung. Below that temperature collisional excitation of H and He are the main cooling sources. Below $10^4 K$ the gas becomes neutral and either molecular cooling or the presence of metals is necessary to further lower the gas temperature.

where the number density of hydrogen is given by $n_{\rm H} = \rho f_{\rm H}/m_{\rm p}$. $f_{\rm H}$ and $f_{\rm He}$ denote the mass fractions of hydrogen and helium with respect to the total gas mass, whose primordial values are $f_{\rm H} = 0.76$ and $f_{\rm He} = 0.24$.

This set of seven equations Eq. 1.75-1.78 and Eq. 1.80-1.82 encoding the equilibrium conditions can be recast into six independent equations for the six unknown variables $n_{\rm H_0}, n_{\rm H_+}, n_{\rm He_0}, n_{\rm He_+} n_{\rm He_{++}}$, and $n_{\rm e}$. Those equations can be solved iteratively starting with $n_{\rm H} = n_{\rm e}$. The solution fixes the cooling and heating rates for every simulation timestep $\Delta t$. In Fig. 1.2 taken from Katz et al. (1996) we show the relative importance of the individual two-body processes for the cooling of a primordial gas composition as a function of temperature. The solid line shows the total cooling rate. At intermediate regimes between $10^4 K$ and $10^6 K$ the most important processes are collisional excitation of H and He. Above $10^6 K$ the gas is fully ionised and bremsstrahlung becomes the most dominant cooling mechanism, below $10^4 K$ the gas is essentially neutral and molecular or metal cooling is necessary to further lower the gas temperature.

### 1.7.2 Star formation

Stars form from cold, dense gas that was able to reach the necessary conditions for star formation through cooling. The physics at play in the inter-stellar medium (ISM) that finally leads to star formation is highly complex. At the relevant scales turbulent and magnetic pressure support the gas against gravitational collapse. Which mechanism finally leads to the formation of overdense clumps with runaway cooling leading to star formation is still a major research topic (Mac Low and Klessen, 2004).

However, neither cosmological simulations nor zoom-in simulations of individual galaxies are currently able to resolve ISM scales on which star formation is happening. Therefore, numerical simulations have to rely on effective models for star formation. A successful and widely used model for star formation in simulations of galaxy formation is the self-regulated two-phase model from Springel and Hernquist (2003), used with some modifications (Vogelsberger et al., 2013) in both the Illustris and IllustrisTNG simulation suites. In this model the ISM is described through two phases, namely a volume filling hot gas component and collapsed cold gas clouds, that are in pressure equilibrium. The cold gas component provides the gas reservoir for star formation but simultaneously engages in constant exchange of mass and energy with the hot ambient gas.

Radiative atomic line cooling processes in a primordial gas composition as laid out in above section can cool the gas only to a temperature of about $10^4 K$. Below this temperature the gas becomes neutral and requires either molecular cooling or the presence of metals. The model of Springel and Hernquist (2003) adopts a threshold density $\rho_{th} = 0.13\ \mathrm{cm}^{-3}$ above which the particles/cells are assumed to enter the self-regulated two-phase model for the ISM and become eligible for star formation. Stars form on a characteristic time scale given by

$$t_* = \frac{m_g}{\dot{m}_{sf}}, \tag{1.83}$$

where $m_g$ is the gas mass and $\dot{m}_{sf}$ the star formation rate (SFR). In the model of Springel and Hernquist (2003), it is set to be a function of the density $\rho$

$$t_* = t_0^* \left( \frac{\rho}{\rho_{th}} \right)^{-1/2}, \tag{1.84}$$

where $t_0^*$ a free parameter set to $t_0^* = 2.2$ Gyr, to reproduce the Kennicutt-Schmidt-law (Kennicutt, 1998), which provides a power-law relation between the total gas surface density $\Sigma_{gas}$ and the star formation surface density $\Sigma_{SFR}$ observationally derived from local spiral galaxies. The star formation rate prescribes how much of the total gas mass $m_g$ is converted into stars,

$$\dot{m}_{sf} = -\dot{m}_{gas}, \tag{1.85}$$

in each timestep $\Delta t$. Integrating Eq. 1.85 yields

$$m_{sf} = m_g \left(1 - e^{-\Delta t / t_*}\right), \tag{1.86}$$

defining a probability

$$p(t_*) := 1 - e^{-\Delta t / t_*} \tag{1.87}$$

for a gas particle/cell of mass $m_g$ to be converted into a star particle. For numerical reasons, the mass of individual stellar particles is kept equal to their parent gas particle/cell mass, by always turning the whole gas particle/cell into a star particle. In the moving mesh code AREPO gas cells change their mass, such that an exception is made when the mass of the gas cell is larger than or equal to twice the initial gas cell mass, $m_g \geqslant 2\ m_{target}$. Then a star particle of mass $m_{target}$ is created leaving the gas cell undestroyed with reduced mass $m_g(t + \Delta t) = m_g(t) - m_{target}$. In such a case the probability for star formation is enhanced by a factor of $m_g / m_{target}$,

$$p_e(t_*) = \frac{m_g}{m_{target}} \left(1 - e^{-\Delta t / t_*}\right). \tag{1.88}$$

Combined, the probability for the formation of a star particle of mass $m_*$ can be written as

$$p_g(t_*) = \frac{m_g}{m_*} \left(1 - e^{-\Delta t / t_*}\right). \tag{1.89}$$

To ensure a given star formation rate, every gas particle/cell is converted into a stellar particle with probability given in Eq. 1.89, that is realised by drawing a random number from a uniform distribution. Gas particles/cells that are above the threshold density $\rho_{th}$ but have not been converted into stellar particles are assumed to exhibit a self-regulated two-phase ISM. They cannot be modelled as an ideal gas anymore. Instead, in the model of Springel and Hernquist (2003) the so called equation of state,

$$P_{\text{eff}} = (\gamma - 1)(\rho_h u_h + \rho_c u_c), \tag{1.90}$$

defines the pressure of the gas, where $\gamma$ is the adiabatic index, $\rho_h$ and $\rho_c$ the densities of the hot and cold gas phase, and $u_h$ and $u_c$ the energies per unit mass in the two components, respectively. Eq. 1.90 determines the hydrodynamic properties of the gas, which in AREPO

are provided to the Riemann solver used to properly update the cell quantities like density $\rho$, velocity $\mathbf{v}$, and pressure $P$ for the next timestep.

In SPH star particles inherit the positions of their parent gas particles, whereas in AREPO they are inserted at the mesh generating points of their parent gas cells. Due to the averages taken across the ISM, each stellar particle represents a single-age stellar population (SSP). In the Illustris and IllustrisTNG simulation suites a Chabrier (2003) initial mass function (IMF) $\Phi_{Ch}(m)$ with

$$m_{sf} = \int_0^\infty m\Phi_{Ch}(m)dm \tag{1.91}$$

is adopted.

### 1.7.3 Supernovae driven galactic winds

During their lifetime and at the end of it stars return hot, metal-enriched gas to their surrounding. The major contribution comes from core collapse supernovae (SNII) of stars more massive than $\sim 13M_\odot$ and from stellar winds of less massive stars during their asymptotic giant branch (AGB) phase. Contributions from other stages of stellar evolution that are significant only for the metallicity content of the galaxy, like type Ia supernovae, can and are taken into account in simulations by distributing the returned, enriched mass among neighbouring gas cells using for example a top-hat function. However, attempting the same approach for the return of mass from core collapse supernovae does not account for galactic winds and their effect on galaxy morphology (Puchwein and Springel, 2013). Simply recycling stellar mass from SNII into the surrounding gas leads to a configuration where all the supernova energy is trapped in the dense star forming region where it is efficiently radiated away, leading to the overcooling problem. To reproduce the observed effects of core collapse supernovae driving large-scale winds, simulations of galaxy formation have to rely on phenomenological models for galactic winds.

In star-forming galaxies, star formation and supernova explosions quickly enter a self-regulated regime, such that wind launching can be directly incorporated into the star formation routine neglecting the actual delay time for SNII originating from the particular SSP formed in the given timestep. This is achieved by adding the wind mass loss rate $\dot{m}_w$ on the left hand side of Eq. 1.85,

$$\dot{m}_{sf} + \dot{m}_w = -\dot{m}_g, \tag{1.92}$$

which can be rewritten using the mass loading factor $\eta_w = \dot{m}_w/\dot{m}_{sf}$,

$$\dot{m}_{sf} + \dot{m}_w = \dot{m}_{sf} + \eta_w \, \dot{m}_{sf} = (1+\eta_w) \, \dot{m}_{sf} = (1+\eta_w)\frac{m_g}{t_*}, \tag{1.93}$$

to yield a differential equation for the change of the gas mass,

$$\dot{m}_g = -(1+\eta_w)\frac{m_g}{t_*}. \tag{1.94}$$

The solution to this equation can be obtained in analogy to the solution of Eq. 1.85 to be

$$m_{sf,w} = m_g \left(1 - e^{-(1+\eta_w)\Delta t/t_*}\right), \tag{1.95}$$

which defines a combined probability for star formation and wind launching,

$$p_{sf,w}(t_*) \coloneqq 1 - e^{-(1+\eta_w)\Delta t/t_*}. \tag{1.96}$$

Like in the case of star formation only, whether a gas particle/cell is converted in any of the possible species is decided probabilistically based on Eq. 1.96 by drawing a random number from a uniform distribution. To ensure the proper ratio between the SFR and wind mass loss rate given by the mass loading, star formation is treated in $1/(1+\eta_w)$ of the cases and wind launching in $\eta_w/(1+\eta_w)$ which again is decided probabilistically. The SFR and wind mass loss rate can therefore also be expressed as

$$\dot{m}_{sf} = \frac{-1}{1+\eta_w} e^{-(1+\eta)\Delta t/t_*}, \tag{1.97}$$

$$\dot{m}_w = \frac{-\eta}{1+\eta_w} e^{-(1+\eta)\Delta t/t_*}. \tag{1.98}$$

The conversion of gas particles/cells into star or wind particles is treated exactly as in the case of star formation only, such that the whole gas particle/cell is converted into a star or wind particle unless its mass is larger than $2 \cdot m_{target}$ in which case a star/wind particle of mass $m_{target}$ is spawned.

In the Illustris 'bipolar' wind model, a wind particle is launched with random sign in the direction given by $\mathbf{v} \times \nabla\phi$, where $\mathbf{v}$ is the gas cells velocity in the rest frame of the corresponding FOF halo, and $\phi$ the gravitational potential. In the IllustrisTNG 'isotropic' wind model this directionality is abandoned for simplicity and wind particles are launched isotropically still causing directional outflows, as they propagate in the direction of least resistance (Pillepich et al., 2018). Wind particles are decoupled from the hydrodynamic interactions until they reach a low density region characterised by a threshold value (typically 10% of the threshold density for star formation) or until they reach a maximum travelling

time (typically 2.5% of the Hubble time at the corresponding redshift). When a wind particle recouples, it deposits all its mass (including metals), momentum and thermal energy into the nearest gas cell in AREPO or is simply converted back to a gas particle in SPH. The latter highlights how gas particles with very different properties (especially metallicity content) can be found sampling the same region, making the inherent inability of proper mixing of gas properties a severe problem in SPH.

Motivated by observations by Okamoto et al. (2010) the velocity of the wind particles is set to scales with the local one-dimensional dark matter velocity dispersion,

$$v_w = \kappa_w \, \sigma_{DM}^{1D}, \tag{1.99}$$

where $\kappa_w$ is a free model parameter. The wind velocity can be used to set the mass loading $\eta_w = \dot{m}_w / \dot{m}_{sf}$ either with a momentum driven or an energy driven ansatz. The momentum driven ansatz assumes that the star formation rate defines the momentum gained by the wind

$$e_p \dot{m}_{sf} = \dot{m}_w v_w, \tag{1.100}$$

where $e_p$ is a constant free model parameter, whereas the energy driven ansatz assumes that the star formation rate defines the total energy obtained by the wind

$$e_w \dot{m}_{sf} = \frac{1}{2} \dot{m}_w v_w^2, \tag{1.101}$$

where $e_w$ is again a constant free model parameter. This yields a mass loading of $\eta_w = e_p / v_w$ for the momentum driven case, and $\eta_w = 2e_w / v_w^2$ for the energy driven case. Both driving mechanisms can be combined into a hybrid form,

$$\eta_w = \frac{1}{v_w^2} \left( e_w + \sqrt{e_w^2 + v_w^2 e_p^2} \right), \tag{1.102}$$

which yields the above limiting cases when either $e_w$ or $e_p$ is set to zero. Both Illustris and IllustrisTNG assume energy driven winds. In such a case the proportionality constant $e_w$ represents the total amount of energy from SNII and AGB star that goes into the wind per solar mass formed, and can be expressed in terms of the mean energy of a SNII event per solar mass formed, $E_{SNII} = 1.73 \cdot 10^{-2} \cdot 10^{51} \mathrm{erg} / M_\odot$, as $e_w = \bar{e}_w E_{SNII}$. The proportionality constant is a free model parameter set to $\bar{e}_w = 1.09$ in Illustris to account for the additional contribution from AGB stars. In order to avoid spurious star formation of recoupled cold wind gas, the IllustrisTNG model provides 10% of the initial energy to a wind particle in thermal form. This requires a modification of the purely energy driven ansatz for estimating the mass loading,

$$\eta_w = \frac{2}{v_w^2} e_w (1 - \tau_w), \tag{1.103}$$

where $\tau_w = 0.1$ is the fraction of energy in thermal form. This and a newly introduced metallicity dependence of the wind energy in IllustrisTNG require a recalibration of wind energy scaling factor to $\bar{e}_w = 3.6$, whereas in this more complicated model $\bar{e}_w$ has lost its original physical interpretation and is reduced to a pure model parameter. Furthermore, the IllustrisTNG model incorporates a redshift scaling of the wind velocity that has previously been successfully applied in semi-analytic models to resolve discrepancies between the outcome of the Illustris model and the observed galaxy stellar mass function across redshift, and introduces a wind velocity floor $v_{w,\mathrm{min}}$ to prevent unphysically large mass loading factors in low mass haloes. Combined, the wind velocity scaling in IllustrisTNG reads

$$v_w = \max[\kappa_w \sigma_{DM}^{1D} (H_0/H(z))^{1/3}, v_{w,\mathrm{min}}]. \tag{1.104}$$

The model can successfully reproduce many observed quantities like the galaxy stellar mass function, galaxy sizes, the stellar mass to halo mass relation, and the gas content of haloes (Pillepich et al., 2018) for galaxies smaller than the Milky Way.

### 1.7.4 Black holes and AGN feedback

A second phenomenon that is crucial for the energy balance of galaxies is feedback from active galactic nuclei (AGNs). This mechanism plays a significant role in galaxies more massive than the Milky Way, as above the corresponding halo mass supernovae driven galactic winds are to weak to drive large scale outflows and to provide sufficient energy input to account for various observational properties. AGN feedback is critical to achieve both, as well as to suppress star formation in massive galaxies leading to their quenching.

The Illustris and IllustrisTNG simulations thus both include a subgrid model for black hole (BH) seeding and evolution with associated AGN feedback. In this model all massive haloes are assumed to host a central black hole. A black hole, which is modelled as a collisionless sink particle, is placed at the potential minimum of a halo when the FOF halo mass reaches a threshold value set to $5 \cdot 10^{10} M_\odot/h$. The central black hole is created from the gas cell with the highest density, and set to have a seed mass of $10^5 M_\odot/h$ in Illustris, and $8 \cdot 10^5 M_\odot/h$ in IllustrisTNG, which is typically much smaller then the mass of the parent gas particle/cell, such that the difference serves as a gas reservoir for accretion onto the black hole. The accretion rate is calculated according to a Bondi-Hoyle-Lyttleton model

$$\dot{M}_{\mathrm{Bondi}} = \frac{4\pi G^2 M_{\mathrm{BH}}^2 \rho}{c_s^3}, \tag{1.105}$$

and is limited by the Eddington accretion rate

$$\dot{M}_{\mathrm{Edd}} = \frac{4\pi G M_{\mathrm{BH}} m_p}{\varepsilon_r \sigma_{\mathrm{T}} c}, \tag{1.106}$$

where $M_{\mathrm{BH}}$ is the black hole mass, $G$ is the gravitational constant, $c$ the speed of light, $m_p$ the proton mass, and $\sigma_{\mathrm{T}}$ the Thompson cross-section. $\varepsilon_r \approx 0.1 - 0.2$ is the radiative efficiency of accretion onto a Schwarzschild black hole (Shakura and Sunyaev, 1973). The local gas density $\rho$ and local sound speed $c_s$ are estimated as a SPH kernel weighted average across the surrounding gas particles/cells. It is either possible to set a constant number of gas particles/cells for this average or to set a target total mass. In short, the black hole accretion rate can be written as

$$\dot{M}_{\mathrm{BH}} = \min\left(\dot{M}_{\mathrm{Bondi}}, \dot{M}_{\mathrm{Edd}}\right). \tag{1.107}$$

In the Illustris model the Bondi accretion rate was modified by a boost-factor $\alpha$ to account for the unresolved structure of the two phase ISM consisting of a hot volume filling phase and cold star-forming clouds (see section 1.7.2). This modification was reverted in the IllusitrisTNG model in order to go back to the classical form of Bondi accretion, as a similar effect can be achieved by choosing a larger black hole seed mass. Furthermore, in the Illustris model the local sound speed was calculated accounting for the relative velocity of the black hole with respect to the surrounding gas. This correction was also omitted in the IllusitrisTNG model, as in this model the black hole is strictly bound to the potential minimum of the halo. Finally, black holes can also increase their mass through mergers, which is implemented to happen as soon as one black hole enters the accretion radius of another black hole under the condition that the relative velocities of the two black holes are smaller than the local sound speed.

In order to mimic the two distinct states of AGNs, black holes are modelled to exhibit two main feedback modes that depend on the strength of the accretion onto the black hole (see Sijacki et al., 2007, and references therein). High black hole accretion rates $\dot{M}_{\mathrm{BH}}$ that are above a fraction of $\chi_{\mathrm{radio}} \approx 0.1$ of the Eddington accretion rate $\dot{M}_{\mathrm{Edd}}$, are typically observed for quasars at high redshift. In case of 'quasar-mode' feedback only a small fraction $\varepsilon_{f,\mathrm{qso}}$ of the quasars radiative energy couples thermally to the surrounding gas and is distributed in a SPH kernel weighted fashion across a number of gas particles/cells with prescribed total mass. The efficiency of the thermal coupling is a free parameter of the model that is chosen

to be $\varepsilon_{f,\mathrm{qso}} \approx 0.05 - 0.1$ in order to reproduce observational results such as the $M_{\mathrm{BH}} - \sigma_*$ relation. In 'quasar-mode' the energy introduced thermally into the gas is given by

$$\Delta \dot{E}_{\mathrm{qso}} = \varepsilon_{f,\mathrm{qso}} \varepsilon_r \dot{M}_{\mathrm{BH}} c^2. \tag{1.108}$$

For low accretion rates below $\chi_{\mathrm{radio}}$ of the Eddington limit, Illustris employs a 'radio-mode' or 'bubble-mode' feedback in order to mimic hot bubbles driven by AGN jets into the surrounding gas. Such bubbles are assumed to arise whenever the black hole has accumulated a certain minimal energy through a mass increase of $\delta M_{\mathrm{BH}}$. The energy released into the gas in this mode is given by

$$\Delta E_{\mathrm{bub}} = \varepsilon_{f,\mathrm{bub}} \varepsilon_r \delta M_{\mathrm{BH}} c^2, \tag{1.109}$$

where $\varepsilon_{f,\mathrm{bub}}$ is the coupling and therefore heating efficiency of the bubble. Both $\delta M_{\mathrm{BH}}$ and $\varepsilon_{f,\mathrm{bub}}$ are free parameters of the model which regulate the duty cycle and energy content of the bubbles and are chosen to reproduce observations. During in-depth analysis of the Illustris simulation, this 'radio-mode' feedback however turned out to deplete groups and cluster of too much of their gas (see Genel et al., 2014, figure 10), such that this mode was replaced by a new 'kinetic-mode' for AGN feedback (Weinberger et al., 2017) in the IllustrisTNG simulation. The 'kinetic-mode' feedback mimics the same jets however through imparting energy in purely kinetic form onto the surrounding gas. The amount of energy injected into the gas is calculated in the same way as for the 'quasar-mode',

$$\Delta \dot{E}_{\mathrm{kin}} = \varepsilon_{f,\mathrm{kin}} \dot{M}_{\mathrm{BH}} c^2, \tag{1.110}$$

however with a different coupling efficiency that is set to $\varepsilon_{f,\mathrm{kin}} = 0.2$, whereas this value is reduced in low density environments which do not allow for an efficient coupling. In analogy to the 'quasar-mode', this energy is distributed amongst the neighbouring gas particles/cells with prescribed total mass in a SPH kernel weighted fashion. The injection of energy in kinetic form is achieved by adding to every gas particle/cell a corresponding momentum with random orientation that changes every timestep. Though this approach introduces some momentum in every individual timestep, these spurious contributions vanish when averaging over time, such that momentum is conserved and the injection of the proper amount of energy is guaranteed. Therefore, and due to the numerical robustness of this approach, it is preferred over other possible choices for the distribution of kinetic energy. In analogy to the scaling of supernovae driven galactic winds, and in order to produce AGN outflows with sufficient strength, a 'kinetic-mode' AGN feedback event is taking place whenever the black hole has accumulated a minimum energy of

$$\Delta E_{\min} = 0.5 f_{re} \sigma_{DM}^2 M_{\text{kernel}} \tag{1.111}$$

through gas accretion as given in Eq. 1.110, where $\sigma_{DM}$ is the one-dimensional dark matter velocity dispersion, $M_{\text{kernel}}$ the gas mass enclosed within the SPH kernel centred at the black hole, and $f_{re}$ a free parameter that sets the bustiness of this feedback mode similar to the duty cycle of the AGN bubbles in the former 'radio-mode' feedback.

In addition to the two main feedback modes for high and low accretion states of black holes, both Illustris and IllustrisTNG include a third 'electro-magnetic' AGN feedback mode that takes into account the significant changes introduced in the otherwise spatially constant UV background by adding to it a contribution from a universal and time-independent AGN spectral energy distribution (SED).

# Chapter 2

# Angular momentum properties of haloes and their baryon content in the Illustris simulation

The content of the following chapter is published in Monthly Notices of the Royal Astronomical Society, Volume 466, Issue 2, p.1625-1647.

# Abstract

The angular momentum properties of virialised dark matter haloes have been measured with good statistics in collisionless N-body simulations, but an equally accurate analysis of the baryonic spin is still missing. We employ the *Illustris* simulation suite, one of the first simulations of galaxy formation with full hydrodynamics that produces a realistic galaxy population in a sizeable volume, to quantify the baryonic spin properties for more than $\sim 320,000$ haloes. We first compare the systematic differences between different spin parameter and halo definitions, and the impact of sample selection criteria on the derived properties. We confirm that dark matter only haloes exhibit a close to self-similar spin distribution in mass and redshift of lognormal form. However, the physics of galaxy formation radically changes the baryonic spin distribution. While the dark matter component remains largely unaffected, strong trends with mass and redshift appear for the spin of diffuse gas and the formed stellar component. With time the baryons staying bound to the halo develop a misalignment of their spin vector with respect to dark matter, and increase their specific angular momentum by a factor of $\sim 1.3$ in the non-radiative case and $\sim 1.8$ in the full physics setup at $z = 0$. We show that this enhancement in baryonic spin can be explained by the combined effect of specific angular momentum transfer from dark matter onto gas during mergers and from feedback expelling low specific angular momentum gas from the halo. Our results challenge certain models for spin evolution and underline the significant changes induced by baryonic physics in the structure of haloes.

## 2.1 Introduction

The origin of the angular momentum of galaxies is an important question in cosmic structure formation, as the spin directly determines the size of rotationally supported objects such as disk galaxies. In the now well established standard paradigm of the ΛCDM concordance cosmology, primordial dark matter density perturbations seeded in an inflationary epoch grow with time due to gravitational instability. Eventually, they decouple from the background expansion, turn around and collapse to form virialised structures. This happens first for small mass systems, which then hierarchically merge into bigger structures (Blumenthal et al., 1984, Davis et al., 1985). The baryons collected within haloes cool out and form galaxies at their centres, giving rise to a hierarchical galaxy formation process (White and Rees, 1978). If the baryons have a non-vanishing specific angular momentum, it should be preserved in the radiative cooling process, such that the gas settles into a rotationally supported disk that forms inside out (Fall and Efstathiou, 1980, Mo et al., 1998), with a size directly related to the magnitude of the spin.

It is thus important to clarify the amount of angular momentum imparted on haloes and on the baryons they contain. Generally, gravitationally self-bound structures gain their initial angular momentum from interactions with the surrounding gravitational tidal field (Hoyle, 1949). This in particular makes it possible that haloes acquire substantial non-vanishing angular momentum even though the gravitational potential is irrotational in character. The amount of angular momentum contained in a galaxy as well as the growth rate in the linear regime was first calculated by Peebles (1969). Doroshkevich (1970) pointed out that this particular growth rate is a consequence of the imposed spherical symmetry and carried out a calculation predicting the angular momentum to grow linearly with time before non-linear effects start to play a significant role. These results were confirmed by early collisionless dark matter only N-body simulations by White (1984) and Barnes and Efstathiou (1987), and form the basis of the so-called tidal torque theory, which describes the acquisition of angular momentum for dark matter haloes (see also Schäfer and Merkel, 2012).

However, once the subsequent evolution of haloes enters the non-linear regime, simple tidal torque theory breaks down, as haloes cannot be regarded any more as isolated objects. Instead, they undergo multiple minor and major mergers. Analytic and semi-analytic models for the acquisition of angular momentum from the orbital angular momentum of infalling mergers (e.g. Vitvitska et al., 2002, Maller et al., 2002, Maller and Dekel, 2002) can successfully extend tidal torque theory and reproduce the spin parameter distribution of haloes as well as the distribution of specific angular momentum inside haloes at $z = 0$. However, such analytic descriptions rely on simplifying and ultimately uncertain assumptions. On the other hand, the acquisition of angular momentum through non-linear processes such as mergers is

followed faithfully in numerical simulations, making them a particularly powerful approach to study this problem.

This has motivated numerous analysis of the angular momentum properties of simulated dark matter only haloes. Avila-Reese et al. (2005) studied the dependence of halo spin on environment, Macciò et al. (2007) investigated the correlation of halo spin with mass and concentration, and Macciò et al. (2008) extended this analysis to the dependence of halo spin on mass and cosmology. Bett et al. (2007) have derived spin parameters for $\sim 1.5 \times 10^6$ dark matter only haloes from the Millennium simulation (Springel et al., 2005) and accurately quantified the spin parameter distribution with the highest statistical power so far. Bullock et al. (2001) extended the analysis to the distribution of specific angular momentum within haloes and found a universal angular momentum profile within the virial radius. The most important result from these studies has been the finding of a nearly universal spin parameter distribution of approximately lognormal form. A closer look at some of the results reported in the literature however also reveals some small quantitative differences, as we will discuss in detail in this paper.

When it comes to baryonic processes, even more interesting differences appear. Although the dynamics of the galaxy and the dark matter are to a large extent determined by the common gravitational potential of the dark matter halo (Rubin and Ford, 1970), so-called feedback processes play an important role in shaping galaxy formation and evolution, primarily through changing the gas dynamics. However, even in absence of feedback mechanisms, it is not trivially possible to extrapolate from dark matter onto baryonic spin properties. This can be already seen in early results from non-radiative hydrodynamical simulations. In particular, van den Bosch et al. (2002) showed in their non-radiative hydrodynamical simulation that even though the 'initial' spin distributions of dark matter and the gas component of haloes are indistinguishable, there is a substantial misalignment between dark matter and the gas component at $z = 3$, with a significant fraction of the gas being counter-rotating. The median misalignment angle reported is $\sim 30^\circ$. Chen et al. (2003), Sharma and Steinmetz (2005), and Gottlöber and Yepes (2007) extended this analysis to $z = 0$ and found a relative enhancement of the gas to dark matter spin parameter of 1.19, 1.44, and 1.39, respectively. However, until recently the analysis of the spin was largely restricted to non-radiative simulations, as full physics simulations of galaxy formation were simply too costly and did not produce realistic galaxy populations.

The impact of baryons onto dark matter in models where star formation and feedback is taken into account was first studied by Bett et al. (2010), who employed a sample of 67 haloes and their dark matter only counterparts and found an increase of the specific angular momentum of dark matter in the inner regions of haloes in the presence of baryons. Bryan

et al. (2013) looked at larger statistical samples of $\gtrsim 3000$ haloes taken from the OWLS simulations and confirmed this finding.

First results on the angular momentum properties of the stellar component of galaxies from a realistic galaxy population taken from the *Illustris* simulation were obtained by Genel et al. (2015) who showed a correlation between galaxy type and specific angular momentum. This correlation was further confirmed by Zavala et al. (2016) using the EAGLE simulation. Furthermore, Genel et al. (2015) observed that galactic winds enhance the spin of stars compared to the dark matter, and that AGN feedback counteracts this effect by damping this enhancement, as also indirectly observed by Bryan et al. (2013). Baldi et al. (2016) studied rotational support in clusters and found, based on their sample of 258 both relaxed and unrelaxed clusters from the MUSIC simulation, little dependence of the gas spin parameter on the implemented baryonic physics.

Teklu et al. (2015) and Rodriguez-Gomez et al. (2017) further investigated the correlation between galaxies and their host haloes. Employing a sample of 622 haloes, with no restriction on their dynamical state, 64 of which host spiral galaxies and 110 ellipticals, Teklu et al. (2015) found that haloes hosting spiral galaxies exhibit on average higher spins, and haloes hosting elliptical on average lower spins. This trend was previously only weakly observed by Sales et al. (2012), who found little evidence for galaxy morphology of 100 Milky Way sized galaxies form the GIMIC Simulation to be connected to halo spin and merging history, and argued that galaxy morphology is rather determined by the misalignment of angular momentum inside the galaxy and its host halo at turnaround. Rodriguez-Gomez et al. (2017) showed that the correlation between galaxy morphology and host halo spin is a strong function of halo mass, as in more massive haloes mergers play an increasingly important role in perturbing the gas distribution of the central galaxy. Zavala et al. (2016) followed the time evolution of the specific angular momentum of different halo components and presented different evolution scenarios for the baryonic component, and their connection to the morphology of the galaxy forming at the halo centre.

In this paper we investigate how the dynamics of the baryonic and the dark matter component of haloes are influenced by feedback processes for a large statistical sample of $\sim 320,000$ haloes from the *Illustris* simulation. Our analysis focuses on the systematic properties of the angular momentum content of whole haloes, and how it changes relative to dark matter only simulations when baryonic physics is included.

This paper is structured as follows. We begin in Section 3.2 with a brief description of our simulation methodology and details on our halo identification and sample selection. We furthermore discuss in detail the effects of sample selection criteria and adopted spin parameter definition on the spin statistics. We then present results for the angular momentum statistics

of dark matter only haloes in Section 3.3.1, followed by results from non-radiative baryonic simulations in Section 2.4 and from the full physics *Illustris* simulation in Section 2.5. In each of these sections we also examine the robustness of our results with respect to resolution, the redshift evolution of the spin statistics, and the dependence of the spin properties on halo mass. Section 2.5 contains a discussion of the effect of feedback onto the baryonic and dark matter spin properties and highlights the main mechanisms responsible for a substantially enhanced spin of the gas component. We give a discussion and our conclusions in Section 3.4, and summarise extensions to the *Illustris* group catalogue in Section 2.7.

## 2.2 Methodology

### 2.2.1 The Illustris simulation suite

The *Illustris* simulation suite consists of a set of cosmological hydrodynamical simulations of a $75\,h^{-1}$Mpc wide periodic cosmological box carried out with the moving mesh code AREPO (Springel, 2010a). Initial Conditions were generated at $z = 127$ and evolved to $z = 0$ with $1820^3$ dark matter particles and $1820^3$ initial gas cells in the highest resolution run, achieving a mass resolution of $6.26 \times 10^6 \mathrm{M}_\odot$ in dark matter and $1.26 \times 10^6 \mathrm{M}_\odot$ in baryonic matter. To investigate numerical convergence, runs with a reduced number of initial dark matter particles and gas cells were performed as well. Furthermore, for every resolution the simulations were carried out with three different physical setups, a dark matter only, a non-radiative, and a full galaxy formation physics setup. An overview of the different *Illustris* simulations and their principal parameters is given in Tab. 4.1.

In the dark matter only simulations, all mass is treated as collisionless dark matter, while the non-radiative setup follows in addition the hydrodynamics of the gas but ignores radiative cooling and star formation. The full physics simulation includes these and further processes related to galaxy formation through a model described in full in Vogelsberger et al. (2013). In brief, unresolved physics of the interstellar medium is modelled in a subgrid fashion, where star formation is regulated by a pressure model that accounts for supernova feedback in the interstellar medium. This model also includes chemical enrichment through explicit tracking of 9 elements. Furthermore, black hole growth through gas accretion and associated energy feedback processes are included. The *Illustris* simulation is one of the first cosmological hydrodynamical simulations of galaxy formation that produces a realistic population of galaxies at $z = 0$. Other recent projects that show similar successes are the EAGLE simulation (Schaye et al., 2015) and the Horizon-AGN simulation (Dubois et al., 2016).

| Simulation | Simulation type | dm | gas |
|---|---|---|---|
| Illustris-1 | full physics hydro. | $1820^3$ | $1820^3$ |
| Illustris-2 | full physics hydro. | $910^3$ | $910^3$ |
| Illustris-3 | full physics hydro. | $455^3$ | $455^3$ |
| Illustris-2-NR | non-radiative hydro. | $910^3$ | $910^3$ |
| Illustris-3-NR | non-radiative hydro. | $455^3$ | $455^3$ |
| Illustris-1-Dark | collisionless dm only | $1820^3$ | - |
| Illustris-2-Dark | collisionless dm only | $910^3$ | - |
| Illustris-3-Dark | collisionless dm only | $455^3$ | - |

Table 2.1: *Illustris* simulation suite: listed are the symbolic name, the physics included, the number of initial dark matter particles, and the number of initial gas cells for every simulation.

The galaxy formation physics model of *Illustris* simultaneously reproduces with reasonable accuracy a number of observed small-scale properties, such as galaxy stellar masses and morphologies, as well as large-scale properties, such as the metal abundance in neutral hydrogen absorption systems, or the radial distribution of galaxies in galaxy clusters (e.g. Vogelsberger et al., 2014a). It is thus interesting to examine the spin distribution of the baryons in such a calculation, which can be viewed as representing one of the most realistic predictions for the large-scale dynamics of the baryons available thus far. This motivation is further strengthened by the use of the AREPO code for the simulation, which follows the gas mass in a quasi-Lagrangian form by means of a fully adaptive mesh that moves with the flow. This approach avoids classical disadvantages of Cartesian adaptive mesh refinement (AMR) codes, such as the occurrence of preferred spin directions along the coordinate axes (e.g. Hahn et al., 2010). Simultaneously, it eliminates traditional problems of smoothed particle hydrodynamics (SPH), such as relatively high numerical noise and the need for an artificial viscosity (Springel, 2010b). We thus expect that AREPO follows the hydrodynamics more accurately than competing numerical approaches, making its predictions for the spin of the baryonic component of haloes all the more interesting.

However, we note that like any other numerical code, AREPO is constantly improved further. In particular, Pakmor et al. (2016) has recently proposed changes in the gradient estimation as well as time integration of the code that improve its accuracy and convergence order in certain situations. The *Illustris* suite analysed here was carried out with a version of the code that did not include these improvements, but as Pakmor et al. (2016) show, they do not affect the results of cosmological simulations of galaxy formation.

### 2.2.2 Measurement of halo properties through an extension of SUBFIND

During the *Illustris* simulation runs, the group finders FOF and SUBFIND (Springel et al., 2001) were applied on the fly, determining a set of basic halo and subhalo properties, as described in detail in the public data release of *Illustris* (Nelson et al., 2015). However, the spin properties we want to analyse here, as well as information about the binding energy of haloes were not part of these properties. Unfortunately, simply computing additional halo properties post-hoc is technically complicated. While the *Illustris* data is stored such that the particle/cell data comprising individual gravitationally bound subhaloes can be retrieved relatively easily despite the large simulation size, this is not readily possible for the particles/cells making up an object defined by its spherical overdensity radius $R_{200}$. Also, computing the binding energy of haloes that consist of a large number or resolution elements (regularly in excess of $10^6$ elements) becomes computationally costly unless sophisticated algorithms are employed.

In order to efficiently measure further halo and subhalo properties for *Illustris*, we have therefore developed an extension of AREPO's group finders that allows the parallel processing of an already existing group catalogue. The membership of individual resolution elements to groups, subhaloes and spherical overdensity haloes is kept exactly as in the existing group catalogue, allowing additional properties of haloes to be measured. The results are then simply added as further fields to the catalogue. A full list of the newly available halo and subhalo properties in the extended group catalogue can be found in Section 2.7[1]. Thanks to the parallel tree solver for gravity in AREPO, one of the quantities we can calculate in this way efficiently is the exact gravitational binding energy of haloes (including spherical overdensity objects), something that has often been only determined in an approximate way in previous analysis of halo spin. The code extension of FOF/SUBFIND is written such that it can run both as a postprocessing option to augment existing catalogues, or as part of the regular group finding, either on-the-fly or in postprocessing. We also note that since the group catalogue is stored in the convenient HDF5 format, the I/O routines of existing analysis code using the group catalogue does not have to be adjusted or changed after the group catalogue has been extended.

For definiteness, we briefly summarise the group definitions adopted by *Illustris*, which we also employ in the following. Friends-of-friends (FOF) groups are determined for dark matter particles as a set of equivalence classes, where any pair of two particles is in the same group if their distance is smaller than a prescribed linking length. For the linking length we

[1] They will be added to the public data release of *Illustris* described by Nelson et al. (2015) upon publication of this paper.

adopt the standard value of 0.2 times the mean particle spacing, $l_{\rm mean} = (m_{\rm dm}/\rho_{\rm dm})^{1/3}$, where $m_{\rm dm}$ is the dark matter particle mass, and $\rho_{\rm dm}$ is the mean dark matter density. Baryonic particles (stars and black holes) and gaseous cells, if present, are then assigned in a second step to the same halo as their closest dark matter particle. Any group constructed in this way corresponds to what we from now on call a FOF-halo. While all groups with at least 32 particles/cells are stored for the *Illustris* simulation, for our analysis we will typically impose a considerably higher minimum particle number in order to prevent numerical noise and possible biases from poorly resolved haloes.

Each FOF-halo is then decomposed by SUBFIND into a set of gravitationally self-bound subhaloes, based on the algorithm described in Springel et al. (2001). To this end, the total mass density at each point is estimated by an adaptive kernel estimation. The resulting density field is then processed with an excursion set technique that finds locally overdense candidate substructures. Each of these overdensities is then subjected to a gravitational unbinding procedure, keeping only the bound part as a genuine substructure. Every resolution element can only be member of one subhalo, and the remaining bound part of the halo, after all smaller substructures have been removed, is called the background subhalo. For each subhalo the particle/cell with the smallest gravitational potential is adopted as its centre.

Finally, around the centre of each background subhalo, which corresponds to the point with the minimum gravitational potential of the underlying FOF-halo, we determine spherical overdensity (SO) groups. In this approach, one finds a spherical region around a given point *in the full particle/cell set* that encloses a certain overdensity with respect to the background density. We will generally employ an overdensity of 200 with respect to the critical density, and denote the corresponding radius and mass of the spherical region as $R_{200}$ and $M_{200}$, respectively. In Fig. 2.1 we depict a typical halo to illustrate the different halo definitions and highlight some of the implications for halo geometry and the calculation of halo properties.

### 2.2.3 Halo sample selection

For our analysis, we select all sufficiently well-resolved haloes that appear to be reasonably relaxed systems. To avoid numerical biases due to resolution effects, following the detailed resolution study of Bett et al. (2007), we exclude all haloes resolved by less than 300 dark matter particles from our FOF-halo and SO-halo samples.[2] We also exclude all haloes that have no gravitationally self-bound component identified by SUBFIND, as these are not haloes in a physical sense.

[2] Note that this imposes a somewhat higher minimum halo mass in the *Illustris* simulations including baryons compared to dark matter only.

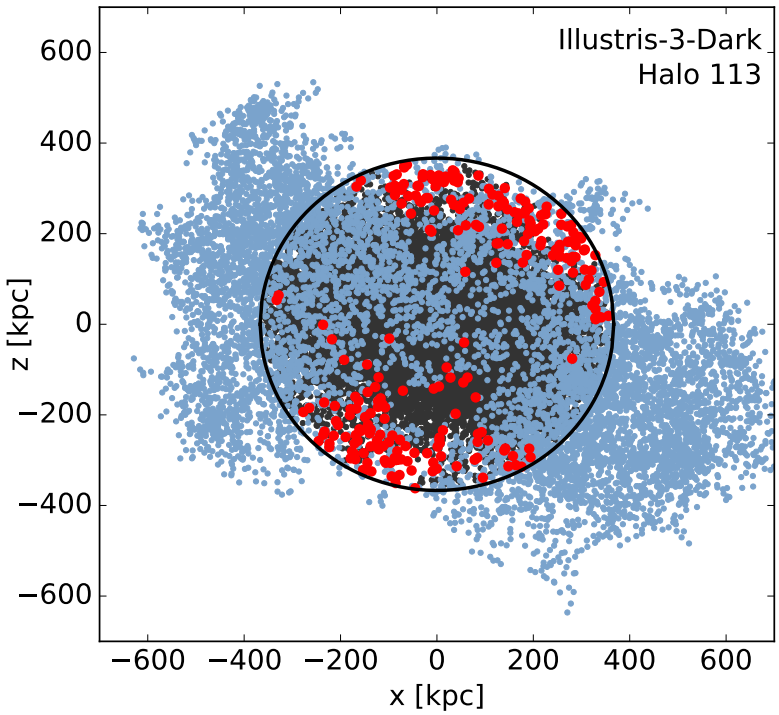


Figure 2.1: Particles making up a randomly selected dark matter halo from Illustris-3-Dark. The black circle indicates $R_{200}$, FOF-halo dark matter particles inside $R_{200}$ are shown in *grey*, FOF-halo dark matter particles outside $R_{200}$ are shown in *blue*, dark matter particles part of the SO-halo definition but not the FOF-halo are shown as *big red* dots. This demonstrates the general fact that FOF-haloes are typically more extended and more massive than their SO-halo counterparts. The number of particles that are part of the SO-halo but not the FOF-halo is usually relatively small, such that SO-haloes can be regarded as the inner regions of FOF-haloes.

Furthermore, we want to study only haloes close to virial equilibrium, in order to avoid, for example, situations where the angular momentum content is dominated by the contribution of the orbital angular momentum of mergers. To this end we calculate the virial ratio,

$$q = \frac{2\,E_{\rm kin}}{E_{\rm pot}} + 1, \tag{2.1}$$

both for our FOF- and SO-halo samples. The total kinetic energy in Eq. (3.3) represents the sum of the bulk kinetic energy of the halo particles/cells and the thermal energy of the gas, if present. In calculating the virial ratio according to Eq. (3.3) we ignore the surface pressure term, which appears in the virial theorem for non-isolated systems (Shapiro et al., 2004) and represents the pressure exerted on the halo by infalling matter. In our approach it is sufficient to calculate the virial ratio in such an approximative way, as we only employ it to filter out systems that have a huge surplus of kinetic energy.

For an isolated structure in equilibrium the expected virial ratio based on the virial theorem is $q = 0$. In Fig. 2.2 we show the distribution of virial ratios of our FOF-halo samples from Illustris-1-Dark and from Illustris-1 against halo mass. In this effectively two-dimensional histogram, the individual mass bins have been independently normalised to take out the variation of halo abundance with mass. The virial equilibrium expectation is denoted by the horizontal blue line. Haloes with positive $q$-values are dominated by potential energy, haloes with negative $q$-values are dominated by kinetic energy. We dismiss all haloes with $q < -1$ from our halo sample, corresponding to haloes having more than twice as much kinetic energy as expected from virial equilibrium. Those objects are often undergoing significant mergers, which can produce highly negative $q$-values.

Both simulations show that the average virial ratio of haloes decreases with halo mass. This reflects the fact that less massive haloes form on average at higher redshifts and thus have more time to virialise by $z = 0$, whereas more massive haloes are still in the process of collapsing and virialising at $z = 0$, which is additionally slowed down by further growth through accretion. More massive haloes are also known to be more elongated on average, consistent with their younger age and more active infall region.

In Fig. 2.3 we show how the virial ratio distributions of the FOF-halo samples of Illustris-1-Dark and Illustris-1 evolve with time. As there are many more low mass haloes than high mass haloes, the distributions are dominated by the mass scale just above the enforced threshold of 300 dark matter particles. Black dots indicate the median virial ratio at the displayed redshifts. For both simulations the contribution of kinetic energy is enhanced at high redshift, pushing the bulk of the haloes further away from the equilibrium value, reflecting their ongoing rapid growth and young age. The virial ratio distribution $P(q)$

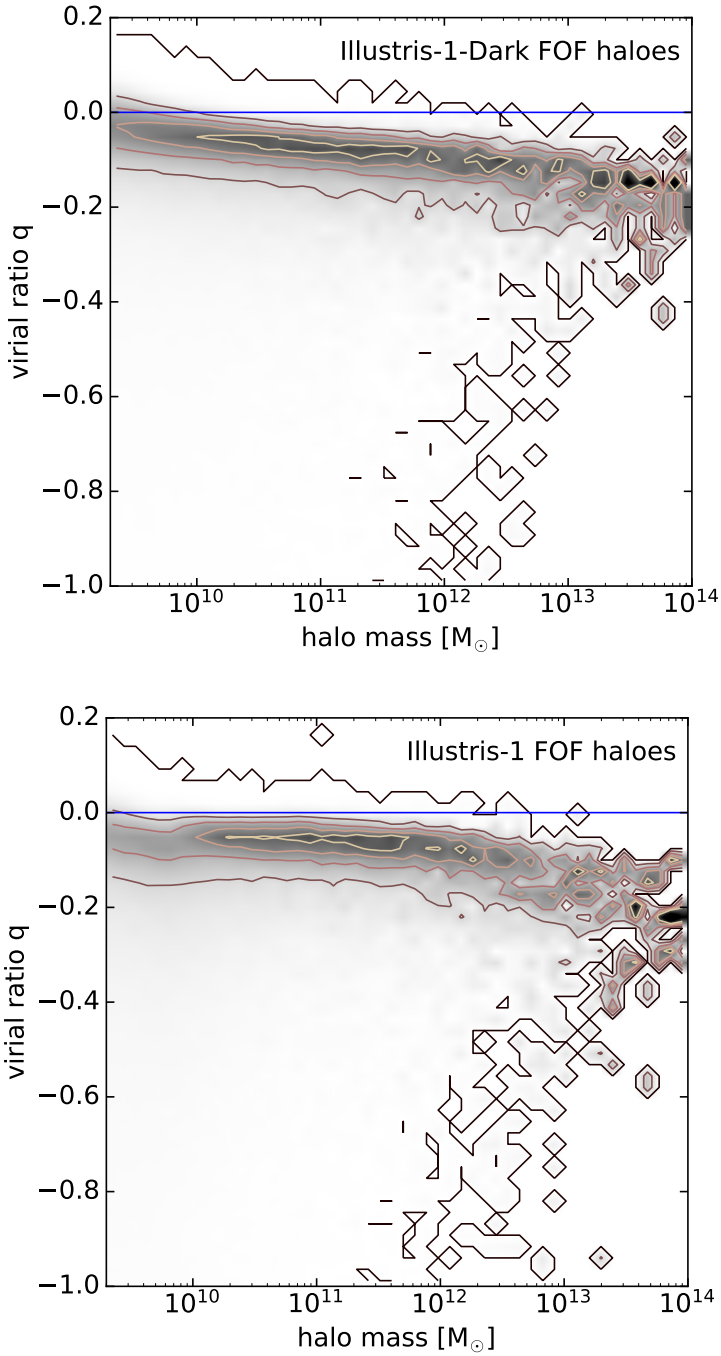


Figure 2.2: Distribution of the virial ratio $q$ of the FOF-halo sample from Illustris-1-Dark and Illustris-1 normalised in every mass bin. The grey shading ranges from a fraction of 0 to 0.2 of all haloes in a mass bin having a given $q$-value. Contours are drawn at constant fractions of 0, 0.05, 0.1, 0.15, and 0.2, respectively. The blue line denotes virial equilibrium. Negative virial ratios correspond to haloes being dominated by kinetic energy. In case of massive haloes this surplus of kinetic energy is due to the halo not being fully collapsed yet. The tail to extreme negative values for less massive haloes is due to mergers.

normalised to the total number of haloes as well as bin size thus peaks at low $q$-values at high redshift and then progressively shifts towards $q = 0$ with decreasing redshift, corresponding to the halo sample becoming more virialised with cosmic time. Our SO-halo sample shows qualitatively the same behaviour. This reflects the fact that cosmic structures are hardly ever in perfect virial equilibrium, but rather in a slowly evolving quasi-equilibrium. However, we caution that the trends displayed here were derived neglecting the pressure surface term, which is smaller both for more massive and younger haloes, as both are undergoing more accretion. A higher absolute value of the negative pressure surface term results in the trends being weaker than shown here. Nevertheless, when comparing halo samples at different redshifts, one thus has to bear in mind that the samples will typically exhibit different degrees of relaxation.

Furthermore, we want to emphasise that there is no universally accepted standard definition of what constitutes a well-resolved, quasi-equilibrium structure in cosmological simulations. Besides a different minimum number of particles and different virial ratio cuts, also criteria such as the offset between the centre of mass and the potential minimum, the abundance of dark matter substructures (Macciò et al., 2007), or the mass fraction in substructures not being bound to the main potential (Neto et al., 2007) have been employed in the literature to discriminate between relaxed and unrelaxed haloes. The effect of the different sample selection criteria on the final values of the derived properties, such as the spin parameter distribution and median spin parameter value for dark matter only haloes, has not been systematically investigated yet.

However, as we will show later, the inferred spin distribution of haloes is equally sensitive to the halo and spin parameter definitions as on the exact set of selection criteria for the halo sample. Which halo definition is considered to be more physical or useful is largely a matter of convention. In this paper, we will present results for both the FOF-halo and SO-halo sample, which can be regarded as the two most important limiting cases. The systematic differences arising from the spin parameter definition are investigated in the next section.

### 2.2.4 Spin parameter definitions

The angular momentum content and degree of rotational support of structures with different mass and spatial extent can be quantified and compared by means of a suitably defined dimensionless spin parameter $\lambda$. Its classic definition,

$$\lambda_{\mathrm{P}} = j_{\mathrm{sp}} \frac{E_{\mathrm{tot}}^{1/2}}{G M_{\mathrm{tot}}^{3/2}}, \tag{2.2}$$

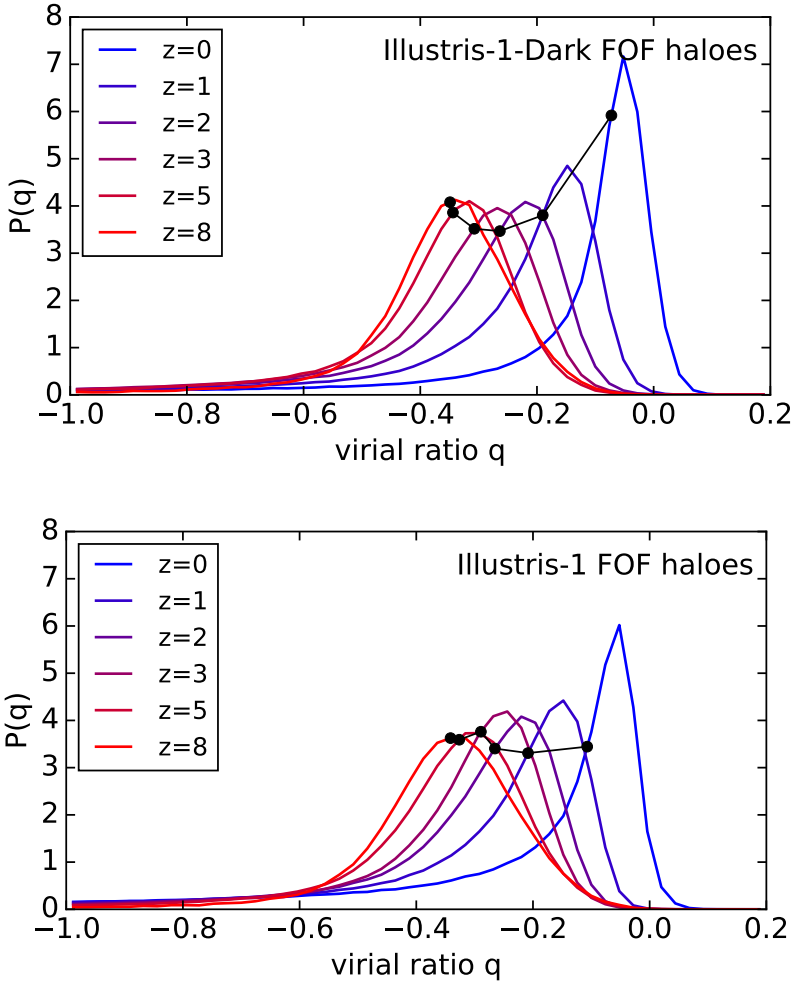


Figure 2.3: Change of the virial ratio distribution of FOF-haloes as a function of redshift, both for Illustris-1-Dark (top panel) and Illustris-1 (bottom panel). Black dots indicate the median virial ratio at every redshift. With decreasing redshift, the FOF-halo sample becomes ever more relaxed, with the median virial ratio shifting continuously towards zero and hence to the expectation value for perfectly relaxed isolated systems.

goes back to Peebles (1969). Here $j_{\rm sp} = J/M$ gives the magnitude of the specific angular momentum per unit mass of the material in question. It is multiplied by a factor composed of the total mass of the system $M_{\rm tot}$, the gravitational constant $G$, and the absolute value of the total energy, $E_{\rm tot} = |E_{\rm kin} + E_{\rm pot}|$, where the kinetic energy is again the sum of the bulk kinetic energy of the halo particles/cells and the thermal energy of the gas. This multiplicative factor expresses the specific angular momentum $j_{\rm sp} = |\mathbf{j}_{\rm sp}|$ in dimensionless form.

Note that the specific angular momentum can be calculated for any subset of the system. If the set is composed of $N$ mass elements, with the $i$-th computational element having mass $m_i$, distance from the halo centre $\mathbf{r}_i$, and velocity $\mathbf{v}_i$ with respect to the centre of mass velocity of the halo, the specific angular momentum is given as

$$\mathbf{j}_{\rm sp} = \frac{\mathbf{J}}{M} = \frac{1}{M}\sum_{i=1}^{N} m_i \mathbf{r}_i \times \mathbf{v}_i, \tag{2.3}$$

with mass $M = \sum_i^N m_i$ of the subset. In a simulation including baryons, the most interesting subsets include the dark matter, the gas, and the stellar component of the halo. If the subset consists of the whole halo, one arrives at $M = M_{\rm tot}$, and the definition of the spin parameter corresponds to that of Peebles (1969).

Early analytic studies of structure formation of dissipationless haloes in the Einstein-de Sitter limit were able to estimate the average value of the spin parameter imparted on density perturbations by gravitational tidal torques. Applying different approaches and simplifying assumptions Heavens and Peacock (1988) found a value of $\lambda_{\rm P} \approx 0.05$, Ryden (1988) a value of $\lambda_{\rm P} \approx 0.09$, and Steinmetz and Bartelmann (1995) arrived at $\lambda_{\rm P} \approx 0.07$. Early dark matter only simulations of the Einstein-de Sitter universe measured systematically lower Peebles spin parameters than suggested by some of these analytic studies. Barnes and Efstathiou (1987) and Warren et al. (1992) quote a value of $\lambda_{\rm P} \approx 0.05$, and Cole and Lacey (1996) found $\lambda_{\rm P} \approx 0.04$ in their simulations.

The Peebles spin parameter definition has however an important practical drawback. The potential binding energy $E_{\rm pot}$ of a self-bound structure is needed to determine its total energy. This can be computationally expensive to measure accurately for an N-body halo, especially if its particle number is large. To avoid this complication, Bullock et al. (2001) proposed an alternative definition of the spin parameter,

$$\lambda_{\rm B} = \frac{j_{\rm sp}}{\sqrt{2} R_{200} v_{200}}. \tag{2.4}$$

In this definition, $R_{200}$ and $v_{200}$ are the virial radius and the circular velocity at the virial radius of the halo, which can be viewed as characteristic length and velocity scales of

the object in question, and are here used to express the specific angular momentum in dimensionless form. The prefactor of $1/\sqrt{2}$ is introduced to make this definition of the spin parameter yield the same value as the definition of Peebles (1969) for the density distribution of a singular isothermal sphere truncated at $R_{200}$, and where all particles are put on circular orbits. Mo et al. (1998) furthermore argue that the two spin parameter definitions are related by $\lambda_{\rm P} = f(c)^{1/2}\lambda_{\rm B}$ for NFW-haloes, where $f(c)$ is a function depending only on the concentration $c$ of the halo.

The Bullock definition has been popular and is widely employed in the literature, as it is easy to calculate and does not require the knowledge of the potential energy of a halo, which is often estimated only approximately to reduce the computational cost. Macciò et al. (2007) quote a median Bullock spin of $\lambda_{\rm B} \approx 0.030$ for their relaxed halo sample, and Avila-Reese et al. (2005) report a value of $\lambda_{\rm B} \approx 0.033$. The values found for the Bullock spin parameter are all systematically lower than spin parameters derived with the Peebles spin parameter definition. This is in agreement with Bullock et al. (2001) who calculated the median spin parameter according to their new definition and the classic definition by Peebles (1969) for the same SO-halo sample and found values of $\lambda_{\rm B} \approx 0.035$ and $\lambda_{\rm P} \approx 0.042$, respectively. Thus, although $f(c)$ is close to unity and the Peebles and Bullock spin parameters are 'approximately' equal, there are clearly systematic differences that have to be taken into account when performing precision measurements.

To highlight these systematic differences between the Peebles and Bullock spin parameter definitions, we calculate the spin according to both definitions for our FOF- and SO-halo samples. The total energy needed for the Peebles spin definition is given by $E_{\rm tot} = |E_{\rm kin} + E_{\rm pot}|$, where we calculate the potential energy with high precision employing the parallel gravity tree solver, as described in Section 2.2.2, and the kinetic energy[3] is again the sum of the bulk kinetic energy of the halo particles/cells and the thermal energy of the gas. To calculate the Bullock spin parameter we express the virial velocity $v_{200} = 10H(z)R_{200}$ via the virial radius $R_{200}$, which is determined for SO-haloes by SUBFIND and contained in the group catalogue. In the case of FOF-haloes, we use the FOF-halo mass $M_{\rm FOF}$ to estimate an equivalent virial radius $R_{200,\rm FOF} = (GM_{\rm FOF}/100H^2)^{1/3}$, which corresponds to the assumption that the FOF-halo has all of its mass contained within a sphere of overdensity 200 relative to the critical density. This is a very crude estimate and highlights the limitation of the Bullock spin parameter definition being designed for spherically symmetric haloes, because only then the values measured operationally for the characteristic radius $R_{200}$ and

[3]Note that in our extended group catalogue $E_{\rm kin}$ contains only the kinetic energy due to the particle and cell velocities. The thermal energy of the gas is stored in $E_{\rm thr}$ and has to be added to $E_{\rm kin}$ to obtain the total physical kinetic energy.

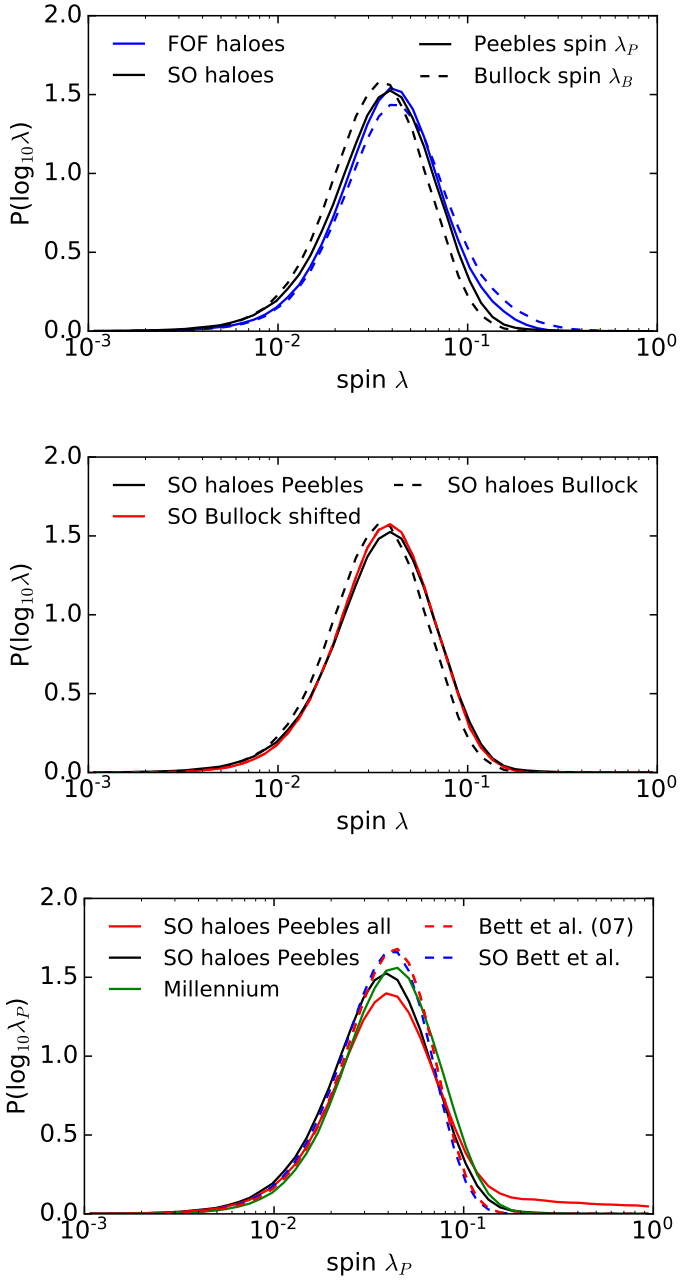


Figure 2.4: *Upper panel*: Comparison of the Peebles and Bullock spin parameter distributions derived from Illustris-1-Dark for dark matter only FOF- and SO-haloes. The Peebles spin definition yields consistent results for the different halo definitions. *Middle panel*: Comparing the spin values derived with the Bullock spin definition for SO-haloes to the Peebles values, ignoring the concentration dependence but taking into account a constant conversion factor of 1.1. *Lower panel*: Comparison of our SO-halo Peebles distribution from Illustris-1-Dark (black solid) and the Millennium Simulation (green solid) to the Peebles distribution from Bett et al. (2007) derived for their cleaned halo sample (red dashed) and SO-halo sample (blue dashed). The red solid line shows the resulting spin distribution from Illustris-1-Dark when all restrictions on the dynamic state of haloes are abandoned. Different sample selection criteria thus explain the observed differences in the spin distributions and their effect has to be borne in mind when aiming for precision measurements.

velocity $v_{200}$ can be expected to make sense. The Bullock spin parameter definition has no built in mechanism to account for the complicated geometry of FOF-haloes.

In the upper panel of Fig. 2.4, we show the spin parameter distributions derived with the Peebles and Bullock spin parameter definitions applied to our FOF- and SO-halo samples, which comprise $\sim 400,000$ and $\sim 360,000$ objects, respectively. The distributions are derived by binning the haloes in the given spin parameter range in 50 equidistant logarithmic bins and normalising the number of haloes per bin by the total number of haloes and the logarithmic bin size, such that $\int_{-\infty}^{\infty} P(\log_{10}\lambda)\ \mathrm{dlog}_{10}\lambda = 1$. With this normalisation the shown distribution is independent of the chosen bin size and the total number of bins.

The Peebles spin parameter definition yields almost the same distribution for FOF- and SO-haloes with median spin parameters of $\lambda_{\mathrm{P,FOF}} = 0.0391$ and $\lambda_{\mathrm{P,SO}} = 0.0365$ for the FOF- and SO-halo samples, respectively. This confirms that the Peebles spin definition produces results that are quite robust with respect to different halo geometries (see also Fig. 2.6). The Bullock definition on the other hand is more sensitive to the halo definition and the complicated geometry of FOF-haloes. As a result, it yields systematically different spin distributions for the two halo definitions. Also the median Bullock spin parameter of the FOF-halo sample, $\lambda_{\mathrm{B,FOF}} = 0.0414$, is substantially larger than the median value for SO-haloes, $\lambda_{\mathrm{B,SO}} = 0.0333$.

The SO-halo result derived with the Bullock spin parameter however resembles the distribution obtained with the Peebles spin parameter in shape, except that the absolute values are systematically shifted to somewhat lower values. In the case of statistically large samples where it is not possible to estimate the concentrations $c$ of every individual halo, the Bullock spin distribution can in fact be simply rescaled by constant factor of 1.1 to yield a spin distribution that almost perfectly reproduces the Peebles spin parameter distribution for a statistically large set of simulated haloes. We explicitly show the shifted Bullock spin parameter distribution in the middle panel of Fig. 2.4 as red line, which comes to lie just on top of the Peebles spin parameter distribution for SO-haloes. Thus, when comparing mean spin values derived with the two different spin definitions we stress that the constant offset factor of 1.1 has to be taken into account. We want to emphasise that this is true only for SO-haloes, and that the Bullock spin should not be applied to FOF-haloes, as this definition cannot properly take into account the complex geometry of FOF-haloes and results in a spin distribution that is different in shape from the others.

To further depict the differences between the two spin parameter definitions, we compare the Peebles and Bullock spin parameter definitions on a halo-by-halo basis. In Fig. 2.5 we show the distribution of spins resulting from the Peebles and Bullock spin parameter definitions being applied to the same FOF-haloes (upper panel) or the same SO-haloes (lower

panel). Identity is indicated as red line. In the case of FOF-haloes the Bullock spin severely overestimates the spin value for a fraction of the haloes, forming the extended tail in the left upper corner of the upper panel of Fig. 2.5. Those are haloes significantly extended beyond $R_{200}$ for which the Bullock spin fails to properly take into account the angular momentum contained in the outer regions of the halo. If SO-haloes are employed, no such systematic bias appears, however, some scatter still remains. Also, the bulk of haloes tends to somewhat higher Peebles than Bullock spin parameters which is another illustration of the constant offset discussed in the middle panel of Fig. 2.4.

Furthermore, in Fig. 2.6 we compare the Peebles (upper panel) and Bullock (lower panel) spin parameters derived for the FOF- and SO-counterparts of the same halo. To this end we create a combined halo sample that contains only haloes that match the selection criteria in both the FOF- and the SO-halo definition. Most haloes scatter around the identity line, which is again indicated in red. However, a few percent of the haloes exhibit a significant enhancement in spin in the FOF definition compared to SO. This fraction is somewhat larger for the Bullock spin definition compared to the Peebles definition. The enhancement occurs in aspherical haloes significantly extended beyond $R_{200}$ in their FOF definition (compare to Fig. 2.1). In the case of the Peebles spin, this enhancement is simply due to additional material, such as from minor mergers at large radii, and affects a smaller number of haloes. On the other hand, when dealing with the Bullock definition this enhancement affects a larger number of haloes and leads to a bias in the resulting mean spin, as this enhancement is not purely of physical nature but partly caused by the fact that FOF-haloes are normalised by virial properties not properly accounting for their true shape. This is also the reason why the Bullock spin parameter distribution of FOF-haloes differs from the SO-halo distribution not only in peak position but also in shape. Thus we want to stress that the Bullock spin parameter appears unsuitable for the FOF-halo definition and should not be applied to intrinsically aspherical FOF-haloes.

To verify our results, we have also applied our group finder and extended halo property calculation to the Millennium Simulation (Springel et al., 2005). From this run we construct an SO-halo sample in the same way we did for *Illustris*, containing $\sim 1.4 \times 10^6$ objects. We plot the resulting Peebles spin parameter distribution as a green line in the lower panel of Fig. 2.4. It is similar to the distribution we obtain from Illustris-1-Dark shown as black line, and exhibits a median value of $\lambda_P = 0.0403$. Note that the imposed 300 dark matter particle cut leads to a higher minimum halo mass in the Millennium Simulation compared to *Illustris* by approximately one order of magnitude. Taking into account the subtle trend of spin with halo mass (compare Fig. 2.10) the Millennium spin distribution is expected to have somewhat higher values. Furthermore, the Millennium Simulation was carried out

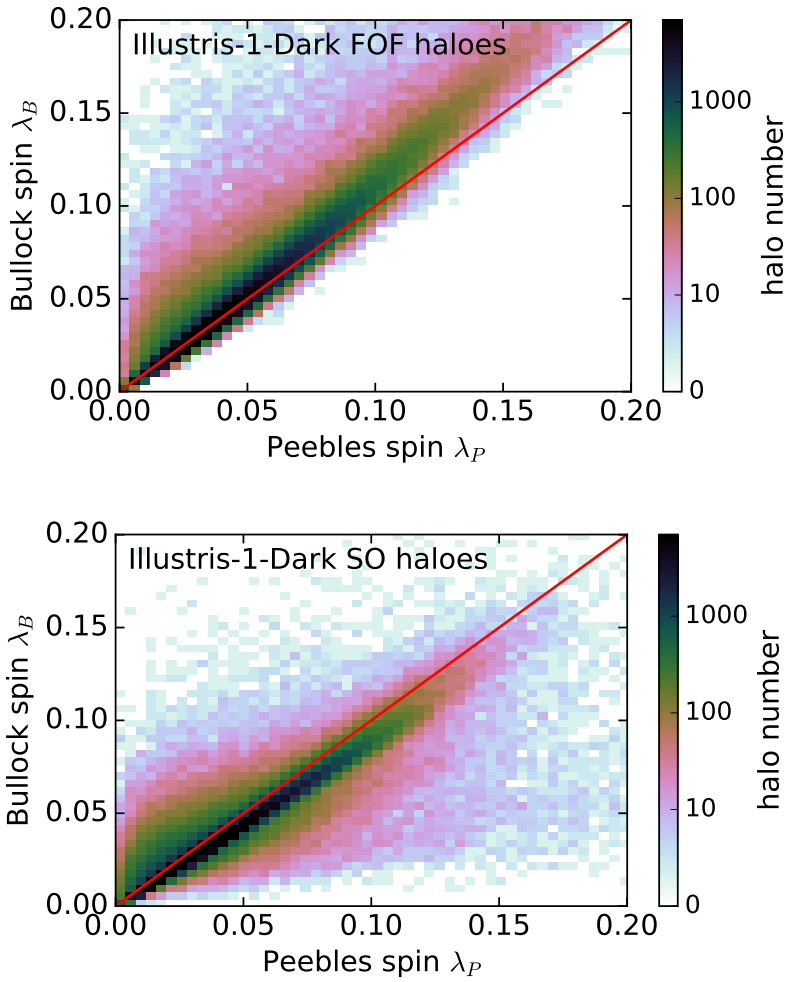


Figure 2.5: Distribution of the spin parameter values derived with the Peebles and Bullock spin definitions when applied to the same FOF-halo (upper panel) or the same SO-halo (lower panel). The colour scale indicates the number of haloes with certain spin values. Haloes with identical Peebles and Bullock spin parameters would fall onto the red line. We find that for SO-haloes the Bullock spin has to be rescaled by a constant factor of 1.1 to reproduce the Peebles value. In case of FOF-haloes the Bullock definition significantly overestimates the spin for a fraction of haloes as it cannot properly account for the aspherically distributed material at large radii and thus should not be applied to FOF-haloes.

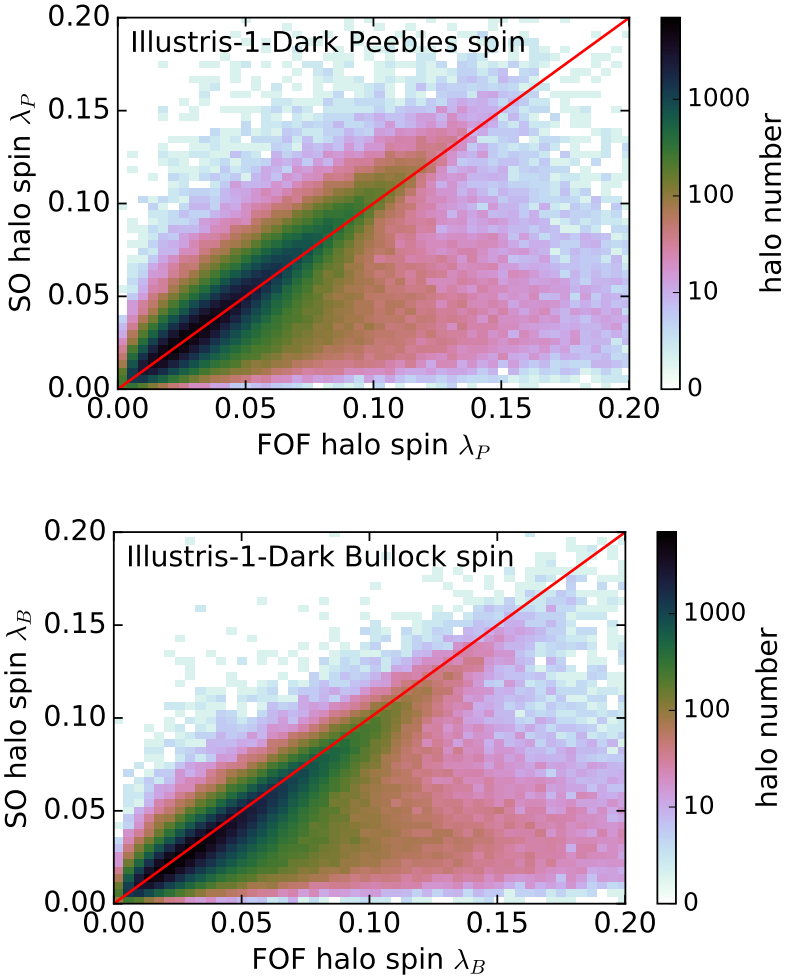


Figure 2.6: Distribution of the Peebles (upper panel) and Bullock (lower panel) spin parameter obtained by applying the given spin definition to the FOF- and SO-counterparts of the same halo. Most haloes scatter around the red identity line. However, a fraction of the haloes, that is larger in case the Bullock spin is applied, exhibit a significant enhancement in spin for the FOF definition compared to SO. Those haloes are significantly extended beyond $R_{200}$ in their FOF-halo definition (compare to Fig. 2.1), causing inaccuracies when the Bullock spin definition is used.

with a WMAP1 cosmology, which has a slightly higher $\sigma_8$ value than *Illustris*. This makes haloes of a given mass collapse earlier in Millennium than in *Illustris*. Comparing the given distributions is thus the same as making a comparison between spin distributions obtained with the same cosmology but derived at somewhat different times. As shown in the bottom left panel of Fig. 2.9, the Peebles spin parameter distribution of SO haloes exhibits a small trend to higher values with decreasing redshift, such that the higher $\sigma_8$ contributes to the spin distribution derived from the Millennium Simulation being slightly shifted to later times and thus to the right with respect to the one derived from *Illustris*. To avoid such ambiguities and facilitate the comparison between different data sets, we argue in Section 2.3.3 that it is best to use the Peebles spin parameter of FOF-haloes, as it is the only measure yielding a spin distribution self-similar in time, and as such is least affected by cosmology.

Our Millennium spin distribution can be directly compared to the most precise dark matter only result from the literature, which is given by the best fit from Bett et al. (2007), independently derived for a cleaned halo sample from the Millennium Simulation using the Peebles spin parameter definition and the new fitting function they proposed (red dashed line, see also Section 2.3.1). The fit to this halo sample is almost identical to their SO-halo sample fit (blue dashed line), and is very close, albeit not identical, to our result. The small residual difference in the spin distribution from Bett et al. (2007) and our study should originate in the details of the selection criteria used to define sets of haloes in quasi-equilibrium. We thus investigate whether sample selection criteria can account for the small differences observed between the spin distributions. We show as red solid line in the lower panel of Fig. 2.4 the spin parameter distribution obtained for our SO-halo sample when requiring only a minimum resolution of 300 dark matter particles (identical to Bett et al., 2007) and that haloes have at least one gravitationally bound component. Imposing no limit on the virial ratio allows ongoing mergers to be included in the sample. The angular momentum of haloes in active merging phases has a large and often dominating contribution of orbital angular momentum, leading to an extended tail of the spin parameter distribution to high values. This tail enters the overall normalisation of the spin distribution and lowers its peak value, but the median of the spin distribution is not affected significantly. The changes induced in the spin distribution by different sample selection criteria are thus exactly of the order of magnitude and of the type of the residual differences observed between our results and the study of Bett et al. (2007), validating that our independent analysis methods are consistent.

## 2.3 Dark matter only results

### 2.3.1 Angular momentum statistics of dark matter haloes at $z = 0$

We begin by presenting the angular momentum properties of dark matter only haloes from Illustris-1-Dark. In Fig. 2.7 we show the spin parameter distributions for FOF- (upper panel) and SO-haloes (lower panel) at $z = 0$. Our FOF- and SO-halo samples comprise $\sim 400,000$ and $\sim 360,000$ objects, respectively. We provide least-square error fits of the two most common fitting functions to the derived Peebles spin parameter distributions. We chose to present results derived with the Peebles spin parameter, as it yields nearly identical spin distributions for both halo definitions when the potential energy of the halo is estimated accurately. The classic analytic approximation for the spin parameter distribution is the lognormal function (e.g. van den Bosch, 1998),

$$P(\log_{10}\lambda) = \frac{1}{\sqrt{2\pi}\sigma} \exp\left[-\frac{1}{2}\left(\frac{\log_{10}(\lambda/\lambda_0)}{\sigma}\right)^2\right], \tag{2.5}$$

where $\lambda_0$ is the peak position and $\sigma$ the width of the distribution. The lognormal function is normalised such that $\int_{-\infty}^{\infty} P(\log_{10}\lambda)\, \mathrm{dlog}_{10}\lambda = 1$. Bett et al. (2007) performed an extended analysis of the Peebles spin parameter distribution of dark matter only haloes from the Millennium Simulation (Springel et al., 2005) and found that their cleaned halo sample is better described by the fitting function

$$P_{\mathrm{B}}(\log_{10}\lambda) = A\left(\frac{\lambda}{\lambda_0}\right)^3 \exp\left[-\alpha\left(\frac{\lambda}{\lambda_0}\right)^{3/\alpha}\right], \tag{2.6}$$

where $\lambda_0$ is again the peak position, $\alpha$ a free fitting parameter, and $A$ the normalisation, such that $\int_{-\infty}^{\infty} P_B(\log_{10}\lambda)\, \mathrm{dlog}_{10}\lambda = 1$. This new fitting function is constructed to rise with the third power for small values and falls off exponentially for large values. However, this specific shape in combination with the free fitting parameter $\alpha$ makes the given function highly flexible.

We fit both functions to the Peebles spin parameter distributions of our FOF- and SO-halo samples. The small panels in Fig. 2.7 show the absolute error of the fits relative to the distribution derived from Illustris-1-Dark in every bin. From the absolute errors in every bin we derive the root mean square error $\varepsilon_{\mathrm{rms}}$ of the fit and list it with the best fit parameters in Tab. 2.2. Based on $\varepsilon_{\mathrm{rms}}$ we find that the new fitting function given by Eq. (2.6) describes the SO-halo spin distribution slightly better, which is consistent with Bett et al. (2007), who derived their fitting function based on a halo sample very similar to their SO-halo sample. The

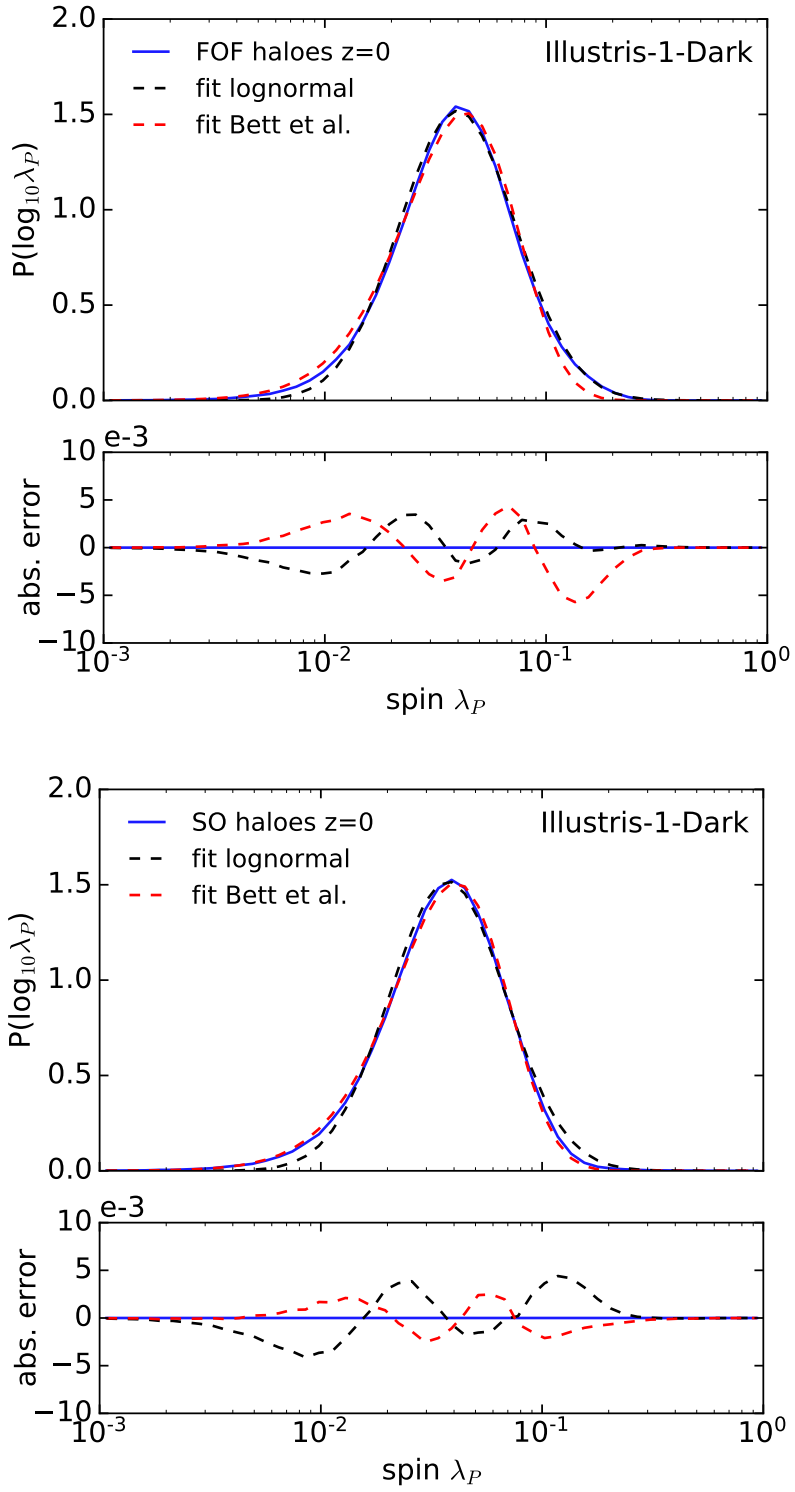


Figure 2.7: Peebles spin parameter distribution (blue) of FOF-haloes (upper panel) and SO-haloes (lower panel) from Illustris-1-Dark. Both distributions are fitted with a lognormal function (dashed black) and a fitting function proposed by Bett et al. (2007) (dashed red). For easier comparison we show the absolute error of the fitting functions with respect to the distribution obtained from Illustris-1-Dark.

| | | | |
|---|---|---|---|
| FOF fit lognormal | $\lambda_0 = 0.040$ | $\sigma = 0.26$ | $\varepsilon_{\rm rms} = 0.0015$ |
| FOF fit Bett et al. | $\lambda_0 = 0.043$ | $\alpha = 3.16$ | $\varepsilon_{\rm rms} = 0.0022$ |
| SO fit lognormal | $\lambda_0 = 0.037$ | $\sigma = 0.26$ | $\varepsilon_{\rm rms} = 0.0020$ |
| SO fit Bett et al. | $\lambda_0 = 0.041$ | $\alpha = 3.15$ | $\varepsilon_{\rm rms} = 0.0011$ |

Table 2.2: Best fit parameters of the analytic fits to the Peebles spin parameter distributions derived from Illustris-1-Dark. We give results both for FOF- and SO-haloes, and in each case for the classic log-normal function and the proposed modified fitting function by Bett et al. (2007).

FOF-halo spin distribution on the other hand is better fit by the classic lognormal function. We find the same behaviour when analysing the Bullock spin parameter distributions. The differences between the two fitting functions lie primarily in the different slopes in the wings of the distribution and the detailed peak shape. However, these differences are relatively small, and which analytic function describes the spin parameter distribution best depends ultimately on the preferred halo definition.

### 2.3.2 Convergence

In Fig. 2.8 we show the Peebles spin parameter distribution for FOF-haloes (upper panel) and SO-haloes (lower panel) derived at three different resolutions of Illustris-Dark (see Tab. 4.1) for halo masses above $1.4 \times 10^{11}\,\mathrm{M}_{\odot}$. This mass limit is set by our selection criteria, which require a halo to be resolved by at least 300 dark matter particles. When applied to Illustris-3-Dark with the coarsest resolution this corresponds to the above value. As there are subtle trends of spin with halo mass a common mass range must be adopted when examining the numerical convergence of our measurements.

Reassuringly, we find very good convergence of the Peebles spin parameter distribution for the three resolutions of Illustris-Dark. The small residual deviations originate in the limited halo sample size and are consistent with the associated counting noise. The convergence is equally good for the Bullock spin parameter distribution, which we refrain from showing explicitly.

### 2.3.3 Redshift evolution of halo spin

In Fig. 2.9 we show the spin parameter distributions obtained with the Peebles (left column) and Bullock (right column) spin parameter definition for FOF- (upper row) and SO-haloes (lower row) from Illustris-1-Dark for different redshifts. Black dots mark the median spin parameters at every redshift.

The Peebles spin parameter definition applied to FOF-haloes yields a remarkably self-similar spin parameter distribution in time, as expected from theory for self-similar dark matter structures. The self-similarity of haloes is only broken by a varying mean concentration $c$ of the NFW radial density profile with halo mass. Less massive haloes are expected to be on average denser, which corresponds to higher values of $c$, and to collapse earlier than more massive haloes (Navarro et al., 1997). This introduces a time dependence of the mean concentration for quasi-relaxed structures thus generally breaking the self-similarity of haloes with respect to both halo mass and time. However, as Navarro et al. (1997) found no correlation of the spin with concentration (see also Bullock et al., 2001), we expect the spin parameter distribution of haloes to be approximately self-similar with mass and time. This feature is realised by the Peebles spin parameter distribution of FOF-haloes which shows only a small evolution of the median spin value from $\lambda_{z=8} = 0.0374$ at $z = 8$ to $\lambda_{z=0} = 0.0391$ at $z = 0$.

The spin parameter distributions derived with other approaches however exhibit non-vanishing trends with redshift. The strongest shift is visible if the Bullock spin parameter definition is applied to FOF-haloes. The residual trends in this distribution are a consequence of imposing a spherical shape on the more complicated geometry of FOF-haloes. The trends in the distributions obtained from the SO-halo definition are probably caused by not taking into account the gravitationally bound matter outside the virial radius $R_{200}$, whose relative mass fraction with respect to the matter inside of $R_{200}$ can change over time, inducing the observed trends.

We conclude that although the SO-halo definition is operationally very clean, it is the Peebles spin parameter definition applied to FOF-haloes that yields physically the most stable and reliable results. Thus, in the following we will restrict ourselves to showing mostly results obtained for FOF-haloes with the Peebles spin parameter definition. We have checked that our analysis carried out for SO-haloes yields qualitatively the same results.

### 2.3.4 Dependence of spin on halo mass

In Fig. 2.10 we show the dependence of the Peebles spin parameter of FOF-haloes from Illustris-1-Dark on the halo mass $M_{\rm FOF}$. This figure shows a two-dimensional histogram where FOF-haloes have been binned according to their mass and spin parameter in 50 equidistant logarithmic bins over the given range. As the absolute number of haloes increases rapidly with decreasing mass, we have normalised every mass bin to unity. The normalised number of FOF-haloes in every mass bin is indicated by the grey shading ranging from a fraction of 0 to 0.2 of the haloes in each mass bin. Contours are drawn at constant fractions

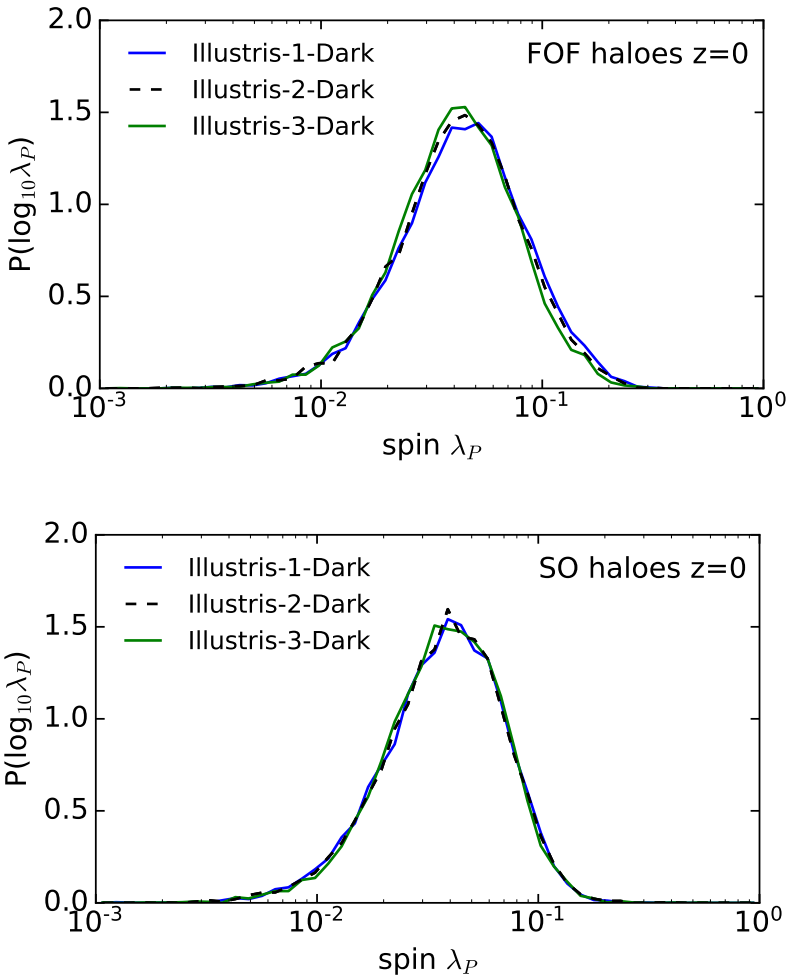


Figure 2.8: Peebles spin parameter distributions of dark matter only FOF-haloes (upper panel) and SO-haloes (lower panel) derived for the three different resolutions of the *Illustris* simulation suite (see Tab. 4.1). We find very good convergence for the three resolutions; the small residual deviations are consistent with noise expected from the limited halo sample size.

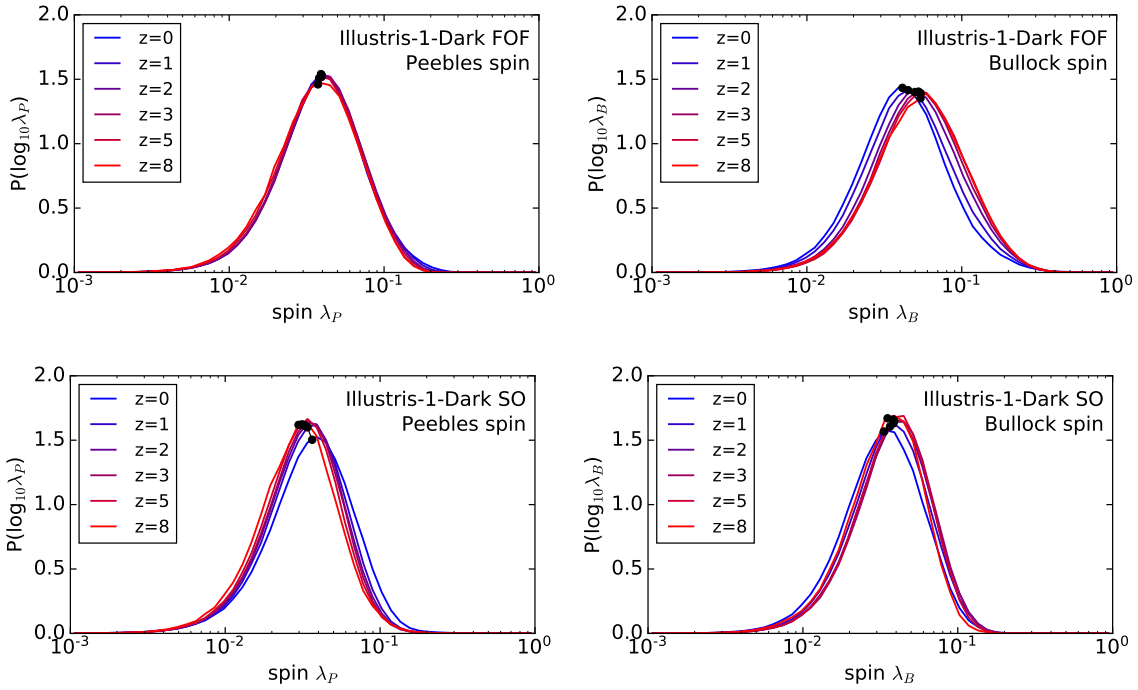


Figure 2.9: Redshift evolution of the spin parameter distribution of FOF-haloes (upper panel) and SO-haloes (lower panel) derived with the Peebles (left column) and Bullock (right column) spin parameter from Illustris-1-Dark. Black dots mark the median spin parameter at every redshift. The Peebles spin parameter distribution of FOF-haloes is perfectly self-similar with respect to time. The other distributions exhibit residual trends with redshift, which are due to shortcomings in the Bullock spin and SO-halo definitions. We thus restrict ourselves in the following on the Peebles spin applied to FOF-haloes, which yields the most robust results.

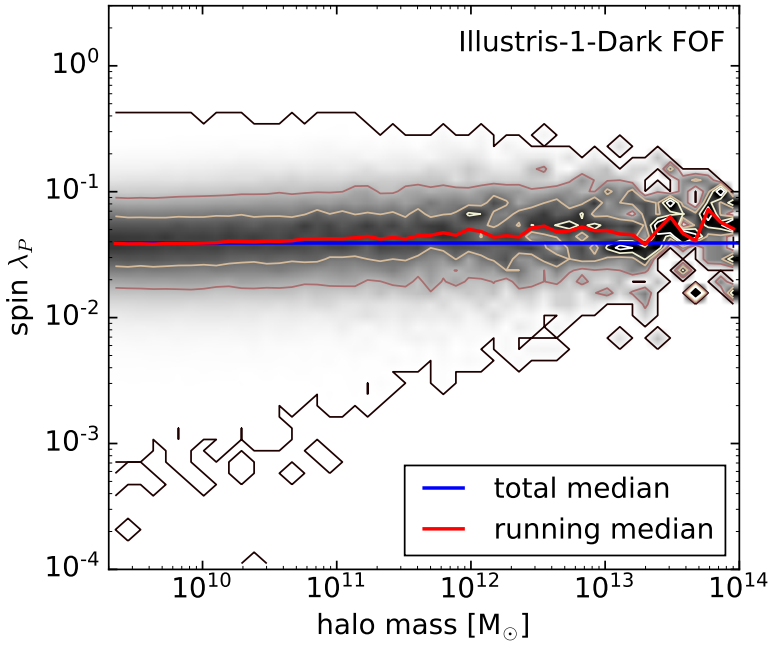


Figure 2.10: Distribution of the Peebles spin parameter with respect to the mass $M_{\mathrm{FOF}}$ of dark matter only FOF-haloes from Illustris-1-Dark, separately normalised in every mass bin. The grey shading ranges from a fraction of 0 to 0.2 of all haloes in a mass bin having a given spin parameter. Contours are drawn at constant fractions of 0, 0.05, 0.1, 0.15, and 0.2, respectively. The total median spin parameter is shown as a blue line, the median of every mass bin as a red line. The median spin parameter slightly increases with increasing halo mass.

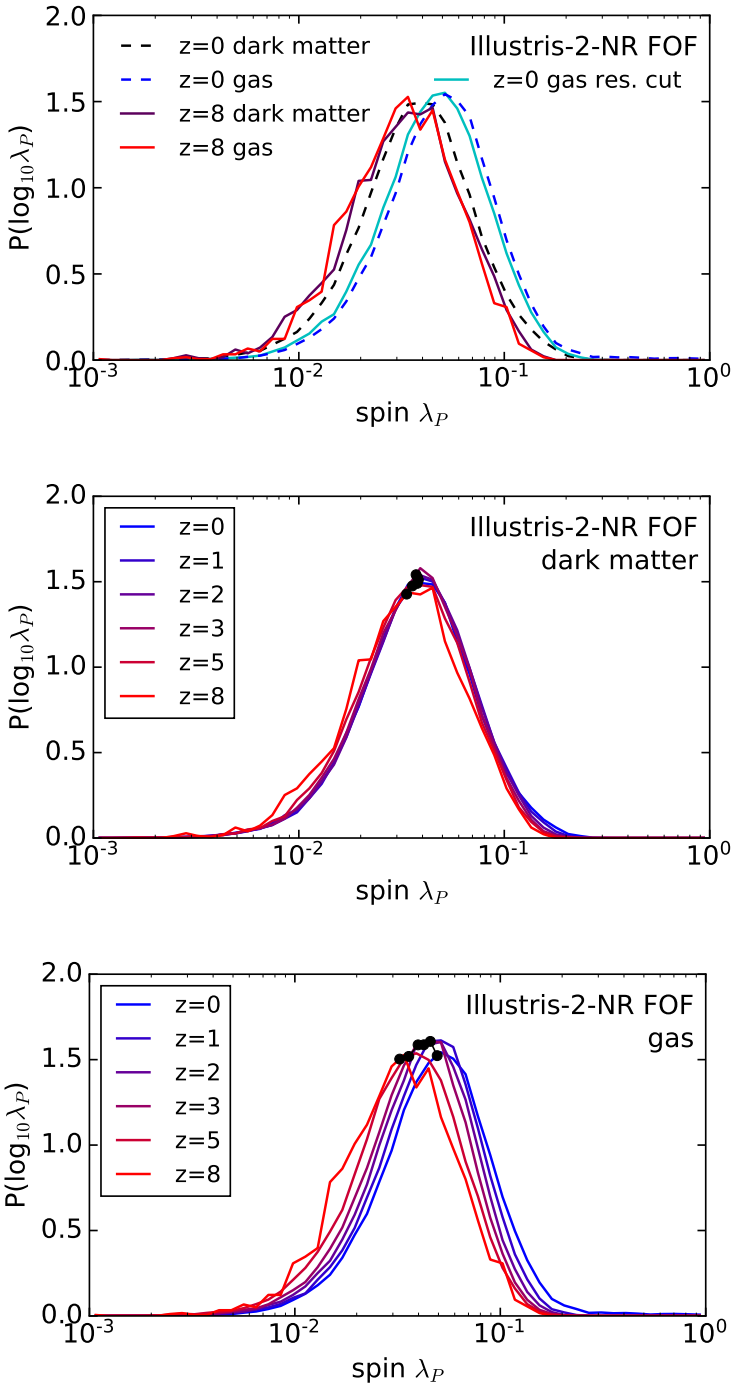


Figure 2.11: Redshift evolution of the dark matter (middle panel) and gas (lower panel) Peebles spin parameter distributions of FOF-haloes from Illustris-2-NR. Black dots mark the median spin parameter at every redshift. The dark matter spin distribution exhibits the same self-similarity in time as the dark matter-only Illustris-1-Dark simulation, however, at somewhat lower spin values. The spin distribution of gas on the other hand systematically shifts to higher spin values, due to a transfer of angular momentum from dark matter to gas. For comparison, we show (upper panel) the spin parameter distributions for dark matter and gas at $z = 8$ (solid line) and $z = 0$ (dashed line), including the gas distribution derived with a stricter mass cut (cyan) to exclude bias due to poorly resolved haloes.

of 0, 0.05, 0.1, 0.15, and 0.2, respectively. The median spin parameter in every mass bin is shown as a red line, the overall median spin parameter as a blue line.

Fig. 2.10 shows a small, but clearly present, systematic increase of the median Peebles spin parameter with halo mass. This trend is presumably caused by two related effects. More massive haloes originating from larger initial density perturbations are not fully collapsed at $z = 0$ yet. Also, they are still actively accreting matter that perturbs their outskirts and slows down the relaxation process. The orbital angular momentum of the involved minor mergers adds to the intrinsic angular momentum of the main halo and leads to an enhanced spin. As we have shown in Fig. 2.1, FOF-haloes are in general much more extended than SO-haloes, such that this effect plays a role in FOF-haloes but not in SO-haloes. This is in agreement with the results from Macciò et al. (2007), who find the trend of spin with halo mass to be less distinctive and consistent with zero for SO-haloes.

## 2.4 Non-radiative simulation results

### 2.4.1 Intrinsic differences between dark matter and gas

At high redshift, baryons experience the same gravitational torques from the surrounding density field as dark matter, and thus are assumed to have identical 'initial' spins (Fall and Efstathiou, 1980). In the absence of any additional physical processes such as star formation and feedback one then naively expects the gas to sustain its initial spin and the correspondence with the dark matter spin.

To test the assumption of gas and dark matter having identical initial spin distributions, van den Bosch et al. (2002) performed non-radiative cosmological simulations that they evolved until a redshift of $z = 3$. Fitting the standard lognormal function to the measured Bullock spin parameter distributions of the dark matter and gas components of their 378 SO-haloes, van den Bosch et al. (2002) derive mean dark matter and gas spin values of $\lambda_{0,\mathrm{dm}} = 0.040$ and $\lambda_{0,\mathrm{gas}} = 0.039$, respectively, confirming that gas and dark matter have identical 'initial' spins[4].

In the upper panel of Fig. 2.11, we show as solid lines the 'initial' dark matter and gas Peebles spin parameter distributions from the non-radiative Illustris-2-NR simulation at $z = 8$ and confirm this result also for the Peebles spin parameter distribution. The derived distributions have median Peebles spin parameters of $\lambda_{\mathrm{dm},z=8} = 0.0335$ and $\lambda_{\mathrm{gas},z=8} = 0.0324$,

[4]Note that there is no clear definition of 'initial' spin to be measured at a distinct cosmic time, as structures acquire their angular momentum continuously by tidal torques from the surrounding large scale gravitational field. However, 'initial' spin usually refers to the spin structures have before strong non-linear interactions and galaxy formation physics start playing a significant role.

respectively, which are equal within statistical fluctuations. The dashed lines in Fig. 2.11 show the same spin parameter distributions at $z = 0$ derived from $\sim 65,000$ FOF-haloes from Illustris-2-NR. Whereas the spin parameter distribution of the dark matter component exhibits only slightly higher values than the 'initial' spin distribution with a median of $\lambda_{\mathrm{dm},z=0} = 0.0377$ at $z = 0$, consistent with the trend in the dark matter only Illustris-1-Dark simulation, the gas component has evolved to substantially higher values with a median spin parameter of $\lambda_{\mathrm{gas},z=0} = 0.0493$. At $z = 0$ this yields a ratio of the median gas to dark matter spin parameter of $\lambda_{\mathrm{gas}}/\lambda_{\mathrm{dm}} = 1.308$, i.e. a $\sim 30\%$ higher spin of the gas than the dark matter.

Similar results have been obtained by Chen et al. (2003) and Sharma and Steinmetz (2005) who performed non-radiative ΛCDM simulations and estimated the mean gas and dark matter spin parameter values from fitting the lognormal to the derived Bullock spin parameter distributions. They arrive at a ratio of mean gas to dark matter spin equal to $\lambda_{0,\mathrm{gas}}/\lambda_{0,\mathrm{dm}} = 1.19$ and $\lambda_{0,\mathrm{gas}}/\lambda_{0,\mathrm{dm}} = 1.44$, respectively, using however much smaller halo sample sizes of 48 and 41 SO-haloes, respectively. The small sample sizes are likely responsible for the variations in the reported size of the effect, but the general trend of having a higher specific angular momentum at $z = 0$ in the gas compared to the dark matter is consistent. Gottlöber and Yepes (2007) quote similar results for more than $10,000$ cluster-sized FOF-haloes with masses larger than $5 \times 10^{13} h^{-1}\mathrm{M}_{\odot}$. Applying the same method as above, modulo some uncertainty by applying the Bullock spin parameter definition to FOF-haloes (see Section 2.2.4), they find a spin parameter enhancement of $\lambda_{0,\mathrm{gas}}/\lambda_{0,\mathrm{dm}} = 1.32$.

Sharma et al. (2012) suggested that the different mechanisms by which dark matter and gas achieve equilibrium lead to an inside-out transport of angular momentum in the dark matter component and an outside-in transport in the gas component. The inside-out transport of angular momentum in the dark matter by dynamical friction of mergers entering the inner halo was also already observed by Zavala et al. (2008). As the dark matter is insensitive to hydrodynamic interactions, and the total gas mass available for gravitational interactions is small compared to the dark matter mass, the processes taking place in the two components are largely decoupled from each other. As SO-haloes exclude the outer regions of gravitationally bound haloes (compare Fig. 2.1), the different transport mechanisms described by Sharma et al. (2012) might explain why the gas to dark matter spin ratio becomes larger than unity for SO-haloes.

When the outer regions are fully included, such as in FOF-haloes, the gas to dark matter spin ratio would be expected to approach unity again in this picture. However, we find an enhanced gas to dark matter spin ratio of the same order of magnitude for FOF-haloes as well, suggesting that different radial redistribution mechanisms of angular momentum in the

two components provide an insufficient explanation. Instead, there must be an additional mechanism by which gas acquires more specific angular momentum than dark matter.

In Fig. 2.11 we show how the Peebles spin parameter distributions of the dark matter (middle panel) and the gas (lower panel) components of FOF-haloes from the Illustris-2-NR simulation evolve with redshift. Black dots mark the median spin parameters at the different redshifts. The dark matter spin parameter distribution exhibits the same self-similarity in time as in the dark matter only Illustris-1-Dark simulation. However, the spin parameter distribution of the gas gradually shifts to higher spin values with decreasing redshift, illustrating a continuous specific angular momentum acquisition in the gas component throughout cosmic time.

This acquisition could be explained by mergers getting ram pressure striped during infall, which leads to a decoupling of their gas and dark matter components. The displacement of the centres of mass of the two components produces a mutual torque of the gas and dark matter components onto each other, allowing a net transfer of angular momentum from the dark matter to the gas. Hydrodynamic shocks and other instabilities occurring in the gas are then crucial for the redistribution of angular momentum inside the gas component, but cannot directly account for transfer of specific angular momentum between dark matter and the gas, as dark matter couples only gravitationally to the gas. The gain of specific angular momentum in the gas is evident in the shift of the gas spin parameter distribution, whereas the corresponding loss of angular momentum in the dark matter distribution is barely visible, as its mass fraction is much larger than that of the gas. Compared to the dark matter spin in the dark matter only Illustris-1-Dark simulation, the gas component gains more specific angular momentum than the dark matter by a factor of 1.26. To compensate for this gain in the gas component, given a cosmic baryon fraction of $f_\mathrm{b} = \Omega_b/\Omega_m = 0.1673$, the dark matter component in the non-radiative run has to transfer $\sim 5.2$ % of its initial spin to the gas. The median dark matter spin parameter in the dark matter only Illustris-1-Dark simulation is $\lambda_\mathrm{DM} = 0.0391$, which leads to an expected reduced spin parameter of the dark matter component in the non-radiative simulation of $\lambda_\mathrm{NR,exp} = 0.0371$ at $z = 0$. In Illustris-2-NR we measure a median spin of $\lambda_\mathrm{NR} = 0.0377$ (also see Fig. 2.16), but as we observe a weak trend of spin with halo mass (see Section 2.4.2), we expect such a deviation caused by the different mass cuts in Illustris-1-Dark and Illustris-2-NR.

Furthermore, as we select our haloes based on a minimum number of dark matter particles only, some haloes in our sample have poorly resolved gas components. To quantify the impact from such objects, we show as cyan line in the upper panel of Fig. 2.11 the gas spin parameter distribution obtained from haloes whose gas component is resolved by at least 300 gas cells. This spin distribution is shifted to slightly smaller spin values compared with

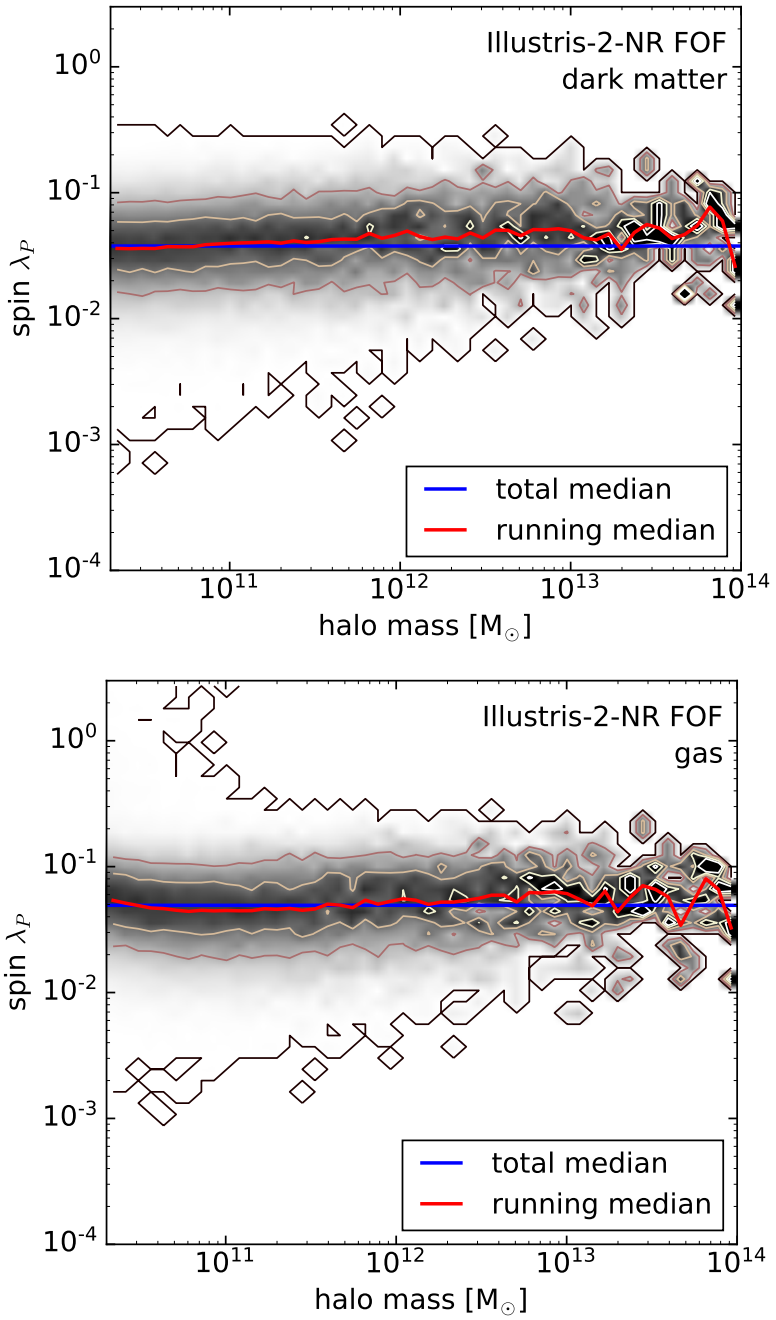


Figure 2.12: Distribution of the dark matter (upper panel) and gas (lower panel) Peebles spin parameter as a function of FOF-halo mass $M_{\mathrm{FOF}}$ for Illustris-2-NR, normalised in every mass bin. The contours are drawn at constant fractions of 0, 0.05, 0.1, 0.15, and 0.2, respectively. The total median spin parameter is shown as blue line, the median of every mass bin as red line. The dark matter spin shows the same trend as in Illustris-1-Dark; the gas spin follows this dark matter trend.

the gas distribution from the full sample, but otherwise exhibits the same behaviour. For this restricted sample we find a median value of $\lambda^*_{\mathrm{gas,z=0}} = 0.0458$, which corresponds to an enhancement factor of 1.17 with respect to dark matter. The expected dark matter spin in the non-radiative simulation is then $\lambda^*_{\mathrm{NR,exp}} = 0.0376$, and thus almost identical to the measured value. However, as poor resolution affects small mass haloes, restricting the sample based on this criterium introduces an even larger discrepancy in the compared mass ranges, which is a source of bias due to the non-negligible trend of spin with halo mass.

Another possible mechanism that could contribute to the gain of specific angular momentum by the gas component is if there is a preferred orientation of the rotation axis of the gas component perpendicular to the infall directions of merging matter. As we show in Section 2.5.5, the gas and dark matter component of FOF-haloes are on average misaligned by $\sim 35^\circ$, such that given this preferred orientation the orbital angular momentum of mergers could on average spin up the gas more than the dark matter. Whether such a preferred orientation of the gas component with infalling matter however exists and what may cause it is left for a future investigation.

### 2.4.2 Dependence of spin on halo mass

In Fig. 2.12 we show the dependence of the dark matter (upper panel) and gas (lower panel) Peebles spin parameter of FOF-haloes from Illustris-2-NR on halo mass $M_{\mathrm{FOF}}$. The two-dimensional histogram was obtained in the same way as for Fig. 2.10. The dark matter exhibits the same trend as already observed in the dark matter only Illustris-1-Dark simulation, with the median Peebles spin parameter increasing slightly with halo mass. The spin parameter of the gas component, though being somewhat higher, follows the same mass trend as observed for the dark matter. The small upward trend in the least massive mass bins is likely due to resolution effects, as the haloes are selected based on being resolved by at least 300 dark matter particles, but there is no limit on the minimum number of gas cells, such that the gas spin parameter of the least massive haloes can be in principle based on only a few dozen cells in gas poor haloes.

## 2.5 Full physics simulation results

### 2.5.1 Dark matter spin statistics

In this section we present the angular momentum properties of the dark matter component of FOF-haloes from the full physics Illustris-1 simulation and compare them to the dark

| | | | |
|---|---|---|---|
| fit lognormal | $\lambda_0 = 0.039$ | $\sigma = 0.27$ | $\varepsilon_{\rm rms} = 0.0018$ |
| fit Bett et al. | $\lambda_0 = 0.042$ | $\alpha = 3.30$ | $\varepsilon_{\rm rms} = 0.0018$ |

Table 2.3: Best fit parameters of the analytic fits to the Peebles spin parameter distributions of the dark matter component derived from Illustris-1. The fit parameters are remarkably similar to the parameters derived for Illustris-1-Dark listed in Tab. 2.2, showing very good convergence of the dark matter properties.

matter properties derived from the dark matter only Illustris-1-Dark simulation. Illustris-1 comprises $\sim 320,000$ FOF-haloes fulfilling our selection criteria.

In Fig. 2.13 we show analytic fits of the lognormal and the fitting function proposed by Bett et al. (2007) to the Peebles spin parameter distribution of the dark matter component at $z = 0$. The best fit parameters as well as the root mean square errors of the fits are listed in Tab. 2.3. These parameters differ only insignificantly from the best fit parameters derived for the Peebles spin parameter distribution of dark matter only FOF-haloes from Illustris-1-Dark that are listed in Tab. 2.2. Furthermore, we show the convergence of the Peebles spin parameter distribution of the dark matter component for the three different resolutions (see Tab. 4.1) of the full physics *Illustris* simulations in Fig. 2.14. We find very good convergence, of the same quality as for Illustris-Dark, with the small deviations originating in the limited halo sample size.

The redshift dependence of the dark matter Peebles spin parameter distribution from Illustris-1 is shown in Fig. 2.15. Black dots mark the median spin parameter at every redshift. We find the same behaviour of the distribution as in the dark matter only Illustris-1-Dark, in the form of an almost perfect self-similarity in time. A small trend of the median spin towards higher values with decreasing redshift is again present, as already observed in the dark matter spin distributions from both Illustris-1-Dark and Illustris-2-NR.

However, the presence of baryons does introduce subtle changes in the dark matter component, which are barely visible at first sight. To highlight this point, we show in Fig. 2.16 the dark matter Peebles spin parameter distributions at $z = 0$ derived from the three different simulation types at the highest available resolution (see Tab. 4.1), the dark matter only simulation Illustris-1-Dark, the non-radiative Illustris-2-NR, and the full physics Illustris-1 simulation. The dark matter Peebles spin parameter distributions derived from these three simulations are remarkably similar. The median spin parameters at $z = 0$ are $\lambda_{\rm DM} = 0.0391$ for Illustris-1-Dark, $\lambda_{\rm NR} = 0.0377$ for Illustris-2-NR, and $\lambda = 0.0379$ for Illustris-1. The simulations including baryons thus have slightly smaller median spin parameters than the dark matter only one. The relative shift of the median values amounts to 3.6% for the non-radiative Illustris-2-NR simulation and to 3.1% for the full physics Illustris-1 simulation compared to the dark matter only Illustris-1-Dark. This shift of the dark matter spin distribution to

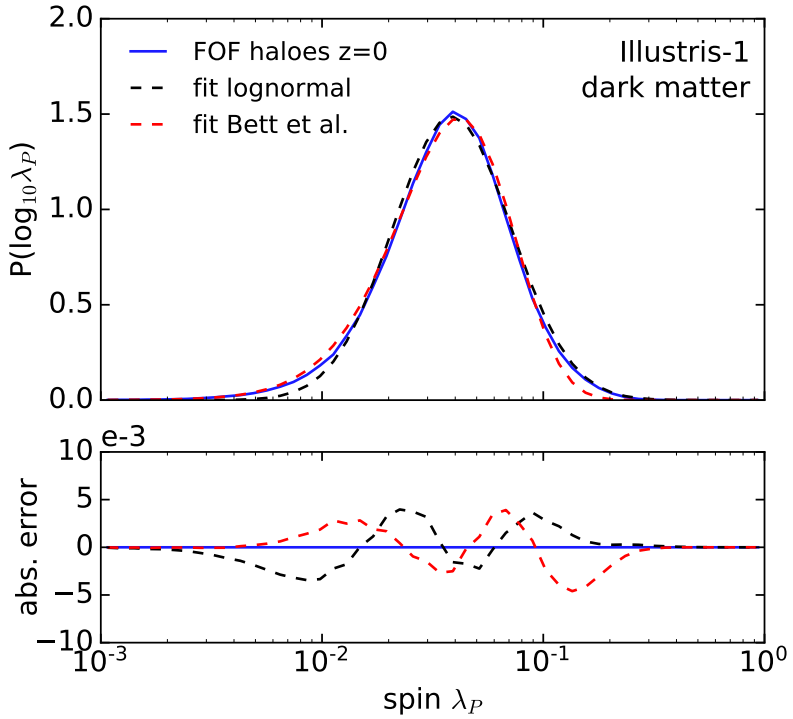


Figure 2.13: Peebles spin parameter distributions of the dark matter component (blue) of FOF-haloes from Illustris-1 at $z = 0$. The distribution is fitted with a lognormal function (dashed black) and a fitting function proposed by Bett et al. (2007) (dashed red). For better comparison we show the absolute errors of the fitting functions with respect to the distribution obtained from Illustris-1.

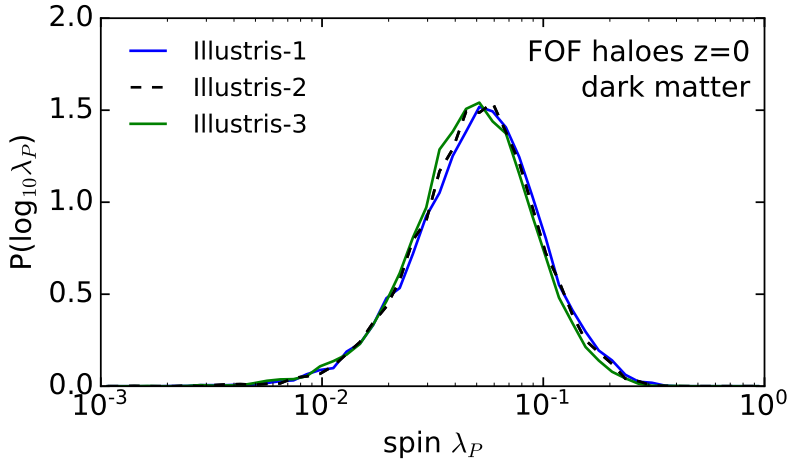


Figure 2.14: Peebles spin parameter distributions of the dark matter component of FOF-haloes for the three different resolutions of the full physics *Illustris* simulations (see Tab. 4.1) at $z = 0$. We find good convergence with the small deviations originating in the limited halo sample size.

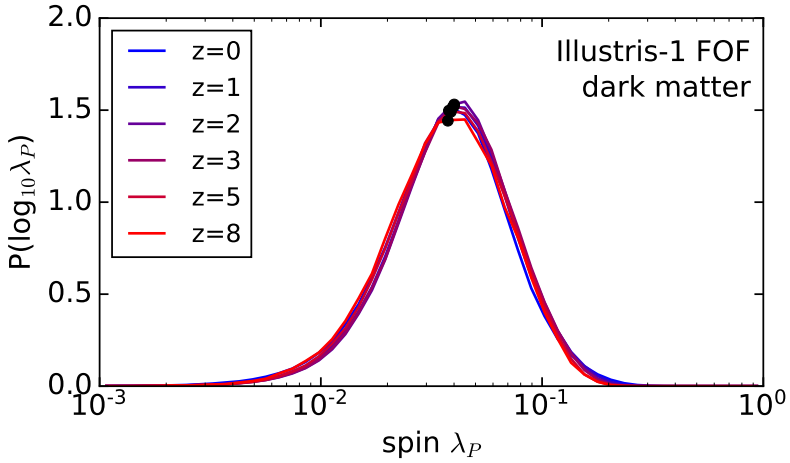


Figure 2.15: Redshift evolution of the Peebles spin parameter distribution of the dark matter component of FOF-haloes from the full physics Illustris-1 simulation. Black dots mark the median spin parameter at every redshift. The spin parameter distribution is self-similar in time confirming the dark matter only results.

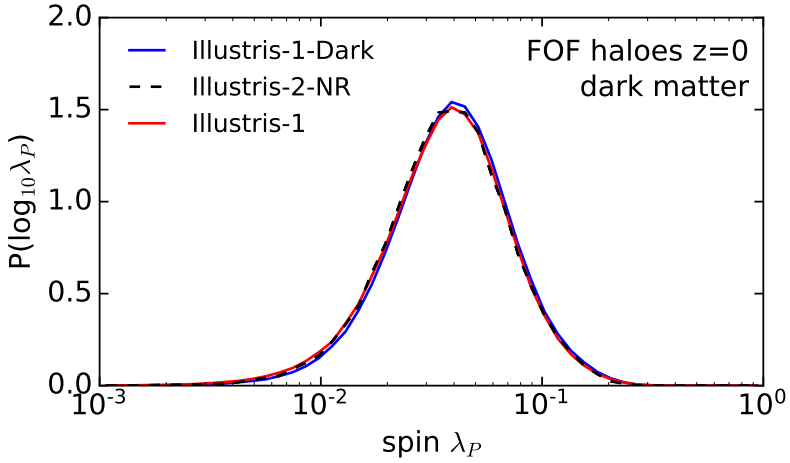


Figure 2.16: Peebles spin parameter distribution of the dark matter components of FOF-haloes at $z = 0$ from Illustris-1, Illustris-2-NR, and Illustris-1-Dark. The distributions derived from the three different types of simulations are remarkably similar. The median spin parameters are $\lambda_{\rm DM} = 0.0391$ for Illustris-1-Dark, $\lambda_{\rm NR} = 0.0377$ for Illustris-2-NR, and $\lambda = 0.0379$ for Illustris-1. Thus the simulations including baryons have a slightly smaller median dark matter spin than in the dark matter only simulation. The relative shift of the median values amounts to 3.6% for Illustris-2-NR and 3.1% for Illustris-1 compared to Illustris-1-Dark, consistent with a transfer of angular momentum from dark matter to gas during mergers.

somewhat smaller values in the presence of a baryonic component can be explained as a reflection of the transfer of angular momentum from the dark matter to the gas during mergers, as discussed in Section 2.4.

### 2.5.2 Spin statistics of baryons in different halo regimes

In this section, we investigate the spin statistics of gas and stars within FOF-haloes from Illustris-1. The baryonic spin is strongly affected by physical processes such as star formation and feedback, which also indirectly impact the dark matter through the change in baryonic density. These physical processes make the efficiency of galaxy formation a strong function of halo mass, hence we expect the baryonic spin to depend on halo mass as well. This motivates us to define three mass ranges in which we are going to examine the spin parameter distributions:

1. $[2 \times 10^{10} \mathrm{M}_\odot, 2 \times 10^{11} \mathrm{M}_\odot]$: SN feedback dominated
2. $[2 \times 10^{11} \mathrm{M}_\odot, 2 \times 10^{12} \mathrm{M}_\odot]$: efficiently star forming
3. $[2 \times 10^{12} \mathrm{M}_\odot, 2 \times 10^{13} \mathrm{M}_\odot]$: AGN feedback dominated

We discuss the association between these mass bins and the individual feedback regimes further blow.

We show the Peebles spin parameter distributions of dark matter, gas, and stars, as well as the combined baryonic and the total spin parameter distributions for Illustris-1 in the above mass bins in Fig. 2.17. As the number of haloes increases rapidly with decreasing halo mass (the number of haloes in the three mass bins are 51383, 7286, and 834, respectively), the overall spin statistic is dominated by haloes just above the lower limit of each mass bin. To reduce noise in the highest mass bin, the spin parameter distributions in Fig. 2.17 have been smoothed with a Gaussian kernel with standard deviation of one bin in spin parameter space and truncated after four bins. The median Peebles spin parameter values in the different mass bins as well as the stellar to gas mass ratios are listed in Tab. 2.4.

Fig. 2.17 demonstrates that the scale-dependent galaxy formation physics breaks the self-similarity of haloes with respect to their spin distribution. In realistic simulations of galaxy formation, the gas spin depends strongly on the halo mass (compare also Fig. 2.19) and is on average about twice as high as the dark matter spin, whereas the stellar spin is only about half as large as the dark matter spin. The general trend of a higher spin of the gas compared with the dark matter, and of a lower stellar spin, is in agreement with findings from Teklu et al. (2015) based on 622 haloes with no restrictions on their dynamical state.

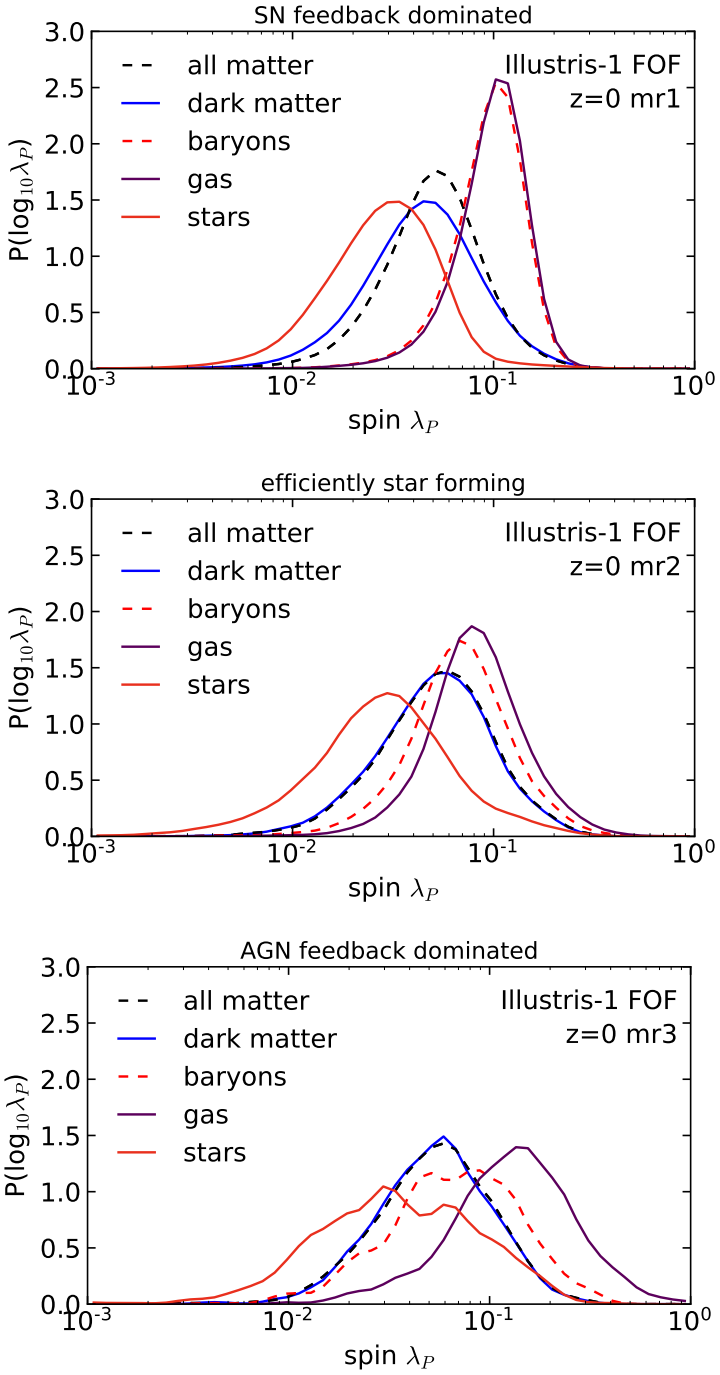


Figure 2.17: Peebles spin parameter distributions of the dark matter, gas, and stellar component of FOF-haloes as well as the combined baryonic spin parameter distribution and the total spin parameter distribution in the three examined mass ranges of the full physics simulation Illustris-1, as discussed in Section 2.5.2. This figure demonstrates that galaxy formation physics breaks the self-similarity of the spin parameter distribution observed in dark matter only simulations.

| range | all | dm | gas | baryons | stars | $\frac{M_*}{M_{\rm gas}}$ |
|---|---|---|---|---|---|---|
| (i) mr1 | 0.0506 | 0.0449 | 0.102 | 0.0985 | 0.0288 | 0.07 |
| (ii) mr2 | 0.0534 | 0.0524 | 0.0814 | 0.0681 | 0.0283 | 0.38 |
| (iii) mr3 | 0.0546 | 0.0541 | 0.133 | 0.0692 | 0.0346 | 1.61 |

Table 2.4: Median Peebles spin parameter values of the different components making up the halo for different halo mass ranges.

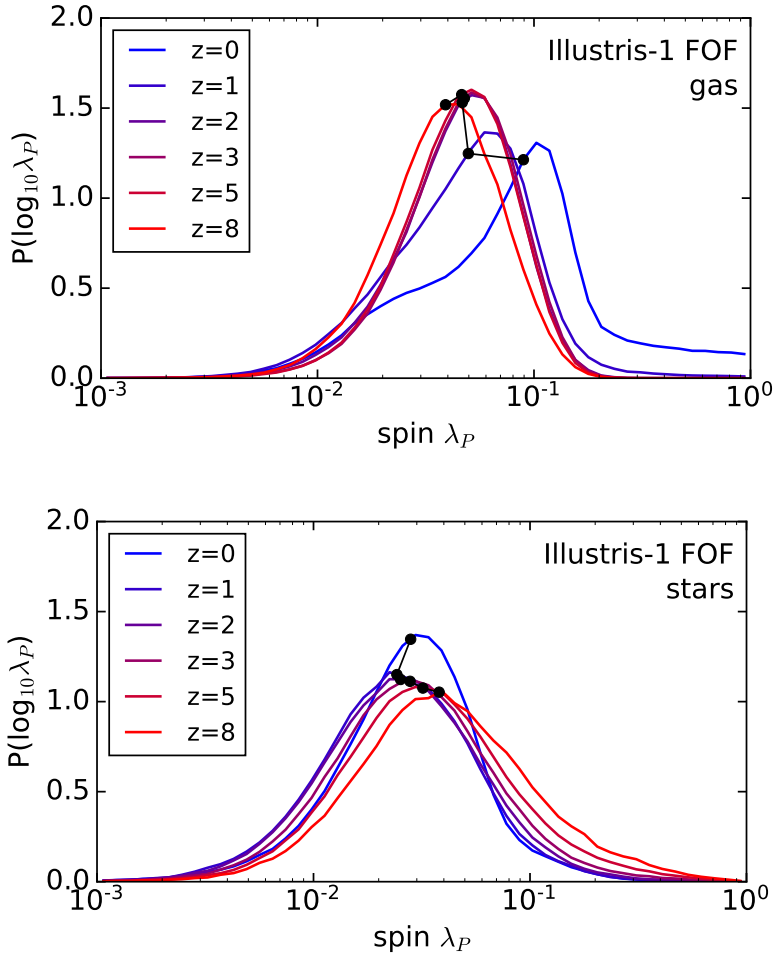


Figure 2.18: Peebles spin parameter distribution of the gas and stellar component in the full physics Illustris-1 simulation as a function of redshift. Black dots mark the median spin parameter at every redshift. Gas increases its specific angular momentum content with cosmic time. The stellar component on the other hand evolves towards slightly smaller median spins. Both components exhibit changes in the shape of their spin distributions.

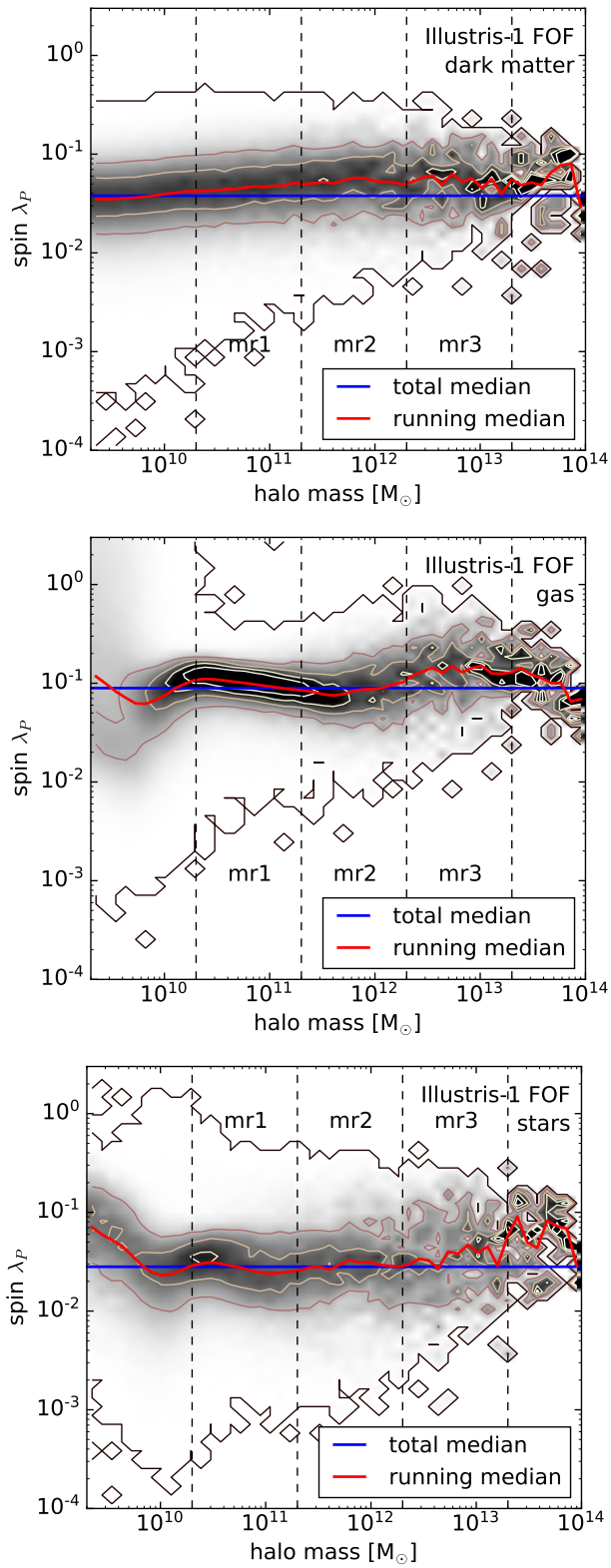


Figure 2.19: Distribution of the dark matter (upper panel), gas (middle panel), and stellar (lower panel) Peebles spin parameter with halo mass $M_{\mathrm{FOF}}$ for Illustris-1 normalised in every mass bin. The grey shading indicates a fraction of 0 to 0.2 of all haloes in a given mass bin having a given spin. Contours are drawn at constant fractions of 0, 0.05, 0.1, 0.15, and 0.2. The total median spin parameter is shown as a blue line, the median of every mass bin as a red line. The dark matter spin shows the same behaviour as in Illustris-1-Dark, the baryonic spin however exhibits a stronger trend with mass that is caused by the impact of feedback. We discuss this trend in more detail in Section 2.5.2.

The baryonic spin distribution of low mass haloes (upper panel) is almost completely determined by the gas spin, as those haloes contain only few stars. With increasing halo mass, the stellar mass to gas mass fraction increases rapidly, and the baryonic distribution shifts to progressively lower spin values (middle and lower panels). The baryonic spin of all haloes from the three mass bins is on average a factor of $\sim 1.8$ larger than the dark matter spin, which is substantially more than the value of $\sim 1.3$ found in the non-radiative Illustris-2-NR simulation. We investigate the origin of this enhancement in detail in Section 2.5.4. The total spin of haloes is thus underestimated by dark matter only simulations by $\sim 13\%$, $\sim 2\%$, and $\sim 1\%$ in the three bins, respectively.

In Fig. 2.18 we show how the Peebles spin parameter distribution of the gas and stellar component of the full FOF-halo sample from the full physics Illustris-1 simulation evolves as a function of redshift. Black dots mark the median spin parameter at every redshift. The specific angular momentum of the gas component continuously grows with cosmic time. The shape of the gas distribution is getting distorted from the classical lognormal after redshift $z = 2$ due to a second bump emerging at the low tail of the distribution. This low spin bump is caused purely by the smallest mass haloes and vanishes completely if we enforce an additional mass cut on our halo sample at $2 \times 10^{10} \mathrm{M}_{\odot}$, equal to the lower bound of the mr1 mass range. This bump could be explained by the gas component of low mass haloes not gaining any angular momentum due to the lack of mergers and efficient feedback at dwarf halo masses, but also could be purely due to poor resolution of the gas component at these halo masses. The stellar component exhibits a more subtle change in the shape of the spin distribution but evolves to only slightly smaller average spin with cosmic time.

In Fig. 2.19 we show the detailed mass dependence of the Peebles spin parameter of FOF-haloes from Illustris-1. This figure shows a two-dimensional histogram where FOF-haloes have been binned according to their mass and spin parameter and was obtained as in Figs. 2.10 and 2.12 with independently normalised mass bins to account for the variation of halo number with mass. The spin parameter of the dark matter component (upper panel) exhibits the same small increase of the median value with increasing halo mass as observed in the dark matter only Illustris-1-Dark simulation. However, the average spin parameters of the gas (middle panel) and the stellar component (lower panel) show a more pronounced trend with mass, which can be understood as a direct consequence of the impact from feedback.

The two feedback processes perturbing the gas and altering the distribution of baryons are galactic winds driven by supernova (SN) explosions and AGN feedback. SNe occur in cold, dense, star-forming gas regions in the inner halo, which have small specific angular momentum. The wind velocity imparted on the gas by a SN event is taken to be linearly proportional to the one-dimensional velocity dispersion of the halo, as motivated by Okamoto

et al. (2010). Details of the prescription can be found in Vogelsberger et al. (2013). For low mass haloes, the winds are more efficient in expelling a fraction of the gas and depleting star formation in the inner regions of the halo. In the *Illustris* simulation, SN feedback plays a major role below a FOF-halo mass of $\sim 2 \times 10^{11} \mathrm{M}_{\odot}$. Haloes above this mass are able to retain most of their gas and to actively form stars. Haloes with FOF-halo masses above $\sim 2 \times 10^{12} \mathrm{M}_{\odot}$ however grow massive enough black holes such that AGN feedback becomes efficient in quenching their star formation and expelling gas from the halo. As black holes are located in the very centre of haloes, AGN feedback also tends to mostly expel gas with low specific angular momentum from the inner halo.

Considering the halo masses at which the different feedback processes are most efficient, it is easy to interpret the detailed trend of the gas spin with halo mass. Below FOF-halo masses of $\sim 2 \times 10^{11} \mathrm{M}_{\odot}$, galactic winds become increasingly effective in expelling low specific angular momentum gas, which leads to an enhanced spin parameter of the remaining gas. Above $\sim 2 \times 10^{12} \mathrm{M}_{\odot}$, AGN feedback becomes strong and efficient in expelling the same low specific angular momentum gas. In between these two mass regimes the galaxies are able to hold on to most of their gas and are efficiently star-forming. Correspondingly, they have a lower than average gas spin parameter in this mass bin.

The trend of stellar spin with halo mass arises from the superposition of two effects. Most stars form at around $z \approx 2$, where the gas component is not yet depleted in its content of low specific angular momentum material (compare to Fig. 2.18). Thus, the bulk of stars forms from the cold, dense gas in the inner halo, which has low specific angular momentum. Furthermore, Zavala et al. (2016) find evidence for old stars to undergo a loss of specific angular momentum (up to 90%) to the outer dark matter halo through dynamical friction, similar to the loss that occurs in the inner dark matter halo to which old stars are attached. The overall low stellar spin determined by old stellar populations can thus be explained by a combination of both effects. Later on, when low specific angular momentum gas is either locked up in stars or expelled from the inner region due to feedback, star formation extends into the gas reservoir with higher specific angular momentum that now refills the inner halo. Thus young stars have an enhanced spin on average, tracking the higher spin parameter of the still available gas (see also Teklu et al., 2015, Zavala et al., 2016). This imprints a trend of spin with halo mass similar to the one exhibited by the gas spin on top of the otherwise constant low stellar spin.

As pointed out by Zavala et al. (2008), and more recently by Zavala et al. (2016) this behaviour is also closely related to the morphology of the galaxy forming at the halo centre. Those authors have shown that if most star formation takes place before turnaround, the stars are attached to dark matter clumps forming the inner halo and likewise loose a significant

fraction of their specific angular momentum to the outer halo, leading to the formation of an elliptical galaxy. On the other hand, when star formation in the inner region is suppressed before turnaround, high specific angular momentum gas can penetrate the inner halo region at later times and form a stellar disc. Thus the precise strength and timing of the feedback events that determines the amount of expelled gas from the inner region and whether it overcomes the gravitational potential of the halo is crucial for the morphology of the central galaxy. In *Illustris* we find a morphological mix of galaxies that is consistent with observations, which makes this simulation particularly suitable for the investigation of the impact of feedback onto the angular momentum properties. Rodriguez-Gomez et al. (2017) further investigate the connection between galaxy morphology, halo spin, and merger history. In future studies it will be crucial to disentangle the feedback induced mechanisms leading to the redistribution of matter and specific angular momentum inside of haloes and to quantify the impact on galaxy morphology.

We refrain from a detailed interpretation of the results at the very high mass end of the distribution as it is affected by small number statistics. Also, we disregard trends below a mass of $10^{10}\mathrm{M}_{\odot}$ as our haloes were selected based on a minimum dark matter particle number and thus the gas and stellar spin parameters below this mass scale can be affected by resolution effects.

### 2.5.3 Specific angular momentum distributions of dark matter and gas

In order to understand whether galactic winds and AGN feedback can on average expel a sufficient amount of low angular momentum gas from the halo to account for the apparent gain of specific angular momentum in the baryonic component we observe, we need to turn to the distribution of specific angular momentum *inside* a halo. This has so far been extensively studied for dark matter only haloes but not for the baryonic component. Bullock et al. (2001) suggested a universal angular momentum profile for the distribution of specific angular momentum inside a halo given by

$$M(< j_{\mathrm{sp}}) = M_{\mathrm{tot}} \frac{\mu\, j_{\mathrm{sp}}}{j_0 + j_{\mathrm{sp}}}, \tag{2.7}$$

where $j_{\mathrm{sp}}$ is the specific angular momentum of dark matter projected onto the rotation axis of the whole halo, $M(< j_{\mathrm{sp}})$ the cumulative dark matter mass of the dark matter with specific angular momentum smaller than a given value $j_{\mathrm{sp}}$, and $M_{\mathrm{tot}}$ denotes the total halo mass. $\mu$ and $j_0$ are two fitting parameters that are not mutually independent. Bullock et al. (2001) derived the universal angular momentum profile from dark matter only SO-haloes, such that $M_{\mathrm{tot}} = M_{200}$.

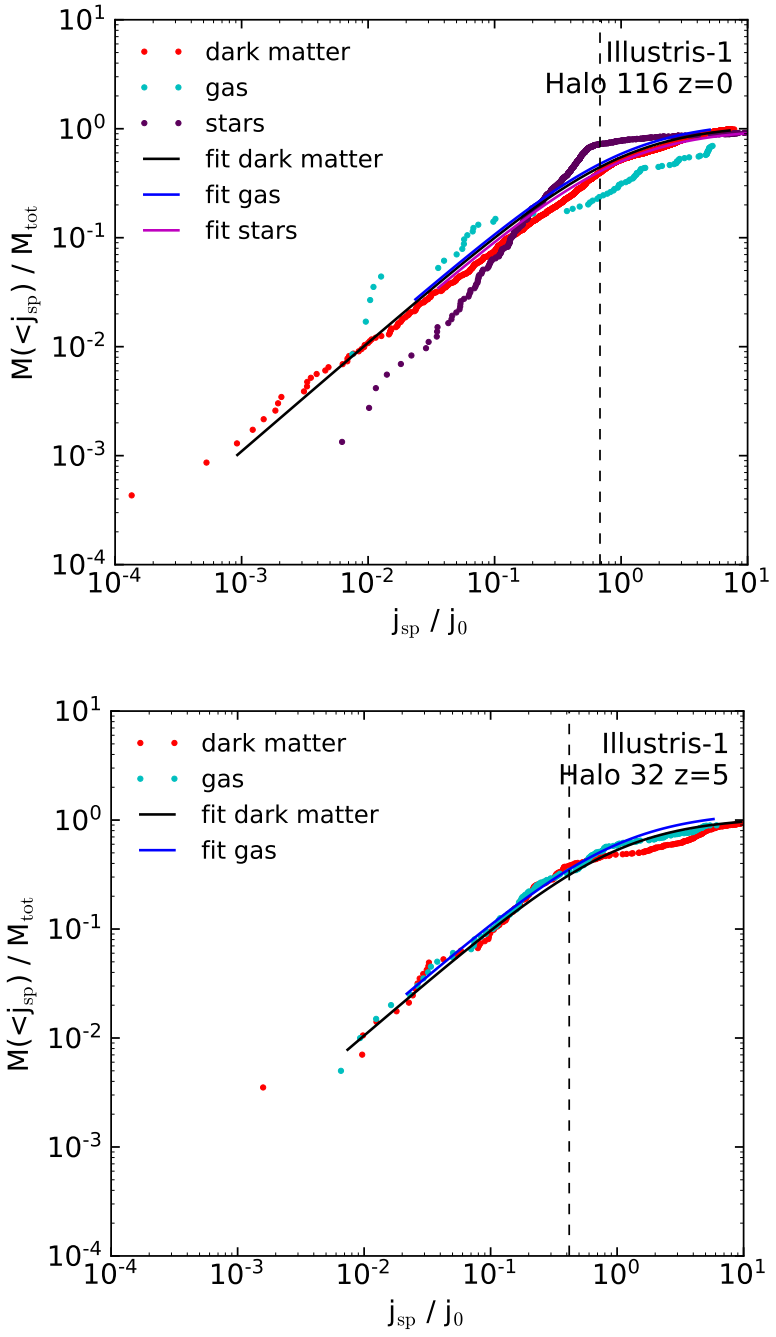


Figure 2.20: Specific angular momentum distributions of a random halo from Illustris-1 at $z = 0$ and $z = 5$, obtained by binning the dark matter, gas, and stars in spherical bins of 1000 dark matter/star particles or gas cells each and calculating the specific angular momentum in each bin. The bins are then sorted by their specific angular momentum value projected onto the normalised total angular momentum of the whole halo. The distributions show the cumulative mass $M(< j_{\rm sp})$ of all bins with $j_{\rm sp}$ smaller than a given value. Solid lines show least square error fits of the universal angular momentum profile to the derived distribution approximated by 50 mean values estimated in equidistant logarithmic bins. At high redshift, the universal profile is a good fit to both the dark matter and gas distributions. However, at $z = 0$, this is true only for dark matter, indicating that the gas distribution gets highly perturbed by feedback processes during the subsequent evolution, causing also the stellar distribution to be perturbed away from the universal profile. The black dashed line marks the average $j_{\rm sp}$ value below which the gas is expelled from the halo due to feedback. See Section 2.5.4 for more details.

Above we deliberately used the term ‘dark matter’ instead of ‘dark matter particle’, as the specific angular momentum distribution is here meant to apply to the mean streaming velocity of the material, not to individual particles. Due to the finite velocity dispersion of the dark matter, a substantial fraction of the dark matter particles can actually be counter-rotating with respect to the net rotation direction. To account for this effect one needs to average over a sufficiently large number of dark matter particles to obtain a fair estimate of the mean streaming velocity and the specific angular momentum. To derive specific angular momentum distributions we thus bin the dark matter particles in spherical shells around the halo centre of 1000 particles each, and use the specific angular momenta and masses of the spherical bins as data points for the distribution.

Because searching the whole simulation volume for particles and cells belonging to every SO-halo is computationally expensive in post-processing, we simplify the present analysis by applying the $R_{200}$ cut only to particles and cells belonging to the corresponding FOF-halo. As we here analyse only very massive and extended haloes, the number of particles/cells being part of the SO-halo but not part of the corresponding FOF-halo is negligible. However, we caution that this is not generally true, especially for low mass haloes. We also want to remark that deriving specific angular momentum distributions for FOF-haloes can be more problematic, as in the outskirts a significant fraction of the angular momentum is carried by the orbital angular momentum of minor mergers, which can have infall trajectories counter-rotating with respect to the main halo. Simply removing the resulting bins with negative specific angular momentum introduces a discrepancy in the total halo mass, such that we refrain from adopting this approach.

In Fig. 2.20 we show the specific angular momentum distributions derived for the different halo components of a randomly selected massive halo from Illustris-1 at $z = 0$ and $z = 5$. We fit the universal angular momentum profiles given by Eq. (3.8) to the dark matter, gas, and stellar specific angular momentum distributions. To this end we bin the data points in 60 equidistant bins in the full $j_{\rm sp}$-range and provide least square error fits to the average values in those bins. We ignore the 10 lowest bins, as those contain only few or no data points at all, leaving 50 values for determining the best fit. Note that $\mu$ and $j_0$ are not independent fitting parameters. Defining $m = M(< j_{\rm sp})/M_{\rm tot}$ one can rewrite Eq. (3.8) as

$$j_{\rm sp}(m) = \frac{m j_0}{\mu - m}, \tag{2.8}$$

such that the universal angular momentum profile can be reduced to a one parameter function where the two fitting parameters $\mu$ and $j_0$ are related by

$$j_{\rm sp}^{\rm tot} = j_0 \int_0^1 \frac{m}{\mu - m} {\rm d}m = j_0 \, [-\mu \, \ln(1 - 1/\mu) - 1]. \tag{2.9}$$

Here $j_{\rm sp}^{\rm tot}$ is the absolute value of the total specific angular momentum of the halo subset considered, and $\mu > 1$.

Fig. 2.20 shows that at high redshifts the dark matter and gas components of a halo have identical 'initial' specific angular momentum distributions and as such also spin parameters. This is a direct consequence of the 'initial' spin of dark matter and gas being caused by large scale tidal torques from the surrounding gravitational field, which acts the same way on all matter species. The universal angular momentum profile, derived for haloes at $z = 0$, turns out be a reasonably good approximation of the specific angular momentum distribution at high redshift, in agreement with dark matter mostly sustaining its 'initial' spin.

Consistently, the universal angular momentum profile is a good fit to the dark matter specific angular momentum distribution at $z = 0$. The gas component at $z = 0$ is however significantly perturbed by the action of feedback which sets in at later times such that the gas distribution does not follow the universal profile any more. This also causes the angular momentum distribution of stars to deviate from the universal profile. Furthermore, the gas distribution lacks the low specific angular momentum part of the gas that is still present in the dark matter, as it was either locked up in stars or expelled by feedback. Though the best fit universal angular momentum profiles are identical for all halo components, the true distributions of the specific angular momentum of gas and stars inside a halo exhibit very different features than prescribed by the universal profile. We have investigated the gas specific angular momentum distributions of many haloes and find a large variety in their distributions with little commonality, thus not lending itself to a description through a simple universal function. Instead, the specific angular momentum distribution of gas inside a halo depends strongly on the particular history of the individual halo.

### 2.5.4 The origin of the baryonic spin enhancement

In Section 2.5.2 we have shown that the baryonic component of haloes shows an enhanced spin compared to the dark matter. Taking the average of all haloes contained in the three examined mass ranges we find a baryon to dark matter spin parameter ratio of $\sim 1.8$. We can use the universal angular momentum profile from Bullock et al. (2001) to estimate the expected enhancement of the baryonic spin parameter when a fraction of the low specific

angular momentum gas is expelled from the halo due to feedback, allowing us to investigate whether this already explains the observed enhancement. To this end, we however need to know how much baryonic mass is on average still present in a halo at $z = 0$.

In a quiet environment with no feedback at work the baryon to total mass ratio of haloes should equal the universal cosmic baryon fraction, $f_\mathrm{b} = \Omega_b/\Omega_m = 0.1673$. With feedback physics at work we find an average baryon to total mass fraction of SO-haloes from Illustris-1 at $z = 0$ of $f_\mathrm{halo} = M_\mathrm{baryons}/(M_\mathrm{dm} + M_\mathrm{baryons}) = 0.0963$, which is significantly below the cosmic baryon fraction. Compared to the cosmic average, SO-haloes thus lose on average $f = (f_\mathrm{b} - f_\mathrm{halo})/f_\mathrm{b} \approx 42\%$ of their initial gas mass.[5] This is in very good agreement with Sharma et al. (2012) who find an excess of low angular momentum gas in their non-radiative simulations that yields an angular momentum distribution incompatible with the exponential density profile of spiral galaxies. Those authors show that this discrepancy cannot be alleviated by different merger histories and the redistribution of angular momentum associated with those, and estimate that haloes have to loose $\sim 40\%$ of their low angular momentum gas for most of their haloes to host disc galaxies.

As feedback occurs in star-forming regions that are comprised of cold, dense, and slowly rotating gas, it expels gas with low specific angular momentum. The high specific angular momentum is then redistributed within the remaining gas creating a new tail of low specific angular momentum gas. This new tail is due to gas that is now entering the inner halo, and will typically be less prominent than before the onset of feedback. In our calculation we therefore assume that it is always the gas with the lowest specific angular momentum that is expelled from the halo. With this ansatz and making use of the fact that gas (and thus baryons, as there are only few stars at high redshift) and dark matter have identical 'initial' universal angular momentum profiles, we can calculate the specific angular momentum of the remaining baryons $j_\mathrm{sp,f}$ by integrating the universal angular momentum profile over the remaining mass, which simply corresponds to integration limits from $f = 0.42$ to 1,

$$\begin{aligned} j_\mathrm{sp,f} &= \frac{j_0}{(1-f)} \int_f^1 \frac{m}{\mu - m} \mathrm{d}m \\ &= \frac{j_0}{(1-f)} \left[-\mu \ln\left(\frac{\mu - 1}{\mu - f}\right) - (1-f)\right]. \end{aligned} \tag{2.10}$$

The factor $1/(1-f)$ is introduced to account for the fact that the specific angular momentum $j_\mathrm{sp,f} = J_\mathrm{f}/(1-f)M_\mathrm{tot}$ is now obtained from the remaining baryons which have a reduced

[5] For FOF-haloes we obtain $f \approx 48\%$ which in the end yields very similar results. However, we carry out our calculation for SO-haloes, because the universal angular momentum profile was shown to hold for this type of halo.

mass of $(1-f)M_{\rm tot}$ compared to the initial mass of the baryonic component. In Fig. 2.20 we indicate the lower integration limit $f$ as black dashed line.

Bullock et al. (2001) found that 90% of their haloes lie in a parameter range of $\mu \in [1.06, 2]$. Inserting these two limiting values[6] in Eq. (3.10) and Eq. (3.11), and taking the ratio of these two equations, we arrive at an enhancement of the specific angular momentum of the baryonic component by

$$\frac{j_{\rm sp,f}}{j_{\rm sp}}\,[\mu = 1.06-2] = 1.63-1.49. \tag{2.11}$$

Thus we find a relative boost in the spin parameter of the baryonic component of $\sim 1.55$ due to expulsion of low specific angular momentum gas from the halo by feedback. Combined with the 'inherent' increase in gas spin discussed in Section 2.4 by a factor of $\sim 1.3$ due to a transfer of specific angular momentum from the dark matter to gas, this yields an overall enhancement by a factor of $\sim 2$ relative to the dark matter spin. This value is somewhat overestimated as it does not take into account that some of the low specific angular momentum gas is locked up in stars or otherwise remains in the halo and contributes to the average baryonic spin at $z = 0$. However, our estimate also assumes instantaneous removal of low angular momentum gas, whereas in reality feedback is a continuous process taking place at the inner halo which is constantly refilled with relatively low angular momentum gas. An analysis invoking tracer particles following the gas flow and recording its history in detail will be crucial to accurately pin down the fraction of low angular momentum gas still remaining in the halo. In this study, we merely provide an estimate of an upper limit for the enhancement of baryonic spin based on the assumption that feedback instantaneously expels gas with the lowest specific angular momentum. In that sense, the observed enhancement of the spin of the baryonic component of $\sim 1.8$ can be solely explained by the combined effects of the removal of low specific angular momentum gas from haloes by feedback and the 'inherent' spin enhancement of the gas component due to angular momentum transfer from dark matter to the gas during halo assembly, which is already captured in non-radiative simulations. As our analysis is based on more than 320 000 haloes, this shows that (in a statistical sense) it is not necessary to invoke cold filamentary gas accretion as an additional source for the enhanced baryonic spin. The enhancement of baryonic spin due to cold flows was discussed in detail by Danovich et al. (2015) using 29 individually selected Milky Way sized galaxies at redshifts $z = 4-1.5$ from a cosmological simulation carried out with

[6] We adopt the values given by Bullock et al. (2001), as those were derived from a statistical sample of $\sim 200$ haloes with $> 6000$ resolution elements, and verified on $\sim 400$ haloes with $> 1000$ resolution elements. We have analysed the angular momentum distributions only for $\sim 20$ individual haloes, but find shape parameters consistent with the given range.

ART. Further support for this mechanism was recently provided by Stewart et al. (2017) based on simulations of a single Milky Way sized galaxy with multiple hydrodynamic codes, strengthening cold filamentary accretion as a code-independent viable mechanism for baryonic angular momentum gain in individual objects. However, Sales et al. (2012) showed that filamentary gas accretion from misaligned filaments can also lead to the opposite behaviour, a reduced spin of the baryonic component and the formation of an elliptical galaxy in the halo centre. The statistical relevance of cold flows as a source for baryonic spin enhancement thus still has to be established in future studies. Our results suggest that this mode may be relevant only in selected objects.

### 2.5.5 Misalignment between the halo components

Finally, we want to briefly analyse the distributions of misalignment angles between the angular momentum vectors of the different halo components and how they evolve with redshift. We quantify the misalignment by the cosine of the misalignment angle between two halo components,

$$\cos(\vartheta) = \frac{\mathbf{J}_1 \cdot \mathbf{J}_2}{J_1 \cdot J_2}, \tag{2.12}$$

where $\mathbf{J}_{1/2}$ are the angular momentum vectors of two different halo components, such as dark matter, gas, or stars and $J_{1/2} = |\mathbf{J}_{1/2}|$ their absolute values. In Fig. 2.21 we show the distribution $P(\cos(\vartheta)$ of misalignments as a function of redshift. Black dots mark the median misalignment at every redshift. The distributions were derived by binning all FOF-haloes from Illustris-1 in 50 equidistant bins, covering the range of misalignments between $\cos(0^\circ) = 1$ (perfectly aligned) and $\cos(90^\circ) = 0$ (perpendicular), and normalising to the total number of haloes as well as the bin size. We refrain from showing the distributions up to $\cos(180^\circ) = -1$ (anti-aligned), as in this range the distributions are a continuous extrapolation of the trend visible in the presented range. We caution that the halo samples are always dominated by the lowest mass haloes whose gas and stellar components can be affected by poor resolution. However, we refrain from imposing an additional mass cut on our halo samples, because this would remove most of the haloes at high redshift.

We find that the dark matter and the stellar component (middle panel), as well as the gas and the stellar component (lower panel) become progressively more aligned towards lower redshift, whereas the misalignment between the dark matter and gas (upper panel) grows with cosmic time. The growing misalignment between the gas and dark matter component is a natural consequence of the feedback mechanisms continuously perturbing the gas but having only indirect and weak effects on the dark matter through the change of the baryonic density distribution.

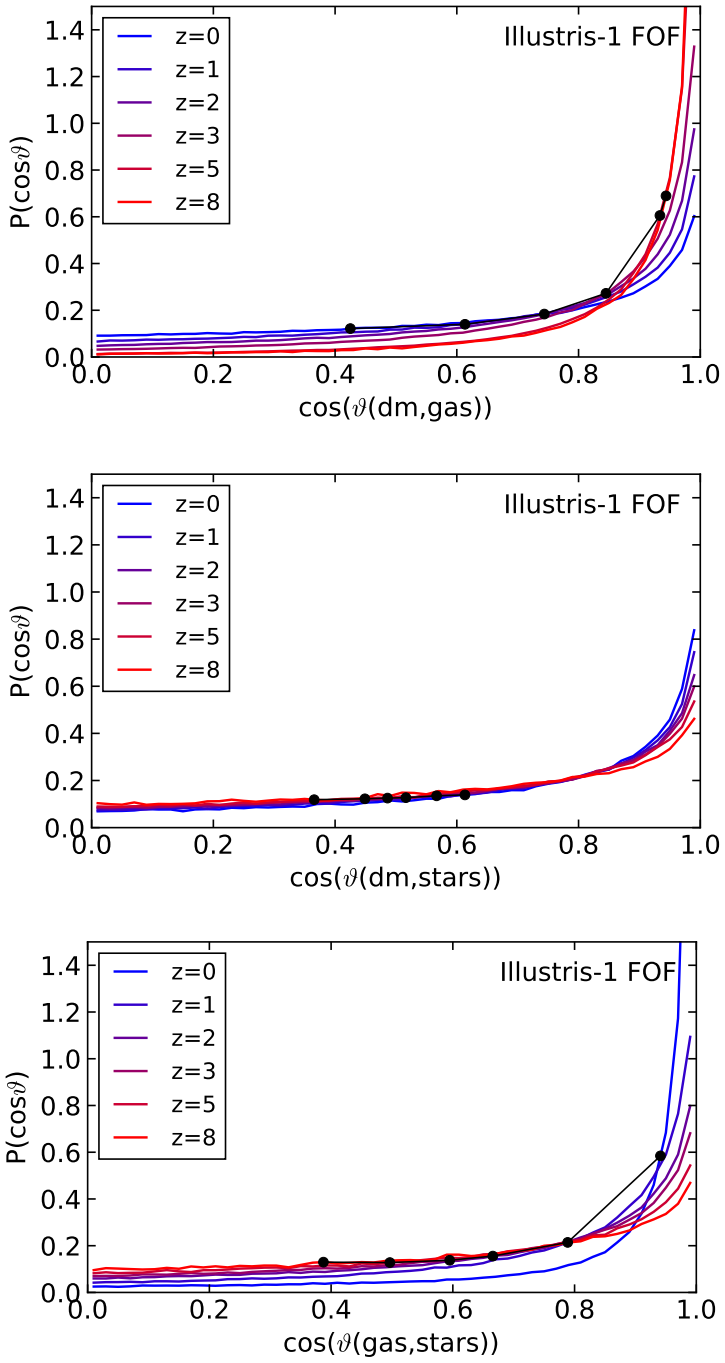


Figure 2.21: Redshift evolution of the distribution of misalignment angles between the different halo components for FOF-haloes from Illustris-1. During cosmic evolution the dark matter and the stellar component (middle panel) as well as the gas and the stellar component (lower panel) become more aligned, whereas the misalignment between the dark matter and gas (upper panel) grows with cosmic time.

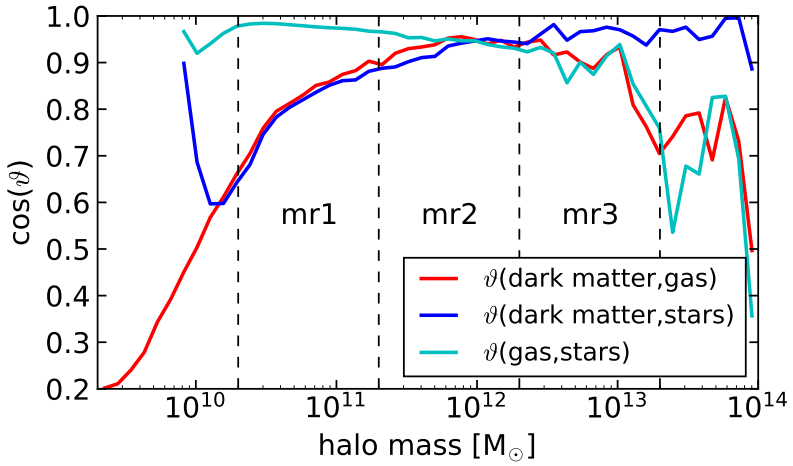


Figure 2.22: Median misalignment between the different FOF-halo components from Illustris-1 as a function of halo mass. Best alignment between all halo components can be found in Milky Way sized haloes where the impact from feedback is weak. In general, the alignment of halo components is a strong function of halo mass, for a detailed discussion see Section 2.5.5.

In Fig. 2.22 we show the median misalignment as a function of halo mass and thus feedback regime at $z = 0$, derived by binning the FOF-haloes from Illustris-1 in 50 equidistant logarithmic bins in the given mass range and calculating the median misalignment $\cos(\vartheta)$ in every bin. The vertical dashed lines single out the three mass ranges introduced in Section 2.5.2. Below a FOF-halo mass of $\sim 10^{10}\mathrm{M}_{\odot}$ the median misalignment between stars and both the dark matter and gas exhibits a steep upward trend that is due to poor resolution of the stellar component. Above $\sim 2 \times 10^{13}\,\mathrm{M}_{\odot}$ our results are affected by small number statistics. Within the singled out intermediate mass ranges we find best alignments of all three components in Milky Way sized haloes where the impact from feedback is weak (see Section 2.5.2). The alignment between dark matter and gas becomes worse in less and more massive haloes, as at those halo masses the gas component is perturbed by galactic winds and AGN feedback, respectively. The median misalignment angle across all three mass ranges is $\vartheta(\mathrm{dm}, \mathrm{gas}) = 34.2°$. Stars are almost perfectly aligned with the gas at small halo masses and exhibit the same misalignment with dark matter as the gas component. With increasing halo mass the stellar component becomes progressively better aligned with dark matter and correspondingly less well aligned with the gas. Within the three mass ranges we find median misalignment angles of $\vartheta(\mathrm{dm}, \mathrm{stars}) = 35.7°$ and $\vartheta(\mathrm{gas}, \mathrm{stars}) = 12.1°$. This trend can be possibly explained by massive haloes hosting elliptical galaxies comprised of mostly old stars, which are subject to gravitational interaction with dark matter but are not affected by

the hydrodynamical interaction that the gas undergoes during the phase of late-time halo assembly. The stellar populations in low mass haloes will be typically younger and thus are expected to exhibit an angular momentum vector oriented along the rotational direction of the gas out of which these stars were formed.

Our results seem generally consistent with previous studies, however a direct comparison is often difficult due to the variety of adopted approaches in the literature, such as measuring the misalignment for specific galaxy types, or only in the inner region of haloes. We leave a detailed investigation of feedback induced misalignments between different halo components, as well as a study of radial trends in the spin alignment to future studies.

## 2.6 Discussion and conclusions

In this work, we have analysed the distribution of halo spins in the *Illustris* simulation suite, one of the first simulations of galaxy formation with full hydrodynamics that produces a realistic galaxy population in a sizeable volume, thus also yielding good statistics, comparable to the best dark matter only simulations that have been used for the study of these properties in the past. Our goal has been a characterisation of the global angular momentum content of haloes as a function of mass and time in this new generation of hydrodynamical simulations, and to highlight the differences with respect to dark matter only results.

To shed some light on the different approaches adopted in the literature for measuring halo spin statistics, we have analysed the systematic differences between the commonly used Peebles and Bullock spin parameter definitions, and between the friends-of-friends (FOF) and spherical overdensity (SO) halo definitions. Also, we have checked the impact of sample selection criteria designed to single out structures in quasi-equilibrium. For this investigation we have employed a large sample of $\sim 400,000$ dark matter only FOF- and $\sim 360,000$ SO-haloes from Illustris-1-Dark. The Peebles definition yields robust spin parameter values for both halo definitions, an advantage over the simpler Bullock parameter which has problems to cope with the extended geometry of FOF-haloes. We find that for SO-haloes the Bullock spin parameter needs to be rescaled by a constant factor of 1.1 to yield the same mean value as the Peebles parameter, when the concentration dependence is ignored. When comparing spin parameters derived with the different definitions it is thus necessary to bear this offset in mind. Finally, we find that sample selection criteria have a small effect on the resulting spin parameter distributions. The differences are of the same order of magnitude as the variations between different results presented in the literature, and thus can explain those discrepancies.

Interestingly, we find that only the Peebles spin parameter definition applied to FOF-haloes yields a spin parameter distribution that is self-similar in time to high accuracy. It is

thus worthwhile to make the extra effort of accurately calculating the gravitational binding energy of haloes and use the Peebles definition to characterise the angular momentum content of haloes. For this purpose, we use the tree-gravity solver of AREPO for all haloes (as well as all subhaloes, but these are not studied here) of the *Illustris* simulation suite and include the corresponding results in a group catalogue extension. Our augmented group catalogue furthermore contains the kinetic energies of FOF- and SO-haloes (and subhaloes) as well as the angular momentum vectors of the dark matter, gas, and steller component of these. A full list of all properties available in the group catalogue extension can be found in Section 2.7, and these data will be added to the public data release of *Illustris* (Nelson et al., 2015).

With respect to the dark matter, we reproduce the well known result of finding essentially no mass- and redshift dependence of the spin parameter distribution. However, the subtle trend of spin with halo mass and the fact that the number of haloes steeply increases with decreasing halo mass causes the average spin of a halo sample to be always dominated by the smaller haloes with lower spin and thus the resolution limit of the simulation. This has to be borne in mind when comparing literature results.

When baryons are added, the dark matter component retains its properties. The baryons, however, exhibit a substantial gain in specific angular momentum that increases towards low redshift. Already in the non-radiative case, where one may naively expect both dark matter and gas to retain their identical initial spins, we find an enhanced gas spin by a factor of $\lambda_{\rm gas}/\lambda_{\rm dm} \approx 1.3$ compared to the dark matter. This gain appears to arise from a transfer of specific angular momentum from dark matter to the gas during late-time halo assembly. This could be explained by infalling substructures getting their gas component ram pressure displaced, leading to a mutual torque between the dark matter and gas components allowing for a net transfer of specific angular momentum from dark matter onto gas. Such a transfer is also reflected in a small deficit of specific angular momentum at $z = 0$ in the dark matter component of the non-radiative simulation compared to the dark matter only simulation. The amount of specific angular momentum missing in the dark matter is exactly what is needed to balance the gain observed in the gas component.

In simulations with active galaxy formation physics the enhancement of the baryonic spin is even larger and leads to an average ratio of $\lambda_{\rm gas}/\lambda_{\rm dm} \approx 1.8$. We derive this value from a large sample of $\sim 320,000$ FOF-haloes from the Illustris-1 simulation. If we assume that galactic winds and AGN feedback expel preferentially low specific angular momentum gas from a halo, we can estimate the expected apparent gain of specific angular momentum in the baryonic component based on the total baryonic mass lost from haloes. On average we find an expected enhancement by a factor of $\sim 1.55$ from this effect. Combing this with the relative enhancement of $\sim 1.3$ expected from the transfer of specific angular momentum

from dark matter to the gas as seen in the non-radiative case, we arrive at a total enhancement by a factor of roughly $\sim 2$ relative to the dark matter spin. Note that this value represents a slight overestimate as our calculation does not take into account some of the low specific angular momentum being locked up in stars and remaining in the halo. However, the good agreement with the actually measured enhancement factor of $\sim 1.8$ shows that these two effects combined are sufficient to explain the higher specific angular momentum of the baryonic content in the full physics simulations. This also casts doubts onto recent suggestions (Stewart et al., 2017) that cold filamentary gas accretion is responsible for the enhanced baryonic spin of haloes.

We also find that the different feedback mechanisms induce a strong dependence of the gas spin on halo mass. In low and high mass haloes, where galactic winds and AGN feedback are most efficient in expelling low specific angular momentum gas, the gas spin is highest. The stellar spin is far less affected, as star-formation takes place in cold, dense gas in the inner region of haloes, where the material is slowly rotating. The stellar component thus has small spin largely independent of halo mass. The baryonic spin is ultimately determined by the gas to stellar mass ratio of haloes which decreases with halo mass. Another consequence from feedback processes perturbing the gas component is a growing misalignment between the dark matter and gas component with cosmic time, which again is largest at halo masses that allow for most efficient feedback. Furthermore, we find that the alignment between the different halo components is a strong function of halo mass.

Our results thus clearly show that the baryonic spin sensitively depends on the galaxy formation physics employed. Highly schematic schemes for the evolution of the baryonic spin component, such as invoked in simple inside-out scenarios for disk formation that assume equal specific spin in dark matter and gas, need therefore be treated with caution. It will be interesting to examine with future simulations how strongly our results for the full physics simulations depend on the details of the feedback modelling invoked to regulate the galaxy formation process. Given the substantial impact of feedback one may be inclined to anticipate a very large range of possible outcomes. However, it appears also possible that the constraint to reproduce basic observational facts such as the galaxy stellar mass function effectively ties down the simulation predictions for the spin properties, independent of the specific realisation of the feedback physics.

## 2.7 Fields of extended group catalogue

For completeness and as a reference, we here provide a full list of all newly available halo and subhalo properties in the group catalogue extension we computed for *Illustris*. These

| Name | description |
|---|---|
| GroupEkin | kinetic energy of FOF-haloes |
| GroupEthr | thermal energy of the gas component of FOF-haloes |
| GroupEpot | potential energy of FOF-haloes |
| Group_J | total angular momentum of FOF-haloes |
| Group_Jdm | angular momentum of the dark matter component of FOF-haloes |
| Group_Jgas | angular momentum of the gas component of FOF-haloes |
| Group_Jstars | angular momentum of the stellar component of FOF-haloes |
| Group_CMFrac | total counter-rotating mass fraction of FOF-haloes |
| Group_CMFracType | counter-rotating mass fractions per type: dark matter, gas, stars |
| Group_Ekin_* | kinetic energy of SO-haloes |
| Group_Ethr_* | thermal energy of the gas component of SO-haloes |
| Group_Epot_* | potential energy of SO-haloes |
| Group_J_* | total angular momentum of SO-haloes |
| Group_Jdm_* | angular momentum of the dark matter component of SO-haloes |
| Group_Jgas_* | angular momentum of the gas component of SO-haloes |
| Group_Jstars_* | angular momentum of the stellar component of SO-haloes |
| Group_CMFrac_* | total counter-rotating mass fraction of SO-haloes |
| Group_LenType_* | number of particles/cells of each matter type in SO-haloes |
| Group_MassType_* | mass per matter type in SO-haloes |
| Group_CMFracType_* | counter-rotating mass fractions per matter type in SO-haloes |

Table 2.5: Full list of all newly available halo properties in the group catalogue extension. A halo can be either defined as a friends-of-friends (FOF) group or a spherical overdensity (SO). The latter can be either with respect to 200 times the critical density (Crit200), 500 times the critical density (Crit500), 200 times the mean density (Mean200), or with the redshift dependent overdensity expected for the generalised top-hat collapse model in a $\Lambda$-cosmology (TopHat200), see Bryan and Norman (1998). The corresponding properties can be accessed by replacing * with the terms in brackets. The different matter types in question are dark matter, gas, stars, and black holes.

additional properties will be made available as part of the public data release (Nelson et al., 2015) of *Illustris*.

| Name | description |
|---|---|
| SubhaloEkin | kinetic energy of subhaloes |
| SubhaloEthr | thermal energy of the gas component of subhaloes |
| SubhaloEpot | potential energy of subhaloes |
| Subhalo_J(*) | total angular momentum of subhaloes |
| Subhalo_Jdm(*) | angular momentum of the dark matter component of subhaloes |
| Subhalo_Jgas(*) | angular momentum of the gas component of subhaloes |
| Subhalo_Jstars(*) | angular momentum of the stellar component of subhaloes |
| Subhalo_CMFrac(*) | total counter-rotating mass fraction of subhaloes |
| Subhalo_CMFracType(*) | counter-rotating mass fractions per type: dark matter, gas, stars |

Table 2.6: Full list of all newly available galaxy properties in the group catalogue extension. Subhaloes corresponding to galaxies are defined as all particles/cells that are gravitationally bound the same potential minimum. Furthermore, we include two more definitions of a galaxy that are closer to the observational approach and include only subhalo particles/cells that are in the stellar half mass radius (InHalfRad) or twice the stellar half mass radius (InRad). The corresponding properties can be accessed by replacing * with the terms in brackets. The different matter types in question are dark matter, gas, stars, and black holes.

# Acknowledgments

We thank the referee for insightful comments that helped to improve the paper. JZ and VS acknowledge financial support from the Deutsche Forschungsgemeinschaft through Transregio 33, “The Dark Universe”, and through the Klaus Tschira Foundation. VS also acknowledges support through the European Research Council under ERC-StG grant EXAGAL-308037. Some of the computations were performed on the HazelHen supercomputer at the High-Performance Computing Center Stuttgart (HLRS) as part of project GCS-ILLU of the Gauss Centre for Supercomputing (GCS). JZ acknowledges support from International Max-Planck Research School for Astronomy and Cosmic Physics at the University of Heidelberg (IMPRS-HD).

# Chapter 3

# The baryonic angular momentum content of haloes in the IllustrisTNG simulations

The content of the following chapter is presented in publishable form, and soon will be submitted as a paper.

# Abstract

Recent hydrodynamical cosmological simulations have succeeded in producing galaxy populations with realistic sizes and morphologies within large cosmological volumes. Crucial for this success is that galaxies and their haloes arrive at the right level of specific angular momentum, as this governs the rotational support of cold star-forming gas. Feedback processes can modify the spin of haloes in ways that are still poorly understood. In this paper, we employ two hydrodynamical simulations with different models for galaxy formation and feedback physics, Illustris and IllustrisTNG, to study their predictions for the baryonic angular momentum content of haloes, and how this depends on the physics parameterisation as well as on the numerical resolution. For non-radiative haloes, the baryonic spin of individual haloes correlates well with the spin of the dark matter component, albeit with a scatter of $\simeq$0.12 dex that increases for lower magnitude of the dark matter spin. With time, an offset between the median baryonic and dark matter spins develops, which is consistent with an on average constant angular momentum transfer from dark matter to baryons. Adding galaxy formation physics increases the scatter between the baryonic and dark matter spins by 0.05 dex, and in addition leads to further substantial relative enhancements of the baryonic spin. We show that this spin enhancement correlates with the amount of gas expelled from haloes due to supernovae explosions and active galactic nuclei (AGN) feedback. This correlation is weak for halo masses mostly affected by supernovae-driven galactic winds, suggesting that galactic winds typically expel gas with on average lower specific angular momentum than the halo mean, but with large scatter due to a baryon cycle that mixes gas with low and high specific angular momentum relatively efficiently. In contrast, in the regime affected by AGN feedback, the angular momentum change is consistent with a model where preferentially low angular momentum gas from haloes is ejected, especially for IllustrisTNG. We show that the combined effect of a fixed angular momentum transfer from dark matter to baryons as a result of hierarchical assembly, and a relative increase of the baryonic spin in proportion to the baryons lost as a result of feedback effects, can explain the overall enhancement of baryonic spin with respect to the dark matter for the well-resolved halo population.

## 3.1 Introduction

In the well established ΛCDM cosmology, galaxies form through the assembly of baryonic matter in potential wells dominated by dark matter. The specific angular momentum of the baryons is crucial for the emerging galaxy sizes and morphologies. While the acquisition of angular momentum during the formation of gravitationally bound structures is a long studied question, only recently hydrodynamical simulations producing realistic galaxy populations in cosmological volumes have made it possible to study the baryonic angular momentum properties of haloes in the highly non-linear regime.

It is generally assumed that baryons initially gain the same specific angular momentum as dark matter, the so-called 'initial' spin, through the interaction of a non-spherical proto-halo with the local gravitational tidal field (Hoyle, 1949). As this process is oblivious to the different physical nature of dark matter and the cosmic gas, the amount of specific angular momentum imparted on a halo should be the same for dark matter and gas, provided they are distributed in the same way. This interaction was worked out by Peebles (1969) and Doroshkevich (1970), and later confirmed in N-body simulations by White (1984) and Barnes and Efstathiou (1987) for the linear regime, establishing the tidal torque theory for angular momentum acquisition of dark matter haloes. However, it is less clear whether the subsequent, non-linear evolutionary stages of haloes introduce important corrections to this picture, for example because significant amounts of angular momentum may be brought into structure through the orbital angular momenta of minor and major mergers.

In fact, early non-radiative simulations have shown that with subsequent structure formation the gas component being subjective to pressure gradients and shocks undergoes a noticeably different evolution with respect to its angular momentum content than dark matter (van den Bosch et al., 2002). Non-radiative simulations follow the gas motions based on the Euler equations without allowing it to radiatively cool and form stars, and hence without including any kind of galaxy formation physics. Already in this basic configuration the spin of the gas at $z = 0$ is enhanced by a factor of $\sim 1.3$ compared to the dark matter spin (e.g. Chen et al., 2003, Sharma and Steinmetz, 2005, Gottlöber and Yepes, 2007), and shows a misalignment with the rotational direction of the dark matter component of order $\sim 30^\circ$ (e.g. van den Bosch et al., 2002, Liao et al., 2017). It is thus not trivially possible to extrapolate from dark matter onto gas properties even in absence of any sophisticated galaxy formation physics.

Even more significant changes in the angular momentum of baryons can be expected in hydrodynamical simulations that account for galaxy formation and evolution physics in a faithful enough fashion to build up realistic galaxies. Such simulations have only become available recently. Examples include the Illustris (Vogelsberger et al., 2014b, Genel et al.,

| **simulation** | **box size** $[h^{-1}\mathrm{Mpc}]$ | **# dark matter particles** | **# initial gas cells** | $m_{\mathbf{dm}}$ $[\mathrm{M}_\odot]$ | $m_{\mathbf{gas}}$ $[\mathrm{M}_\odot]$ | **cosmology** |
|---|---|---|---|---|---|---|
| TNG100(-1) | 75 | $1820^3$ | $1820^3$ | $7.46 \times 10^6$ | $1.39 \times 10^6$ | PLANCK15 |
| TNG100-2 | 75 | $910^3$ | $910^3$ | $5.97 \times 10^7$ | $1.11 \times 10^7$ | PLANCK15 |
| TNG100-3 | 75 | $455^3$ | $455^3$ | $4.77 \times 10^8$ | $8.90 \times 10^7$ | PLANCK15 |
| TNG300 | 205 | $2500^3$ | $2500^3$ | $5.88 \times 10^7$ | $1.10 \times 10^7$ | PLANCK15 |
| Illustris | 75 | $1820^3$ | $1820^3$ | $6.26 \times 10^6$ | $1.26 \times 10^6$ | WMAP7 |
| Illustris-Dark | 75 | $1820^3$ | - | $7.52 \times 10^6$ | – | WMAP7 |
| Non-radiative | 75 | $910^3$ | $910^3$ | $5.01 \times 10^7$ | $1.01 \times 10^7$ | WMAP7 |

Table 3.1: Basic numerical parameters of the IllustrisTNG and Illustris simulations analysed in this work. Listed are for every simulation its symbolic name, the periodic box size, the number of dark matter particles, the number of initial gas cells, the dark matter mass, the average mass of the baryonic resolution elements, and the employed cosmology.

2014) and IllustrisTNG (Springel et al., 2018) simulations, the EAGLE (Schaye et al., 2015) simulation, and the HorizonAGN simulations (Dubois et al., 2016). All these calculations have produced reasonably realistic galaxy populations in representative volumes of the universe. In particular, they are not affected by the 'overcooling problem' and the related angular momentum problem, hence they are representing new, statistically powerful tools to study the baryonic spin of haloes at late times, when the evolution is highly non-linear and strongly impacted by galaxy formation processes. The success of the simulations was enabled by diverse sets of subgrid models for unresolved aspects of the galaxy formation physics, constituting a major uncertainty of the simulations. In this situation, analysing the spin of baryons could provide an interesting avenue to test these physics parameterisations, especially when a comparison to observations can be carried out as well.

Based on a compilation of observational data, Fall (1983) showed that the specific angular momentum of the stellar component of galaxies as a function of galaxy mass falls on parallel tracks for spiral and elliptical galaxies, respectively. Romanowsky and Fall (2012) extended the original study by adding $\sim 100$ nearby galaxies, providing the basis for allowing Fall and Romanowsky (2013) to refine their conclusion in saying that spiral galaxies have a factor of $\sim 5$ larger stellar spin than ellipticals at a given mass.

First results on the rotational support of the stellar component of galaxies from hydrodynamical simulations were obtained by Genel et al. (2015) using $\sim 30.000$ galaxies from the Illustris simulation and by Zavala et al. (2016) using $\sim 4.000$ galaxies from EAGLE. Both studies employing different hydrodynamical simulations confirmed above observational trends at $z = 0$. Swinbank et al. (2017) extended the study of the galaxy specific angular

momentum to stellar mass relation to higher redshift ($z = 0.3 - 1.7$) using 405 star-forming galaxies from MUSE and KMOS.

More detailed observational studies however show that the individual morphological galaxy types are subject to intrinsic variations. Based on 260 elliptical galaxies from the ATLAS$^{3D}$ survey, later extended to 370 ellipticals from the MASSIVE and ATLAS$^{3D}$ surveys by Veale et al. (2017) and Emsellem et al. (2011) revealed that elliptical galaxies are not a uniform class but can be divided into slow and fast rotators based on their stellar velocity fields. Obreschkow and Glazebrook (2014) employed the THINGS sample to measure the stellar and baryonic specific angular momentum of 16 nearby spiral galaxies and showed that the specific stellar angular momentum at given stellar mass depends on the bulge-to-total mass ratio. The derived relation between specific baryonic angular momentum and total baryonic mass was further confirmed by Elson (2017) employing 37 spiral galaxies from the WHISP survey. Based on 488 galaxies from the SAMI survey, Cortese et al. (2016) found that elliptical fast rotators and spiral galaxies are not confined to two parallel tracks in the stellar specific angular momentum versus galaxy mass plane, but rather continuously connect pure disks with bulge dominated systems as a function of growing bulge-to-total mass ratio.

The position of these galaxies in the stellar specific angular momentum versus galaxy stellar mass plane could be well reproduced by simulated galaxies from EAGLE (Lagos et al., 2017). Employing the so far largest sample of $\sim 2300$ galaxies from the MaNGA survey, Graham et al. (2018) showed a bimodality between slow and fast rotators of all morphological types. These findings advocate for the stellar mass and specific angular momentum of galaxies being the fundamental properties giving rise to the Hubble sequence. The detailed interplay between morphological and kinematic properties of galaxies can be investigated in great depth in future given (optical) morphological classification of simulated galaxies.

Recent years have seen great theoretical advances in the understanding of galaxy and halo spin, and in providing links to large-scale dynamics. Teklu et al. (2015) studied the connection between galaxy morphology and host halo spin, employing 622 haloes and their galaxies from the Magneticum Pathfinder simulation and finding that spiral galaxies reside in haloes with on average higher spin than elliptical galaxies. Studying 100 Milky Way-sized galaxies from the GIMIC simulation, Sales et al. (2012) on the contrary found little evidence for this trend, as well as for an impact form mergers on to galaxy spin and morphology. Rodriguez-Gomez et al. (2017) showed that the correlation between galaxy morphology and host halo spin is a strong function of halo mass, and that mergers play an increasingly important role in perturbing the gas distribution of the central galaxy with increasing halo mass, reconciling the above findings. Employing massive galaxies from EAGLE, Lagos et al.

(2018) investigated the impact of mergers on the stellar spin of galaxies and found that the gas content of mergers has the largest impact on the galaxy spin, and is more important than the orbital parameters of a merger, or whether it is a minor or major merger. They furthermore showed that on average mergers decrease the stellar spin of galaxies due to dry (gas-poor) mergers redistributing angular momentum to larger radii, whereas wet (gas-rich) mergers co-rotating with the galaxy efficiently increase the stellar spin, largely due to young stellar populations formed from the gas component driven by the merger in the galaxy centre.

An inside-out transport of specific angular momentum by dynamical friction associated with mergers entering the inner halo has been seen in the stellar component along with the same finding for dark matter by Zavala et al. (2008), as both stars and dark matter are of collisionless nature. Gas on the other hand exhibits an outside-in transport of specific angular momentum induced by mergers (Sharma et al., 2012).

The above studies show that multiple dynamical processes can lead to a redistribution of the specific angular momentum in the gas and stars forming a galaxy, whose superposition results in the observed galaxy spin. However, many studies agree that within gravitationally self-bound haloes, in which this redistribution takes place, the initial specific angular momentum of the baryonic component is not conserved, but rather appears enhanced by up to a factor of $\sim 2$. Based on a statistical estimate from $\sim 320.000$ haloes of the Illustris simulation, (Zjupa and Springel, 2017) have suggested that the enhancement of the baryonic spin compared to the dark matter originates in galactic feedback that expels preferentially low angular momentum gas. In this paper, we build upon our previous work and investigate the impact of feedback onto the emerging baryonic angular momentum properties in more detail, employing both the IllustrisTNG and Illustris simulations, two hydrodynamical cosmological simulations of structure formation that produce realistic galaxy populations, but are based on two different models for galaxy formation and feedback physics. This makes it particularly interesting for looking for common trends as well as differences that can inform about the nature of the feedback processes, and how they relate to the spin content of haloes. We will also examine how well the spin of the baryonic components converges as a function of numerical resolution.

We structure the rest of the paper as follows. In Section 3.2, we give a brief overview of the Illustris and IllustrisTNG simulations and discuss the feedback mechanisms employed to produce a realistic galaxy population. We also provide detailed information on halo and galaxy identification and sample selection, as well as on the calculation of the angular momentum properties. We present our main results in Section 3.3, where we first show the fundamentally different behaviour of the spin of baryons compared to dark matter. We also examine how feedback-driven galactic outflows affect the emerging baryonic spin. In

Section 3.4, we discuss and confront our findings with an analytical estimate of the baryonic spin enhancement. Finally, we present our conclusions and a summary in Section 3.5.

## 3.2 Methodology

### 3.2.1 The Illustris and IllustrisTNG simulations

We employ two sets of hydrodynamical cosmological simulations of structure formation with varying physical models, the Illustris and IllustrisTNG simulations, to investigate their statistical predictions for the halo spin, focusing on the impact of different galactic feedback models on the baryonic angular momentum content. Both simulation suites have as a primary model the same $75\,h^{-1}$Mpc wide periodic cosmological box with identical initial conditions but different cosmology, and evolve it from $z = 127$ to $z = 0$ with $1820^3$ dark matter particles and $1820^3$ initial gas cells using the moving-mesh code AREPO (Springel, 2010a). This corresponds to a mass resolution of $6.26 \times 10^6 \mathrm{M}_\odot$ in dark matter and $1.26 \times 10^6 \mathrm{M}_\odot$ in baryonic matter in the Illustris simulation and $7.46 \times 10^6 \mathrm{M}_\odot$ in dark matter and $1.39 \times 10^6 \mathrm{M}_\odot$ in baryonic matter in IllustrisTNG (TNG100)[1].

IllustrisTNG was carried out with the PLANCK15 cosmology (Planck Collaboration et al., 2016a) and used an updated version of AREPO with improved accuracy in gradient estimates and the time integration (Pakmor et al., 2016), whereas Illustris was run with the WMAP7 cosmology (Komatsu et al., 2011) and an older version of the AREPO code. We also make comparisons to a dark matter only counterpart of Illustris and TNG100, the Illustris-Dark simulation that has a mass resolution of $7.54 \times 10^6 \mathrm{M}_\odot$ in dark matter, and the TNG300 simulation which simulates a significantly larger cubic volume of $205\,h^{-1}$Mpc in one dimension, however at the price of a reduced mass resolution by a factor of 8. TNG300 thus has a significant number of rare massive objects like galaxy clusters that due to their mass are well resolved even at reduced resolution. We strengthen our analysis of numerical convergence by also analysing two lower resolution versions of the TNG100 model, with $2 \times 910^3$ (named TNG100-2) and $2 \times 455^3$ (TNG100-3) resolution elements, respectively. Finally, we consider for comparison a non-radiative version of the Illustris simulation, carried out at $2 \times 910^3$ resolution. An overview of the different simulations and their governing parameters is given in Table 3.1.

[1]Though both Illustris and TNG100 simulate the same amount of resolution elements in a $75\,h^{-1}$Mpc box, the differences in $h$ coming from the cosmological parameters adopted for the respective simulation result in a physical size of the simulated volume at $z = 0$ being $\sim 106.5$ Mpc for Illustris and $\sim 110.7$ Mpc for TNG100. The larger volume covered in TNG100 together with updated values for $\Omega_m$ results in a slightly higher initial mass per element in TNG100 compared to Illustris.

While being broadly successful, detailed analysis of the galaxy population predicted by the Illustris simulation has revealed a number of tensions with observables. For example, starting at a halo mass of $\sim 10^{12} M_{\odot}$ Illustris was increasingly overproducing stars with decreasing halo mass compared to the observed stellar mass to halo mass relation (see Pillepich et al., 2018, figure 4, bottom left panel). At a halo mass of $\sim 2 \times 10^{11} M_{\odot}$, Illustris galaxies exhibit $\sim 2$ times as much stellar mass within a fixed 30 kpc inner radius than the observed average.

In order to better reproduce the observed galaxy stellar mass function and the resulting $z = 0$ stellar mass to halo mass relation 'The Next Generation Illustris' simulation project (IllustrisTNG) introduced a number of changes to the original Illustris galaxy formation physics models. The most important modifications consist of a slightly updated galactic wind model, and a drastically altered treatment of black hole feedback. The new wind model introduces a redshift and metallicity scaling of the wind velocity, and a minimum velocity floor for low mass haloes. This has alleviated the discrepancies with observations in TNG100, as a higher wind velocity at injection is able to build up a higher pressure on the infalling gas and to drive large-scale outflows that significantly deplete low mass haloes of their baryons and thus lead to a lower star formation.

At the high mass end, haloes in Illustris were found to be depleted of most of their diffuse baryons by AGN feedback that for typically low accretion rates at low redshifts drives hot bubbles into the halo gas mimicking AGN radio activity (Sijacki et al., 2007). The particular model employed in Illustris for AGN feedback at low BH accretion rates was removing more gas from haloes above $\sim 2 \times 10^{12} M_{\odot}$ than is observed (see Genel et al., 2014, figure 10). This motivated a new kinetic AGN feedback model (Weinberger et al., 2017) in the TNG simulations that drives less strong outflows and is able to achieve arrested cooling flows in large haloes by effectively heating the intra-cluster medium (ICM).

For a full description of the Illustris galaxy formation model we refer to Vogelsberger et al. (2013), for a complete list of all changes and improvements applied to this original model and constituting the TNG100 model we point to Pillepich et al. (2018), and to (Weinberger et al., 2017) for details on the AGN model. We also want to note that TNG100 for the first time includes the treatment of ideal magnetohydrodynamic (MHD) as described by Pakmor and Springel (2013) in a full cosmological volume.

In this work we are especially interested in how these altered feedback processes impact the baryonic angular momentum content of haloes. In this context, outflows are particularly important as they not only carry away gas mass from haloes but also angular momentum. Depending on whether the specific angular momentum content of the outflowing gas is lower or higher than the halo average, the baryonic spin parameter of the remaining halo gas can

both increase or decrease. The magnitude of this effect will not only depend on the strength of the feedback processes but also to which gas they couple, and how they do this in detail.

Indeed, the mechanisms of how supernovae and AGN drive outflows are fundamentally different, and thus their impact on the spin content could also be quite different. Recall that AGN are the most powerful sources of energy in the universe which expel a fraction of the gas they accrete as collimated outflows. As an AGN sits in the potential minimum of its host halo, it is surrounded by the lowest angular momentum gas in the halo. In the IllustrisTNG black hole model, the feedback directly couples to this gas, whereas in Illustris also gas more in the periphery of haloes can become subject to feedback heating. This may translate into differences of how effectively AGN-driven outflows can drain haloes of their lowest angular momentum gas.

Supernova-driven winds are yet of a different nature. The thermal and kinetic energy they provide to the surrounding gas is not necessarily sufficient to expel the immediately affected gas, instead strong fountain-like gas flows can be induced in haloes. Supernova winds are thus actively redistributing baryons and angular momentum in haloes and constitute a major driving force for the baryon cycle in the circum-galactic medium (CGM). The gas that is ultimately pushed out of a halo as a result of galactic wind feedback has thus diverse origin and as such can be both of low and high specific angular momentum. Which is realised more often in the mean can be a sensitive function of the wind parameterisation. This in turn could make the halo spin an interesting indirect probe of these feedback processes.

### 3.2.2 The spin parameter and its measurement

Haloes in Illustris and IllustrisTNG are identified by the FOF group-finder algorithm that links all dark matter particles within a linking length of 0.2 times their mean particle spacing into a FOF halo. Baryons are assigned to their closest dark matter particle and are incorporated into the corresponding FOF halo. In a second step, the SUBFIND algorithm (Springel et al., 2001) identifies all gravitationally self-bound components within each FOF halo, yielding so-called subhaloes. The largest of these substructures is identified with the central galaxy, the others represent satellite galaxies and/or dark matter subhaloes. Around the potential minimum of the central subhalo, spherical overdensity mass estimates (which consider the full matter field not just the FOF halo) are also computed, for a set of different overdensities that are commonly in use.

We obtain the angular momentum properties of haloes and galaxies by executing an extended version of the group finders FOF and SUBFIND (Springel et al., 2001) on the outputs of the simulations described above. The corresponding modifications of the SUBFIND code are described in detail in Zjupa and Springel (2017), where they have already been applied

to Illustris. However, to be able to apply this extension to the TNG300 simulation, which required scalability to more than 24.000 computing cores, a substantial technical restructuring of the SUBFIND extension was necessary, especially with respect to the internal memory management, but the basic functionality was kept the same.

In our code the specific angular momentum of a halo (or any subhalo or spherical overdensity region of this halo) with $N$ mass elements is calculated according to

$$\mathbf{j}_{\rm sp} = \frac{\mathbf{J}}{M} = \frac{1}{M}\sum_{i=1}^{N} m_i \mathbf{r}_i \times \mathbf{v}_i, \tag{3.1}$$

where the index $i$ refers to the $i$-th computational element with mass $m_i$, distance from the halo centre $\mathbf{r}_i$, and velocity $\mathbf{v}_i$ with respect to the centre of mass velocity of the halo. $M = \sum_i^N m_i$ is the total mass of the group of resolution elements. These can also be subsets of the halo, for example the dark matter, gas, or stellar component.

The same applies to the calculation of the specific angular momentum of galaxies in its various definitions, although galaxy-specific quantities are not analysed in this work. For a full list of properties calculated with the SUBFIND extension we refer to the tables in appendix A of Zjupa and Springel (2017) and to the public data release of Illustris (Nelson et al., 2015, www.illustris-project.org). Similarly to Illustris, we plan to release the spin data for TNG100 and TNG300 as part of the forthcoming IllustrisTNG public data release.

Based on the specific angular momentum properties we calculate the dimensionless spin parameter $\lambda$ according to the definition of Peebles (1969),

$$\lambda_{\rm P} = j_{\rm sp} \frac{E_{\rm tot}^{1/2}}{G M_{\rm tot}^{3/2}}, \tag{3.2}$$

where $j_{\rm sp} = J/M$ is the absolute value of the specific angular momentum per unit mass of the chosen subset, $M_{\rm tot}$ the total mass of the system, $G$ the gravitational constant, and $E_{\rm tot} = |E_{\rm kin} + E_{\rm pot}|$ is the total energy, where the kinetic energy is the sum of the bulk kinetic energy of the subsets particles/cells and the thermal energy of the gas, if present. Note that a computationally efficient computation of the gravitational potential energy is non-trivial for large haloes, a task we solve with the tree algorithm used by SUBFIND for the gravitational unbinding. The multiplicative factor $E_{\rm tot}^{1/2}/(GM_{\rm tot}^{3/2})$ expresses the specific angular momentum $j_{\rm sp} = |\mathbf{j}_{\rm sp}|$ in dimensionless form, providing a measure with which the angular momentum content of structures with different mass and spatial extent can be compared directly. When we consider different components of a halo, like dark matter or gas, this factor is kept the same and always computed for the full halo.

In the following, we will employ the Peebles spin parameter definition and hence drop the 'P'-index. We refrain from using the alternative Bullock spin parameter definition (Bullock et al., 2001), as we have shown in Zjupa and Springel (2017) that the Peebles definition yields a spin parameter distribution that evolves least with redshift. This is theoretically preferred given the approximate self-similarity of dark matter haloes.

### 3.2.3 Halo sample selection

We aim to select well-resolved haloes in dynamical quasi-equilibrium for our study, ensuring that the properties we derive are neither affected by numerical effects nor by objects at peculiar stages of their evolution. To this end we adopt similar selection criteria as in Zjupa and Springel (2017), which required a halo to have a gravitationally self-bound component identified by SUBFIND, and to have a minimum resolution of 300 dark matter particles. The latter follows Bett et al. (2007) and appears to guarantee sufficient numerical resolution in dark matter-only simulations. As we will see later on, convergence of the baryonic spin requires however significantly higher resolution, hence we will later on raise the minimum halo mass threshold as required to yield quantitatively robust results.

Furthermore, to any sample of our haloes we apply a further cut to select only those reasonably close to dynamical equilibrium. Such a cut can be performed based on the so-called virial ratio,

$$q = \frac{2\,E_{\mathrm{kin}}}{E_{\mathrm{pot}}} + 1, \tag{3.3}$$

where $E_{\mathrm{pot}}$ is the potential energy and $E_{\mathrm{kin}}$ is the sum of the kinetic energy contained in the particle and cell velocities and the thermal energy of the gas.

A virial ratio equal to $q = 0$ signals that a halo is in virial equilibrium, while negative values indicate a surplus of kinetic energy. At $q = -1$ haloes, have twice the kinetic energy they have in virial equilibrium. We remove all haloes with $q < -1$ from our samples, thereby reducing a contamination with objects undergoing mergers where the angular momentum is dominated by the orbital angular momentum of the objects around the common centre of mass instead of by ordered rotation around the potential minimum.

When applied to friends-of-friends haloes, the above selection procedure yields a sample size of 320.963 FOF haloes in Illustris, 345.334 FOF haloes in TNG100, and 402.831 haloes in Illustris-Dark. Note that even though these three simulations have the same initial conditions phases and comoving box size, the halo sample size varies because the 300 dark matter particle cut is applied to all simulations irrespective of whether they contain baryons or not, and because of the different feedback models in Illustris and TNG100. We note that

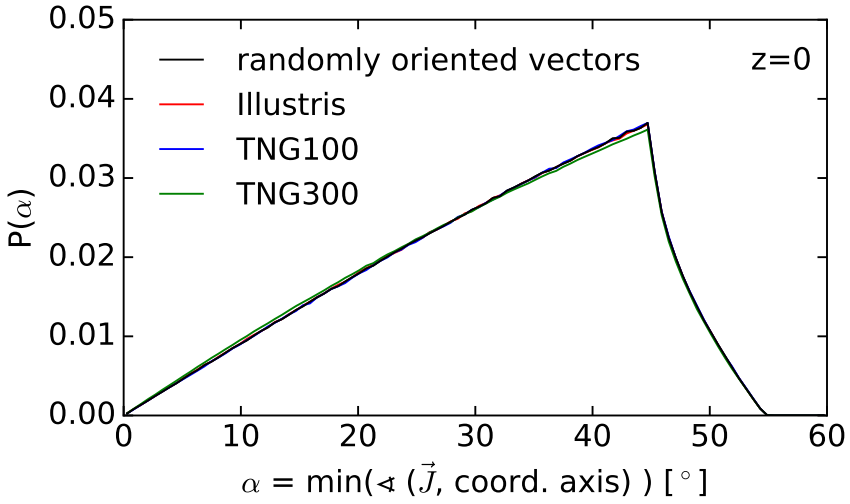


Figure 3.1: Distribution of the minimum angle $\alpha$ between the angular momentum vectors of haloes from Illustris (red line) and any of the coordinate axes of the simulation box. The equivalent distributions for TNG100 and TNG300 are shown as blue and green lines, respectively. We also plot the distribution obtained from $10 \times 10^6$ vectors with orientations uniformly distributed on the unit sphere. The good agreement between all three distributions demonstrates the isotropy of the angular momentum distribution in the simulations, and the absence of grid-locking effects that can occur in simulations with Cartesian grids.

the TNG300 simulation yields to a FOF halo sample of 1.306.962 objects according to this selection, highlighting its much higher statistical power.

In the following analysis, in addition to friends-of-friends (FOF) haloes we will mostly adopt haloes in their spherical overdensity (SO) defintition, in favour of their more cleanly defined outer boundary and the elimination of halo pairs that are linked by feeble particle bridges. For definiteness, we will use SO haloes defined within an overdensity of 200 relative to the mean cosmic density (not critical density), as these halo masses are generally very similar to FOF halo masses and tend to minimise effects of spurious late-time halo mass evolution (More et al., 2015). We note, however, that all our results are insensitive to this choice and are very similar if SO haloes with 200 times relative to critical density or FOF haloes are used instead.

### 3.2.4 Angular momentum on an unstructured moving mesh

Within AREPO dark matter is treated as collisionless particles that couple gravitationally to the gas whose hydrodynamical evolution is computed on a moving unstructured mesh in a quasi Lagrangian way, such that the cell flow and geometry follows the mass flow. At

the same time, this approach being only quasi Lagrangian allows for some mass exchange across cell boundaries and as such for actual mixing of gas and metals. One advantage of the unstructured geometry of the Voronoi mesh is that for large enough volumes it should ensure that the angular momentum vectors do not align with the three coordinate axes of the simulation box, which tends to happen in Cartesian grid codes (Hahn et al., 2010). We here want to briefly test this aspect explicitly.

The potential alignment of the halo angular momentum with coordinate axes of the simulation box can be tested by comparing the distribution of angles between the angular momentum vectors and each coordinate axes against the same distribution derived from a set of randomly oriented (angular momentum) vectors in three dimensional space. To this end, we draw $10^7$ unit vectors with random directions in three-dimensional space. For each vector we calculate the angles to the three coordinate axes, and select the smallest of these three angles, called $\alpha$ in the following. In Figure 3.1, we show the distribution of the smallest angle $\alpha$ derived from the set of random vectors as a black solid line. We repeat the calculation for the baryonic angular momentum vectors of haloes from Illustris, TNG100, and TNG300 (see our selection criteria above), and show the obtained distributions in Fig. 3.1. No deviation from the random distribution is visible, confirming that there is no appreciable alignment of halo angular momentum with the principal axes of the simulation box.

## 3.3 Results

### 3.3.1 The spin distributions of TNG and Illustris

We begin by comparing the dark matter spin distributions of haloes in order to review mechanisms that impact the spin in the absence of more complex galaxy formation physics. In Figure 3.2, we show the spin parameter distributions derived from Illustris, TNG100, their dark matter only counterpart Illustris-Dark, and TNG300. The distributions are obtained by binning the spin parameters in 50 equidistant logarithmic bins over the given range, and normalising to the total number of haloes as well as to the bin size. From Fig. 3.2 it becomes apparent that the shape of the spin distribution is very well converged for the given simulations. It can be well approximated by a log-normal function (see e.g. Bett et al., 2007, Teklu et al., 2015, Zjupa and Springel, 2017).

The TNG300 simulation exhibits the largest shift of its dark matter spin parameter distribution to higher values, with a median spin of $\lambda_{\mathrm{TNG300}} = 0.041$ compared to the dark matter only Illustris-Dark median spin value of $\lambda_{\mathrm{DM}} = 0.0391$. The main reason for this is the small but distinct increase of median dark matter spin with halo mass (see Zjupa and

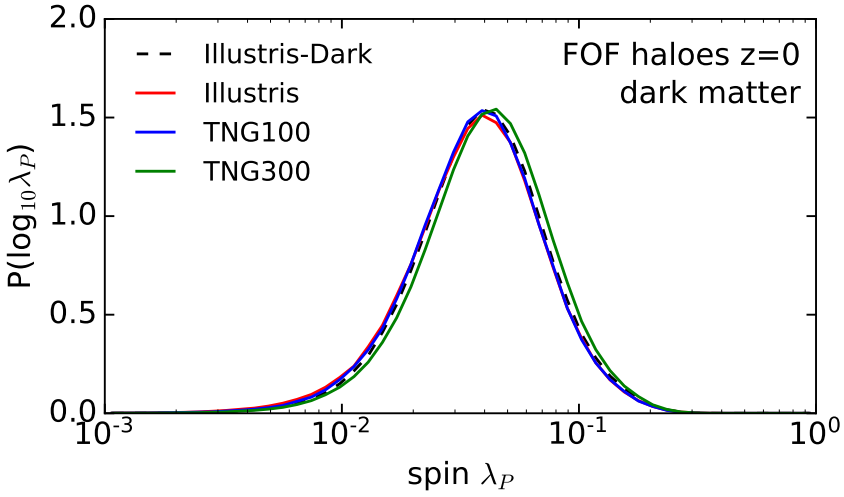


Figure 3.2: Dark matter spin parameter distribution of FOF haloes at $z = 0$ for Illustris, its dark matter only counterpart Illustris-Dark, TNG100, as well as TNG300. The distributions derived from these different types of simulations are remarkably similar, but not identical. While Illustris and TNG100 are extremely close, their dark matter counterpart Illustris-Dark (which has equivalent mass resolution) shows a slightly higher spin. The more coarsely resolved, but larger volume simulation TNG300 shows also a small, more noticeable shift to a higher average dark matter spin.

| range | all | dm | gas | baryons | stars | $\frac{M_*}{M_{\rm gas}}$ |
|---|---|---|---|---|---|---|
| TNG100 | | | | | | |
| mr1 | 0.0433 | 0.0423 | 0.0820 | 0.0799 | 0.0109 | 0.05 |
| mr2 | 0.0495 | 0.0484 | 0.0763 | 0.0653 | 0.0165 | 0.25 |
| mr3 | 0.0534 | 0.0519 | 0.103 | 0.0766 | 0.0306 | 0.42 |
| Illustris | | | | | | |
| mr1 | 0.0506 | 0.0449 | 0.102 | 0.0985 | 0.0288 | 0.07 |
| mr2 | 0.0534 | 0.0524 | 0.0814 | 0.0681 | 0.0283 | 0.38 |
| mr3 | 0.0546 | 0.0541 | 0.133 | 0.0692 | 0.0346 | 1.61 |

Table 3.2: Median Peebles spin parameter values of different halo components in the TNG100 and Illustris simulations, for different halo mass ranges. We give results for the spin distribution of the total matter, the dark matter part, the gas, all baryons, and the stars. The last column gives the average stellar mass to gas mass fractions, highlighting the relative contributions of stars and halo gas to the total baryonic spin. The three broad mass ranges correspond to those shown in Fig. 3.3: the 'mr1' mass range is a regime where supernovae driven galactic winds are efficient, the 'mr2' range where neither galactic winds nor AGN can prevent galaxies from efficient star formation, and the 'mr3' mass range where galaxies exhibit strong AGN feedback.

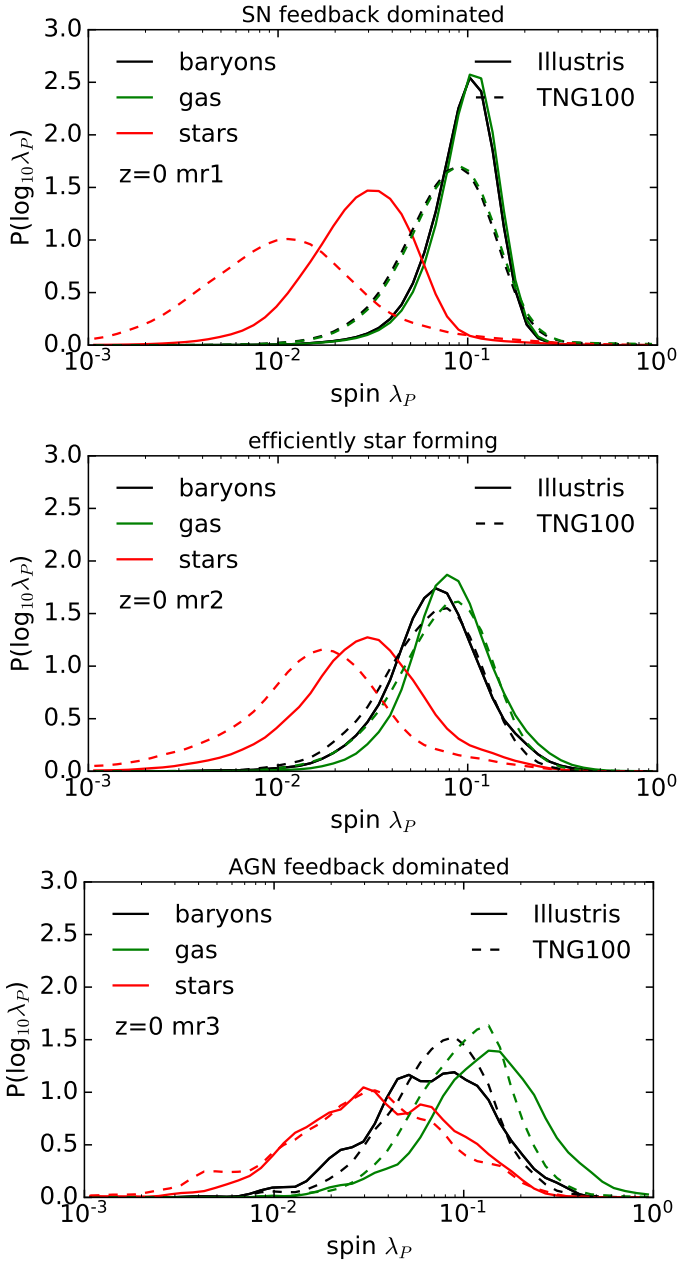


Figure 3.3: Comparison of the baryonic, gas, and stellar spin parameter distributions of FOF haloes from Illustris and TNG100, in three different mass ranges at $z = 0$. The mass ranges are given by $2 \times 10^{10} < M/\mathrm{M}_\odot < 2 \times 10^{11}$ (designated as mr1), $2 \times 10^{11} < M/\mathrm{M}_\odot < 2 \times 10^{12}$ (mr2), and $2 \times 10^{12} < M/\mathrm{M}_\odot < 2 \times 10^{13}$ (mr3), and are shown from top to bottom. They can be loosely associated with different feedback regimes, which are here denoted as 'SN feedback dominated', 'efficiently star forming', and 'AGN feedback dominated'. All the different spin distributions are reasonably well described by log-normals, but especially in the lowest mass bin, substantial differences between the Illustris and TNG100 simulations exist. Note in particular that in the mr1 mass range, the spin distribution of the gas happens to coincide closely with the spin distribution of all the baryons, for both Illustris and TNG100, simply because the contribution of the stars is negligible by mass. But interestingly, the baryonic spin distributions of the two simulations do not agree with each other for these low halo masses; the Illustris model has a higher baryonic spin on average than TNG in this mass range. The agreement between the models is much better for higher halo masses, as seen in the bottom panel, where in particular the stellar spin distributions are quite similar. The median spin values for each mass bin and each of the different components are given in Tab. 3.2.

Springel, 2017, figure 10). As TNG300 was performed at a lower mass resolution than the other simulations shown in this plot (by a factor of 8), but was subjected to the same minimum 300 dark matter particles per halo cut we apply to all our simulations, the minimum halo mass in the TNG300 sample shown in Fig. 3.2 is about an order of magnitude higher than in the other simulations. The lack of low mass haloes in the TNG300 sample combined with the slight increase of dark matter spin with halo mass leads to a higher median dark matter spin and a slightly shifted spin distribution in the TNG300 simulation.

For Illustris and TNG100, the impact of the presence of baryons onto the dark matter spin distributions is so small that it is not readily visible in Fig. 3.2, but a small and statistically significant effect is there nevertheless. It can be best seen in the median spin values (corresponding to good approximation to the location of the peak values of the distributions), which are $\lambda_{\mathrm{Illustris}} = 0.0379$ for Illustris and $\lambda_{\mathrm{TNG100}} = 0.0381$ for TNG100. Thus these simulations including baryons exhibit an almost identical median spin parameter, which is however $\sim 3\%$ lower than the median spin from the dark matter only simulation. As we will confirm later, this can be explained through a small but systematic angular momentum transfer from dark matter to the gas during the assembly and evolution of haloes. We shall discuss this effect in more detail later on.

In Figure 3.3, we compare the spin distributions of different halo components in the full-physics TNG100 and Illustris simulations, in three different halo mass ranges. These three mass bins are given by (i) $[2 \times 10^{10}\mathrm{M}_{\odot}, 2 \times 10^{11}\mathrm{M}_{\odot}]$, (ii) $[2 \times 10^{11}\mathrm{M}_{\odot}, 2 \times 10^{12}\mathrm{M}_{\odot}]$, and (iii) $[2 \times 10^{12}\mathrm{M}_{\odot}, 2 \times 10^{13}\mathrm{M}_{\odot}]$. Those mass bins broadly correspond to regimes in which (i) galaxies exhibit strong feedback due to galactic winds launched by supernovae (SN), (ii) where galaxies are efficiently star forming as their haloes are massive enough to be less affected by galactic winds and simultaneously not yet massive enough to host an AGN, and (iii) where galaxies are dominated by AGN feedback. We refer to these mass bins as mr1, mr2, and mr3, respectively. The number of haloes in each of those three mass bins is (i) 51.383, (ii) 7.286, and (iii) 834 for Illustris and (i) 50.614, (ii) 7.974, and (iii) 1.011 for TNG100.

As the number of haloes falling into a mass bin decreases rapidly with increasing halo mass we smooth the derived distributions with a Gaussian kernel with standard deviation of one bin in spin parameter space and which is truncated after four bins to reduce the noise. The resulting median spin parameter values in the different mass bins as well as the stellar to gas mass ratios for the two simulations are listed in Table 3.2.

Both similarities and differences between TNG100 and Illustris are striking in Fig. 3.3. By far the largest difference in baryonic spin coming from employing different feedback models is visible in the stellar spin of low mass haloes. In the lowest mass range displayed in

the top panel of Fig. 3.3, the median stellar spin in Illustris is about $\sim 2.5$ times larger than in TNG100. This difference in the median of the stellar spin parameters becomes smaller with increasing halo mass and vanishes above a halo mass of $\sim 2 \times 10^{12} \mathrm{M}_{\odot}$. The substantially lower stellar spin in low mass haloes in TNG100 can be understood as a consequence of the stronger winds employed in TNG100 compared to Illustris, which more effectively suppresses star formation. As gas with low angular momentum accumulates in the inner region where it reaches higher densities and cools more efficiently, this gas forms stars first (see also El-Badry et al., 2018, section 3). After the lowest angular momentum reservoir is depleted by either star formation or expulsion of gas due to galactic outflows, star formation will extend into increasingly higher angular momentum gas that is then replenishing the inner regions. Thus in this picture the more stars are formed the higher will their specific angular momentum be, as they will form from gas with increasing average spin. Therefore, the lower stellar mass formed in low mass haloes in TNG100 directly translates into a smaller stellar spin.

We note however that even at fixed stellar mass, central galaxies residing in low mass haloes are a constant factor of $\sim 2$ smaller in TNG100 than in Illustris, bringing them into good agreement with observations (see Pillepich et al., 2018, figure 4, bottom right panel). There is hence a secondary effect in TNG100 that adds to the lower spin of the stellar component of low mass haloes, probably related to differences in the baryon cycle in the two simulations. The smaller galaxy sizes in TNG100 contribute to a smaller stellar spin parameter, but the bulk of the effect can be attributed to the smaller stellar mass formed.

Interestingly, the gas spin of low mass haloes in TNG100 is also somewhat lower than in Illustris. In case of the gas component, this is a consequence of more compact galaxies, including their gas disks, residing in lower mass haloes in TNG100 compared to Illustris. This discrepancy vanishes for halo masses of the Milky Way's halo mass that fall into our mr2 mass range. For even higher halo masses the gas spin derived from TNG100 is however again smaller than in Illustris. To properly understand how this comes about we will have to discuss the role of feedback in driving baryonic loss from haloes, and the associated change of the baryonic angular momentum content of haloes.

Note that the baryonic spin is dominated by the gas spin at low halo masses, as in those haloes the stellar mass is negligible compared to the stellar mass. The ratio of stellar to gas mass increases with increasing halo mass, shifting the baryonic spin to intermediate values between the gas and the stellar spin. For our highest mass bin, both the total baryonic spin and the stellar spin tend to be fairly similar for TNG and Illustris, but the latter shows a substantially larger spin parameter for the remaining gas in the haloes. As we shall see later, this is related to the much higher baryonic deficit in Illustris.

### 3.3.2 Model and resolution dependence of the median spin for different halo components

The differences seen in Fig. 3.3 at low halo masses motivate us to look into the question of convergence of the spin parameter measurements. The TNG simulation suite is particularly well suited for this task thanks to its sequence of runs with differing mass resolution but otherwise identical set-up.

In Figure 3.4, we consider the convergence of the median spin as a function of halo mass, for different SO halo components. We derive the medians by binning haloes into equidistant logarithmic bins of width $\log(2)$ over the displayed mass range, and then measuring the median of each bin. Only bins with at least 10 haloes are shown.

The first five panels of Fig. 3.4 give results for the total SO halo spin, the dark matter spin, the gas, the stars, and the total baryonic spin. In each case we include results for the three TNG100 models with different mass resolution, allowing an assessment of numerical convergence. We include Illustris as well, to allow an evaluation of physics model induced differences. Finally, the TNG300 results included as well show the magnitude of finite box size effects, especially when compared to TNG100-2, which has the same mass resolution.

Looking at the results for the different halo components, it is clear that the dark matter spin and the total halo spin (which is dominated by the dark matter) can be quite reliably predicted by the simulations, even down to a low resolution corresponding to a few hundred particles per halo. However, a sobering aspect of these results is that this is not at all true for the baryonic components. Especially for the stellar spin content of haloes, robust quantitative values require a far higher number of resolution elements. Only for halo masses in excess of $\sim 4 \times 10^{11}\,\mathrm{M}_\odot$ reasonably converged results for TNG100 can be expected. In particular, this means that the results we obtained previously for baryons in the mass bin ‘mr1’ have to be taken with a grain of salt, as they are still subject to sizeable resolution effects.

As far as the dark matter component is concerned, the spin is nearly invariant with halo mass, but TNG300 reveals hints at a small decline of the mean spin towards the largest haloes, which are also the ones that have the youngest ages. The spin in the stellar component tends to grow with halo mass, except for very low halo masses in TNG, where clear resolution effects appear.

The baryons typically show a substantial enhancement of their spin relative to the dark matter value, but for halo masses of $\sim 10^{14} h^{-1}\mathrm{M}_\odot$ and above, this effect largely vanishes, both for TNG and Illustris. The spin parameter of the gas largely tracks that of all the baryons in most cases, which reflects the fact that the stellar mass is subdominant compared to the gas mass in almost all haloes. An exception occurs for halo masses around $10^{13}\,h^{-1}\mathrm{M}_\odot$ in Illustris, where the gas has a very high spin parameter, considerably exceeding both that of

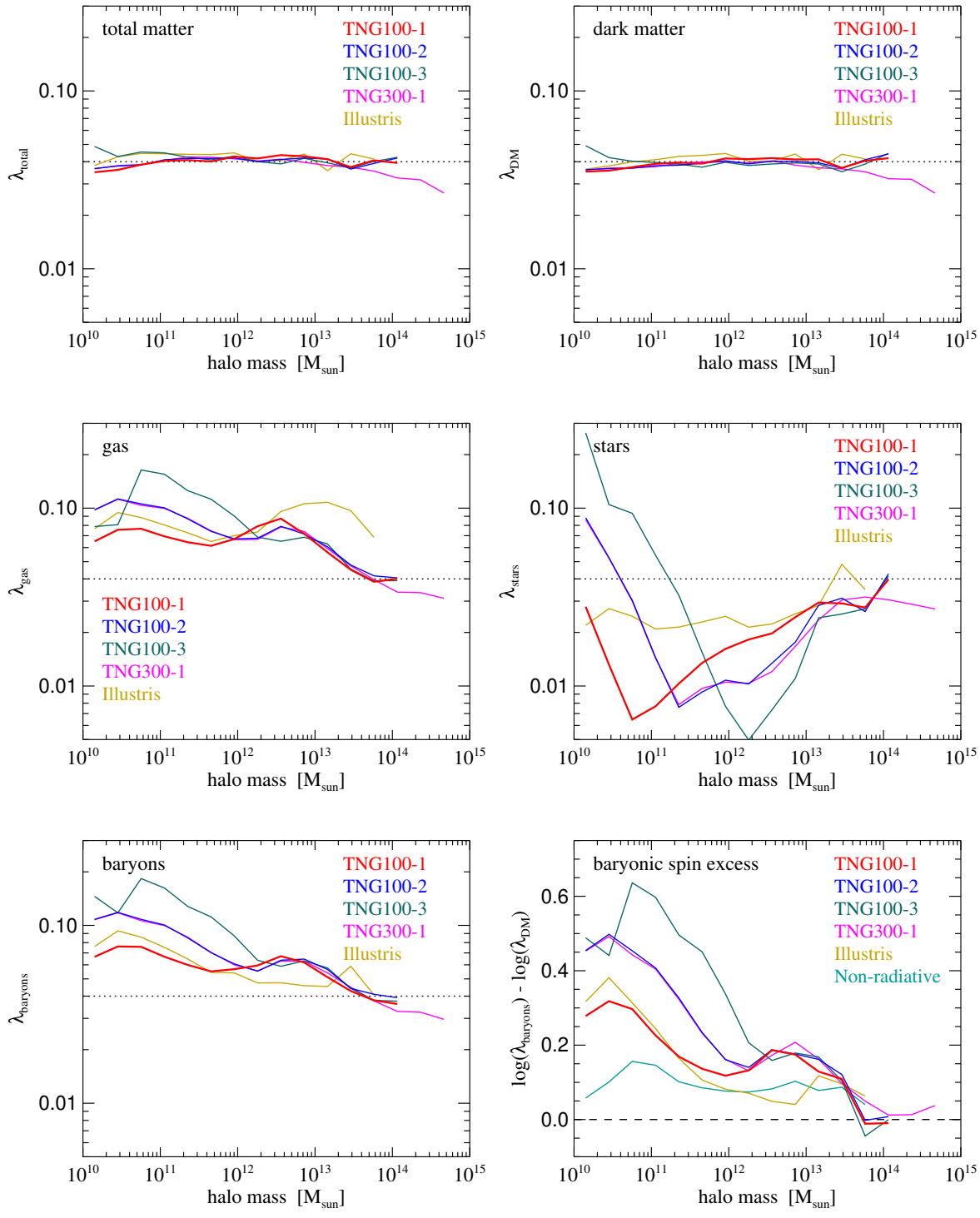


Figure 3.4: The median spin parameter in different SO halo components as a function of halo mass, for different simulation models. The first five panels give results for the total halo spin, the dark matter spin, the gas, the stars, and the total baryonic spin, as labelled. In these panels we include results for the three different TNG100 models, allowing an assessment of numerical convergence, and we include Illustris as well, highlighting model differences. Comparing the also included TNG300 result to TNG100-2 (which has the same mass resolution) illustrates finite box size effects. The dotted reference line at $\lambda = 0.04$ is reproduced in all five panels to guide the eye. The bottom right panel shows the offset between the median baryonic spin and the dark matter spin. In this panel, the non-radiative Illustris simulation is also shown, for comparison.

all baryons and that of the stars. This is here possible due to a very small gas-to-stellar mass ratio, as a result of extreme baryonic loss by AGN feedback in these haloes.

For studying the change of baryonic angular momentum content in haloes it is instructive to look at the difference between the median baryon and dark matter spins, as a function of halo mass. We show this in the bottom right panel of Fig. 3.4, where we also include the non-radiative Illustris simulation, for comparison. Again, we see that TNG100 and Illustris results can only be trusted quantitatively for halo masses above $\sim 4 \times 10^{11}\,\mathrm{M}_\odot$. In this regime, the baryonic spin enhancement in TNG is substantially larger than in the non-radiative simulation, whereas it is marginal in Illustris. Interestingly, there is a characteristic "bump" in the spin excess of TNG, setting in at about $10^{12}\,h^{-1}\mathrm{M}_\odot$. We attribute this to the effects of AGN feedback. For halo masses of $10^{14}\,h^{-1}\mathrm{M}_\odot$ and above, the spin excess appears to vanish completely. To the extent that it is associated with baryon loss, we would then expect that haloes of this size retain close to their universal baryon fraction, something that we will confirm later on.

### 3.3.3 Spin correlations between baryons and dark matter

Our analysis of the median spins in Fig. 3.4 showed that already non-radiative simulations show an offset in their mean spins. Such non-radiative simulations follow the gas flow as prescribed by the Euler equations without including any star formation or galaxy evolution physics, and to the extent that the spin is imparted by large-scale gravitational tidal torques it may at first seem surprising that such differences arise. However, during infall the gas component of mergers is getting ram pressure striped which leads to a displacement of the centres of mass of the dark matter and gas component of the merger opening a channel for specific angular momentum transfer through a mutual torque. The finding that the dark matter loses to good approximation the amount of angular momentum that is gained by the gas obeying angular momentum conservation is a strong argument in favour of this mechanism (see Zjupa and Springel, 2017, section 4).

Furthermore, Liao et al. (2017) showed in non-radiative smoothed particle hydrodynamics (SPH) simulations that only on average $\sim 80\%$ of the halo gas originates from the same Lagrangian region as the dark matter making up the halo. This number varies strongly for individual haloes, as it depends on the individual accretion histories during which the gas that experiences pressure forces during infall is separated from collisionless dark matter. Liao et al. (2017) showed that the average misalignment of $\sim 30^\circ$ between the dark matter and gas angular momentum vectors (see also van den Bosch et al., 2002) is already imprinted in the non-overlapping spatial origin of the two components and is preserved during halo

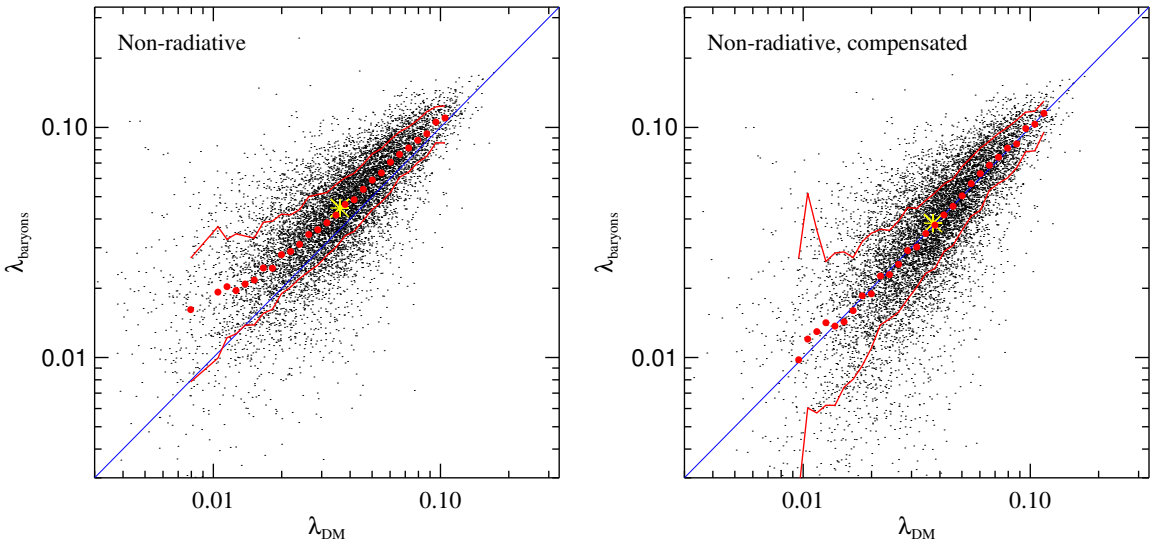


Figure 3.5: *Left panel:* Correlation between the spin parameter in baryons relative to the spin parameter in dark matter, for haloes in the non-radiative Illustris simulation. The diagonal blue line shows the one-to-one relation. The yellow star gives the median of both spin distributions, whereas the red circles show the medians for the $\lambda_{\rm baryons}$ distributions in fine logarithmic bins of $\lambda_{\rm DM}$. The solid red lines indicate the central $1\sigma$ percentiles containing 68 percent of these distributions. *Right panel:* The same data, but here an angular momentum transfer of fixed size was assumed between dark matter and baryons. This restores an essentially perfect one-to-one relation.

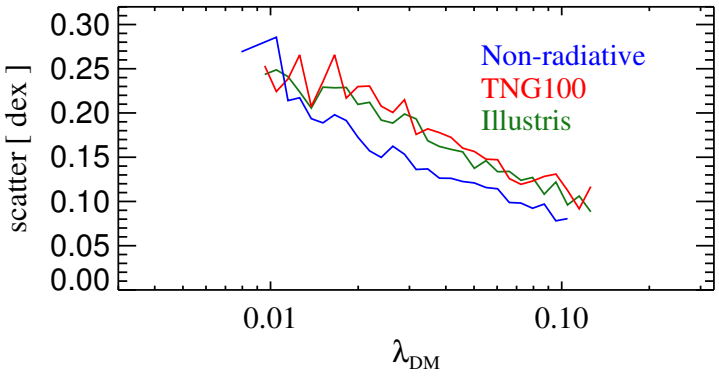


Figure 3.6: Scatter of the baryonic spin parameter around the dark matter spin in the $\lambda_{\rm baryons} - \lambda_{\rm DM}$ relation of haloes. The blue line shows the result for the non-radiative Illustris simulation displayed in Fig. 3.5, while the red and green lines give the TNG100 and Illustris simulations, as labelled.

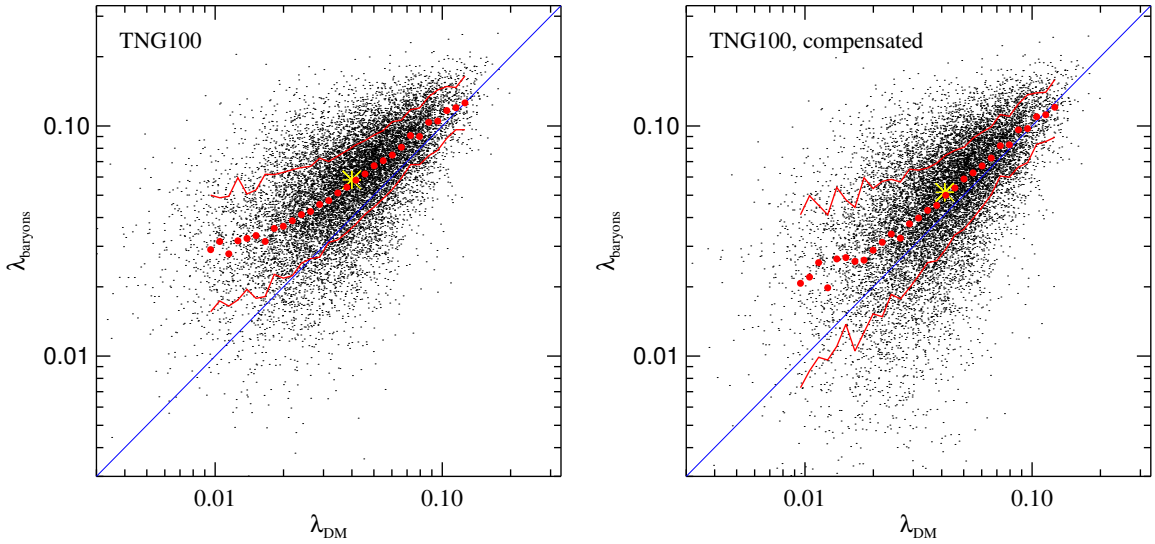


Figure 3.7: Correlation between the spin parameter in baryons and the spin of the dark matter in haloes in the TNG100 simulation. The left panel shows the data for TNG100 at $z = 0$, while the right panel attempts to compensate for an angular momentum transfer from dark matter to the gas, assuming the same magnitude as measured for the Illustris non-radiative simulation. In both panels, the red circles give the median baryonic spin in small bins of dark matter spin, while the solid red lines enclose 68 percent of the distribution. The correction applied in the right panel is clearly insufficient to restore a one-to-one relation for the medians.

assembly. The dark matter and gas which come from different Lagrangian regions will also experience different tidal torques which might contribute to the enhanced gas spin at $z = 0$.

Another possibility that could contribute to a reduced dark matter spin and an increased gas spin in the presence of a gas component, is that the gas may slightly reorient the whole halo with respect to the large scale structure in such a way that the acquisition of angular momentum through tidal torques and accretion is systematically modified. Whether the gas component can really change the orientation of the dark matter halo with respect to the large scale structure is an open question for future studies.

To shed more light on these question, we consider in Figure 3.5 the correlation of the baryonic spin relativ to the dark matter spin on the basis of individual haloes. The left panel shows simply the plain correlation between the two spin values, with their respective medians marked by a yellow star. We have also grouped the dark matter haloes into narrow bins of dark matter spin, with the baryon spin medians of the respective bins marked with red circles. Clearly, there is on average an offset towards higher baryonic spin than expected for a one-to-one relation between the two components, and the relative size of this offset shows a clear dependence on the size of the dark matter spin itself.

But, in fact, the offset is approximately of constant absolute size, i.e. $\lambda_{\rm baryons} - \lambda_{\rm DM}$ is independent of the dark matter spin. Hence, the offset can be removed by assuming that on average there are processes at work during non-linear halo assembly and evolution that transfer a fixed amount of spin from the dark matter to the gas. Such processes could include ram-pressure stripping, or pressure torques on non-spherical haloes. In the right panel of Fig. 3.5 we show the relation between the spin parameters if we assume that on average such a constant angular momentum transfer (in terms of the spin parameter) has happened between dark matter and baryons, allowing us to correct for it by computing

$$\lambda'_{\rm DM} = \lambda_{\rm DM} + \Delta\lambda \tag{3.4}$$

$$\lambda'_{\rm baryons} = \lambda_{\rm baryons} - (\Omega_{\rm dm}/\Omega_b)\Delta\lambda \tag{3.5}$$

The right panel shows that a value of $\Delta\lambda = 0.0013$ can explain the observed offset, corresponding to a change of about 3 percent in the dark spin of haloes which have the median spin.

Interestingly, Fig. 3.5 also reveals that there is a significant scatter between the magnitude of the baryonic spin and the dark matter spin, even in a non-radiative simulation. We show this scatter explicitly in Figure 3.6, which also highlights that it grows towards smaller spin values. Around the median spin, the scatter between baryonic and dark matter spins is about 0.12 dex. However, this scatter increases significantly by about 0.05 dex when full physics

simulations are considered, as shown by the results for TNG and Illustris included in the figure.

In Figure 3.7 we repeat the exercise of correlating the baryonic spin with the dark matter spin, but this time for the TNG100 simulation. Here the scatter plot reveals that not only the scatter is enlarged, but also the offset of the baryonic component relative to the DM is stronger. Furthermore, the dependence of the baryonic spin excess on the DM spin appears to be enhanced. In the panel Fig. 3.7, we nevertheless do the experiment of applying the non-radiative spin enhancement correction from above to this full physics simulation. Unsurprisingly, this is not able to fully account for the spin enhancement of the baryons. Something else most therefore play a prominent role in TNG.

### 3.3.4 Baryon mass loss and spin modification

To gain a better understanding of how this baryonic angular momentum excess emerges, we have to turn to the baryonic content of haloes and how it is impacted in its properties by supernova driven winds and AGN feedback. Without any feedback, gravitationally bound structures would be expected to contain a baryon fraction that roughly equals the cosmic baryon fraction, $\Omega_b/\Omega_m$. However, both supernovae and AGN drive large scale outflows that can significantly deplete haloes of their baryons, and alongside reduce their angular momentum content. As a result, the average specific angular momentum of the baryons staying in the halo can both increase or decline.

We obtain important clues about this by considering the relative increase in the baryonic spin, and by correlating it with the baryon deficit of the corresponding halo. We define the baryonic deficit $b$ as the fraction of baryons missing to give the halo a universal mix of baryons. Here and in the following, this quantity is computed from the dark matter mass $M_{\rm DM}$ and the baryonic mass $M_b$ of a halo as follows,

$$b = 1 - \frac{\Omega_{\rm DM}}{\Omega_b}\frac{M_b}{M_{\rm DM}}, \tag{3.6}$$

where $\Omega_{\rm DM}$ and $\Omega_b$ are the cosmic dark matter and baryon fractions in units of the critical density, respectively.

In Figure 3.8, we show the median spin excess as a function of $b$ for different mass ranges in TNG100, TNG300, and Illustris. We restrict outselves to relatively massive halo bins where we saw in Fig. 3.4 signs of reasonably robust convergence. Interestingly, the haloes in the AGN mass regime show a strong correlation of the baryonic spin enhancement with the baryon loss, whereas such a correlation seems to be very weak or absent for low halo masses.

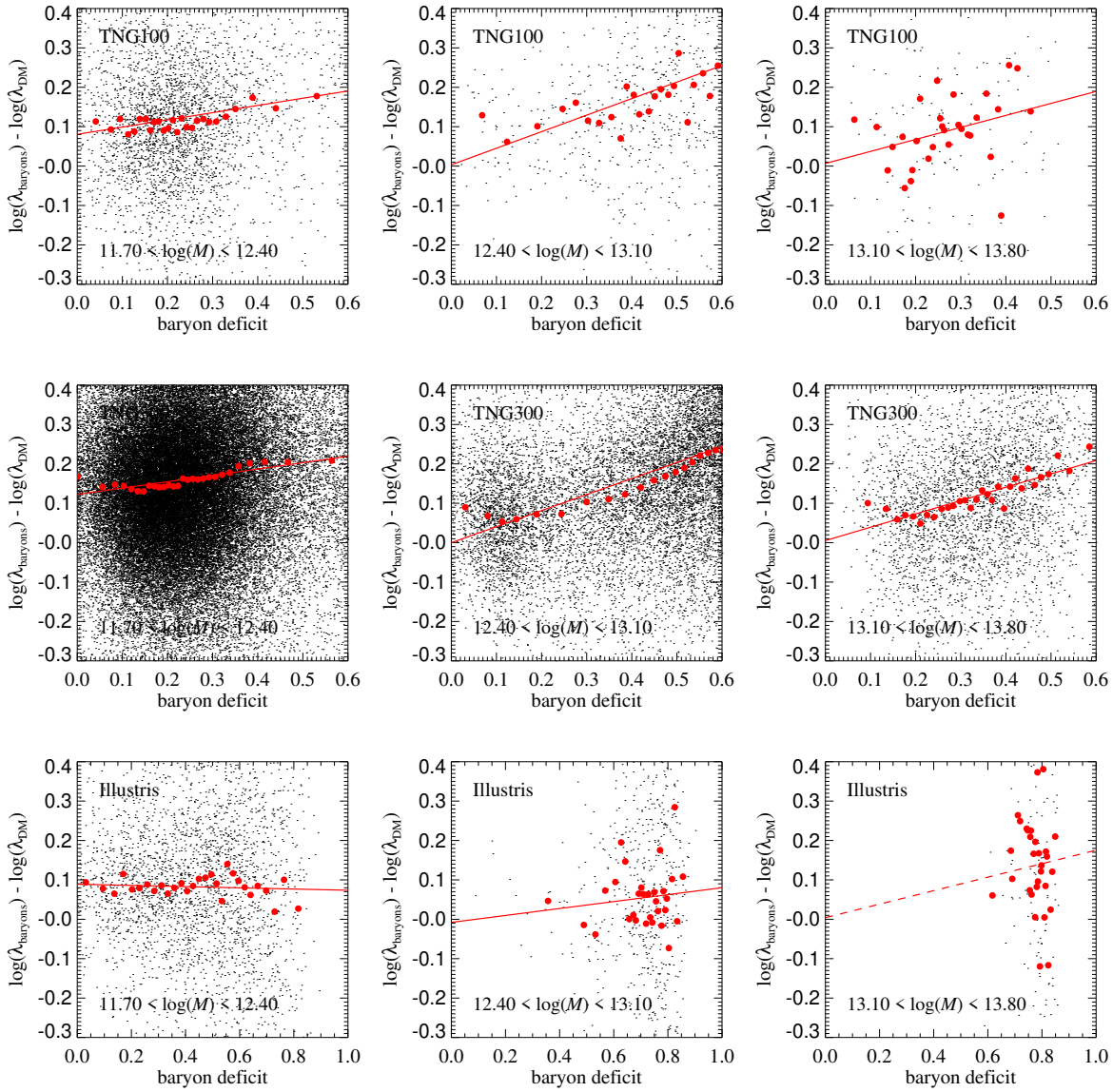


Figure 3.8: Excess of the baryonic spin parameter over the dark matter spin as a function of the baryon deficit $b$ of haloes, for different simulation models and mass bins, as labelled. The top row gives results for TNG100, the middle row for TNG300, and the bottom row for Illustris. The red circles show the median spin excess in narrow bins of baryon deficit. The solid red lines are linear regression fits to the red points, except for the bottom right panel, where the simulation data covers such a narrow range in baryon deficit that a direct fit gives an unphysical result. Instead, the dashed red line shows a fit that is forced to go through the origin of the plot. Notice that the $x$-axis range is extended for Illustris compared to the TNG simulations in order to accommodate the larger baryon losses occurring for this simulation, and that the strength of the correlation estimated for Illustris is thus noticeably weaker than for TNG.

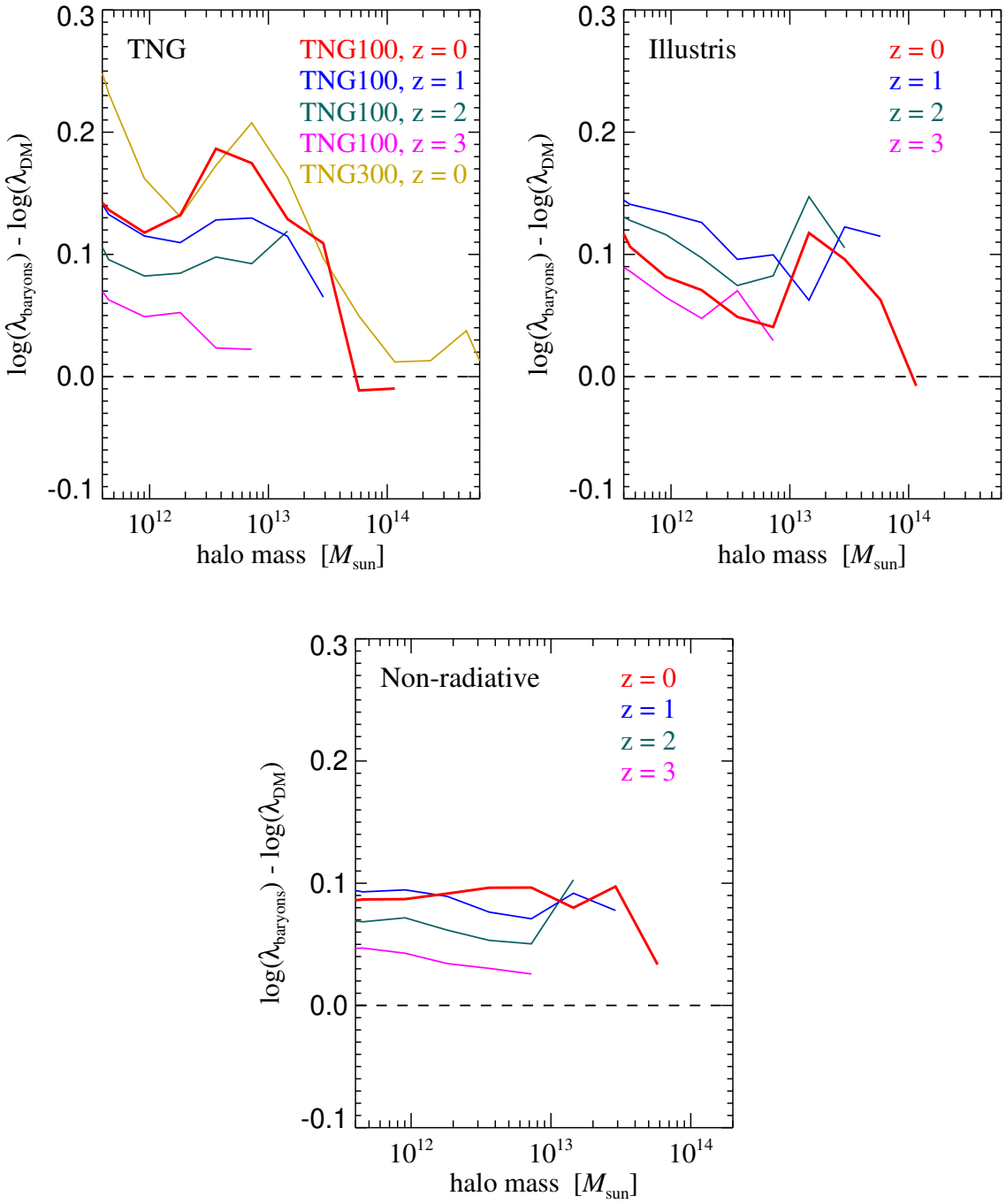


Figure 3.9: Redshift evolution of the median spin parameter excess of baryons over dark matter as a function of halo mass, for TNG (top left), Illustris (top right), and non-radiative Illustris (bottom). In the TNG case, we also include the TNG300 simulation for comparison at $z = 0$, demonstrating that these results are reliable in terms of numerical resolution. In all cases, the baryonic spin excess grows with time, starting at negligible levels at high redshift. Especially for TNG, a larger amplitude is reached than in the non-radiative simulation, highlighting that additional causes for a spin parameter increase exist. Interestingly, in Illustris, the growth of the median baryonic spin parameter excess stops at late times for the massive haloes shown here, returning to a similar level as seen in the non-radiative case.

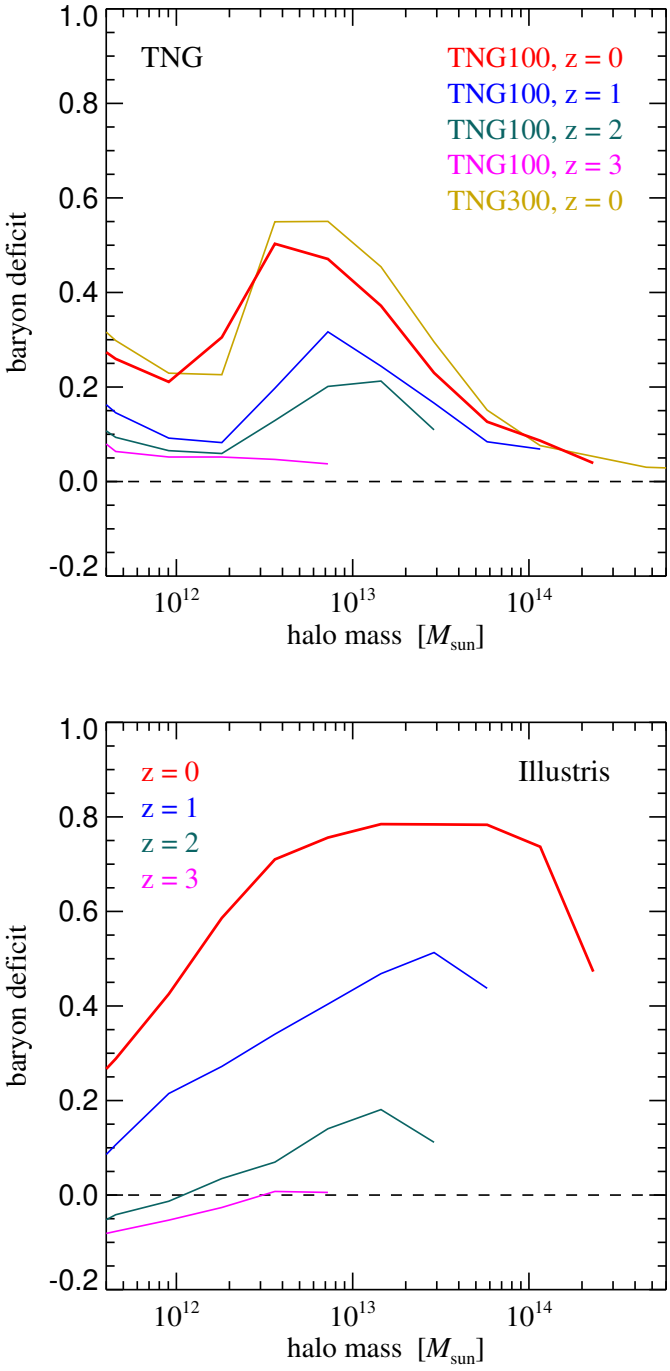


Figure 3.10: Fractional baryonic deficit at different times in the TNG (top panel) and Illustris simulations (bottom panel), as a function of halo mass. At the lowest halo masses shown here, $4 \times 10^{11}\,M_{\odot}$, the baryon loss occurs through supernova feedback and is higher in TNG than in Illustris, at least at high redshift. The TNG models show a characteristic bump in the baryon loss that occurs at late times and sets in sharply at halo masses $2-3 \times 10^{12}\,M_{\odot}$. This is clearly caused by AGN feedback. The AGN impact in Illustris is generally much stronger and more extended in halo mass.

In Illustris, the effect is harder to establish as the most massive bin essentially shows only very large baryonic losses, to the extent that a fit to the measured medians (the red data points) is not meaningful. However, forcing a fit to go through the origin returns the dashed line in this case, which is a result at least consistent with that obtained for the next lower mass bin. Still, the effect for Illustris is quite a bit smaller than for TNG.

The fact that the high-mass bump is really due to AGN can be confirmed by looking at the evolution of the spin excess and the baryonic mass loss as a function of time, seen in Figures 3.9 and 3.10, respectively. Especially for TNG, the offset in the baryonic spin coincides with strong mass loss induced by AGN. In general, we find that the amount of initial baryons expelled by haloes by $z = 0$ differs strongly between the two simulations, Illustris and TNG100, due to the different prescriptions of supernova and AGN feedback.

It is also interesting to note that while the mass loss in Illustris is considerably more extreme than in TNG, it kicks in earlier, and produces in the end a smaller spin enhancement in well-resolved haloes than in TNG. This is probably both a reflection of the different time and mass dependence of this channel, where TNG's AGN-feedback becomes more sharply active. It also reflects the different type of feedback. Whereas TNG inputs large momentum kicks at the very centre of haloes, the Illustris thermal bubble feedback simple heats gas in the surroundings of the centre, and sometimes also in the halo periphery. Thus, the TNG feedback affects the lowest angular momentum gas that is preferential in the halo centres much more directly, explaining the different behaviour we see here.

## 3.4 Discussion

The above results reveal that there are at least two effects at work that drive the enhancement of the baryonic spin content of haloes. One consists of a possible (small) transfer of spin from DM to gas as seen in non-radiative simulations. Another lies in an enhancement of the specific baryonic spin in haloes due to outflow of gas, provided the outflowing gas has a lower specific angular momentum than the average baryonic angular momentum content of the corresponding halo. The interpretation of these findings is made complicated by the high resolution requirements for obtaining quantitatively converged values for the median spin in the baryonic components. With this caveat in mind, we now discuss whether these two processes are sufficient to explain our baryonic spin measurements for the TNG simulations.

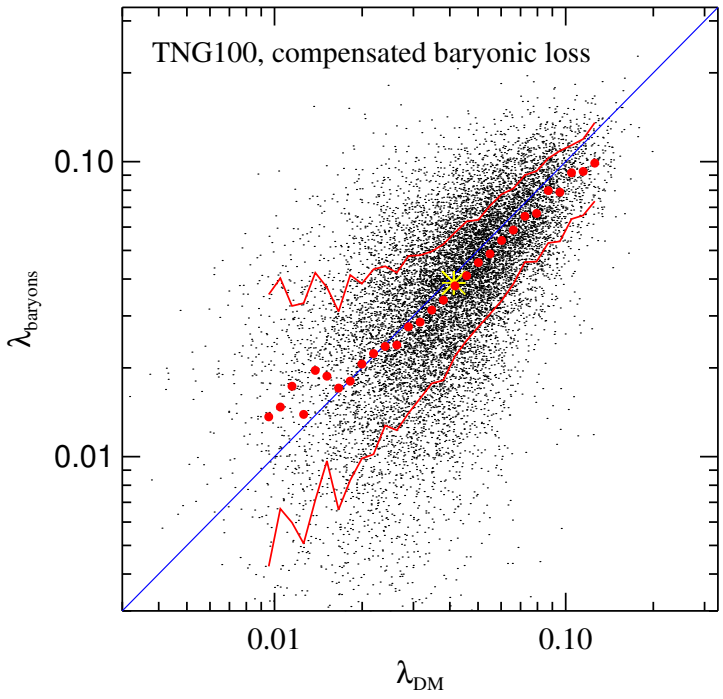


Figure 3.11: Correlation between baryonic spin parameter and dark matter spin parameter in the TNG100 simulation after the baryonic spins have been corrected for the mean relative spin increase expected for the baryon deficit measured for the corresponding halo. In addition, a constant transfer of angular momentum from dark matter to the baryons, taken to be the same as inferred for the non-radiative Illustris simulation, has been corrected for. The red points show medians of the resulting baryonic spin in narrows bins of dark matter spin, while the red lines enclose 68 percent of the corresponding distributions. The correction approximately recovers a one-to-one correlation between baryonic and dark matter spins (blue line).

### 3.4.1 Explaining the baryonic and dark matter spin offset in IllustrisTNG

We first test whether the two identified mechanisms can account for the median spin differences between the baryonic and dark matter components seen in TNG. To this extent we repeat the correction test shown in Fig. 3.7 for TNG100, but this time we also account for the median increase of the baryonic spin due to the loss of baryons. To describe the latter, we use the expression

$$\log \lambda'_{\rm baryon} = \log \lambda_{\rm baryon} + b/3, \tag{3.7}$$

which corresponds to the fitted red line in the four panels on the top right in Fig. 3.8, i.e. for haloes of size $\sim 2.5 \times 10^{12} h^{-1} \mathrm{M}_{\odot}$ and larger in TNG100 and TNG300.

The result of applying both corrections to the baryonic and dark matter spins is shown in Figure 3.11. While the resulting correlation is not perfectly consistent with a one-to-one relation, we consider it actually surprisingly good, suggesting that this simple model captures the bulk of the effects that introduce the offsets in the first place.

### 3.4.2 Relating spin enhancement to the expected mean spin distribution within haloes

We now turn to checking whether such a spin increase is at all plausible for the given size of the mass loss. To this end we examine this picture with an analytical estimate for the expected baryonic spin. We can calculate an estimate for the enhancement of baryonic spin in the whole halo population by making use of the universal angular momentum profile for the distribution of specific angular momentum inside a halo:

$$M(< j_{\rm sp}) = M_{\rm tot} \frac{\mu\, j_{\rm sp}}{j_0 + j_{\rm sp}}, \tag{3.8}$$

where $j_{\rm sp}$ is the specific angular momentum of matter projected onto the rotation axis of the halo, $M(< j_{\rm sp})$ the cumulative mass of matter with specific angular momentum smaller than a given value $j_{\rm sp}$, and $M_{\rm tot}$ the total halo mass. The universal angular momentum profile was originally derived by Bullock et al. (2001) for dark matter only haloes, however in Zjupa and Springel (2017) we have shown that it is also valid for the gas distribution at high redshift before feedback physics starts to mix and redistribute the gas in haloes.

The two fitting parameters $\mu$ and $j_0$ are not independent of each other. Defining $m = M(< j_{\rm sp})/M_{\rm tot}$ one can rewrite Eq. (3.8) as

$$j_{\rm sp}(m) = \frac{m\, j_0}{\mu - m}, \tag{3.9}$$

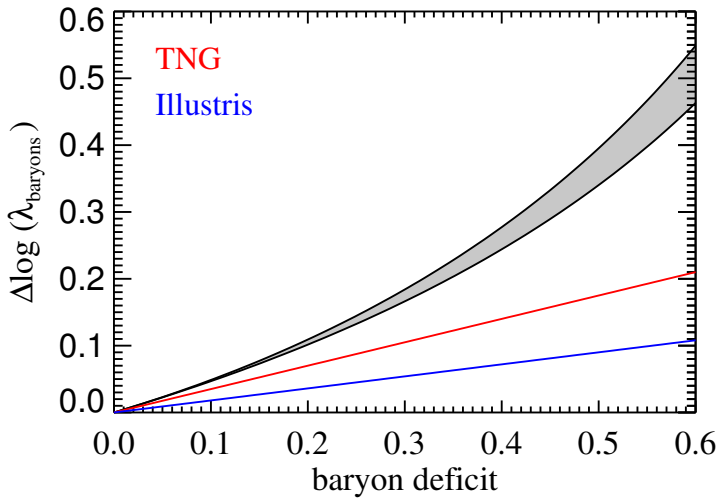


Figure 3.12: Analytic prediction (grey shaded area) for the baryonic spin parameter enhancement of haloes as a function of their baryonic deficit, under the assumptions that the expelled gas consists of baryons with the lowest specific angular momentum in the halo, and that the universal angular momentum profile of Bullock et al. (2001) provides a good description of the internal spin distribution within haloes. The boundaries of the grey region correspond to the typical range of the shape parameter inferred for this distribution from collisionless cosmological simulations. For comparison, the red and blue lines show the measured correlations of spin enhancement as a function of baryonic loss for the TNG and Illustris simulations, as labelled.

such that the universal angular momentum profile can be reduced to a one parameter function where the two fitting parameters $\mu$ and $j_0$ are related by

$$j_{\rm sp}^{\rm tot} = j_0 \int_0^1 \frac{m}{\mu - m} {\rm d}m = j_0 \left[-\mu \ \ln(1 - 1/\mu) - 1\right], \tag{3.10}$$

where $j_{\rm sp}^{\rm tot}$ is the absolute value of the total specific angular momentum of the halo subset considered, and $\mu > 1$. If a given fraction $f$ of the total initial gas content with lowest angular momentum is expelled from the halo the resulting specific angular momentum $j_{\rm sp,f}$ can be calculated as:

$$\begin{aligned} j_{\rm sp,f} &= \frac{j_0}{(1-f)} \int_f^1 \frac{m}{\mu - m} {\rm d}m \\ &= \frac{j_0}{(1-f)} \left[-\mu \ \ln\left(\frac{\mu - 1}{\mu - f}\right) - (1-f)\right]. \end{aligned} \tag{3.11}$$

The factor $1/(1-f)$ is introduced to account for the fact that the specific angular momentum $j_{\rm sp,f}$ is now obtained from the remaining baryons which have a reduced mass of $(1-f)M_{\rm tot}$ compared to the initial mass of the baryonic component.

Given this we can make a prediction for the spin enhancement of the baryonic component as a function of the expelled low angular momentum gas fraction $f$. Thereby we have to take into account that the shape parameter $\mu$ varies in haloes, with 90% of the haloes falling into a shape parameter range of $\mu \in [1.06, 2]$ (Bullock et al., 2001). These two limiting values yield an approximate upper and a lower limit for the maximum baryonic spin enhancement $j_{\rm sp,f}/j_{\rm sp}$.

In Figure 3.12, we show the spin enhancement resulting from this estimate based on the (Bullock et al., 2001) profile. The grey shaded area indicates the expected range for the maximum baryonic spin enhancement due to different shape parameters $\mu$. This assumes that the expelled baryonic mass is given by the lowest specific angular momentum tail of the internal spin distribution, thus representing the upper envelope of what is possible through this mechanism. We note that there is also a corresponding lower envelope (not shown) that would correspond to the case that the highest angular momentum material is ejected. This is not realised in any of our models, rather we see a spin enhancement, as shown earlier. In fact, the TNG and Illustris spin enhancements as measured in Figure 3.8 lie well within the envelope, which is reassuring. However, as they are only moderately smaller than the maximum, the feedback is indeed relatively selective in removing preferentially low angular momentum material.

In Zjupa and Springel (2017) we had already speculated that the Illustris results are consistent with the assumption that the feedback expels strictly the lowest angular momentum gas from haloes. However, this conclusion was based on a much less restrictive mass cut, and hence dominated by low mass haloes which are not fully converged with respect to their baryonic spin, as our refined analysis in this paper shows.

### 3.4.3 TNG model variations

In order to confirm the above interpretations, at least qualitatively, we finally look at some model variations of TNG stemming from the TNG-model test suite discussed in Pillepich et al. (2018). These simulations have $2 \times 512^3$ resolution elements and were run in a small box of $25\,h^{-1}$Mpc size, given them a bit lower resolution than TNG100. They are seriously hampered in statistical power but can still give important clues about the relative impact of different aspects of the physics model.

In Figure 3.13, we show a sample of such model variations, focusing on the mass dependence of the spin enhancement (top panel), and the mass dependence of the corresponding baryonic mass loss (bottom panel). We compare the default TNG physics models with a scenario where all black hole modelling is disabled, and with simulations that employ either faster or slower galactic winds, with factor of two modifications in the wind speed but compensating changes in the mass loading such that the overall energetics remained unchanged. The faster wind model means that supernova winds can unbind more gas, whereas the slower winds substantially slow star formation in haloes, but without being able to permanently expel baryons.

The results of Fig. 3.13 confirm the basic expectations for these model changes. The slow wind model does not produce much baryon loss, which in turn causes the AGN feedback to kick in all the more strongly as more gas is left when it becomes active. In contrast, the faster wind causes larger baryon loss already in low mass haloes. The no-BH model on the other hand shows no distinctive increase in the spin enhancement at the mass scale where the AGN normally kick in. These test runs hence confirm the general connections between baryonic mass loss and baryonic spin enhancement identified for the TNG and Illustris simulations.

## 3.5 Summary and conclusions

In this paper, we have employed two hydrodynamical simulation sets with different models for galaxy formation and feedback physics, IllustrisTNG and Illustris, to accurately characterise the specific angular momentum content in different halo components as a function of halo

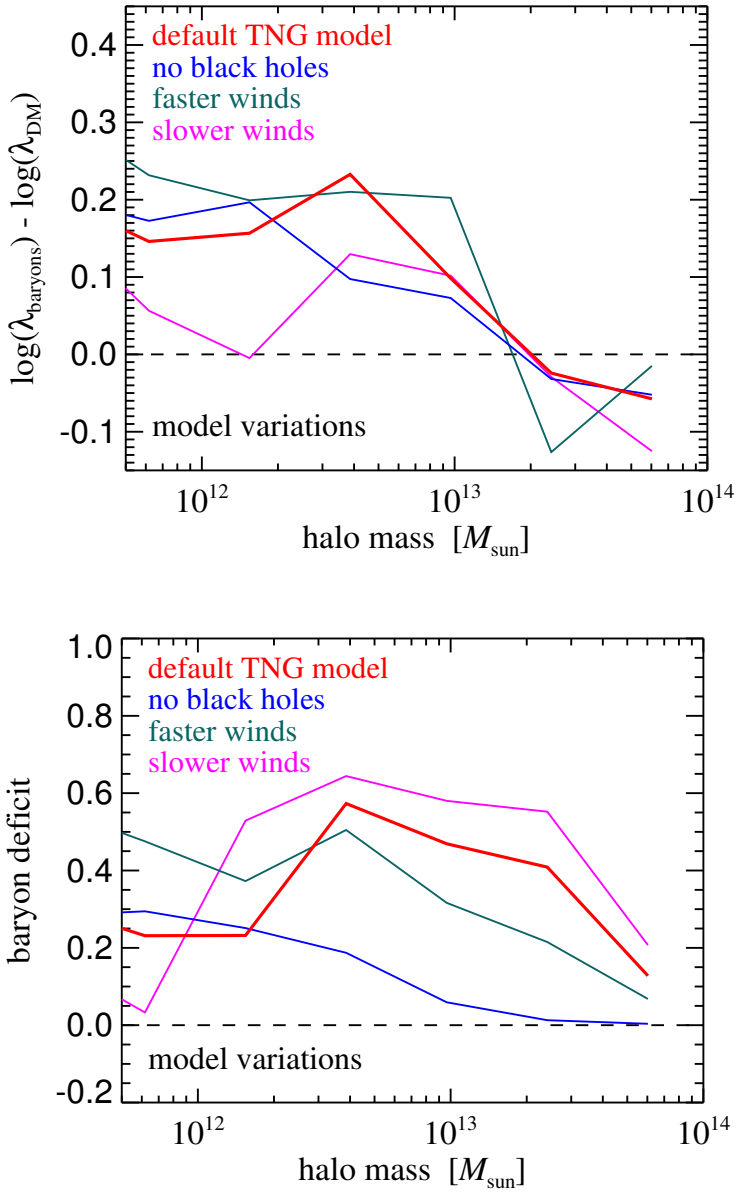


Figure 3.13: Baryonic spin excess (top panel) and baryonic mass loss (bottom panel) as a function of halo mass, for a number of TNG model variations, as labelled. The simulations shown here are comparatively small $2 \times 256^3$ runs in a $25\,h^{-1}$Mpc box, and were done as part of the original test suite when developing the TNG model. The final TNG parameterisation of the physics (shown in red) is here compared to a corresponding model where the black hole modelling was disabled (blue). In the simulations labelled 'faster wind' and 'slower wind', the wind parameterisation was changed instead, making them twice as fast (but with lower mass loading to keep the kinetic energy flux in the winds fixed), or twice slower (at higher mass flux).

mass. A particular focus of our analysis has been on studying the enhancement of the baryonic spin with respect to the dark matter spin in haloes hosting a realistic galaxy population arising through strong feedback processes, and to identify some of the mechanisms responsible for regulating the angular momentum content of the corresponding haloes.

Most of the angular momentum of haloes is expected to be imparted before turnaround through tidal torques from the large scale gravitational field on the gas and the dark matter that make up a forming halo. In this process, the gas is expected to acquire a very similar initial specific angular momentum than the dark matter. During the subsequent non-linear evolution of haloes, the spin content of the halo components can be potentially modified, in particular through merger processes, or the expulsion of some of the baryons. Whether any of these processes is really important can be best answered with full hydrodynamical simulations of cosmic structure formation.

For non-radiative simulations we find consistent spins between baryons and dark matter at high redshift, but with time a small offset between these two components develops. We interpret this as a small but systematic angular momentum transfer from the dark matter to the gas, possibly mediated by mergers or pressure effects. For redshift $z = 0$, a transfer of a fixed amount of angular momentum from dark matter to the gas, independent of the size of the dark matter spin parameter itself, can explain the distortion in the spin distributions of these two components. At the median spins, this transfer amounts to a lowering of the dark matter spin by about 3.5 percent, and a corresponding increase of the baryonic spin by about 26 percent, keeping the total spin content of the haloes invariant. In non-radiative simulations, this can thus explain why the gas spin within haloes is on average a factor of $\sim 1.3$ larger than the dark matter spin (see also Chen et al., 2003, Sharma and Steinmetz, 2005, Gottlöber and Yepes, 2007).

For the full physics simulations TNG and Illustris, considerably larger enhancements of the baryonic spin are however observed. We have shown that these spin enhancements correlate with the amount of baryons lost by feedback processes. This correlation is particularly strong for the halo mass regime affected by AGN feedback, whereas it is weak or absent for haloes affected by mass loss due to galactic winds. We explain the spin enhancement by the preferential removal of low angular momentum gas from haloes due to AGN feedback, a process that works particularly well for the TNG black hole feedback model, as it directly couples to the very central gas in haloes. In Illustris, the AGN feedback expels even more gas mass, but the feedback couples also to gas components in outer halo regions, reducing its ability to selectively affect the gas with the lowest specific angular momentum. Consequently, we measure a lower baryonic spin increase in Illustris than in TNG as a function of the baryonic deficit of haloes. The strength of this spin enhancement is lower than the maximum

possible if strictly the lowest angular momentum gas was expelled, but it is still comparable to this upper envelope, highlighting that the lost gas has indeed substantially lower mean specific spin than the full halo.

Supernova-driven outflows arising from the galactic wind model employed by the simulations appear less capable in selectively removing low angular momentum gas. Rather, individual outflow events can remove gas of both low and high angular momentum. However, as these effects take place in haloes that are not particularly well resolved, this behaviour needs to be checked with higher resolution simulations. This cautionary remark is based on a convergence study for the mean spins of the different baryonic components, where we have shown that much higher numerical resolution than for the dark matter is required to measure the corresponding baryonic spin values in a quantitatively robust way.

We conclude that the baryonic spin content of haloes hosting galaxy populations with realistic stellar masses and morphologies is globally regulated mainly by two processes. The first on is a transfer of angular momentum from dark matter to gas during halo assembly, the second is the preferential removal of low angular momentum gas from haloes by their central black hole. The two mechanisms in combination can explain the overall amount of angular momentum that is measured in the baryonic component of IllustisTNG haloes, and can thus be identified as crucial mechanisms regulating the baryonic spin available for the forming galaxy population. Given that these processes of spin evolution depend on the detailed feedback parameterisation, as our comparison between TNG and Illustris has shown, we have also identified an interesting connection between baryonic spin parameter, halo gas content, and ultimately galaxy sizes, which perhaps can be fruitfully used to constrain the feedback models themselves.

## Acknowledgments

JZ would like to thank Frank van den Bosch for useful comments. JZ and VS acknowledge financial support from the Deutsche Forschungsgemeinschaft through Transregio 33, “The Dark Universe”, and through the Klaus Tschira Foundation. VS also acknowledges support through the European Research Council under ERC-StG grant EXAGAL-308037. Some of the computations were performed on the HazelHen supercomputer at the High-Performance Computing Center Stuttgart (HLRS) as part of project GCS-ILLU of the Gauss Centre for Supercomputing (GCS). JZ acknowledges support from International Max-Planck Research School for Astronomy and Cosmic Physics at the University of Heidelberg (IMPRS-HD).

# Chapter 4

# The impact of feedback driven galactic outflows on the Lyman-$\alpha$ absorption properties of diffuse gas

# Abstract

Galaxies expel a large fraction of their gas through feedback driven galactic outflows that partially reach and perturb the IGM. However, large-scale cosmological hydrodynamical simulations incorporating both supernovae and AGN feedback as drivers of galactic outflows and yielding a realistic galaxy population have thus far been missing. In order to investigate the impact of outflows on the state of the IGM in the most clean way, we have run a suite of simulations of varying boxsize both with the presently most complete set of galaxy formation physics as realised in the IllustrisTNG (TNG) model, as well as with the Quick Lyman-$\alpha$ (QLA) technique we implemented in the moving-mesh code AREPO, yielding an unperturbed IGM. We use our simulation suite alongside the TNG100 simulation to investigate changes in the statistical properties of the IGM introduced by galactic outflows. We find a larger volume fraction of the IGM at densities around the cosmic mean to be at temperatures of $10^{4.5} - 10^{5.5}$K, and thus exhibiting a smaller neutral hydrogen fraction, leading to less Lyman-$\alpha$ absorption. Though we detect no significant difference between the flux PDF of perturbed and unperturbed gas, we find the Lyman-$\alpha$ flux power spectrum of the perturbed gas to exhibit $\sim 10\%$ more power at large scales at $z = 3$, and up to $\sim 20\%$ more at $z = 2$, relative to the unperturbed power spectrum, whereas a similar amount of power is lacking at small scales below a characteristic transition scale. We further investigate the role of quasar-hosting and star-forming galaxies at centres of haloes in changing the state of the surrounding gas out to $\sim 3$ Mpc. Interestingly, there are significant differences in the excess Lyman-$\alpha$ absorption as a function of impact parameter depending on the galaxy properties, which can be largely explained by the higher temperature of the perturbed gas around galaxies with strong feedback.

## 4.1 Introduction

During their evolution galaxies expel a large fraction of their gas through feedback driven galactic outflows. The hot and metal-enriched gas penetrates both the circum galactic medium (CGM) as well as the inter-galactic medium (IGM) changing the state of the diffuse cosmic gas. Major observational efforts have been undertaken in the past decades to map out the statistical properties of the IGM using the Lyman-$\alpha$ forest.

The prime quantities of interest are the Lyman-$\alpha$ effective optical depth and the mean transmitted flux that are used to put constraints on the thermal and ionisation state of the IGM. Early measurements of seven high resolution quasar spectra in the redshift range $2.5 < z < 5$ observed with the Keck telescope were used by Rauch et al. (1997) to derive the flux decrement distribution function (FDDF) and to put constraints on the temperature of the IGM. Schaye et al. (2000) have used nine high-resolution, high signal-to-noise quasar spectra obtained with the HIRES spectrograph (Vogt et al. 1994) on the Keck telescope and with the UCL echelle spectrograph of the Anglo Australian Telescope to measure the evolution of the effective optical depth in the redshift range $2 < z < 4.5$. Kim et al. (2007) measured the evolution of the effective optical depth in the redshift range $1.7 < z < 4$ based on 18 high-resolution, high signal-to-noise quasar spectra obtained with UVES on VLT, as well as based on a large compilation of observational data from the literature, and present the Lyman-$\alpha$ flux probability distribution function (PDF) for three redshifts in the redshift range $2 \lesssim z \lesssim 3$. Faucher-Giguère et al. (2008) employed 86 high-resolution, high signal-to-noise quasar spectra observed with the ESI and HIRES spectrographs on Keck, and with the MIKE spectrograph on Magellan to measure the evolution of the Lyman-$\alpha$ effective optical depth in the redshift range $2 < z < 4.2$. Becker et al. (2013) measured the Lyman-$\alpha$ mean transmitted flux using 6065 quasar spectra from the Sloan Digital Sky Survey DR7 in the redshift range $2 < z < 5$ confirming a gradual evolution of the ionisation and thermal state of the IGM. The resulting mean flux was used by Becker and Bolton (2013) together with temperature measurements from Becker et al. (2011) to constrain the intensity of the ionising UV background and highlight the contribution from star-forming galaxies. In the upcoming decade, these studies will be carried to the next level with larger statistical samples yielding more precise results based on large quasar surveys such as WEAVE and DESI.

Besides the flux decrement distribution function, or equivalently the flux PDF, the other major (and more sensitive) statistics providing insight in the distribution and state of the diffuse gas on large scales is the Lyman-$\alpha$ flux power spectrum. Croft et al. (1999) first used the Lyman-$\alpha$ forest observed in 19 quasar spectra to measure the one-dimensional matter power spectrum from Lyman-$\alpha$ absorption at $z = 2.5$ with statistical errors of $\sim 20\%$ due to limited sample size. This was followed by similar work by McDonald et al. (2000),

Croft et al. (2002), Kim et al. (2004), and Viel et al. (2004), each limited to a few dozen spectra. The statistical errors on the power spectrum measured from the transmitted flux in the Lyman-$\alpha$ forest could for the first time be pushed below 1% by McDonald et al. (2006) who obtained 3035 high-redshift ($z > 2.3$) quasar spectra from SDSS. Palanque-Delabrouille et al. (2013) employed two independent methods to derive the one-dimensional Lyman-$\alpha$ transmitted flux powerspectrum from 13 821 high quality, high signal-to-noise quasar spectra from SDSS-III/BOSS DR9 in the redshift range $2.2 < z < 4.4$, improving the precision of the measurement by another factor of 2-3.

To better understand the significance of galactic outflows in changing the properties of the cosmic gas with respect to its primordial state, studies of the statistical properties of the IGM have been complemented by observations of lines of sight towards background quasars which intersect the gas immediately surrounding foreground galaxies and foreground quasars, probing their impact on the directly adjacent gas. The first background quasar spectrum in close projection of only 108 kpc transverse distance from a foreground quasar at $z \approx 2.436$ was obtained by Prochaska and Hennawi (2009) with the HIRES spectrograph on Keck, who found a large excess of cold $T \sim 10^4$K gas mass causing excess Lyman-$\alpha$ absorption in the obtained spectrum. Prochaska et al. (2013b) extended this analysis to a statistical sample of 74 quasar pairs taken from Hennawi et al. (2006), who obtained 149 moderate resolution background quasar spectra from Gemini, Keck, MMT, and SDSS at close separations from foreground quasars in the redshift range $1.8 < z < 4.0$, to investigate the CGM of the foreground quasar. Those authors find a large gas mass of $M_{\rm CGM} > 10^{10}\,{\rm M}_\odot$ of cold $T \sim 10^4\,{\rm K}$ and metal-enriched $z > 0.1\,z_\odot$ gas extending to at least the virial radius of the foreground quasar hosting halo. Such systems are expected to evolve into massive elliptical (red and dead) galaxies at $z = 0$. Mapping the properties of gas around high redshift quasars can thus provide significant insight into galaxy evolution processes.

Rakic et al. (2012) employed background quasar spectra from the Keck Baryonic Structure Survey (KBSS) to probe the gaseous environments around 679 star-forming galaxies at $z \approx 2.4$ with transverse separations from the line of sight to the background quasar out to 2 Mpc. The large statistical size of their sample allows the authors to investigate the Lyman-$\alpha$ absorption due to neutral hydrogen as a function of distance from the galaxy centre. Rudie et al. (2012) extend this analysis to 886 star-forming galaxies from KBSS in the redshift range $2 \lesssim z \lesssim 2.8$ with transverse separations from background quasars sightlines out to 3 Mpc, equally to Rakic et al. (2012) finding significant excess Lyman-$\alpha$ absorption out to at least 2 Mpc.

Separating galaxies into star-forming and quasar-hosting allows to independently investigate the impact of supernovae winds and AGN feedback driven outflows on the properties

of the gas immediately surrounding the galaxy, as well as on the statistical properties of the IGM. Theoretically, this distinction can for example be made by using the observation that star-forming galaxies with dominant supernovae driven winds usually reside in haloes of mass below $\sim 10^{12}$ $M_\odot$, where supernovae driven winds can propagate further outwards with decreasing halo mass due to shallower gravitational potentials. Galaxies residing in haloes with halo mass above $\sim 10^{12}$ $M_\odot$ will typically host an AGN that during active phases is observed as a quasar outshining the whole galaxy and (presumably) driving large scale outflows.

First theoretical attempts to investigate the significance of outflows by probing the excess Lyman-$\alpha$ absorption in the Lyman-$\alpha$ forest as a function of impact parameter were undertaken by Meiksin et al. (2017) employing the Sherwood simulations. The Sherwood simulation suite (Bolton et al., 2017) contains a variety of boxsizes with different resolutions and different physics models, including feedback from supernovae driven winds but lacking a model for AGN feedback driving large scale outflows, run to $z = 2$ with the SPH code P-Gadget3 (Springel, 2005) and aimed at investigating the Lyman-$\alpha$ forest properties in the redshift range $2 < z < 5$. Meiksin et al. (2017) show that while galactic winds driven by supernovae explosions can well explain the excess Lyman-$\alpha$ absorption around star-forming galaxies, this is not true for the excess absorption around quasars. The excess Lyman-$\alpha$ absorption around quasars measured by Prochaska et al. (2013a) is significantly larger towards the halo centre than the Sherwood predictions, emphasising the need and importance of AGN feedback for understanding the state of the gas around massive galaxies and of the diffuse gas in the IGM.

The study presented here is novel in two aspects. First, we for the first time investigate both the statistical properties of the IGM as well as the signatures of outflows as a function of impact parameter including both supernovae and AGN feedback yielding a realistic galaxy population in a large volume. To this end we compute a suite of simulations of varying boxsize with both the model of galaxy formation physics including supernovae and AGN feedback as realized in the IllustrisTNG (TNG) model, as well as the Quick Lyman-$\alpha$ (QLA) technique that we have implemented in the moving-mesh code AREPO yielding an unperturbed IGM. This allows us to compare the properties of the diffuse gas arising in a universe with active galaxy evolution and feedback with respect to their unperturbed state in the most clean way. Second, using the TNG100 simulation form the IllustrisTNG simulation suite (see Pillepich et al., 2018), we are able to extend our analysis up to halo masses of $\sim 10^{13.5}\,M_\odot$ thanks to the large cosmological volume of $75\,h^{-1}$Mpc covered by TNG100 and its good statistics up to this halo mass, whereas the previous study by Meiksin et al. (2017) was limited to halo masses of $\sim 10^{12}\,M_\odot$. Covering this extended halo mass range is

of special importance, as only haloes of mass above $\sim 10^{12}\,\mathrm{M}_{\odot}$ tend to host AGN at their centres that are responsible for initiating major feedback mechanisms that cause galaxy quenching and a significant change of the state of the cosmic gas.

We structure the rest of this study as follows. First, we provide a description of how we extract synthetic Lyman-$\alpha$ absorption spectra from the simulation output in Section 4.2.1, and how we calibrate the mean Lyman-$\alpha$ absorption to observational measurements in 4.2.2. In Section 4.2.3 we present the Quick Lyman-$\alpha$ (QLA) technique that we have implemented in AREPO to simulate an unperturbed IGM and present our suite of simulations with the QLA model as well as including galaxy evolution physics and galactic feedback in Section 4.2.4. Comparing those two types of simulations, we show in Section 4.3 how and to what extent galactic outflows impact the statistical properties of the IGM. In Section 4.4, we then investigate the role of individual haloes with star-forming and quasar-hosting galaxies at their centres in driving large scale outflows that cause the observed impact. We summarise and conclude in Section 4.5. Finally, we discuss numerical convergence properties of our approach in Section 4.6.

## 4.2 Methodology

### 4.2.1 Extracting Lyman-$\alpha$ forest spectra

We probe the properties of the IGM as they arise in the different physical models through synthetic Lyman-$\alpha$ absorption spectra that are derived from the simulation output. This is achieved by means of a line of sight generating code originally written by Volker Springel for the SPH code GADGET. This code drives random lines through the simulation box whereas each absorption spectrum is subdivided into a given number of pixel $n_{\mathrm{pix}}$. All gas cells whose smoothing radius intersects with a pixel contribute with their properties to this pixel in a weighted fashion. Provided the density of neutral hydrogen, the gas temperature and gas velocity this code calculates in a self-consistent way the optical depth $\tau$ taking into account the thermal broadening of the absorption lines and the kinematic Doppler shift.

In detail the code proceeds as follows. An absorbing cloud of neutral hydrogen with column density $N_{\mathrm{HI}}$ that is narrow and at rest along the line of sight creates an absorption profile

$$\tau(v) = \sigma_{\alpha}(v) N_{\mathrm{HI}}, \tag{4.1}$$

where the shape of the line can be written as

$$\sigma_\alpha(v) = \sigma_0 \frac{c}{\sqrt{\pi}\, b} \exp\left(-\frac{v^2}{b^2}\right) \tag{4.2}$$

(Miralda-Escude and Rees, 1993), with the velocity relative to the line centre $v$, the speed of light $c$, and the width of the Gaussian $b$. The cross-section $\sigma_0$ is given by

$$\sigma_0 = f\lambda_0 \left(\frac{3\pi\sigma_T}{8}\right)^{1/2}, \tag{4.3}$$

where $f$ is the oscillator strength, $\lambda_0$ the Lyman-alpha wavelength, and $\sigma_T$ the Thomson cross-section. Note that

$$\int \sigma_\alpha(v)\, \mathrm{d}v = \sigma_0 c, \tag{4.4}$$

independent of $b$. If the line-shape is dominated by thermal broadening, the width of the line is determined by the one-dimensional velocity dispersion $\sigma_v$ of the absorbing gas, such that

$$b^2 = 2\sigma_v^2. \tag{4.5}$$

The velocity dispersion follows from thermal equilibrium, i.e.

$$\frac{3}{2}kT = \frac{1}{2}m_H(\sigma_v^2 + \sigma_v^2 + \sigma_v^2), \tag{4.6}$$

and hence

$$b = \left(\frac{2kT}{m_\mathrm{H}}\right)^{1/2}. \tag{4.7}$$

The absorption from multiple absorbers along the line of sight in a periodic simulation box of comoving size $L_\mathrm{com}$ at redshift $z$ is then calculated as follows. The distances along the box are mapped into velocity space through

$$v = v_\mathrm{rec} + \frac{x}{L_\mathrm{com}} v_\mathrm{max}, \tag{4.8}$$

where $v_\mathrm{max} = H \cdot a \cdot L_\mathrm{com}$ is the velocity width of the box at given redshift, $v_\mathrm{rec}$ the recession velocity at that redshift, $H(a)$ the Hubble constant, and $a = 1/(1+z)$. If we have a continuous hydrogen distribution along the line of sight, with comoving number density $n_\mathrm{H}(x)$ and peculiar velocity $v_\mathrm{pec}(x)$, the optical depth at a comoving position $x$ in the box is given by

summing over all the absorbers in the box,

$$\tau(x) = \int_0^{L_{\rm com}} \frac{n_{\rm HI}}{a^2}\,\sigma_0\,\frac{c}{\pi^{1/2}\,b(y)}\exp\left[-\frac{[v_{\rm pec}(y) - \frac{(x-y)^\star}{L_{\rm com}}v_{\rm max}]^2}{b^2(y)}\right]{\rm d}y. \tag{4.9}$$

Here the $()^\star$-distance refers to the nearest periodic image. The absorption line code computes this integral after pixelizing the sightline through the box as a sum, with $x$ and $y$ effectively becoming pixel-indices. The optical depth is then converted to the Lyman-$\alpha$ transmitted flux via $F = e^{-\tau}$.

For this study, we have updated and extended this sightline generating code such that it can derive synthetic spectra at predefined coordinates. In this way the Lyman-$\alpha$ forest spectra generated by the code can be used to probe specific environments and column densities. We will use the code in this mode to study the impact of outflows on the Lyman-$\alpha$ absorption at different impact parameters from galaxy centres. This approach uses Lyman-$\alpha$ absorption to examine the physical extent of galactic outflows. To this end, we have extended the absorption line generating code to also run on simulation output files in HDF5 format allowing it to be directly applied to the latest generation of hydrodynamical simulations. Furthermore, we have restructured this code to run with a parameter file in a similar manner as is done in AREPO, which besides other smaller changes highly facilitates the usability of the absorption spectra generating code for our and for future studies.

### 4.2.2 Adjusting the mean flux to the observed effective optical depth

In order to compare statistical properties of the Lyman-$\alpha$ forest to observational results, it is necessary to first adjust the mean flux measured in the simulation output to the observed value. An offset between the observed mean flux and the one measured in simulations is a common issue that arises due to the poorly constrained UV background that is included in simulations as a time-varying but spatially constant heating source. Poor constraints on the amplitude, shape, and time evolution of the UV background yield a discrepancy in the specific intensity of the UV background at any point in time that translates into a altered background neutral hydrogen density and thus an offset in the Lyman-$\alpha$ optical depth and mean flux. Fortunately, it is possible to accommodate for this discrepancy in post processing by rescaling the effective optical depth $\tau_{\rm HI}^{\rm eff}$ to yield the observed mean flux. Lukić et al. (2015) have performed two otherwise identical test runs with different UV backgrounds taken from Haardt and Madau (1996) and Faucher-Giguère et al. (2009), and have shown that a constant rescaling of the mean flux of one of the simulation to the other, results into

Lyman-$\alpha$ statistics such as the flux PDF and the one-dimensional flux power spectrum (see next section) being converged within a few percent.

Several measurements of the mean flux or equivalently the effective optical depth at various redshift ranges exist in literature (e.g. Kim et al., 2007, Faucher-Giguère et al., 2008, Calura et al., 2012, Becker et al., 2013). For our study we chose to calibrate the effective optical depth to the measurements by Kim et al. (2007), as those cover the full redshift range of interest in our study and provide in addition observational measurements of the flux PDF in this redshift range that we can directly compare to our results. Furthermore, Kim et al. (2007) derive a 'general' fit to the evolution of the effective optical depth based on observational data derived in their study as well as taken from McDonald et al. (2000), Schaye et al. (2003), Tytler et al. (2004), Kirkman et al. (2005), and Janknecht et al. (2006) that is given by

$$\tau_{\rm HI}^{\rm eff} = (0.0023 \pm 0.0007)(1+z)^{(3.65\pm0.21)}. \tag{4.10}$$

We use this power-law fit to determine a target effective optical depth at each redshift. In every random sample of Lyman-$\alpha$ lines of sight we iteratively solve for a calibration factor $f_c$ that yields $< e^{\tau/f_c} >= e^{\tau_{\rm HI}^{\rm eff}}$ using all pixel of all spectra, and apply the final $f_c$ to rescale the optical depth in every pixel. We use this calibration procedure for all results presented throughout this chapter.

### 4.2.3 Quick Lyman-$\alpha$ technique

In order to investigate the impact galactic outflows have on the IGM, we have implemented the most commonly used numerical approach to simulate the unperturbed IGM, the so called *Quick Lyman-$\alpha$* technique, as a separate module in AREPO. The Quick Lyman-$\alpha$ approach reduces the physics applied to the gas to cooling and star formation, making this ansatz computationally way less expensive than a full hydrodynamical simulation of the same size, to the cost of not having realistic galaxies and correspondingly no feedback. The emerging properties of the diffuse gas on large scales however are considered to be little affected. However, the validity of this belief has not been rigorously tested so far, a task we want to undertake in this study.

The Quick Lyman-$\alpha$ technique, omitting any more sophisticated galaxy formation physics, simply crudely converts all gas particles or cells above an overdensity threshold and below a temperature threshold into star particles. Both parameters can be provided to the code. We adopt an overdensity threshold of 1000 times the critical density $\rho_{crit}$ (which is well within gravitationally self-bound haloes commonly defined by $200 \cdot \rho_{crit}$), and no

temperature threshold. The later is in contrast to e.g. Bolton et al. (2017) who adopt a temperature threshold of $10^5 K$. However, inspecting the temperature-density relation of all gas elements (in TNG-2, see next section) we have found the fraction of gas cells in the whole simulation volume with temperature above $10^5 K$ and densities below $1000 \cdot \rho_{crit}$ to be negligible, such that the results of the simulation will not depend on adopting this temperature threshold. Nevertheless, we have implemented a temperature threshold into the Quick Lyman-$\alpha$ module that can be set to this or any other chosen value in order to keep the module as flexible as possible for future use.

Furthermore, we have implemented the Quick Lyman-$\alpha$ module in AREPO in a way that allows the user to run a comparison simulation with Quick Lyman-$\alpha$ module to a simulation with more sophisticated physics employed in the easiest way possible without having to touch the configuration of the original simulation. To achieve that the Quick Lyman-$\alpha$ module replaces solely the starformation routine within AREPO to the above prescription. All additional physics has to be disabled additionally by setting the governing parameters of those physical models to values disabling these physics. For the current state of AREPO galactic winds are disabled by setting the wind energy to zero, black holes formation and emerging AGN feedback is disabled by setting the minimum friends-of-friends halo mass in which a black hole seed is inserted to any value significantly above the largest cluster mass at $z = 0$, and finally magnetic fields are disabled by setting the initial field strength to zero. We explicitly list the changes necessary to run AREPO with Quick Lyman-$\alpha$ to facilitate the use of this module for future users and want to stress at this point that if the comparison simulation is performed with any additional physics, it has to be explicitly disabled in the setup by the user.

### 4.2.4 IllustrisTNG and IllustrisQLA simulations

To investigate the impact of galactic outflows on the properties of the IGM in the most clean way, we run a suite of simulations of varying boxsize with the moving-mesh code AREPO (Springel, 2010a) with galaxy formation physics as encompassed in the IllustrisTNG model (TNG) described in detail in Chapter 1 of this thesis, as well as with the Quick Lyman-$\alpha$ (QLA) technique described in the previous section that yields an unperturbed IGM. Our suite contains two volumes of $\sim 32$ Mpc$/h$ and $\sim 16$ Mpc$/h$ run to $z = 2$, referred to as level 2 and level 3, respectively. Each volume is evolved in time from the same initial conditions with both the TNG and QLA physics models. The simulation volumes are initialised with $768^3$ dark matter particles and $768^3$ gas cells at level 2, and by $384^3$ dark matter particles and $384^3$ gas cells at level 3. This setup was chosen such that the mass resolution is kept constant to the TNG100 mass resolution of $7.46 \cdot 10^6 \mathrm{M}_\odot$ in dark matter mass and $1.39 \cdot 10^6 \mathrm{M}_\odot$ in the initial

| simulation | volume | initial dm | initial gas |
|---|---|---|---|
| TNG100 | 75 Mpc/h | $1820^3$ | $1820^3$ |
| IllustrisTNG-2 | 31.648 Mpc/h | $768^3$ | $768^3$ |
| IllustrisQLA-2 | 31.648 Mpc/h | $768^3$ | $768^3$ |
| IllustrisTNG-3 | 15.824 Mpc/h | $384^3$ | $384^3$ |
| IllustrisQLA-3 | 15.824 Mpc/h | $384^3$ | $384^3$ |

Table 4.1: IllustrisTNG simulation and our reference runs: listed are the symbolic name, the simulation volume, the number of initial dark matter particles, and the number of initial gas cells for every simulation. The reference runs have been chosen in such a way that the mass resolution is kept constant at $7.46 \cdot 10^6 \mathrm{M}_\odot$ for the dark matter particles and $1.39 \cdot 10^6 \mathrm{M}_\odot$ for the initial gas cells.

gas cell mass. The TNG100 simulation evolves a 75 Mpc$/h$ wide periodic cosmological box from $z = 127$ to $z = 0$ with $1820^3$ dark matter particles and $1820^3$ initial gas cells. TNG100 as well as all simulations from our suite are carried out with the PLANCK15 cosmology (Planck Collaboration et al., 2016b) and employ an updated version of AREPO with improved accuracy ensuring second order convergence (Pakmor et al., 2016). The TNG100 simulation complements our simulation suite and an overview of the simulations employed in this study is given in Tab. 4.1. Our unique setup allows us to directly compare the properties of the cosmic gas probed by the Lyman-$\alpha$ forest as they arise within exactly the same large scale structure given the two different physical models not only statistically but also on a line by line basis.

## 4.3 The impact of feedback on the statistical properties of the IGM

First, we investigate how galactic outflows change the statistical properties of the IGM with respect to an unperturbed gas reservoir as it is obtained in *Quick Lyman-$\alpha$* simulations. To this end, we derive 1000 synthetic Lyman-$\alpha$ spectra at random positions from each of the TNG-3, QLA-3, TNG-2, QLA-2, and TNG100 simulations. Thereby, at each simulation level we use the same seed to initialise the random number generation for choosing the direction and positions at which the lines of sight will be derived. Therefore, and due to the identical initial conditions at each simulation level, Lyman-$\alpha$ spectra derived from simulations with the same boxsize probe the same large scale structure as it appears in the two physics models and can be compared on a line by line basis.

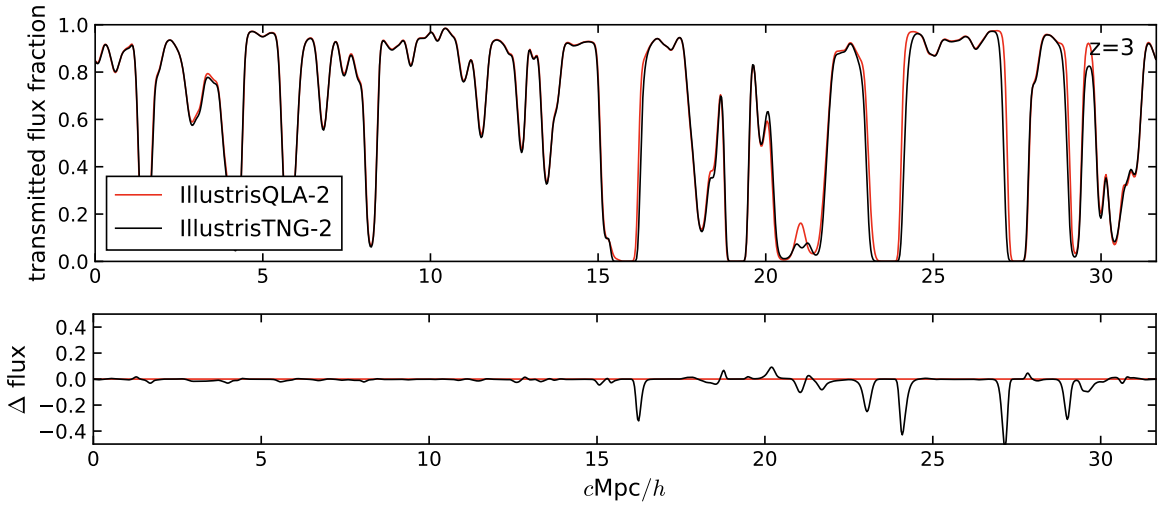


Figure 4.1: *Top panel* : Randomly selected synthetic Lyman-$\alpha$ absorption spectrum probing the exact same large scale structure in presence of hot galactic outflows (black) and in case of an unperturbed inter-galactic gas (red) at $z = 3$. *Bottom panel* : Absolute difference between the transmitted flux in the presence of outflows (black) with respect to an unperturbed gas (red). Distinct regions with considerably less transmitted flux and thus higher Lyman-$\alpha$ absorption appear when the IGM is penetrated by outflows.

Furthermore, to properly resolve the gas structure, the derived Lyman-$\alpha$ spectra have to be subdivided into at least as many pixel as correspond to the one-dimensional number of resolution elements of the given simulation. Therefore, we resolve the Lyman-$\alpha$ lines of sight at simulation levels 3 and 2 with 1024 pixel, and the lines of sight derived from the TNG100 simulation with 2048 pixel. We present a detailed resolution study in Section 4.6.

In the top panel of Fig. 4.1 we show a synthetic Lyman-$\alpha$ absorption spectrum derived along a randomly chosen coordinate axis and a random position probing the exact same large scale structure in the TNG-2 (black) and QLA-2 (red) simulations at $z = 3$. As we derive Lyman-$\alpha$ spectra from simulation output at a fixed redshift and not on a backwards light-cone, we show the Lyman-$\alpha$ absorption as a function of distance instead of redshift. It can be seen that large regions of the IGM are not affected by galaxy physics (e.g. the region $0 - 15$ $c\mathrm{Mpc}/h$) showing no difference in Lyman-$\alpha$ absorption in the two physics models, whereas at some other distinct regions of the IGM the gas exhibits more Lyman-$\alpha$ absorption in presence of galactic outflows. To better visualise this additional absorption, we show in the bottom panel of Fig. 4.1 as a black solid line the absolute difference $\Delta$ flux between the transmitted flux in the presence of outflows (TNG model) and the transmitted flux in case of an inter-galactic gas that is unperturbed by galactic feedback (QLA model).

The red solid line indicates the reference value from an unperturbed IGM. It can be seen that in certain regions of the IGM the cosmic gas exhibits significantly stronger Lyman-$\alpha$ absorption, which are visible as downwards spikes in $\Delta$ flux in the bottom panel of Fig. 4.1 at e.g. 16 $c$Mpc$/h$, 23 $c$Mpc$/h$, 24 $c$Mpc$/h$, and 27 $c$Mpc$/h$. Regions with less Lyman-$\alpha$ absorption visible as upwards spikes also occur (e.g. 20 $c$Mpc$/h$), however are less frequent and significantly less prominent than regions of excess Lyman-$\alpha$ absorption.

The difference in the Lyman-$\alpha$ flux thus shows that there are reoccurring regions with systematically less transmitted flux and thus higher gas density when galactic feedback is taken into account. The increase in gas density in the IGM is caused by galactic outflows which transport matter from small to large scales altering the density distribution of the cosmic gas. This is in agreement with observational findings by Prochaska and Hennawi (2009) and Prochaska et al. (2013b), who find an excess of cold gas mass causing larger Lyman-$\alpha$ absorption in the vicinity of quasar-hosting galaxies. Furthermore, outflows also heat the diffuse gas increasing its ionisation state. This reduces the neutral hydrogen fraction consequently leading to a higher transmitted flux, explaining why galactic outflows can also cause less observed Lyman-$\alpha$ absorption. Based on the random Lyman-$\alpha$ spectra we inspected, we see regions with less transmitted flux in the presence of outflows to be more frequent and prominent than regions with more transmitted flux. Drops in the transmitted flux can only be caused by a higher gas density, leading to the conclusion that the presence of additional matter in the IGM that was expelled from galaxies has a larger impact on the statistics of the Lyman-$\alpha$ forest than the changes induced by an overall higher temperature. In the remained of this section, we will employ statistical properties of the IGM to make more reliable statements about the outflow induced changes in the state of the diffuse gas as probed by the Lyman-$\alpha$ forest than is possible based on the inspection of individual absorption spectra.

### 4.3.1 Flux probability distribution function

In Fig. 4.2 we show the primer Lyman-$\alpha$ forest statistic, the Lyman-$\alpha$ flux probability distribution function (PDF) at $z = 3$ and $z = 2$, derived from 1000 random lines of sight from the TNG-3, QLA-3, TNG-2, QLA-2, and TNG100 simulations, normalised to the mean flux from Kim et al. (2007) (see Section 4.2.2). The Lyman-$\alpha$ spectra are resolved by 1024 pixel in all simulations but TNG100, where we employ 2048 pixel per spectrum (see Section 4.6 for a detailed resolution study). The flux PDF is given by the number of pixel whose flux values fall into bins of $F \pm \frac{1}{2}\Delta F$, with central flux value $F$ covering the range $[0, 1]$ and bin size $\Delta F$, normalised to the total number of pixel. For the results presented in Fig. 4.2 we chose $\Delta F$ such as to obtain 50 bins in the displayed parameter range.

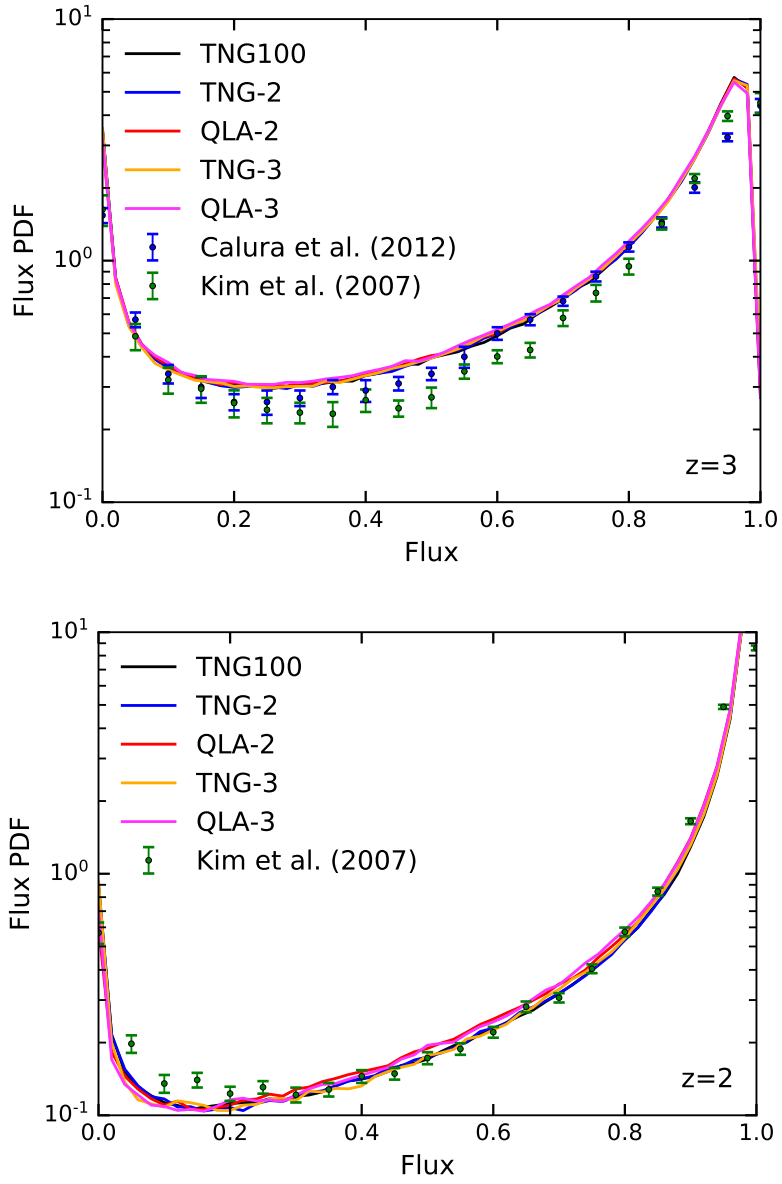


Figure 4.2: Lyman-$\alpha$ flux probability distribution function (PDF) derived from 1000 random lines of sight from the TNG-3, QLA-3, TNG-2, QLA-2, and TNG100 simulations at $z = 3$ (*top panel*) and $z = 2$ (*bottom panel*). The Lyman-$\alpha$ spectra are resolved by 2048 pixel if taken from TNG100, and by 1024 pixel otherwise. For comparison we show observational data from Kim et al. (2007) and Calura et al. (2012).

For comparison we show observational measurements of the flux PDF from Kim et al. (2007) at $z = 2$ and $z = 3$, and from Calura et al. (2012) at $z = 3$. We find good agreement of the simulation results with observational data, though our results do not always intersect with the $1\sigma$ error-bounds of the observations. A similar discrepancy is evident between the observational results themselves. In their study, Kim et al. (2007) show that continuum fitting, removing metals and the remaining metal contamination, as well as pixel noise lead to large systematic uncertainties that can be larger than the statistical errors. Nevertheless, the errors displayed for the measurements of Kim et al. (2007) and Calura et al. (2012) are statistical errors only, explaining the discrepancy between the different observational measurements. Furthermore, these statistical errors are derived from measurements of sometimes less than 10 quasar spectra per redshift bin with reportedly large intrinsic variations, such that the derived results suffer severely from small number statistics.

Given the differences between the different observational measurements and compared to the simulation results, the flux PDF obtained from the TNG and QLA simulations are remarkably similar, despite the changes in the transmitted flux seen in individual spectra in presence of outflows. It is possible that over the large sample of 1000 random spectra the effects from outflows average out to yield an almost identical flux PDF, rendering the approximation of the inter-galactic gas as being unperturbed viable for statistical analysis. To balance regions of lower flux caused by a higher gas density in presence of outflows would require equivalently many regions of increased flux caused by a higher temperature, which we did not find inspecting a random (albeit small) sample of individual Lyman-$\alpha$ forest spectra. However, it is also possible that the flux PDF being a one-point statistic is simply not sensitive enough to capture the signatures of galactic outflows. Therefore, in the next section we derive the next higher order statistic, the Lyman-$\alpha$ flux power spectrum.

### 4.3.2 Lyman-$\alpha$ flux power spectrum

The power spectrum of the Lyman-$\alpha$ flux is the Fourier transform of the two-point auto-correlation function of the Lyman-$\alpha$ flux. We obtain the Lyman-$\alpha$ flux power spectrum in analogy to the matter density power spectrum through a Fourier transform of the excess flux defined as

$$\delta_F = \frac{F_{\mathrm{obs}}}{F_{\mathrm{mean}}} - 1. \tag{4.11}$$

To be consistent with the McDonald et al. (2000) definition of the Lyman-$\alpha$ flux power spectrum we multiply the obtained power spectrum by the characteristic velocity scale $v_{\mathrm{max}} = H \cdot a \cdot L_{\mathrm{com}}$ of the simulation with one-dimensional boxsize $L_{\mathrm{com}}$ in comoving coordinates.

In this definition, the wave vector is given by $k = 2\pi/l$ with $l$ being the wavelength of the corresponding Fourier mode measured in km/s. We calculate the wavelength as $l = v_{\rm max} \cdot \lambda_{\rm com}/L_{\rm com}$, where $\lambda_{\rm com}$ is the physical wavelength of the respective mode in comoving coordinates.

In the top panels of Fig. 4.3 and Fig. 4.4 we show the flux power spectrum derived in the above described way from the TNG-3, QLA-3, TNG-2, QLA-2, and TNG100 simulations, normalised to the mean flux from Kim et al. (2007), at $z = 3$ and $z = 2$, respectively. In addition we show observational measurements from McDonald et al. (2006) at $z = 3$. We obtain very good agreement with the observational data around $k \sim 10^{-2}$, whereas the observational measurements exhibit increasingly higher values towards larger scales (smaller $k$) than our results for the flux power spectrum. Again, the apparent discrepancy between the observational and theoretical results is likely due to the displayed errors being statistical errors only, not taking into account the substantial systematic errors in the observational data.

In the bottom panel of Fig. 4.3 and Fig. 4.4 we show the ratio of the flux power spectra derived from simulations including galaxy evolution and feedback physics with respect to the flux power spectra obtained from an unperturbed inter-galactic gas (TNG divided by QLA) at the two resolution levels 2 (blue line) and 3 (yellow line). The black dashed line indicates the power measured from an unperturbed IGM. The ratios are well converged between the resolution levels at both redshifts. The presence of outflows leads to a very clear suppression of power at small scales (large $k$), precisely balanced by an excess of power at large scales (small $k$) with a characteristic transition scale at $k_t \sim 2 \cdot 10^{-2}$ s/km. Furthermore, the deviation of the flux power spectrum obtained from the perturbed IGM with respect to the flux power spectrum measured from an unperturbed gas grows with time exhibiting a difference of up to $\sim 10\%$ at $z = 3$, and $\sim 20\%$ at $z = 2$. This can be understood through outflows transporting increasing amounts of matter from galaxies to large scales. The higher gas density in selected patches of the inter-galactic gas thus leads to more observed Lyman-$\alpha$ absorption at large scales, and the lack of the same matter in the vicinity of galaxies from where it has been expelled leads to the corresponding drop of power in the Lyman-$\alpha$ flux at small scales. Galactic outflows thus have a visible and significant impact on the shape of the Lyman-$\alpha$ flux power spectrum, rendering this statistic a powerful probe of the state of the IGM. In return, this can also be used as an effective way to put constraints on theoretical subgrid models for galactic feedback employed in hydrodynamical simulations, and especially the strength of the employed feedback mechanisms.

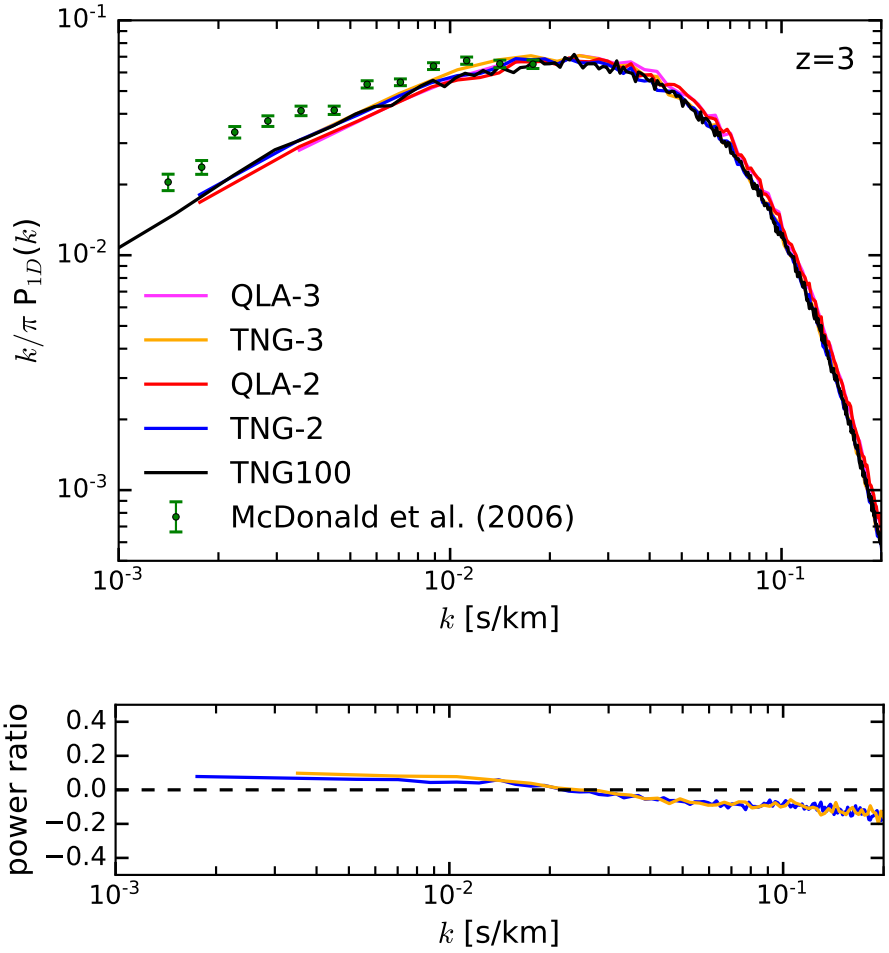


Figure 4.3: *Top panel* : Lyman-$\alpha$ flux power spectrum derived from 1000 random Lyman-$\alpha$ absorption spectra from the TNG-3, QLA-3, TNG-2, QLA-2, and TNG100 simulations at $z = 3$, resolved by 2048 in case of TNG100, and by 1024 pixel otherwise. For comparison we show observational data from McDonald et al. (2006). *Bottom panel* : Ratio of flux power spectra derived from the TNG simulations including galaxy evolution and feedback physics with respect to the power spectra derived from an unperturbed gas as given by the QLA simulations. Black dashed line indicates the power in an unperturbed IGM. The ratios are well converged between the resolution levels and exhibit a characteristic transition scale at $k_t \sim 2 \cdot 10^{-2}$ s/km. At small physical scales above $k_t$ the flux power spectrum exhibits up to $\sim 10\%$ less power in the presence of outflows compared to the unperturbed IGM, and correspondingly more power at large physical scales below $k_t$. This characteristic change in the flux power spectrum can be understood as an effect from galactic outflows transporting matter from small, galactic scales to large scales.

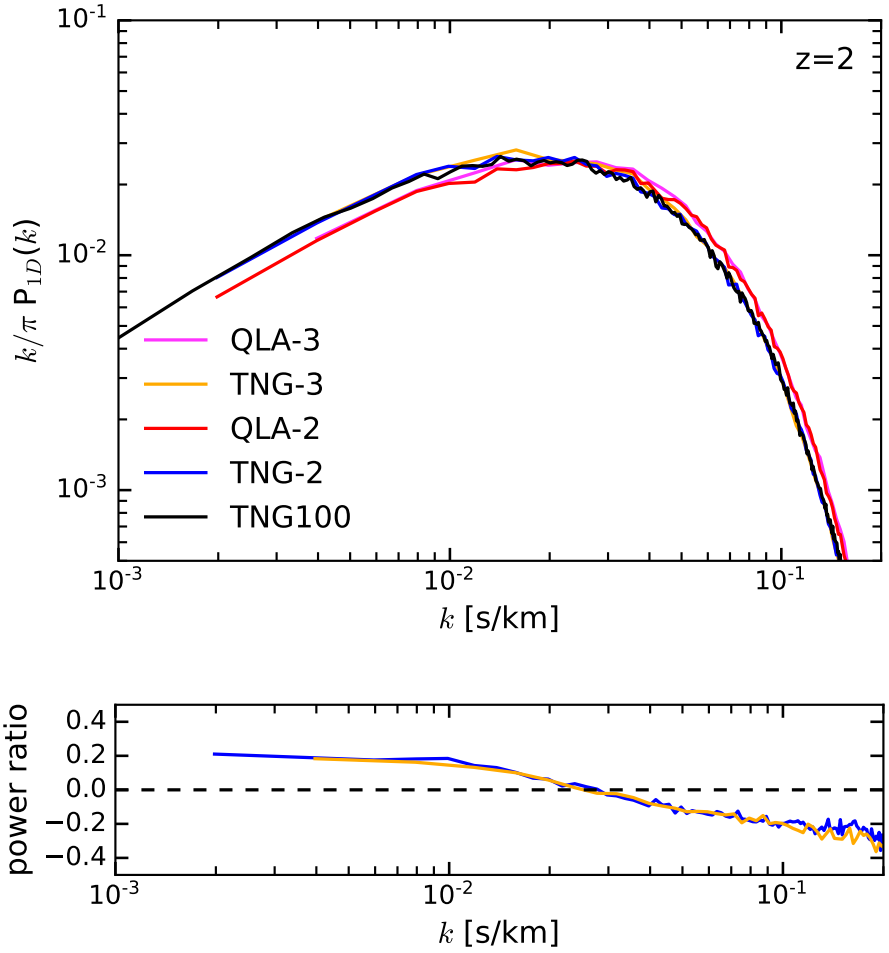


Figure 4.4: *Top panel* : Lyman-$\alpha$ flux power spectrum derived from 1000 random Lyman-$\alpha$ absorption spectra from the TNG-3, QLA-3, TNG-2, QLA-2, and TNG100 simulations at $z = 2$, resolved by 2048 in case of TNG100, and by 1024 pixel otherwise. For comparison we show observational data from McDonald et al. (2006). *Bottom panel* : Ratio of flux power spectra derived from the TNG simulations including galaxy evolution and feedback physics with respect to the power spectra derived from an unperturbed gas as given by the QLA simulations. Black dashed line indicates the power in an unperturbed IGM. The ratios are well converged between the resolution levels and exhibit a characteristic transition scale at $k_t \sim 2 \cdot 10^{-2}$ s/km. At small physical scales above $k_t$ the flux power spectrum exhibits up to $\sim 20\%$ less power in the presence of outflows compared to the unperturbed IGM, and correspondingly more power at large physical scales below $k_t$. This characteristic change in the flux power spectrum can be understood as an effect from galactic outflows transporting matter from small, galactic scales to large scales.

### 4.3.3 Thermal state of the IGM

Finally, we investigate the role of outflows in changing the thermal state of the IGM. In Fig. 4.5 and Fig. 4.6 we show the temperature-density distribution of the diffuse inter-galactic gas in the two different kinds of simulations, QLA-2 (top panel) and TNG-2 (bottom panel), at $z = 3$ and $z = 2$, respectively. We obtain the displayed phasediagram by binning the individual pixel of all 1000 randomly derived spectra on a $200 \times 200$ grid in the displayed parameter space. The fraction of all pixel falling into each individual grid cell is colour-coded, with blue corresponding to most pixel occupying a given phasespace region and green the least. The displayed two-dimensional histogram thus corresponds to a volume-weigthed statistic.

It becomes evident that in presence of galaxy evolution physics and galactic feedback more gas at densities around the cosmic mean exhibits a temperature of $10^{4.5} - 10^{5.5} K$ compared to the unperturbed IGM. Most of the inter-galactic volume however still follows the equation of state of the inter-galactic gas. The relation between temperature and density of the inter-galactic gas is given by a power law equation of state (Hui and Gnedin, 1997, Valageas et al., 2002),

$$T = T_0(1+\delta)^{\gamma-1}, \tag{4.12}$$

where $\delta$ is the gas overdensity with respect to the cosmic mean, and $T_0$ and $\gamma$ are two independent fitting parameters with typical values of $T_0 \approx 10^4 K$ and $1 \leqslant \gamma \lesssim 1.6$ (e.g. Lukić et al., 2015). We show the IGM equation of state as dashed black line in Fig. 4.5 and Fig. 4.6. Both at $z = 3$ and $z = 2$, we adopt parameter values of $\gamma = 1.45$ and $T_0 = 10^{3.95} K$ in case of unperturbed gas (QLA-2), and $T_0 = 10^4 K$ in case the gas is heated by outflows (TNG-2), to approximate the bulk of the inter-galactic gas colour-coded in blue. This shows that galactic outflows have a net heating effect on the IGM moving most of the diffuse gas to overall slightly higher temperatures reflected in the higher offset value $T_0$ that is necessary to fit the temperature-density relation of the inter-galactic gas in the presence of outflows.

Furthermore, the fact that galactic outflows heat more diffuse gas to temperatures particularly around $10^{4.5} - 10^{5.5} K$ has significant implications for the Lyman-$\alpha$ absorption statistics. This range covers both the characteristic temperature associated with the Lyman-$\alpha$ transition, $T_{\mathrm{Ly}\alpha} = h_\mathrm{p} \nu_{\mathrm{Ly}\alpha} / k_\mathrm{B} \approx 1.18 \cdot 10^5\ K$, where $h_\mathrm{p}$ is the Planck constant, $k_\mathrm{B}$ the Boltzmann constant, and $\nu_{\mathrm{Ly}\alpha}$ the Lyman-$\alpha$ transition frequency, as well as the only one third higher characteristic temperature necessary to ionise neutral hydrogen, $T_\mathrm{ion} = h_\mathrm{p} \nu_\mathrm{ion} / k_\mathrm{B} \approx 1.57 \cdot 10^5\ K$. In thermal equilibrium, the gas velocities of the diffuse gas, and thus also the energies of the local radiation field, follow the Maxwell-Boltzmann distribution. Therefore, a higher average

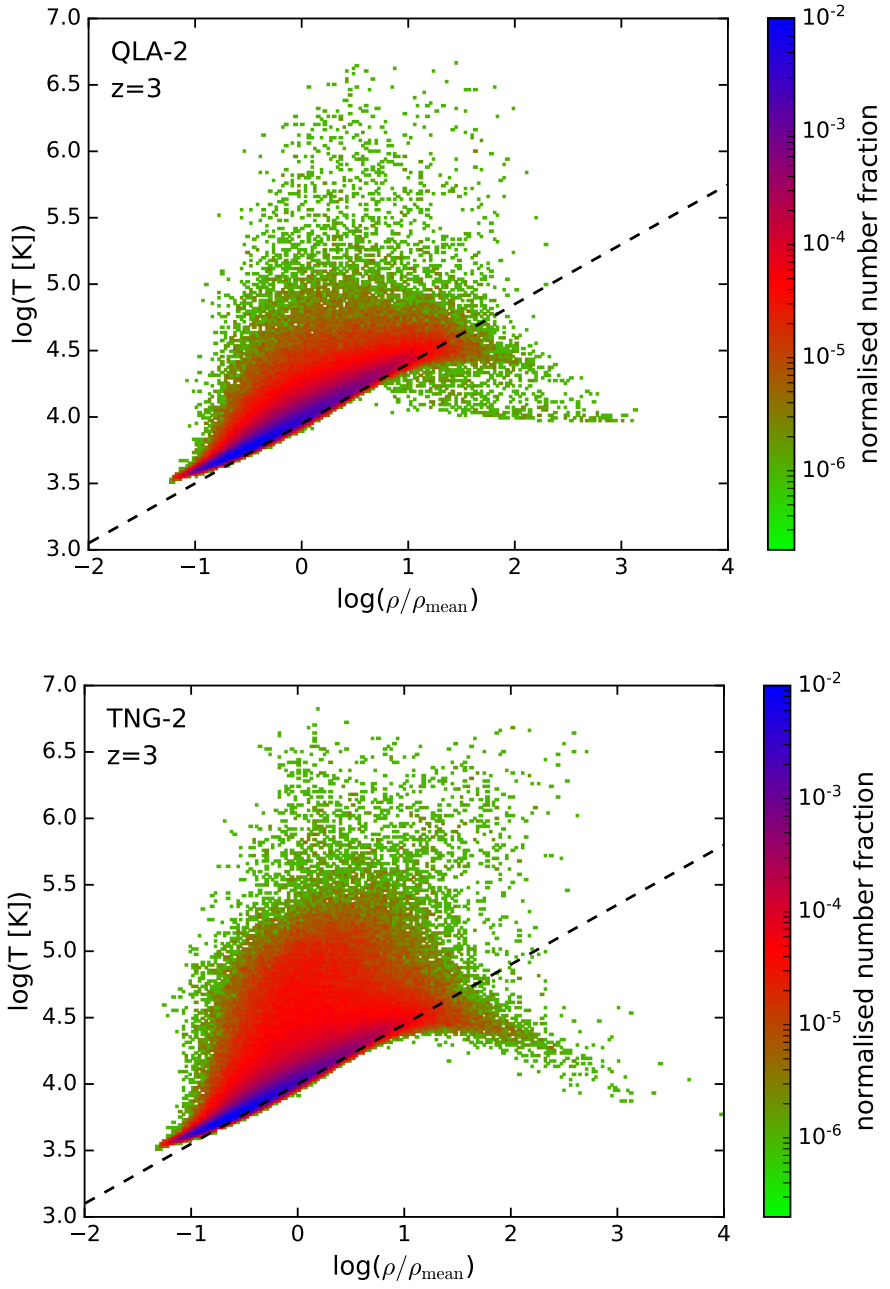


Figure 4.5: Temperature-density distribution of the unperturbed gas (*top panel*) and of the gas in presence of galactic outflows (*bottom panel*) at $z = 3$. The two-dimensional histograms are obtained by binning the individual pixel of all 1000 randomly derived Lyman-$\alpha$ absorption spectra on a $200 \times 200$ grid in the displayed parameter range. Dashed lines indicate the IGM equation of state $T = T_0(1+\delta)^{\gamma-1}$ (Hui and Gnedin, 1997) with $\gamma = 1.45$ and $T_0 = 10^{3.95}K$ in case of unperturbed gas, and $T_0 = 10^4 K$ if the gas is heated by outflows.

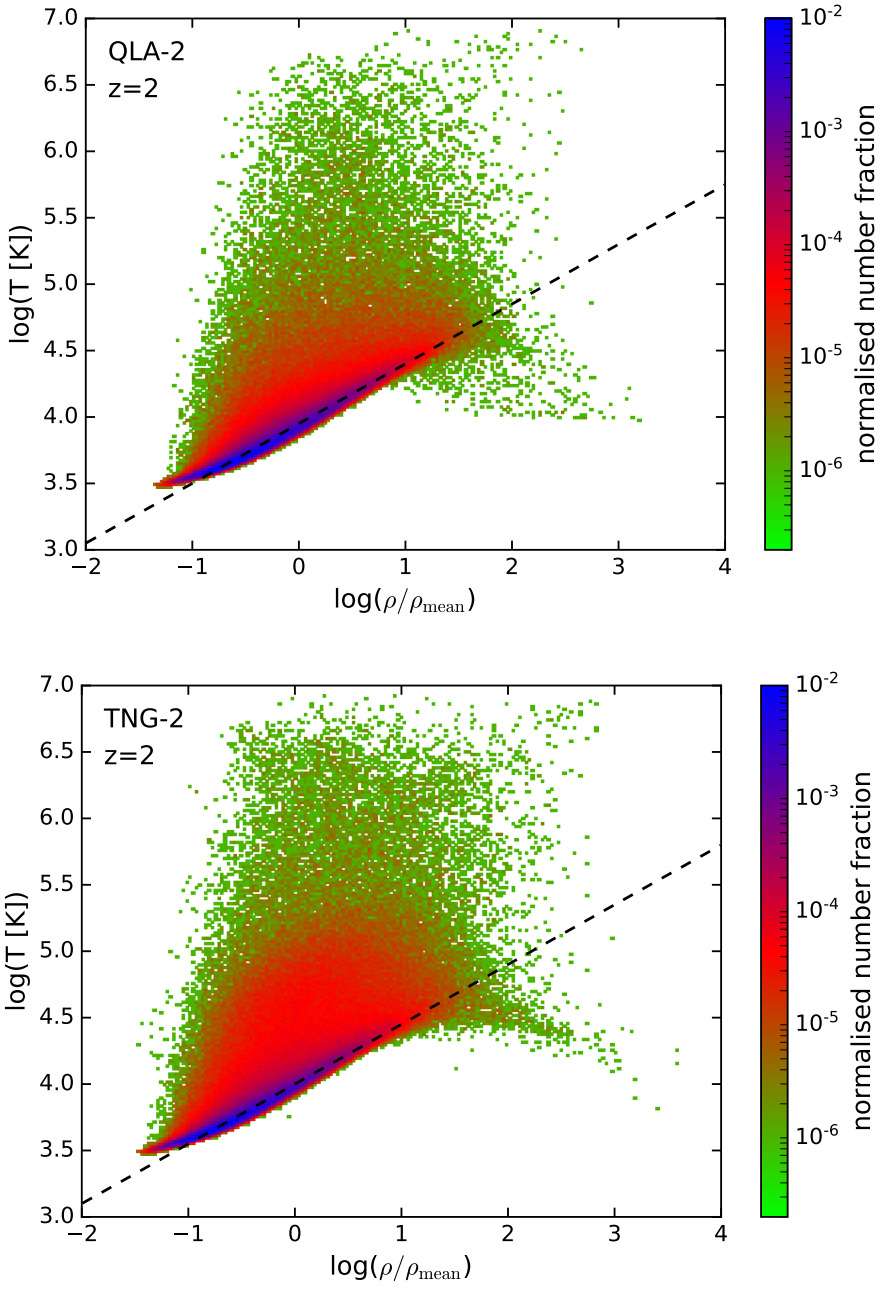


Figure 4.6: Temperature-density distribution of the unperturbed gas (*top panel*) and of the gas in presence of galactic outflows (*bottom panel*) at $z = 2$. The two-dimensional histograms are obtained by binning the individual pixel of all 1000 randomly derived Lyman-$\alpha$ absorption spectra on a $200 \times 200$ grid in the displayed parameter range. Dashed lines indicate the IGM equation of state $T = T_0(1+\delta)^{\gamma-1}$ (Hui and Gnedin, 1997) with $\gamma = 1.45$ and $T_0 = 10^{3.95}K$ in case of unperturbed gas, and $T_0 = 10^4 K$ if the gas is heated by outflows.

temperature in general shifts more gas to higher velocities and thus equilibrated photons to higher energies that are above the threshold values for Lyman-$\alpha$ absorption and for ionisation of neutral hydrogen. If, as is the case here, the mean temperature of the gas and the characteristic temperature needed for the ionisation of hydrogen are close, a substantial fraction of up to more than 50% of all photons in equilibrium with the diffuse gas will have sufficient energies to ionise neutral hydrogen. The higher temperature of the IGM covering specifically the range $10^{4.5} - 10^{5.5} K$ thus leads to a higher ionisation fraction and lower neutral hydrogen fraction in the gas causing less observed Lyman-$\alpha$ absorption. Additionally, more gas having temperatures close to the characteristic Lyman-$\alpha$ absorption temperature will lead to a higher fraction of the neutral hydrogen being in the first excited state and thus unavailable for Lyman-$\alpha$ absorption caused by a luminous background source.

## 4.4 The impact of feedback on the gaseous surroundings of haloes

In this section, we investigate the role of haloes exhibiting strong and weak feedback in impacting their gaseous surroundings by driving large scale outflows, which change the state of the IGM and the observed Lyman-$\alpha$ absorption properties within and outside their virial radii. Galaxies at the centres of haloes expel hot and metal-enriched gas due to outflows driven by supernovae and by AGN feedback. Below a FOF-halo mass of $\sim 2 \times 10^{11} \mathrm{M}_{\odot}$, galactic winds launched by supernovae are strong enough to expel a significant fraction of a galaxies gas, which increases with decreasing halo mass. Above a halo mass of $\sim 2 \times 10^{11} \mathrm{M}_{\odot}$ the gravitational potential becomes deep enough to suppress galactic winds. In this mass range, galaxies hold on to most of their gas and undergo efficient star-formation. Above $\sim 2 \times 10^{12} \mathrm{M}_{\odot}$, AGN feedback sets in, expelling again large fractions of gas from galaxies.

### 4.4.1 Dependence of Lyman-$\alpha$ absorption on halo mass

As the two major feedback mechanisms dominate at different galaxy and thus halo mass scales, we first investigate the Lyman-$\alpha$ forest in the vicinity of haloes with different halo mass. The large simulation volume of TNG100 provides sufficient statistics that we can extend our study up to halo masses of $\sim 10^{13.5} \mathrm{M}_{\odot}$. Previous related studies where limit by their simulation volume as well as by the lack of a subgrid model for AGN feedback (Meiksin et al., 2017) that render a study of haloes above a mass of $\sim 10^{12} \mathrm{M}_{\odot}$ superfluous. This study thus for the first time shows the role of AGN feedback in impacting the properties of the IGM and changing the observed Lyman-$\alpha$ absorption statistics.

For this analysis, we select haloes with friends-of-friends (FOF) halo mass of $[10^{11}\mathrm{M}_\odot$, $10^{11.5}\mathrm{M}_\odot, 10^{12}\mathrm{M}_\odot, 10^{12.5}\mathrm{M}_\odot, 10^{13}\mathrm{M}_\odot]$ from the TNG100 simulation at redshifts $z = 2$, $z = 2.4$, and $z = 3$. For every target halo mass we select 10 haloes with mass closest to the target mass. We probe the gas properties in the vicinity of each halo through the statistics of the measured Lyman-$\alpha$ absorption.

For every halo we derive multiple sets of Lyman-$\alpha$ forest spectra, whereas each set contains a constant number of Lyman-$\alpha$ spectra derived at predefined distances from the halo centre along a chosen radial direction. In Fig. 4.7 we show a schematic overview of our procedure to derive Lyman-$\alpha$ forest spectra as a function of impact parameter $b$. We look at each halo from three pairwise perpendicular projections, labelled as projection 1, 2, and 3 in Fig. 4.7. Due to the asymmetry of haloes and the directionality of outflows these projections can be regarded as independent observations of different objects. Furthermore, for each projection we select four radial directions along which we probe the signature of outflows. The radial directions are selected randomly but under condition to be offset by at least 30° from any of the other selected directions. The precise value of 30° is a choice we make to ensure that no two radial directions probe the same environments, but it can be set to a larger (or smaller) value according to the requirement of a given study.

For every radial direction we select thirteen positions shown symbolically as black dots, along which we will derive synthetic Lyman-$\alpha$ forest spectra constituting one set. We chose positions in an equal logarithmic spacing starting at an impact parameter of $b = 10$ $c$kpc from the halo centre and ending at $b = 10$ $c$Mpc. The halo centre is indicated by the cross symbol in Fig. 4.7 and is set to the potential minimum. At every chosen position we derive Lyman-$\alpha$ lines of sight according to the procedure described in Section 4.2.1. In our setup this results into 1560 individual Lyman-$\alpha$ spectra per redshift and halo mass and 120 spectra per given impact parameter.

We resolve the Lyman-$\alpha$ spectra presented in this section by 2048 pixel which corresponds approximately to the one-dimensional resolution of the TNG100 simulation and is required to avoid numerical artefacts (see Section 4.6). Furthermore, we rescale the optical depth of the derived Lyman-$\alpha$ forest spectra with a constant calibration factor $f_c$ at every redshift. The calibration factor is derived for every redshift from our samples of 1000 randomly selected lines of sight (see Section 4.2.2), such that the mean flux of the random Lyman-$\alpha$ forest samples probing the mean properties of the IGM is rescaled to the mean flux by observed Kim et al. (2007).

For each line of sight we calculate the Lyman-$\alpha$ absorption equivalent width at a given impact parameter $b$ according to

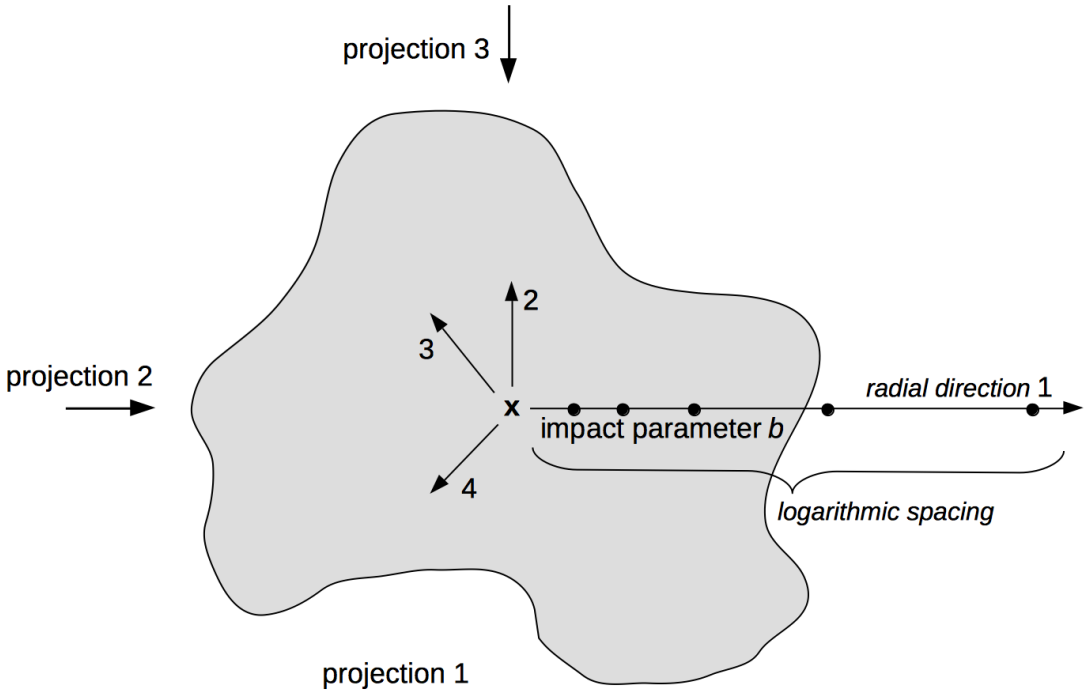


Figure 4.7: Schematic representation of our procedure to derive Lyman-$\alpha$ forest spectra as a function of impact parameter $b$. Every halo can be looked at along the three coordinate axes of the simulation box corresponding to three different projections. For every projection an arbitrary number of radial directions (here 4) can be chosen along which the Lyman-$\alpha$ absorption will be probed as a function of the distance from the halo centre set to the potential minimum. All radial directions are required to be separated from their neighbouring lines by a minimum separation angle (here set to 30°). Along each radial direction a number of positions is chosen along which Lyman-$\alpha$ lines of sight will be shot. For our analysis we select 13 positions in equal logarithmic spacing starting at an impact parameter of $b = 10\ c\mathrm{kpc}$ and ending at $b = 10\ c\mathrm{Mpc}$.

$$w(b,\Delta v) = \frac{\lambda_\alpha}{c} \int_{v_{\rm halo}-\Delta v/2}^{v_{\rm halo}+\Delta v/2} \left[1 - e^{-\tau_\alpha(b,v)}\right] {\rm d}v \tag{4.13}$$

(Meiksin et al., 2017), where $\lambda_\alpha = 1215.67$ Å is the rest frame Lyman-$\alpha$ wavelength, $c$ the speed of light, and $\tau_\alpha$ the Lyman-$\alpha$ optical depth. The integral is centred at the halo position in velocity space $v_{\rm halo}$ corresponding to the effective recession velocity of the halo away from the observer, and is performed over a velocity window of width $\Delta v$. The parameter $b$ indicates the given distance from the halo centre at which the equivalent width is derived.

Given synthetic Lyman-$\alpha$ forest spectra with a constant number $n_{\rm pix}$ of pixel, we derive the equivalent width as follows. First, we locate the halo centre in velocity space by calculating the halo recession velocity induced by the Hubble flow and adding the peculiar velocity of the halo, $v_{\rm rec} = H \cdot a \cdot x_{\rm com} + v_{\rm pec}$, where $H$ is the Hubble parameter, $a$ the scale factor, $x_{\rm com}$ is the halo centre in comoving coordinates, and $v_{\rm pec}$ the peculiar velocity of the halo. The maximum recession velocity that can be reached in a simulated volume of one-dimensional boxsize $L_{\rm com}$ in comoving coordinates is given by the characteristic velocity scale $v_{\rm max} = H \cdot a \cdot L_{\rm com}$. Dividing $v_{\rm max}$ by the number of pixel $n_{\rm pix}$ gives the velocity width of each pixel in a given spectrum, whereby the 0th pixel in each spectrum starts at recession velocity of zero, $v_{\rm rec} = 0$, and the last pixel ends at $v_{\rm rec} = v_{\rm max}$. This allows us to identify the pixel containing the halo centre in velocity space. In a next step we calculate how many pixel are necessary to cover a given velocity window of width $\Delta v$ centred at $v_{\rm rec}$. Knowing the relevant pixel range, the integral in Eq. 4.13 becomes a sum of $(1 - e^{-\tau_{\alpha,{\rm pix}}})$ over all pixel in the identified pixel range normalised by the number of pixel in the given range.

The equivalent width can be used to define the excess Lyman-$\alpha$ absorption with respect to the mean IGM value (Prochaska et al., 2013a),

$$\delta_F(b,\Delta v) = \frac{w(b,\Delta v) - w_{\rm IGM}}{\Delta\lambda_\alpha - w_{\rm IGM}}, \tag{4.14}$$

where $\Delta\lambda_\alpha = \lambda_\alpha \Delta v/c$ and $w_{\rm IGM} = \Delta\lambda_\alpha(1-\exp[-\tau_{\rm eff}])$ with $\tau_{\rm eff}$ being the effective Lyman-$\alpha$ optical depth of the IGM. The excess absorption is referred to as $\delta_F$, as technically the quantity in Eq. 4.14 corresponds to the fractional change in the transmitted flux with respect to the mean IGM value, and as such also can be negative corresponding to a deficiency in absorption. Based on the quality of the obtained spectra, observational measurements typically employ velocity windows of width $\Delta v = 500$ s/km (Rudie et al., 2012), $\Delta v = 1000$ s/km (Steidel et al., 2010, Rakic et al., 2012), or $\Delta v = 2000$ s/km (Prochaska et al., 2013a). Throughout this study we thus adopt a velocity window of width $\Delta v = 1000$ s/km. Note, that the absolute values of both the Lyman-$\alpha$ equivalent width and excess absorption depend

strongly on the chosen velocity window, such that a comparison to observations requires the exact same velocity window to be adopted.

In Fig. 4.8, Fig. 4.9, and Fig. 4.10 we show the Lyman-$\alpha$ absorption equivalent width (top panels) and excess absorption (bottom panels) as a function of impact parameter for the five halo mass bins at $z = 3,\ 2.4$, and 2, respectively. The corresponding physical distance at each redshift is shown at the top of each panel. Each dot corresponds to the mean value obtained from all 120 lines of sight per mass bin derived at the same impact parameter. The displayed error bars correspond to the so called standard error, which is the standard deviation divided by an additional factor of $\sqrt{N-1}$, where $N = 120$ is the number of the individual measurements contributing to the mean. The mean virial radii of haloes of each mass are shown as dashed vertical lines and are colour-coded correspondingly.

For comparison, we also derive the equivalent width and excess absorption for 1000 randomly selected Lyman-$\alpha$ spectra centred at a random pixel in the spectrum. These random measurements show that the average Lyman-$\alpha$ equivalent width in the IGM decreases with redshift. The excess absorption fluctuates around zero, with $\sim 2/3$ of the displayed error bars overlapping with zero, which provides a great consistency check both for the theoretically expected absolute value for random measurements as well as the statistical error distribution.

The profiles of both the equivalent width and the excess absorption as a function of distance from the halo centre $b$ exhibit exactly the same shapes, as the excess absorption is a linear function of the equivalent width only. In the following, we therefore will focus our discussion on the physically the more intuitively understandable excess absorption, whereas the interpretation applies equally to the Lyman-$\alpha$ equivalent width.

For all redshifts and all halo masses, the profiles of the excess Lyman-$\alpha$ absorption as a function of distance from the halo centre $b$ exhibit to first order the same general trend of decreasing with increasing impact parameter, showing most Lyman-$\alpha$ absorption in the halo centre and approaching the mean IGM value at large distances. However, prominent second order trends develop with redshift. Fig. 4.8 shows that at $z = 3$, before feedback processes had much time to perturb the gas distribution, the normalisation of the profiles of the excess absorption is monotonously increasing with halo mass. Except for small fluctuations, the profile for the next higher halo mass lays always above the profile derived for haloes of smaller mass. More massive haloes are denser, and with higher overall density also the density of neutral hydrogen and thus the Lyman-$\alpha$ absorption is increased. At redshift $z = 2.4$ shown in Fig. 4.9 this monotonous trend is however broken up by the profile form the largest halo mass bin. For haloes of $10^{13}\mathrm{M}_{\odot}$ the excess Lyman-$\alpha$ absorption is suppressed within the mean virial radius and the profile lays below both the profiles of haloes with halo mass of $10^{12.5}\mathrm{M}_{\odot}$ and $10^{12}\mathrm{M}_{\odot}$. This trend continues towards lower redshift. At $z = 2$ shown in

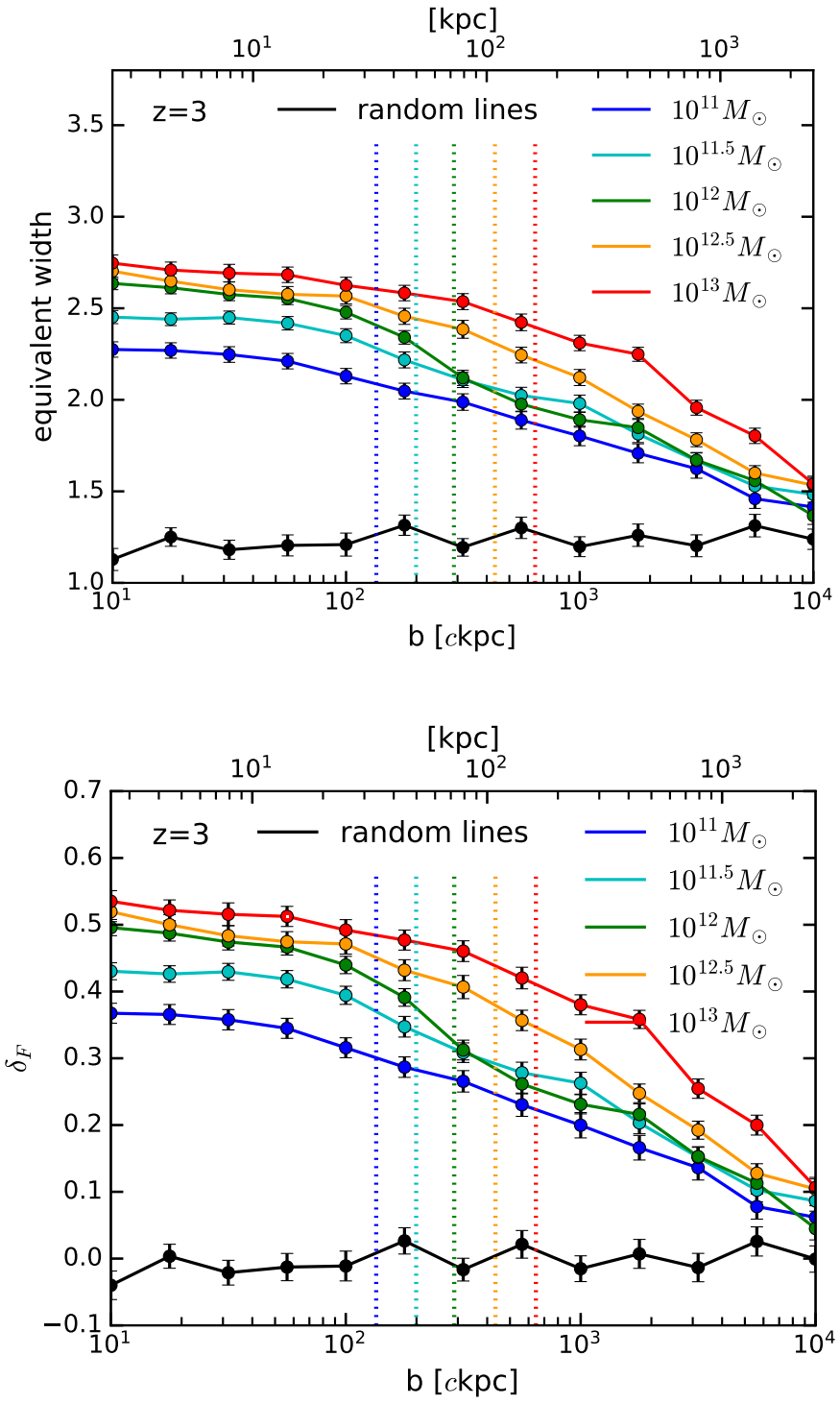


Figure 4.8: Lyman-$\alpha$ absorption equivalent width (*top panel*) and excess absorption (*bottom panel*) as a function of impact parameter $b$ for five different halo mass bins at $z = 3$. Error bars correspond to the standard error derived from 120 independent Lyman-$\alpha$ spectra contributing to each measurement. Dashed lines correspond to the mean virial radii at each halo mass, colour-coded correspondingly. For comparison, we show the same quantities derived from randomly placed Lyman-$\alpha$ lines of sight in black.

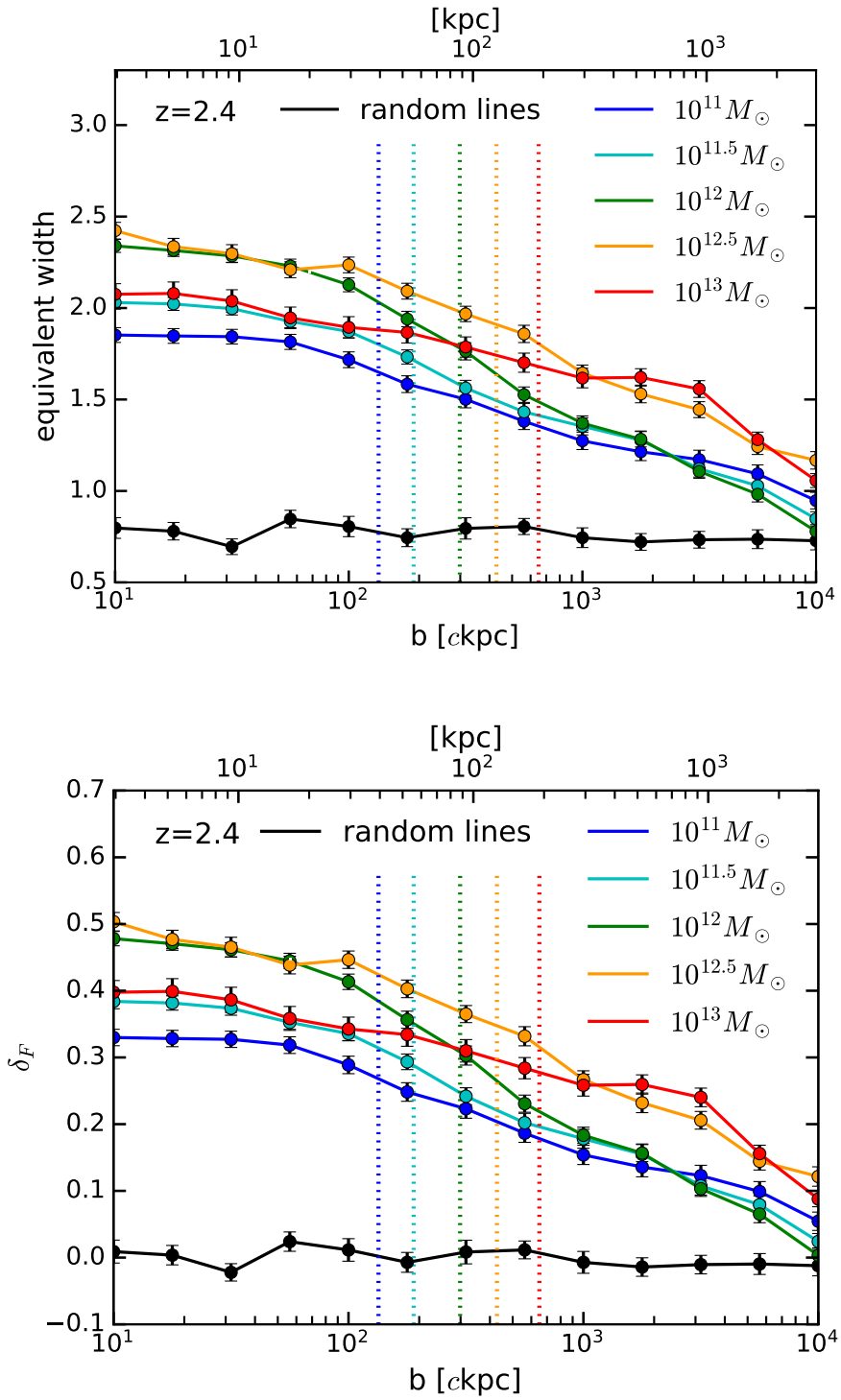


Figure 4.9: Lyman-$\alpha$ absorption equivalent width (*top panel*) and excess absorption (*bottom panel*) as a function of impact parameter $b$ for five different halo mass bins at $z = 2.4$. Error bars correspond to the standard error derived from 120 independent Lyman-$\alpha$ spectra contributing to each measurement. Dashed lines correspond to the mean virial radii at each halo mass, colour-coded correspondingly. For comparison, we show the same quantities derived from randomly placed Lyman-$\alpha$ lines of sight in black.

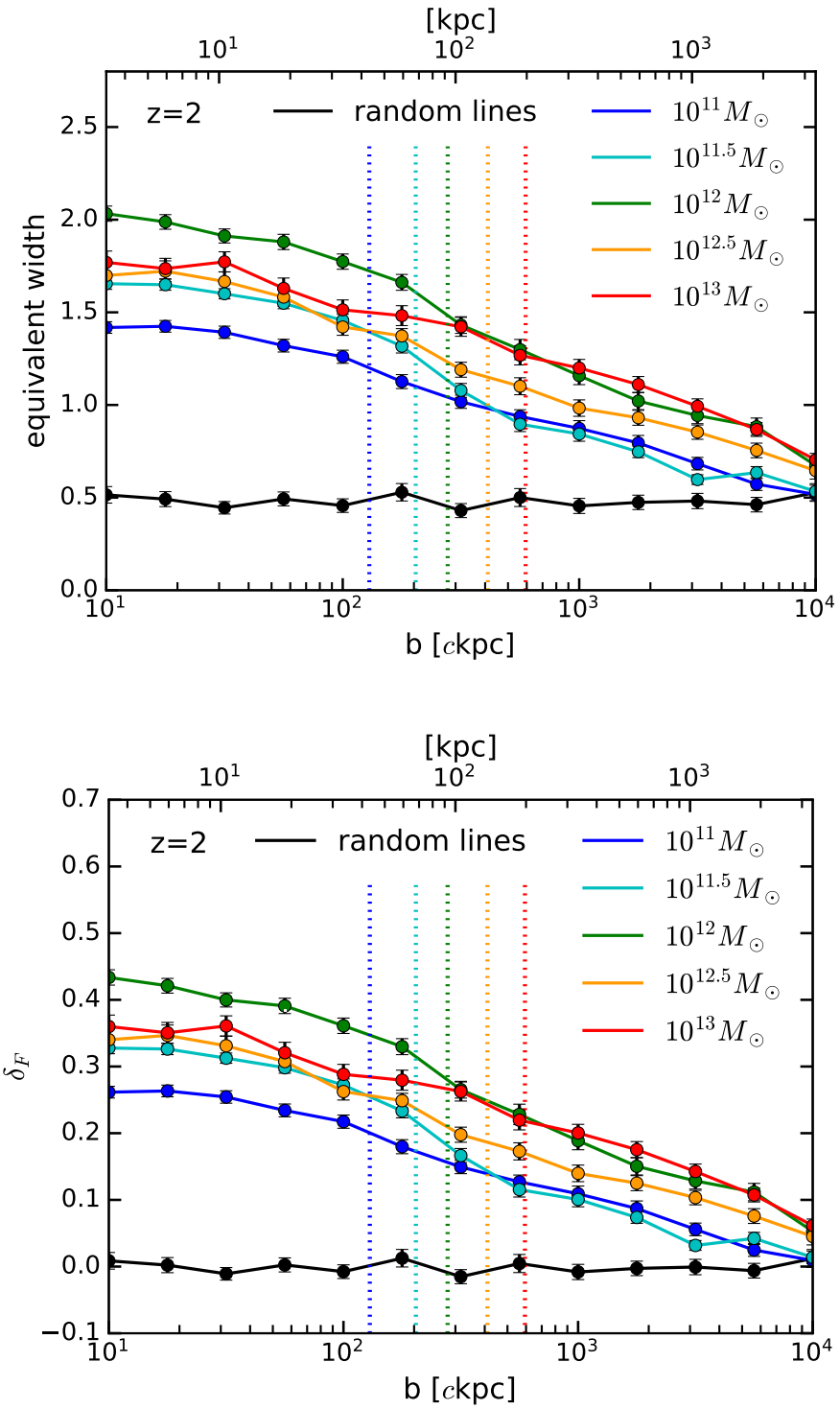


Figure 4.10: Lyman-$\alpha$ absorption equivalent width (*top panel*) and excess absorption (*bottom panel*) as a function of impact parameter $b$ for five different halo mass bins at $z = 2$. Error bars correspond to the standard error derived from 120 independent Lyman-$\alpha$ spectra contributing to each measurement. Dashed lines correspond to the mean virial radii at each halo mass, colour-coded correspondingly. For comparison, we show the same quantities derived from randomly placed Lyman-$\alpha$ lines of sight in black.

Fig. 4.10 the excess Lyman-$\alpha$ absorption of $10^{13}M_{\odot}$ haloes is further supressed and also the profile for haloes of mass $10^{12.5}M_{\odot}$ now exhibits the same trend as the profile of $10^{13}M_{\odot}$ haloes at $z = 2.4$. Finally, at $z = 2$ the excess absorption around haloes of both $10^{12.5}M_{\odot}$ and $10^{13}M_{\odot}$ is suppressed also at large distances from the halo centre reaching the level of $10^{11}M_{\odot}$ haloes. This depletion of excess Lyman-$\alpha$ absorption especially inside the virial radius of massive haloes is due to AGN feedback driving large scale outflows and heating the halo gas. In the next section we investigate in more detail the impact of feedback driven outflows on the excess Lyman-$\alpha$ absorption as a function of distance from the halo centre.

### 4.4.2 Dependence of Lyman-$\alpha$ absorption on feedback strength

In order to investigate in more detail the role of AGN feedback but also supernovae driven winds in changing the gas distribution in the CGM and IGM as well as heating the diffuse gas, as a next step we investigate the functional shape of the Lyman-$\alpha$ equivalent width and excess absorption as a function of impact parameter for haloes exhibiting strong and weak feedback. To make such a comparison we select four most relevant friends-of-friends (FOF) halo target masses, $[10^{11}M_{\odot}, 10^{12}M_{\odot}, 10^{12.5}M_{\odot}, 10^{13}M_{\odot}]$. For each target mass we select 100 haloes from the TNG100 simulation at redshifts $z = 2$, $z = 2.4$, and $z = 3$ with mass closest to the target mass. From these larger halo sample we select subsamples of 10 haloes that have the smallest and largest stellar mass, as well as the smallest and largest black hole mass for which we then derive Lyman-$\alpha$ absorption spectra as a function of impact parameter, according to the same procedure as described in the previous section. We select the halo subsamples based on the halo stellar mass, as the amount of stars formed directly determines how many supernovae events will happen. The stellar mass at a given redshift therefore serves as the most direct proxy for the cumulative amount of supernovae feedback a halo has undergone. In short, haloes with large stellar mass will have exhibited strong supernovae feedback, haloes with small stellar mass will have exhibited weak supernovae feedback. The same logic applies to the subsamples selected based on black hole mass. Haloes with large black hole mass will have undergone a high accretion onto the central black hole and therefore experienced strong AGN feedback, haloes with low black hole mass will have had weak AGN feedback.

For testing purposes we have also used the local star formation rate and the local black hole accretion rate as tracers for strong and weak supernovae and AGN feedback, respectively. However, the rates are subject to strong, short-term fluctuations in time, such that the local rates do not give a fair estimate of how active a halo's central galaxy was undergoing star formation or accretion onto its central black hole throughout its evolution. Furthermore, it is important to keep in mind that feedback driven outflows do not have an instantaneous effect

on the diffuse gas, but rather propagate with a finite velocity outwards, such that their impact reaches increasingly larger distances always with a given delay. Therefore, we restore to the total stellar mass and black hole mass as the most reliable tracers for the integrated effect from the respective feedback mechanisms.

Furthermore, to understand where the differences in the Lyman-$\alpha$ equivalent width and excess absorption come from, we also derive for each individual spectrum the integrated gas column density and mean (volume-weighted) temperature of the gas falling into the range selected by a given velocity window of $\Delta v = 1000$ km/s centred at the halo position in velocity space. In the following figures, we show the mean of the gas column densities and the median of the mean temperature values as a function of impact parameter averaged over 120 Lyman-$\alpha$ spectra that contribute to each individual impact parameter bin. We have chosen to show the median of the mean temperature values to be not biased to larger values by single spectra with particularly hot gas given the logarithmic scale, but find qualitatively the same temperature profiles if we employ the mean.

Before presenting our results, we would like to briefly recapitulate the basic relationship between gas (column) density, temperature, and Lyman-$\alpha$ absorption that will allow us to interpret the following results and pin down the cause for feedback induced changes in the Lyman-$\alpha$ absorption. If the fraction of neutral hydrogen that causes Lyman-$\alpha$ absorption in gas remains unchanged, a higher gas column density directly (linearly) translates into a higher Lyman-$\alpha$ optical depth and thus higher Lyman-$\alpha$ absorption. However, changes in temperature induce a change in the ionisation state of the gas and thus in the amount and fraction of neutral hydrogen with respect to the remainder of the gas. A higher temperature leads to a higher ionised gas, less neutral hydrogen, and thus less Lyman-$\alpha$ absorption. A lower temperature correspondingly leads to more Lyman-$\alpha$ absorption, given a constant gas column density. Having this in mind, in the following we will present Lyman-$\alpha$ equivalent widths and excess absorption as a function of distance from the halo centre at various halo masses and redshifts and discuss the feedback induced differences.

In Fig. 4.11, Fig. 4.13, Fig. 4.15, and Fig. 4.17 we show the Lyman-$\alpha$ absorption equivalent width (top panel) and excess absorption (bottom panel) as a function of impact parameter for the four target halo masses at $z = 3$. Again, in the following we will focus our discussion on the Lyman-$\alpha$ excess absorption, whereas the same interpretation applies to the Lyman-$\alpha$ equivalent width due to the linear dependence between those two quantities. In Fig. 4.12, Fig. 4.14, Fig. 4.16, and Fig. 4.18 we show the corresponding total gas column densities and mean temperature values of the gas for the four target halo masses at $z = 3$.

The excess Lyman-$\alpha$ absorption at $z = 3$ around haloes with target mass of $10^{11}\mathrm{M}_{\odot}$ and $10^{12}\mathrm{M}_{\odot}$ decreases equally for all halo subsamples with different properties, however with

some minor variations in amplitude which we will discuss later. Correspondingly, except for minor variations, there is no difference in the gas column density and mean temperature profiles as function of impact parameter of the different halo subsamples at a target halo mass of $10^{11}\mathrm{M}_{\odot}$ shown in Fig. 4.12. For haloes with target mass $10^{12}\mathrm{M}_{\odot}$, however, the temperature profiles exhibit a significant offset out to about a distance of $\sim 1$ $c$Mpc from the halo centre. Haloes with a large stellar mass, as well as haloes with a large black hole mass have a significantly higher temperature within the mean virial radius of the respective halo sample than haloes with a small stellar mass or small black hole mass. The higher temperature arises from stronger supernovae feedback that is directly caused by a larger stellar mass formed. Hot supernovae driven winds heat the surrounding gas, whereas their impact becomes weaker with distance from the halo centre as the volume of pristine gas across which the thermal wind energy is distributed grows to the third power of distance from the halo centre. We see the same behaviour of the temperature profile for haloes with a large black hole mass though AGN activity is very limited at these halo masses, as the black hole mass correlates with the stellar mass of haloes. This correlation comes about as the growth of both black hole and stellar mass is fuelled by accretion of gas onto the halo, such that high accretion rates lead to both a massive central black hole and a large stellar mass in the halo, and vice versa. At this point, we would like to already point out that in very massive haloes, who undergo strong AGN feedback, but whose deep potential wells limit the reach of supernovae driven winds to the central region of haloes, the stellar mass equally correlates with the black hole mass and here traces the black hole mass and thus AGN activity.

Despite the significant differences in the temperature profiles of $10^{12}\mathrm{M}_{\odot}$ haloes shown in Fig. 4.14 no deviation of the excess Lyman-$\alpha$ absorption profiles for the different halo subsamples is visible. This is due to the fact that despite the large difference in temperature, the mean temperature is significantly below the characteristic ionisation temperature of hydrogen, $T_{\mathrm{H,ion}} \approx 1.57 \cdot 10^5$ $K$, and thus will have negligible impact on the neutral hydrogen present in the gas (see also Section 4.3.3). Starting at a halo mass of $10^{12.5}\mathrm{M}_{\odot}$ the offset between the temperature profiles of haloes with large black hole and stellar mass with respect to haloes with small black hole and stellar mass becomes even more distinct, and the profiles converge to a common value only at distances from the halo centre larger then $\sim 2$ $c$Mpc. As the now constant mean temperature inside the mean virial radius is for the first time above the ionisation temperature of neutral hydrogen this translates into a characteristic change in the functional shape of the excess Lyman-$\alpha$ absorption profiles which inside the virial radius exhibit significantly less excess absorption for haloes with large black hole and stellar mass compared to haloes with small black hole and stellar mass, and converge to the same values outside the virial radius.

The same behaviour is seen in haloes with target mass of $10^{13}M_{\odot}$, whereas these halo sample even exhibits what appears to be a crossover of the excess Lyman-$\alpha$ absorption profiles of haloes with strong and weak feedback. However, due to the rarity of objects of this halo mass, in contrary to all other samples, at the target mass of $10^{13}M_{\odot}$ we had to span a quiet wide halo mass range in oder to apply our statistical subsample selection. Thus at the target mass of $10^{13}M_{\odot}$, haloes with large black hole and stellar mass are also significantly more massive with respect to their total mass than haloes that are selected for the subsamples with low black hole and stellar mass. As in this mass range the halo subsamples with strong feedback are generally more massive, their density profiles as a function of impact parameter also exhibit higher values than the profiles derived from the halo subsamples with weak feedback. This is true also for the other two redshifts, $z = 2.4$ and $z = 2$, presented in the following, but not true for any target halo mass but $10^{13}M_{\odot}$. The higher column density in haloes with strong feedback at $10^{13}M_{\odot}$ leads to a higher Lyman-$\alpha$ absorption outside the virial radius, where the difference between the temperature of the gas in the subsamples with strong and weak feedback shrinks. The combined effect of a higher temperature and a higher gas column density in more massive $10^{13}M_{\odot}$ haloes with strong AGN feedback leads to what is perceived as a characteristic crossover scale of the excess Lyman-$\alpha$ absorption profiles at the virial radius. However, correcting for the offset introduced by the different mean halo mass of the subsamples results in a behaviour that is identical to what we observe for haloes with target halo mass of $10^{12.5}M_{\odot}$, where beyond the virial radius excess Lyman-$\alpha$ absorption profiles converge to the same values.

The described characteristic relation of excess Lyman-$\alpha$ absorption profiles of haloes with strong and weak AGN feedback at target halo mass of $10^{12.5}M_{\odot}$ and $10^{13}M_{\odot}$ becomes increasingly more prominent with decreasing redshift. In Fig. 4.23 and Fig. 4.25 we show the Lyman-$\alpha$ absorption equivalent width (top panel) and excess absorption (bottom panel) as a function of impact parameter for these target halo masses at $z = 2.4$, and in Fig. 4.31 and Fig. 4.33 at $z = 2$. Correspondingly, we show the total gas column densities and mean temperature values in 4.24 and Fig. 4.26 for these massive haloes at $z = 2.4$, and in 4.32 and Fig. 4.34 at $z = 2$. The increasing depletion of excess Lyman-$\alpha$ absorption with time inside the virial radius of massive haloes is a characteristic signature of active AGN feedback heating the cosmic gas.

In Fig. 4.21 and Fig. 4.29 we show the Lyman-$\alpha$ absorption properties of haloes with target mass of $10^{12}M_{\odot}$ at $z = 2.4$ and $z = 2$, respectively, as well as the corresponding column density and temperature profiles in 4.22 and Fig. 4.30. At this target halo mass at all examined redhsifts we consistently find no differences in the excess Lyman-$\alpha$ absorption profiles of haloes with strong and weak feedback that exceed statistical fluctuations. As

discussed already for the profiles at $z = 3$, the absence of differences in the excess Lyman-$\alpha$ absorption is due to an unchanged gas column density contributing to the absorption, as well as due to the mean temperature (albeit being significantly offset for haloes with strong and weak feedback) being substantially below the ionisation temperature for neural hydrogen. Examining Fig. 4.29 in more detail a slight offset of the excess Lyman-$\alpha$ absorption of haloes with small black hole mass to higher values can be detected. The offset is similar to the offset of the excess Lyman-$\alpha$ absorption of $10^{12}\mathrm{M}_{\odot}$ haloes with large stellar mass at $z = 3$ shown in Fig. 4.13. This behaviour is likely due to some of the haloes that were selected for the respective sample being located in a high density environment, e.g. in the vicinity of a large galaxy cluster. As we employ only 10 haloes for which we mock 12 independent observations each, even one or two of our objects being located in a special environment can have the observed systematic impact on the excess Lyman-$\alpha$ absorption.

Finally, in Fig. 4.19 and Fig. 4.27 we show the Lyman-$\alpha$ absorption properties of haloes with target mass of $10^{11}\mathrm{M}_{\odot}$ at $z = 2.4$ and $z = 2$, respectively, as well as the corresponding gas column density and temperature profiles in 4.20 and Fig. 4.28. Interestingly, we find an inverted temperature evolution with redshift with respect to all other target halo masses. At $10^{11}\mathrm{M}_{\odot}$ the temperature profiles divert from each other with decreasing redshift, however, the mean temperature does not grow with time. Also, the temperature profiles of the halo subsamples with large stellar and black hole mass tracing strong supernovae feedback, lay below the temperature profiles of haloes with weak feedback. Naively, we would have expected supernovae winds to heat the gas and produce an opposite trend. However, the mean temperature of all halo samples is substantially below the temperature necessary to ionise neutral hydrogen, such that the differences in the mean temperature will not affect the excess Lyman-$\alpha$ absorption. Furthermore, at $z = 2.4$ haloes with target mass of $10^{11}\mathrm{M}_{\odot}$ are the only ones to exhibit a small offset in the gas column density profiles between the halo samples with strong and weak supernovae winds. This is likely due to a higher number of the same haloes being selected for the subsamples with small stellar and black hole mass, and with large stellar and black hole mass, compared to other target halo masses and redshifts. Thus the profiles of the respective samples follow each other very accurately opening up what appears to be a gap between the two sets of profiles. At $z = 2$ the gas column density profiles of $10^{11}\mathrm{M}_{\odot}$ haloes again exhibit no features dependent on halo properties. Nevertheless, we find a growing separation of the excess Lyman-$\alpha$ absorption with time that is driven by the differences in stellar mass of the halo subsamples. Both at $z = 2.4$ and $z = 2$, we find significantly more Lyman-$\alpha$ absorption in haloes with small stellar mass compared to a large stellar mass, to a given extent also traced by the black hole mass. We interpret this as not being caused by the strength of supernovae winds but rather by the consumption of gas for

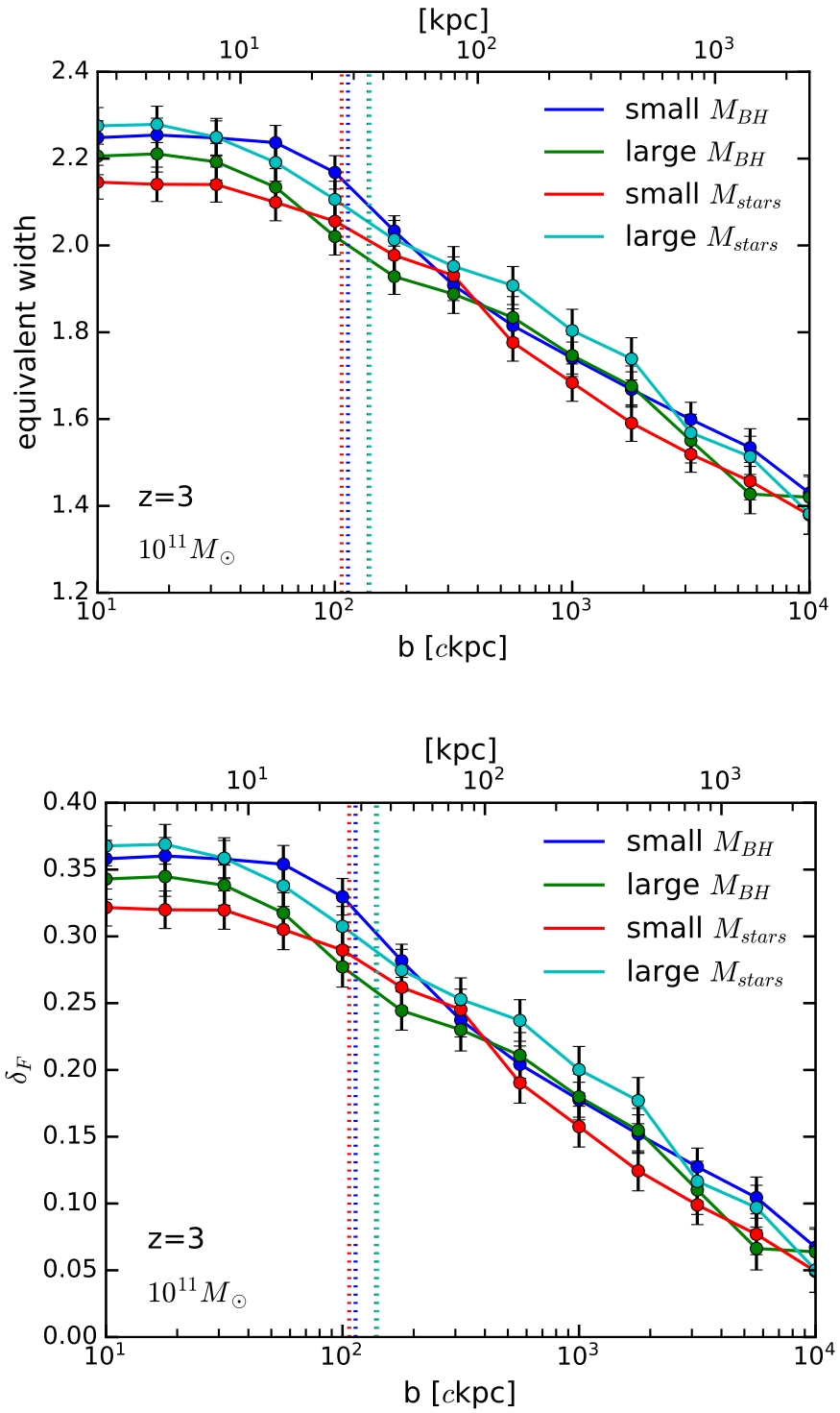


Figure 4.11: Lyman-$\alpha$ absorption equivalent width (*top panel*) and excess absorption (*bottom panel*) as a function of impact parameter $b$ for haloes of $10^{11}\mathrm{M}_\odot$ at $z = 3$ split into exhibiting strong (cyan) and weak (red) supernovae driven winds, and strong (green) and weak (blue) AGN feedback driven outflows. Error bars correspond to the standard error derived from 120 independent Lyman-$\alpha$ spectra contributing to each measurement. Dashed lines correspond to the mean virial radii of each halo sample, colour-coded correspondingly.

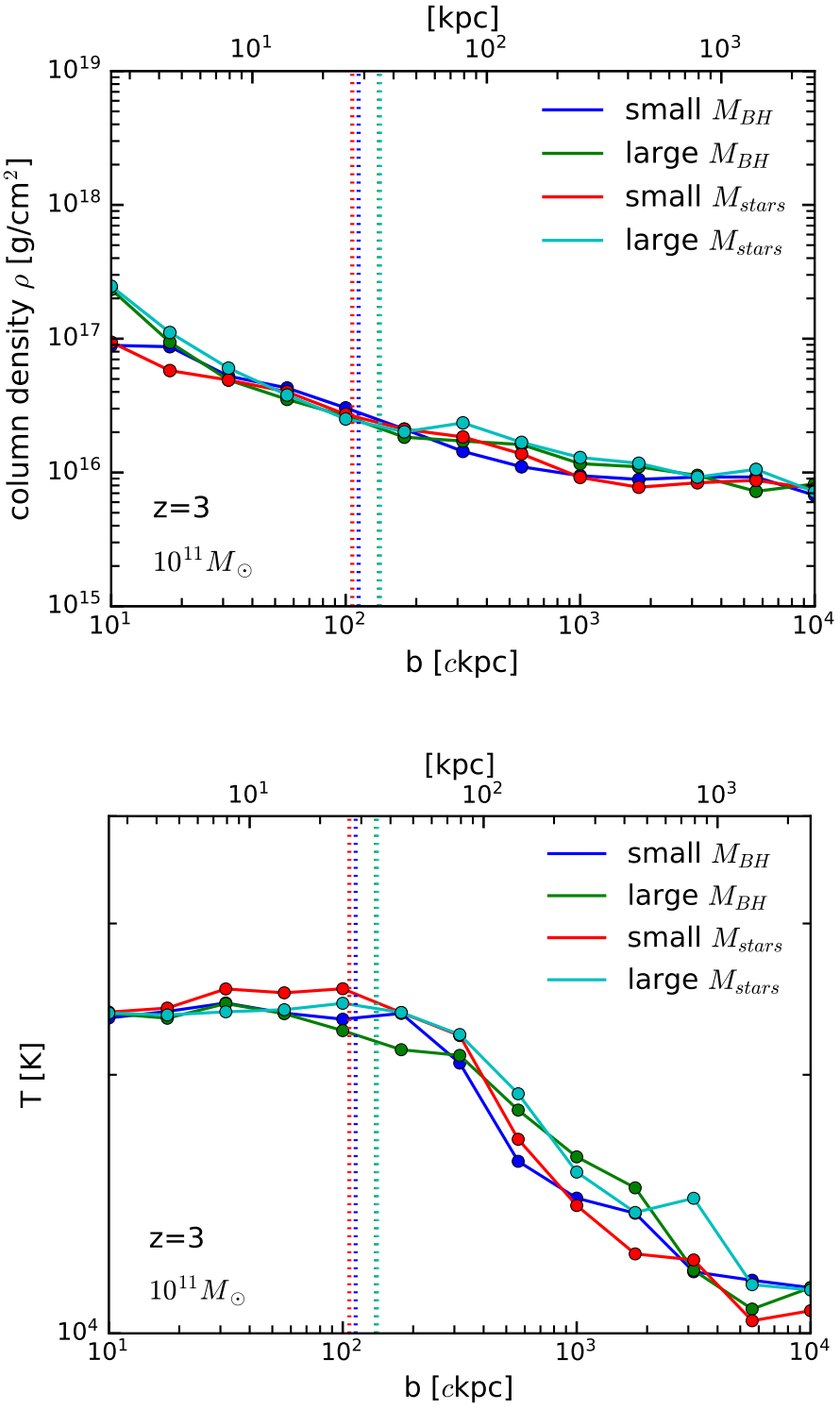


Figure 4.12: Integrated total column density (*top panel*) and median temperature (*bottom panel*) of the gas leading to the previously shown excess Lyman-$\alpha$ absorption as a function of impact parameter $b$ for haloes of $10^{11}\mathrm{M}_\odot$ at $z = 3$ split into exhibiting strong (cyan) and weak (red) supernovae driven winds, and strong (green) and weak (blue) AGN feedback driven outflows. Dashed lines correspond to the mean virial radii of each halo sample, colour-coded correspondingly.

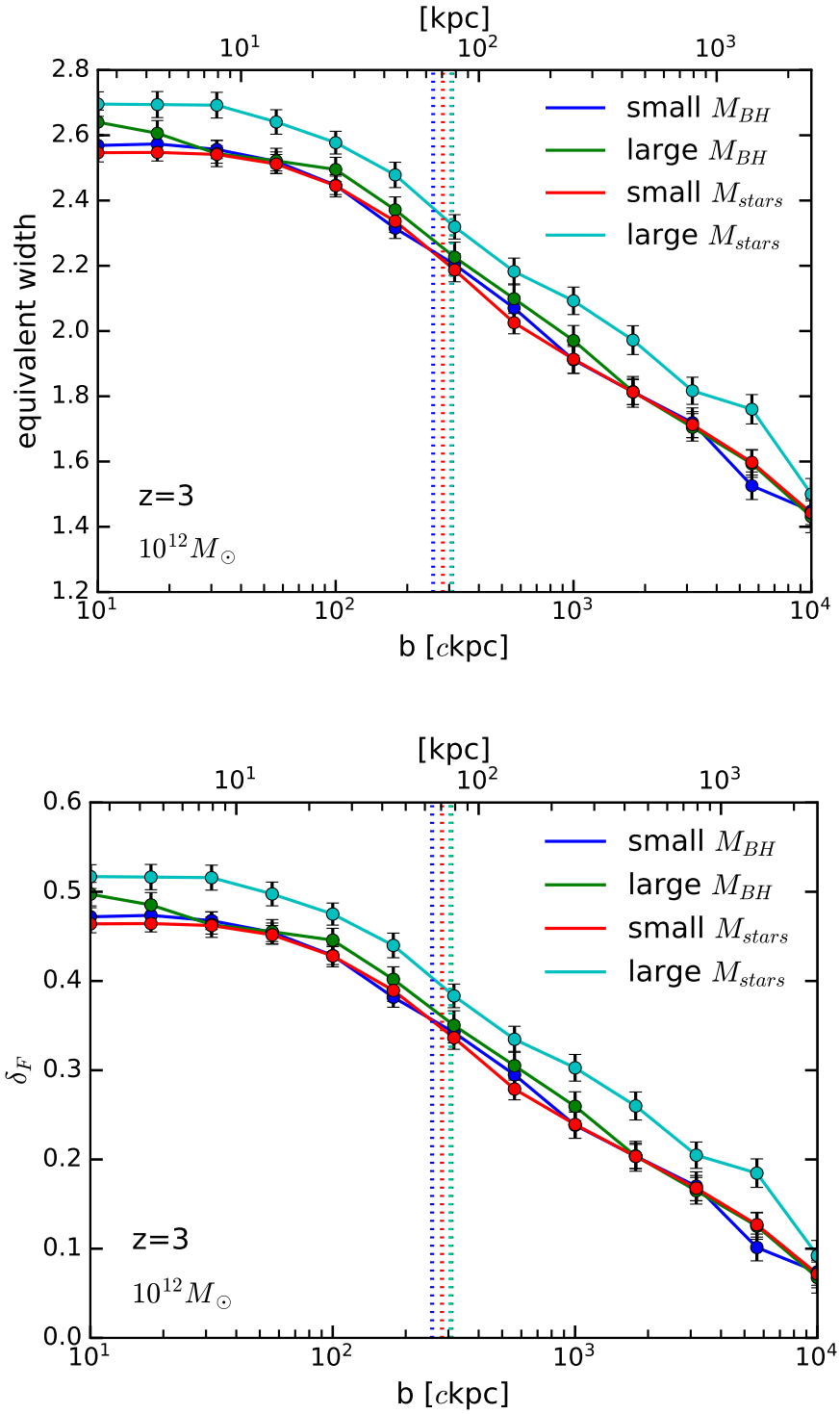


Figure 4.13: Lyman-$\alpha$ absorption equivalent width (*top panel*) and excess absorption (*bottom panel*) as a function of impact parameter $b$ for haloes of $10^{12}\mathrm{M}_\odot$ at $z = 3$ split into exhibiting strong (cyan) and weak (red) supernovae driven winds, and strong (green) and weak (blue) AGN feedback driven outflows. Error bars correspond to the standard error derived from 120 independent Lyman-$\alpha$ spectra contributing to each measurement. Dashed lines correspond to the mean virial radii of each halo sample, colour-coded correspondingly.

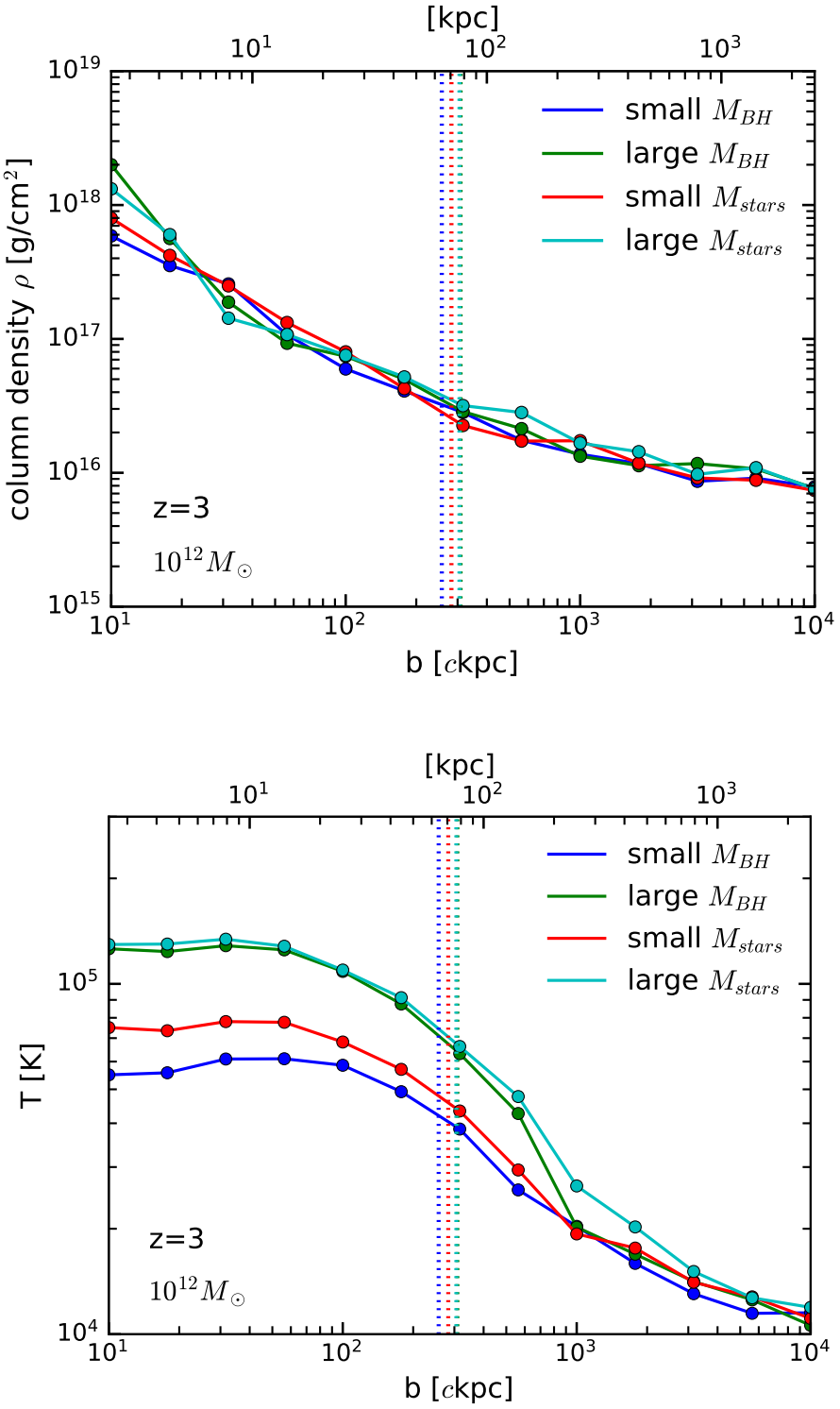


Figure 4.14: Integrated total column density (*top panel*) and median temperature (*bottom panel*) of the gas leading to the previously shown excess Lyman-$\alpha$ absorption as a function of impact parameter $b$ for haloes of $10^{12}\mathrm{M}_\odot$ at $z = 3$ split into exhibiting strong (cyan) and weak (red) supernovae driven winds, and strong (green) and weak (blue) AGN feedback driven outflows. Dashed lines correspond to the mean virial radii of each halo sample, colour-coded correspondingly.

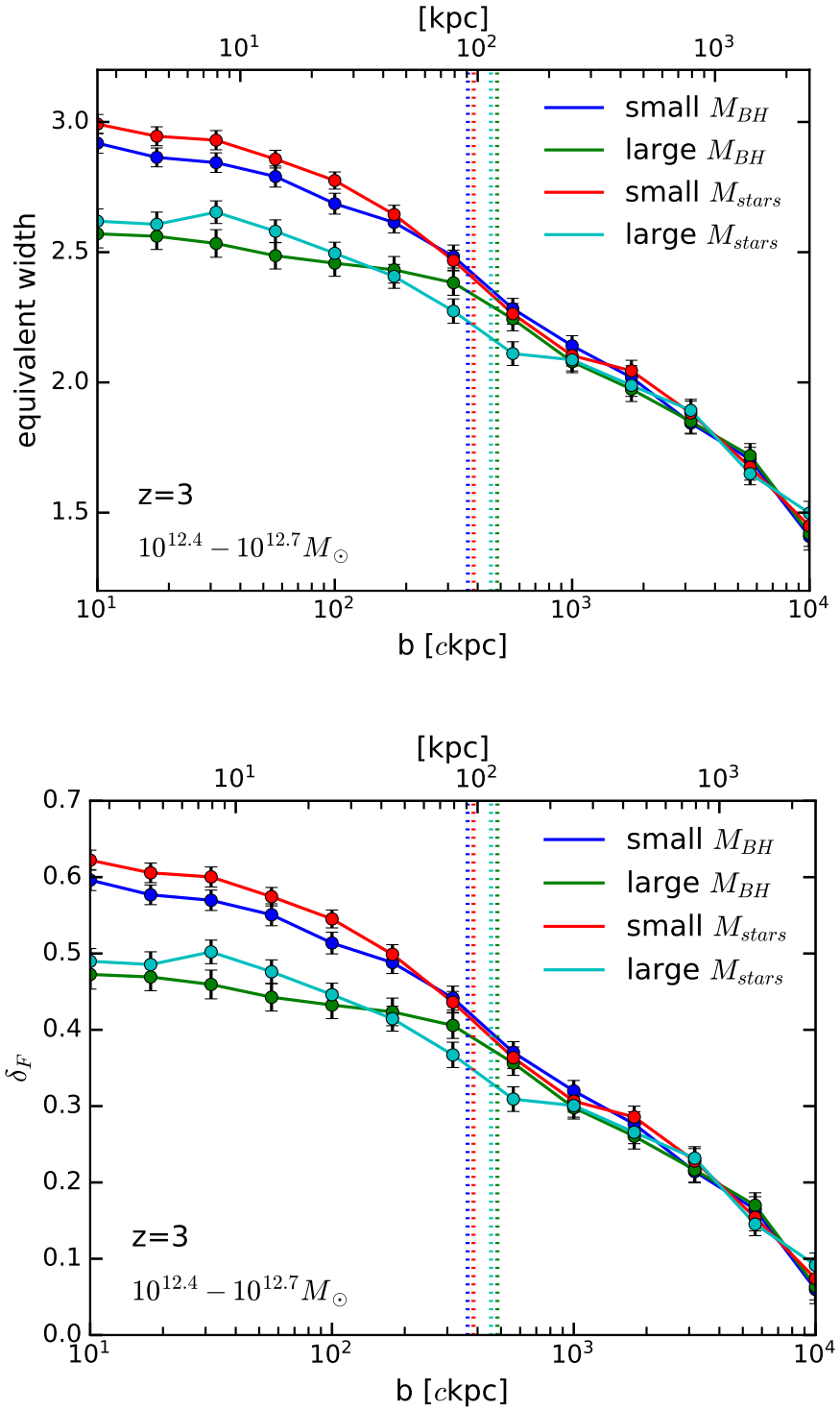


Figure 4.15: Lyman-$\alpha$ absorption equivalent width (*top panel*) and excess absorption (*bottom panel*) as a function of impact parameter $b$ for haloes of $10^{12.5}\mathrm{M}_\odot$ at $z = 3$ split into exhibiting strong (cyan) and weak (red) supernovae driven winds, and strong (green) and weak (blue) AGN feedback driven outflows. Error bars correspond to the standard error derived from 120 independent Lyman-$\alpha$ spectra contributing to each measurement. Dashed lines correspond to the mean virial radii of each halo sample, colour-coded correspondingly.

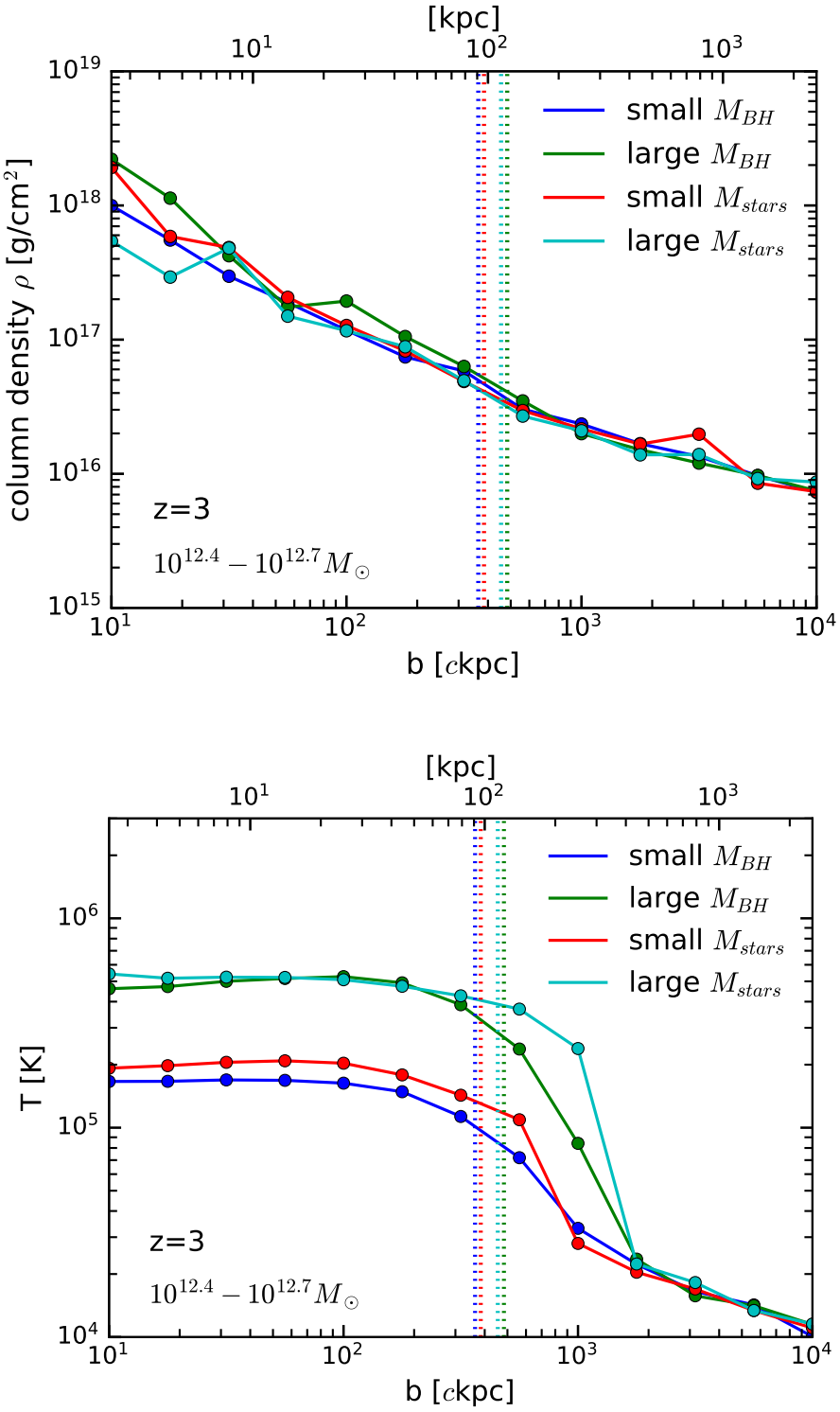


Figure 4.16: Integrated total column density (*top panel*) and median temperature (*bottom panel*) of the gas leading to the previously shown excess Lyman-$\alpha$ absorption as a function of impact parameter $b$ for haloes of $10^{12.5}$M$_\odot$ at $z = 3$ split into exhibiting strong (cyan) and weak (red) supernovae driven winds, and strong (green) and weak (blue) AGN feedback driven outflows. Dashed lines correspond to the mean virial radii of each halo sample, colour-coded correspondingly.

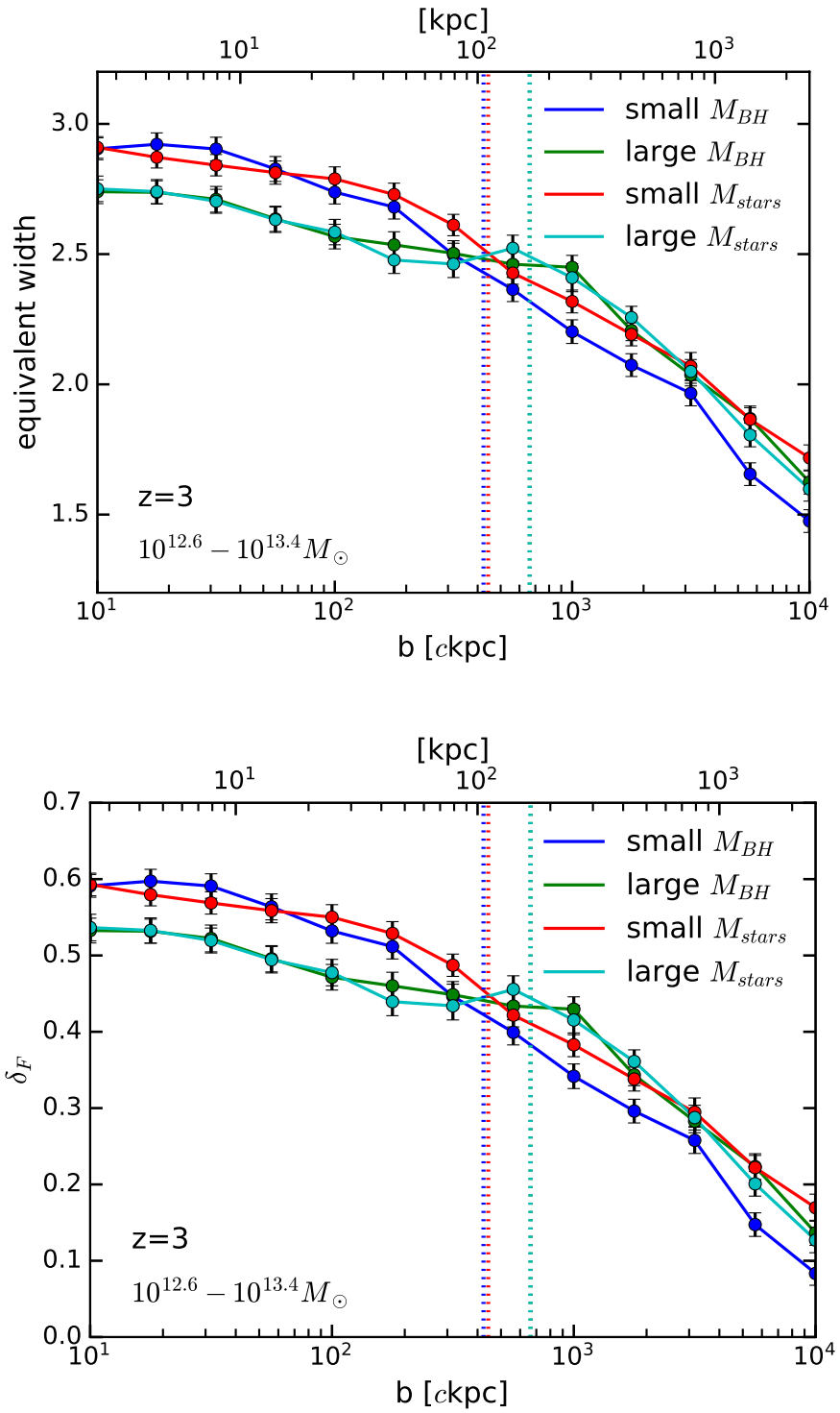


Figure 4.17: Lyman-$\alpha$ absorption equivalent width (*top panel*) and excess absorption (*bottom panel*) as a function of impact parameter $b$ for haloes of $10^{13}\mathrm{M}_\odot$ at $z = 3$ split into exhibiting strong (cyan) and weak (red) supernovae driven winds, and strong (green) and weak (blue) AGN feedback driven outflows. Error bars correspond to the standard error derived from 120 independent Lyman-$\alpha$ spectra contributing to each measurement. Dashed lines correspond to the mean virial radii of each halo sample, colour-coded correspondingly.

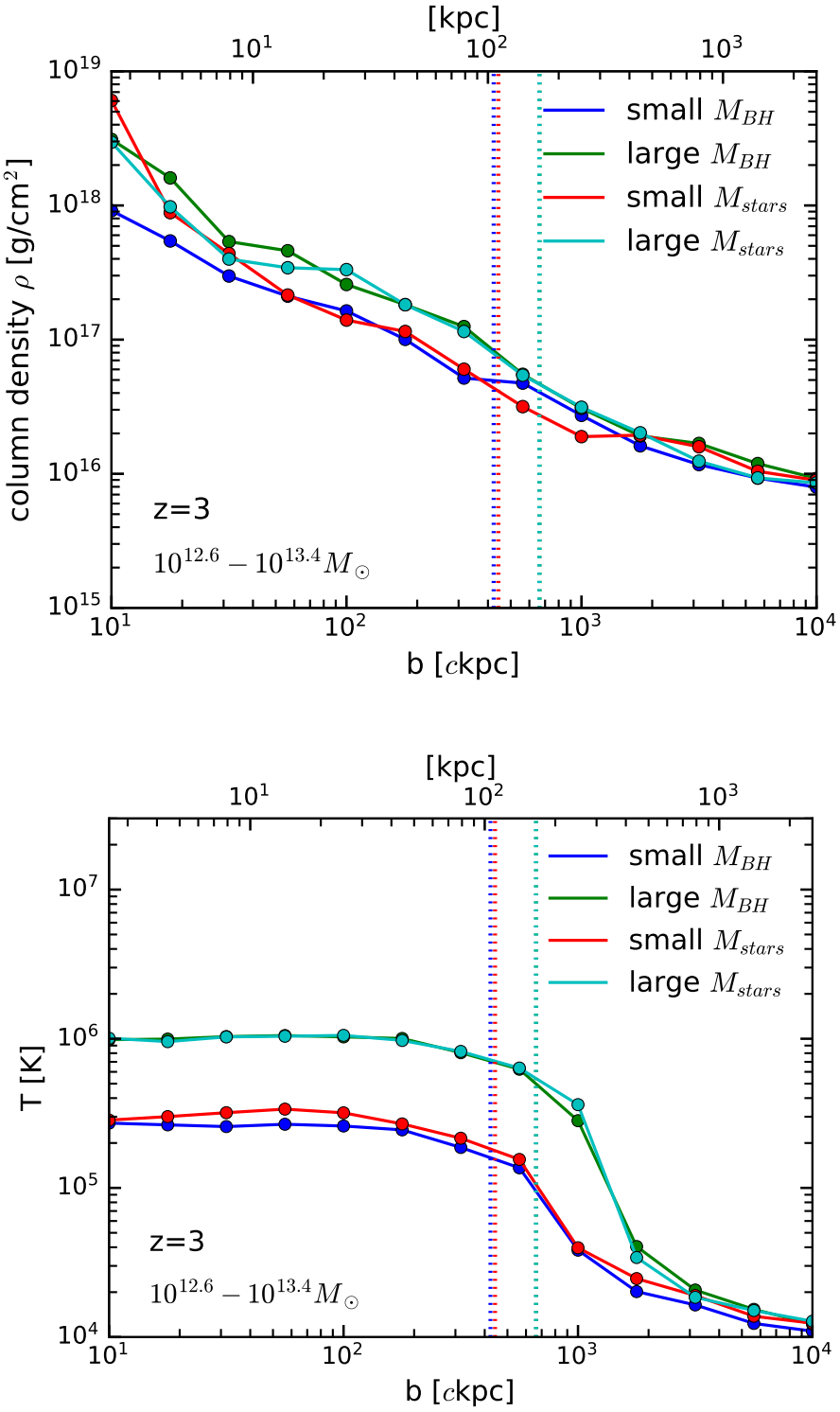


Figure 4.18: Integrated total column density (*top panel*) and median temperature (*bottom panel*) of the gas leading to the previously shown excess Lyman-$\alpha$ absorption as a function of impact parameter $b$ for haloes of $10^{13}\mathrm{M}_\odot$ at $z = 3$ split into exhibiting strong (cyan) and weak (red) supernovae driven winds, and strong (green) and weak (blue) AGN feedback driven outflows. Dashed lines correspond to the mean virial radii of each halo sample, colour-coded correspondingly.

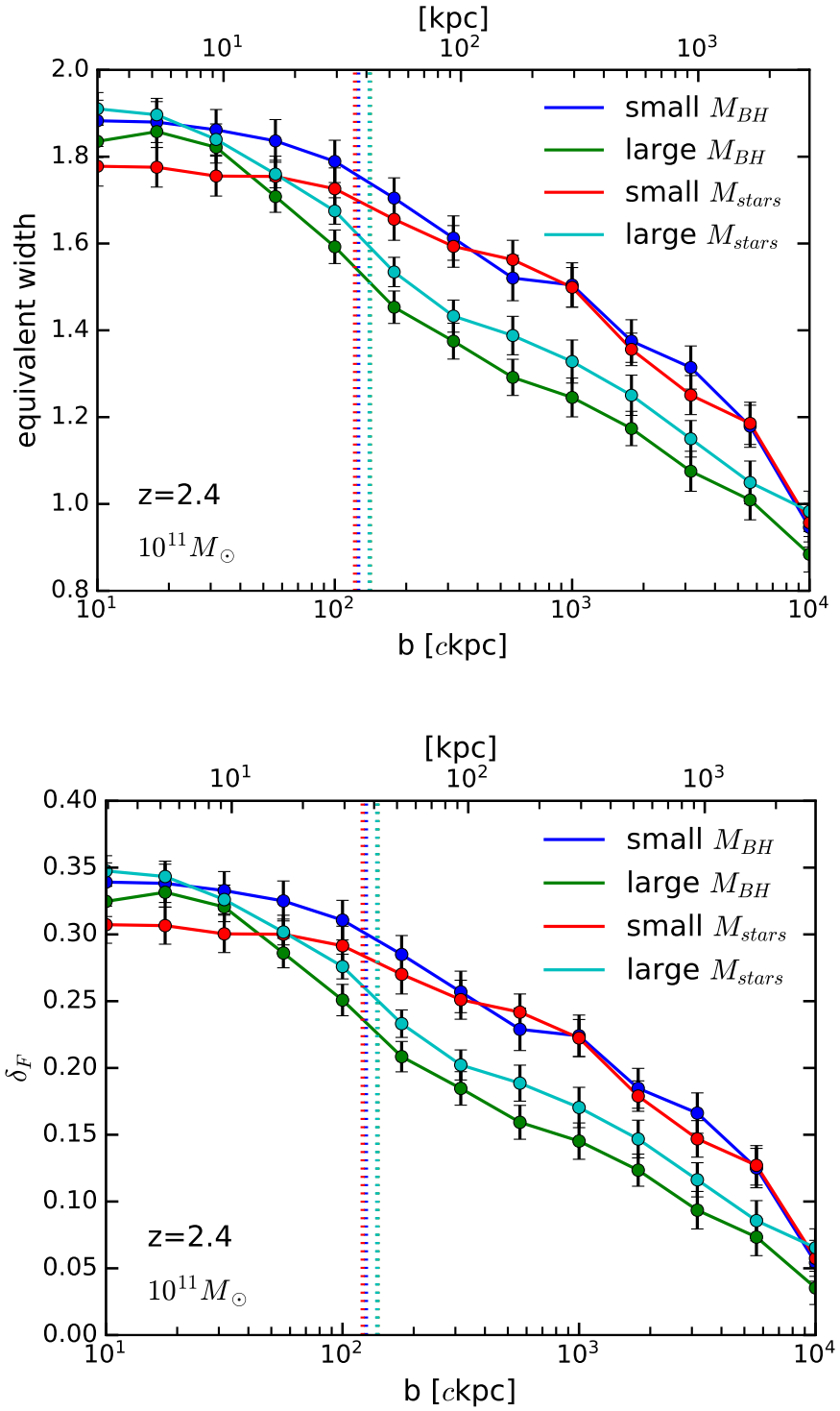


Figure 4.19: Lyman-$\alpha$ absorption equivalent width (*top panel*) and excess absorption (*bottom panel*) as a function of impact parameter $b$ for haloes of $10^{11}\mathrm{M}_\odot$ at $z = 2.4$ split into exhibiting strong (cyan) and weak (red) supernovae driven winds, and strong (green) and weak (blue) AGN feedback driven outflows. Error bars correspond to the standard error derived from 120 independent Lyman-$\alpha$ spectra contributing to each measurement. Dashed lines correspond to the mean virial radii of each halo sample, colour-coded correspondingly.

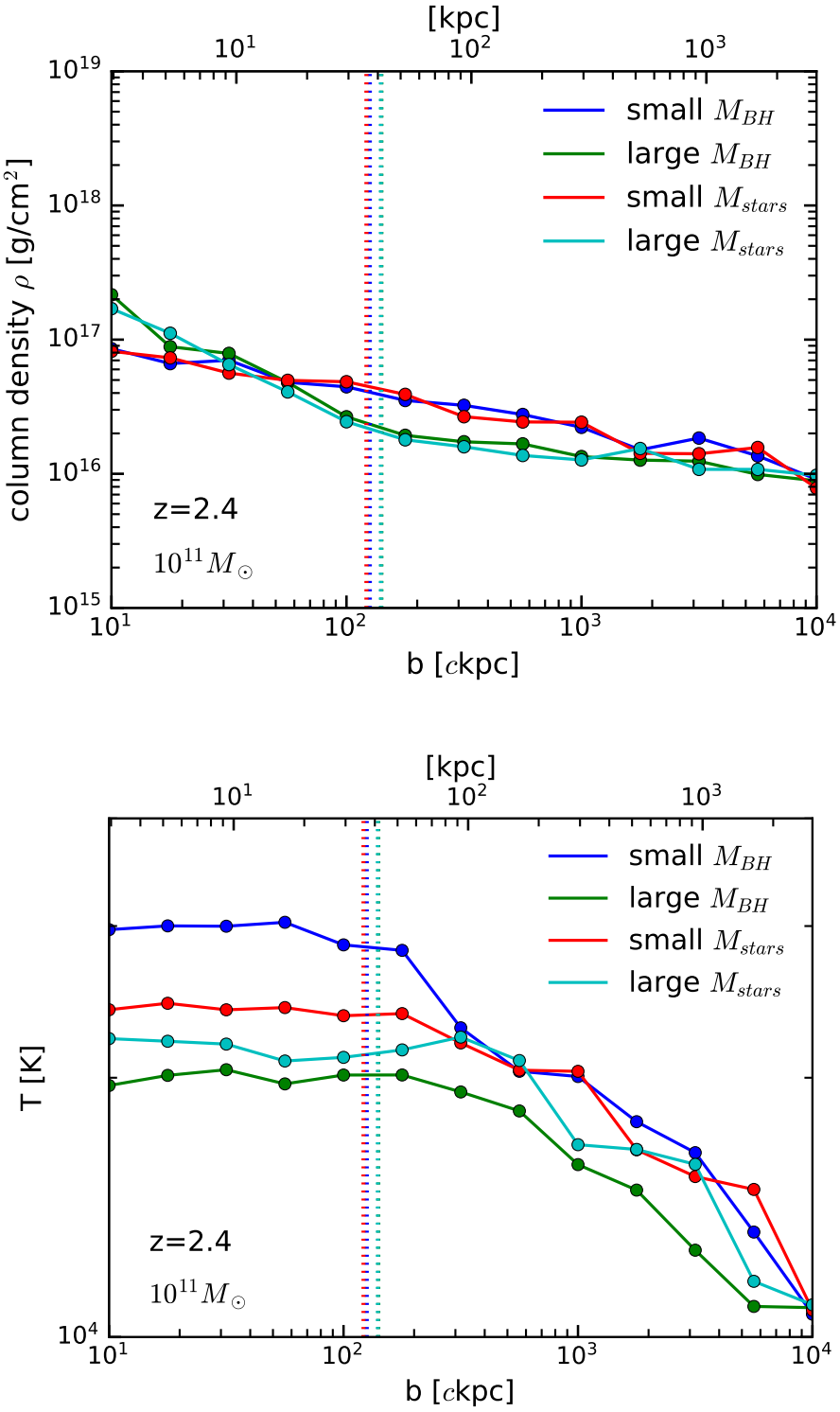


Figure 4.20: Integrated total column density (*top panel*) and median temperature (*bottom panel*) of the gas leading to the previously shown excess Lyman-$\alpha$ absorption as a function of impact parameter $b$ for haloes of $10^{11}$M$_\odot$ at $z = 2.4$ split into exhibiting strong (cyan) and weak (red) supernovae driven winds, and strong (green) and weak (blue) AGN feedback driven outflows. Dashed lines correspond to the mean virial radii of each halo sample, colour-coded correspondingly.

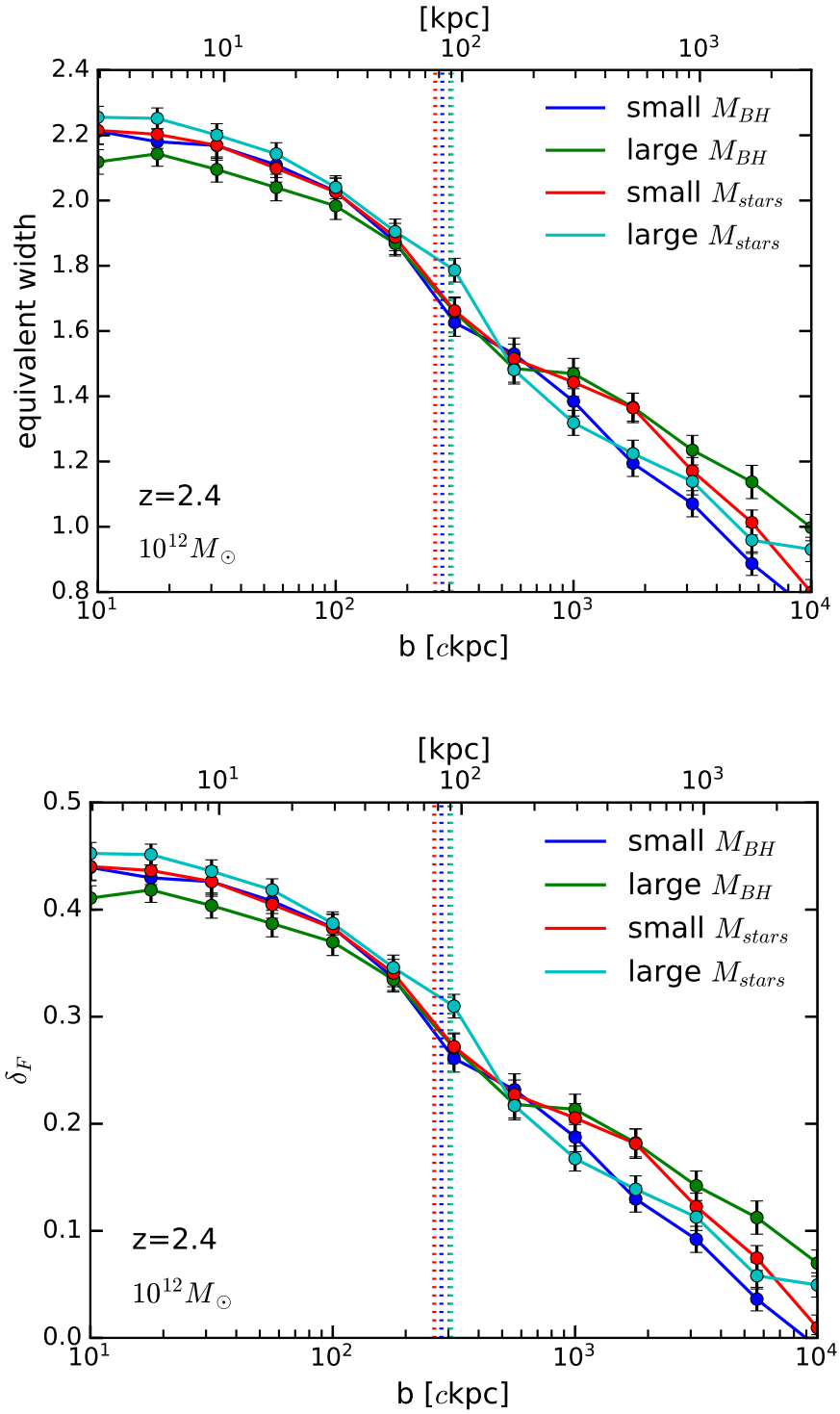


Figure 4.21: Lyman-$\alpha$ absorption equivalent width (*top panel*) and excess absorption (*bottom panel*) as a function of impact parameter $b$ for haloes of $10^{12}\mathrm{M}_\odot$ at $z = 2.4$ split into exhibiting strong (cyan) and weak (red) supernovae driven winds, and strong (green) and weak (blue) AGN feedback driven outflows. Error bars correspond to the standard error derived from 120 independent Lyman-$\alpha$ spectra contributing to each measurement. Dashed lines correspond to the mean virial radii of each halo sample, colour-coded correspondingly.

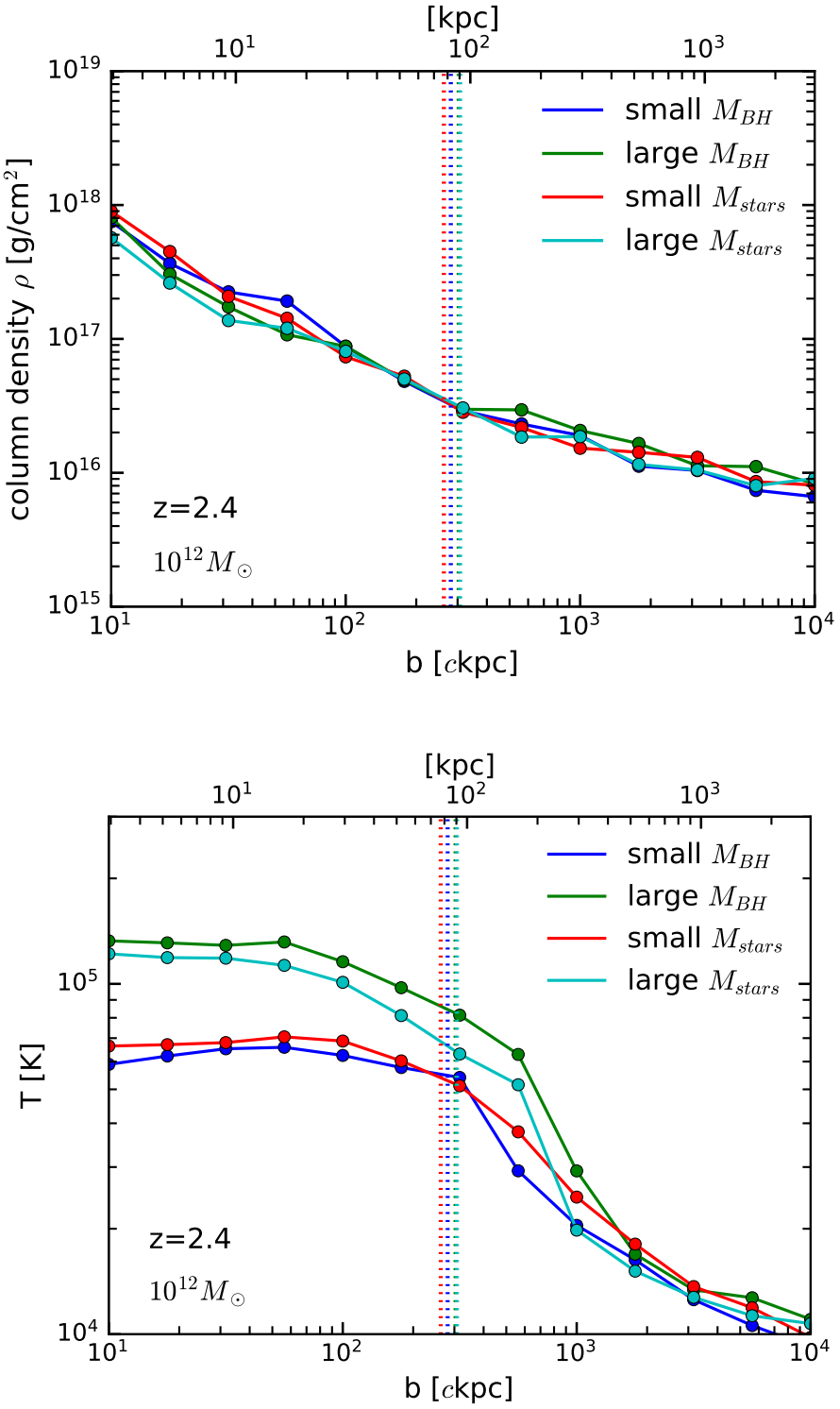


Figure 4.22: Integrated total column density (*top panel*) and median temperature (*bottom panel*) of the gas leading to the previously shown excess Lyman-$\alpha$ absorption as a function of impact parameter $b$ for haloes of $10^{12}\mathrm{M}_\odot$ at $z = 2.4$ split into exhibiting strong (cyan) and weak (red) supernovae driven winds, and strong (green) and weak (blue) AGN feedback driven outflows. Dashed lines correspond to the mean virial radii of each halo sample, colour-coded correspondingly.

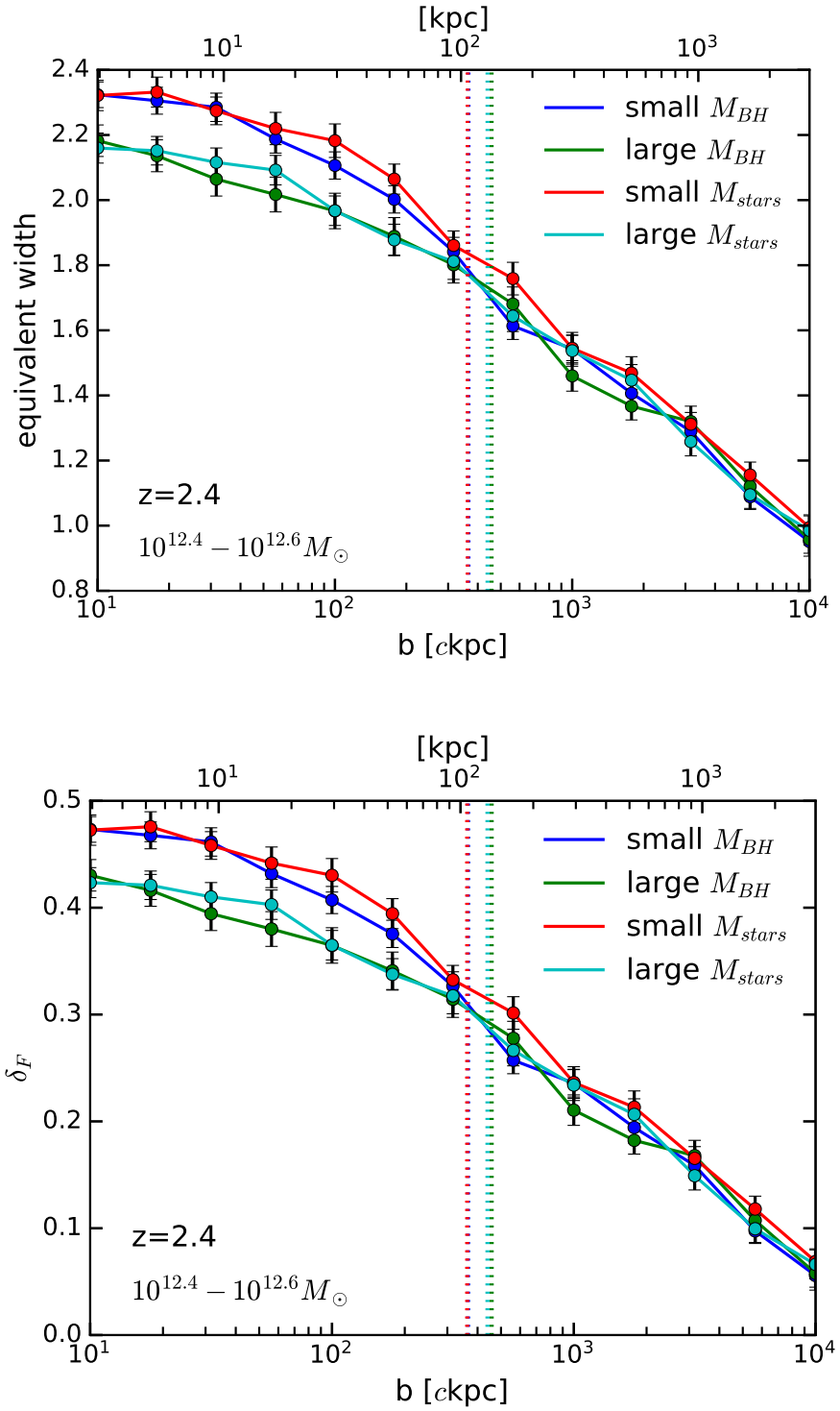


Figure 4.23: Lyman-$\alpha$ absorption equivalent width (*top panel*) and excess absorption (*bottom panel*) as a function of impact parameter $b$ for haloes of $10^{12.5}\mathrm{M}_\odot$ at $z = 2.4$ split into exhibiting strong (cyan) and weak (red) supernovae driven winds, and strong (green) and weak (blue) AGN feedback driven outflows. Error bars correspond to the standard error derived from 120 independent Lyman-$\alpha$ spectra contributing to each measurement. Dashed lines correspond to the mean virial radii of each halo sample, colour-coded correspondingly.

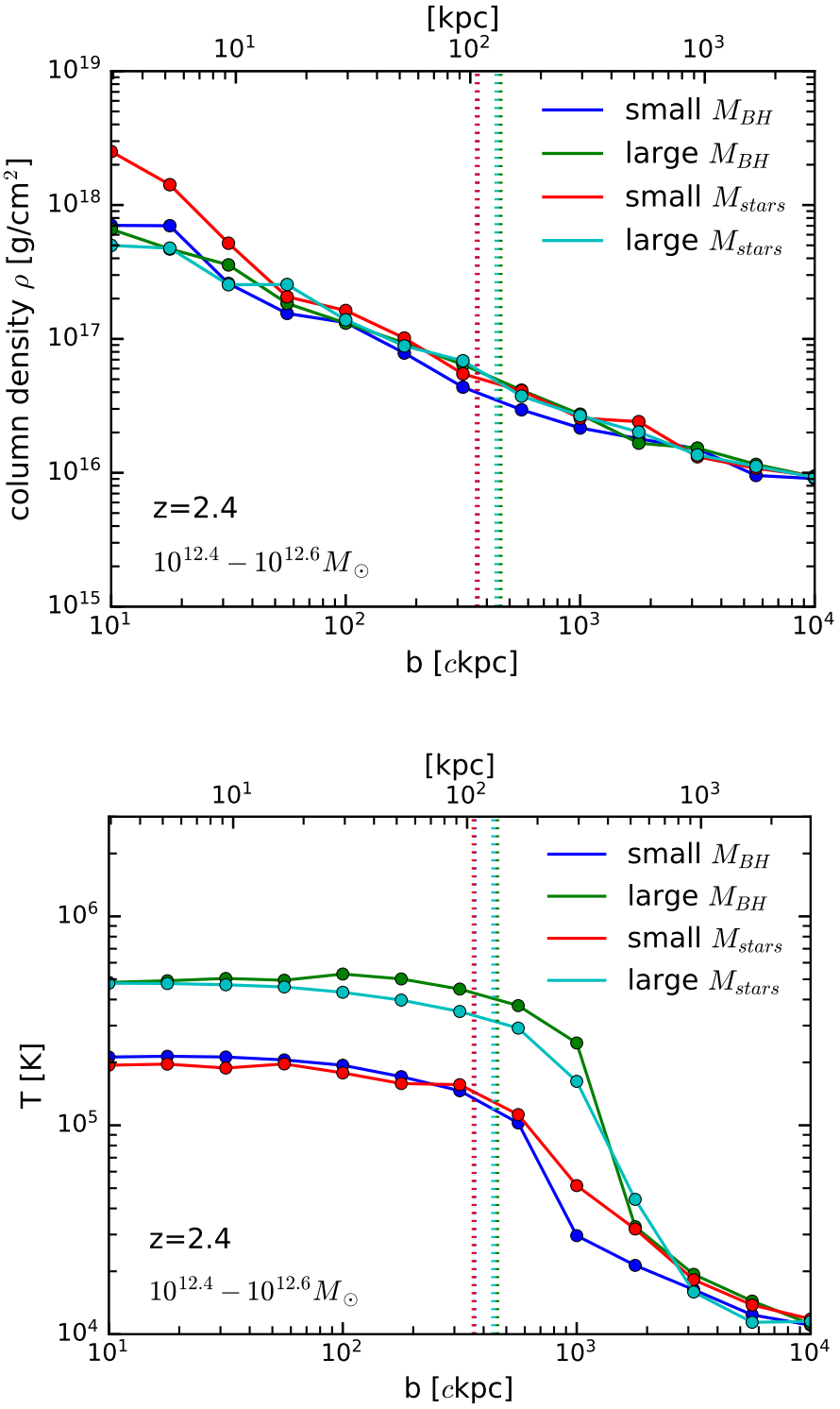


Figure 4.24: Integrated total column density (*top panel*) and median temperature (*bottom panel*) of the gas leading to the previously shown excess Lyman-$\alpha$ absorption as a function of impact parameter $b$ for haloes of $10^{12.5}$M$_\odot$ at $z = 2.4$ split into exhibiting strong (cyan) and weak (red) supernovae driven winds, and strong (green) and weak (blue) AGN feedback driven outflows. Dashed lines correspond to the mean virial radii of each halo sample, colour-coded correspondingly.

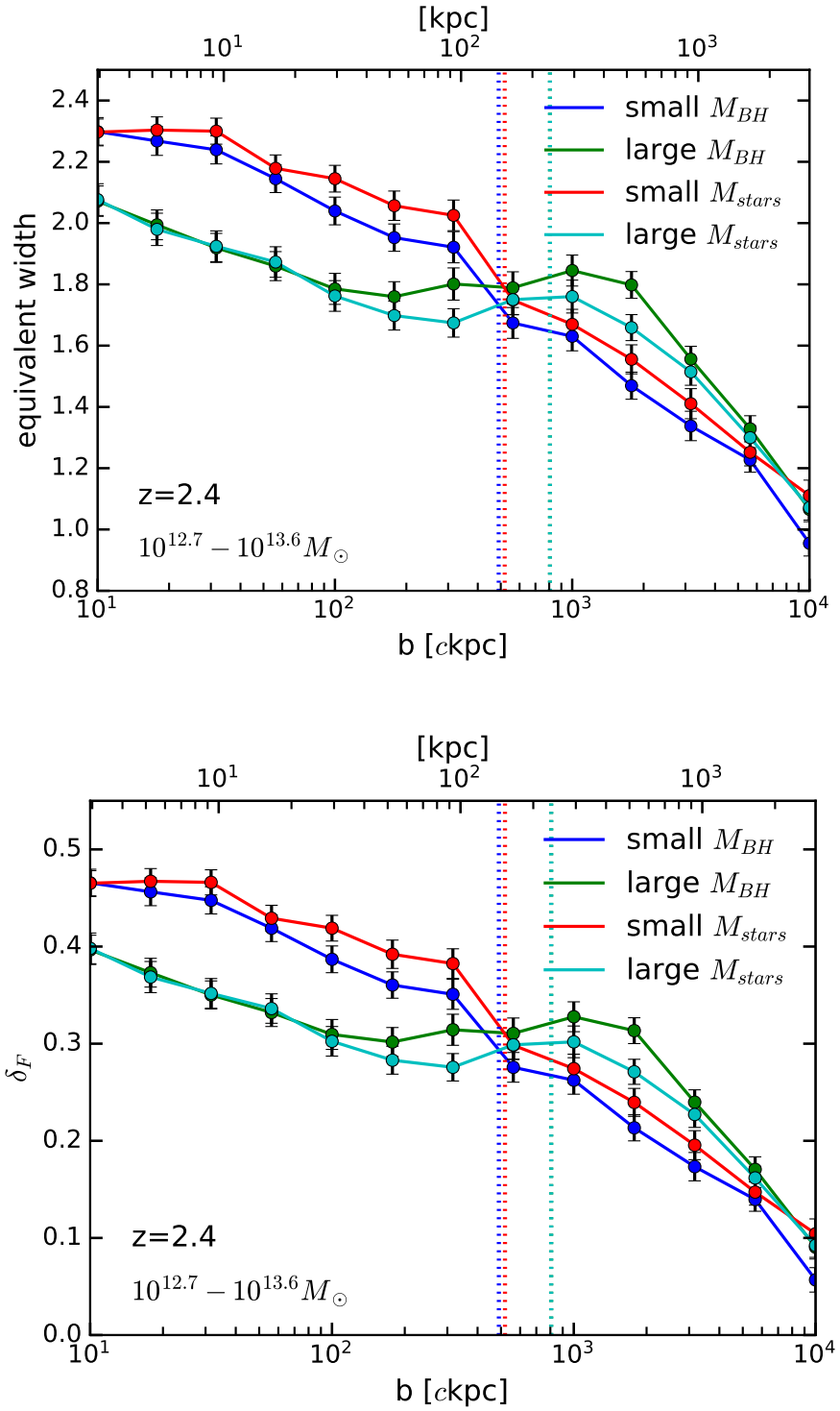


Figure 4.25: Lyman-$\alpha$ absorption equivalent width (*top panel*) and excess absorption (*bottom panel*) as a function of impact parameter $b$ for haloes of $10^{13}\mathrm{M}_\odot$ at $z = 2.4$ split into exhibiting strong (cyan) and weak (red) supernovae driven winds, and strong (green) and weak (blue) AGN feedback driven outflows. Error bars correspond to the standard error derived from 120 independent Lyman-$\alpha$ spectra contributing to each measurement. Dashed lines correspond to the mean virial radii of each halo sample, colour-coded correspondingly.

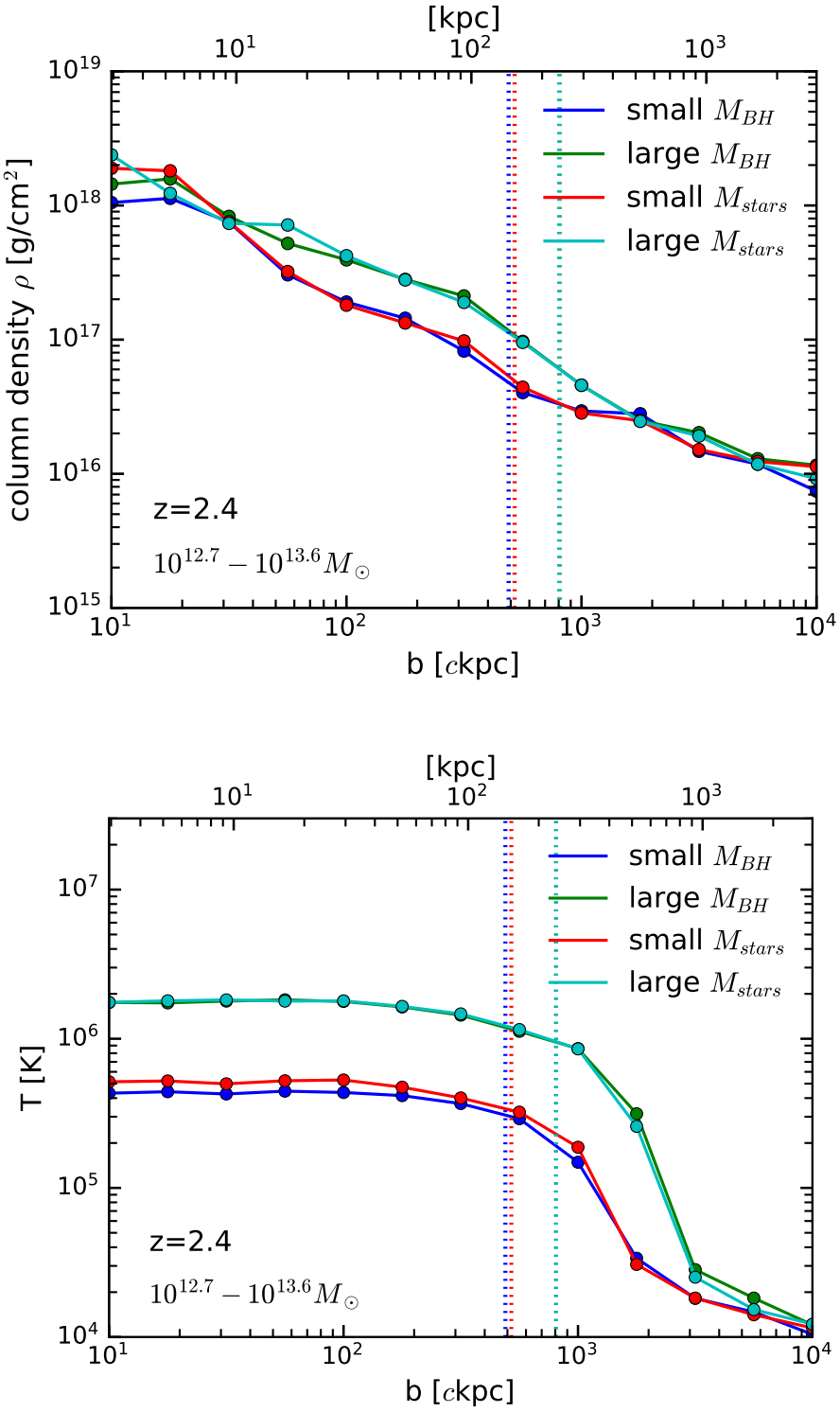


Figure 4.26: Integrated total column density (*top panel*) and median temperature (*bottom panel*) of the gas leading to the previously shown excess Lyman-$\alpha$ absorption as a function of impact parameter $b$ for haloes of $10^{13}$M$_\odot$ at $z = 2.4$ split into exhibiting strong (cyan) and weak (red) supernovae driven winds, and strong (green) and weak (blue) AGN feedback driven outflows. Dashed lines correspond to the mean virial radii of each halo sample, colour-coded correspondingly.

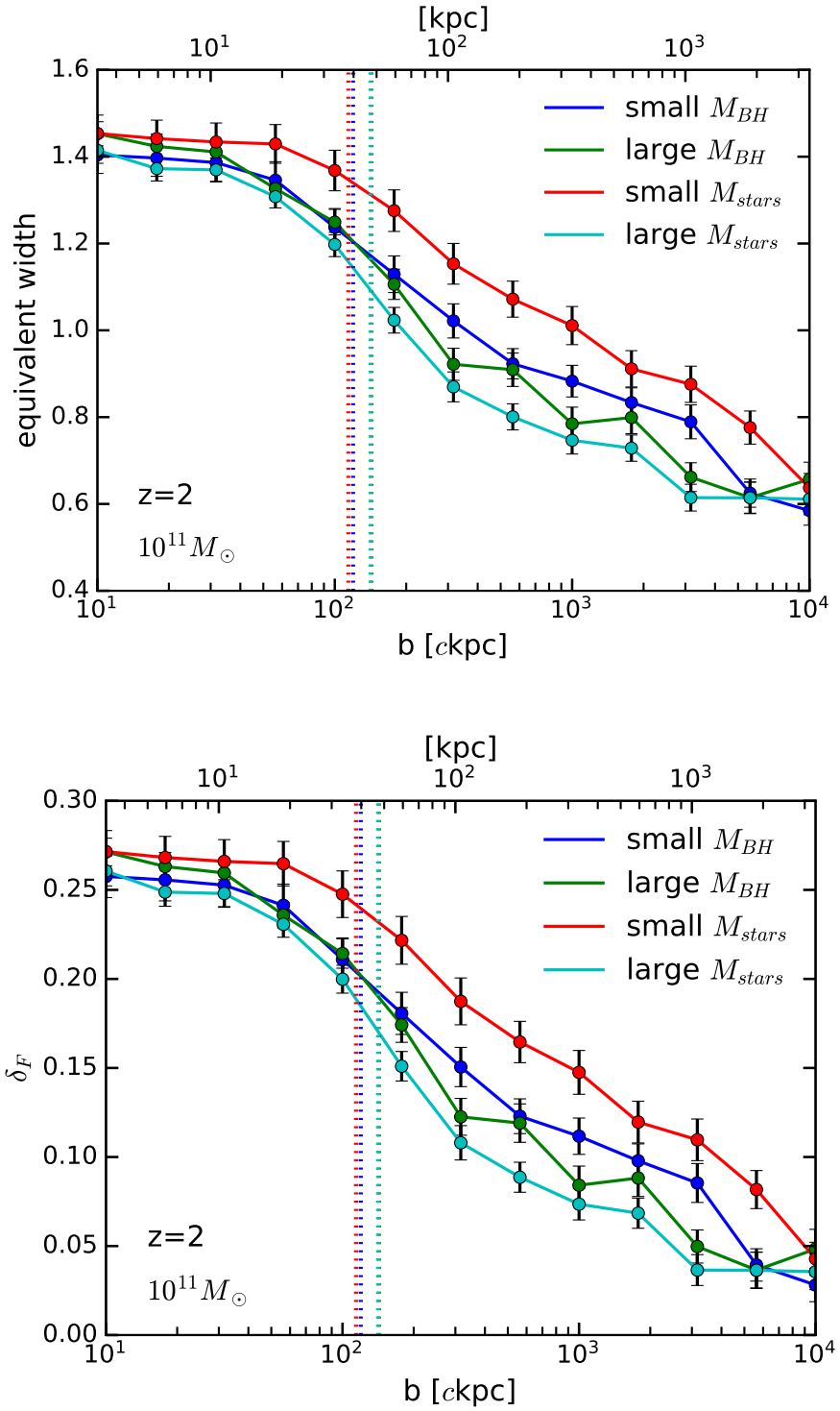


Figure 4.27: Lyman-$\alpha$ absorption equivalent width (*top panel*) and excess absorption (*bottom panel*) as a function of impact parameter $b$ for haloes of $10^{11}\mathrm{M}_\odot$ at $z = 2$ split into exhibiting strong (cyan) and weak (red) supernovae driven winds, and strong (green) and weak (blue) AGN feedback driven outflows. Error bars correspond to the standard error derived from 120 independent Lyman-$\alpha$ spectra contributing to each measurement. Dashed lines correspond to the mean virial radii of each halo sample, colour-coded correspondingly.

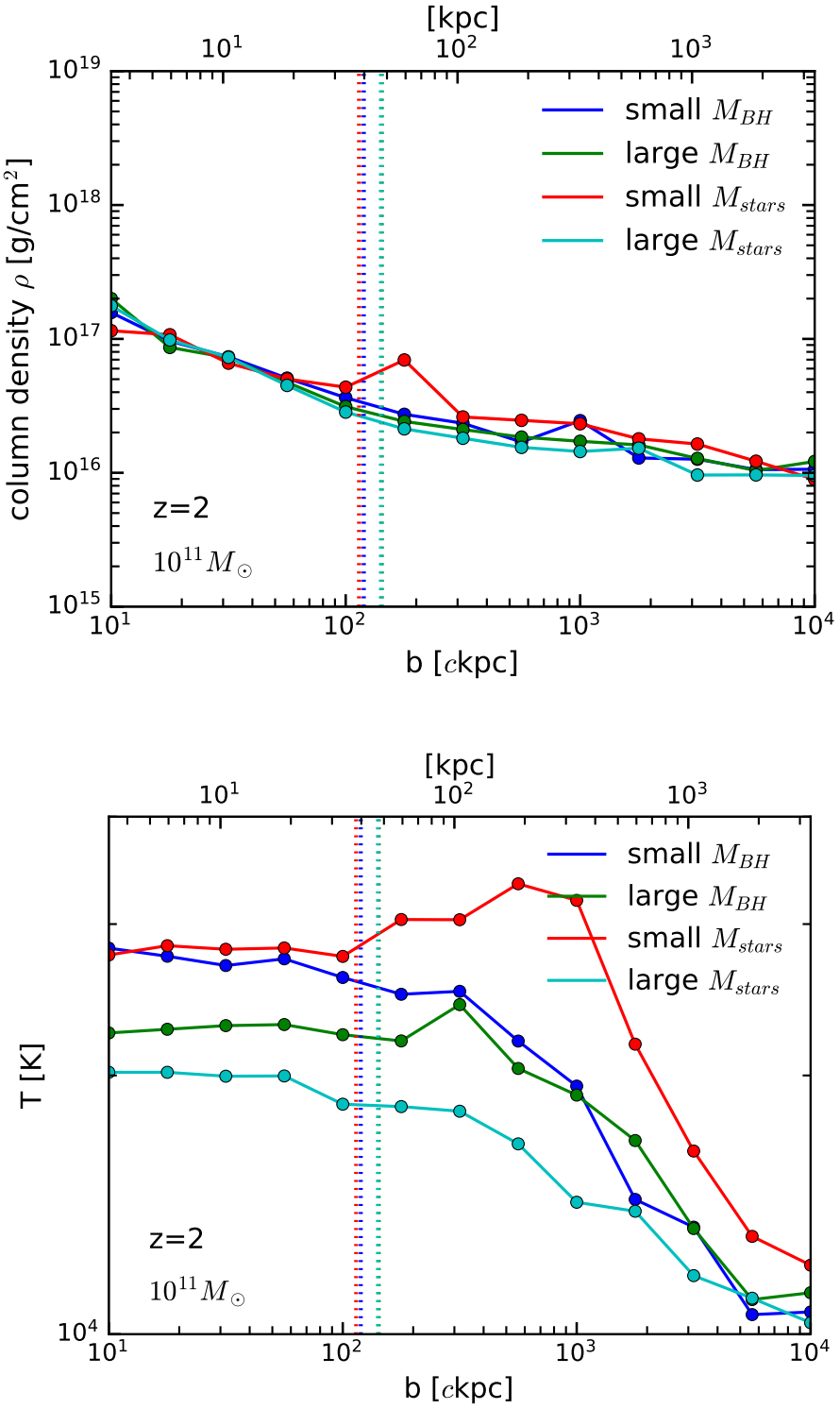


Figure 4.28: Integrated total column density (*top panel*) and median temperature (*bottom panel*) of the gas leading to the previously shown excess Lyman-$\alpha$ absorption as a function of impact parameter $b$ for haloes of $10^{11}\mathrm{M}_\odot$ at $z = 2$ split into exhibiting strong (cyan) and weak (red) supernovae driven winds, and strong (green) and weak (blue) AGN feedback driven outflows. Dashed lines correspond to the mean virial radii of each halo sample, colour-coded correspondingly.

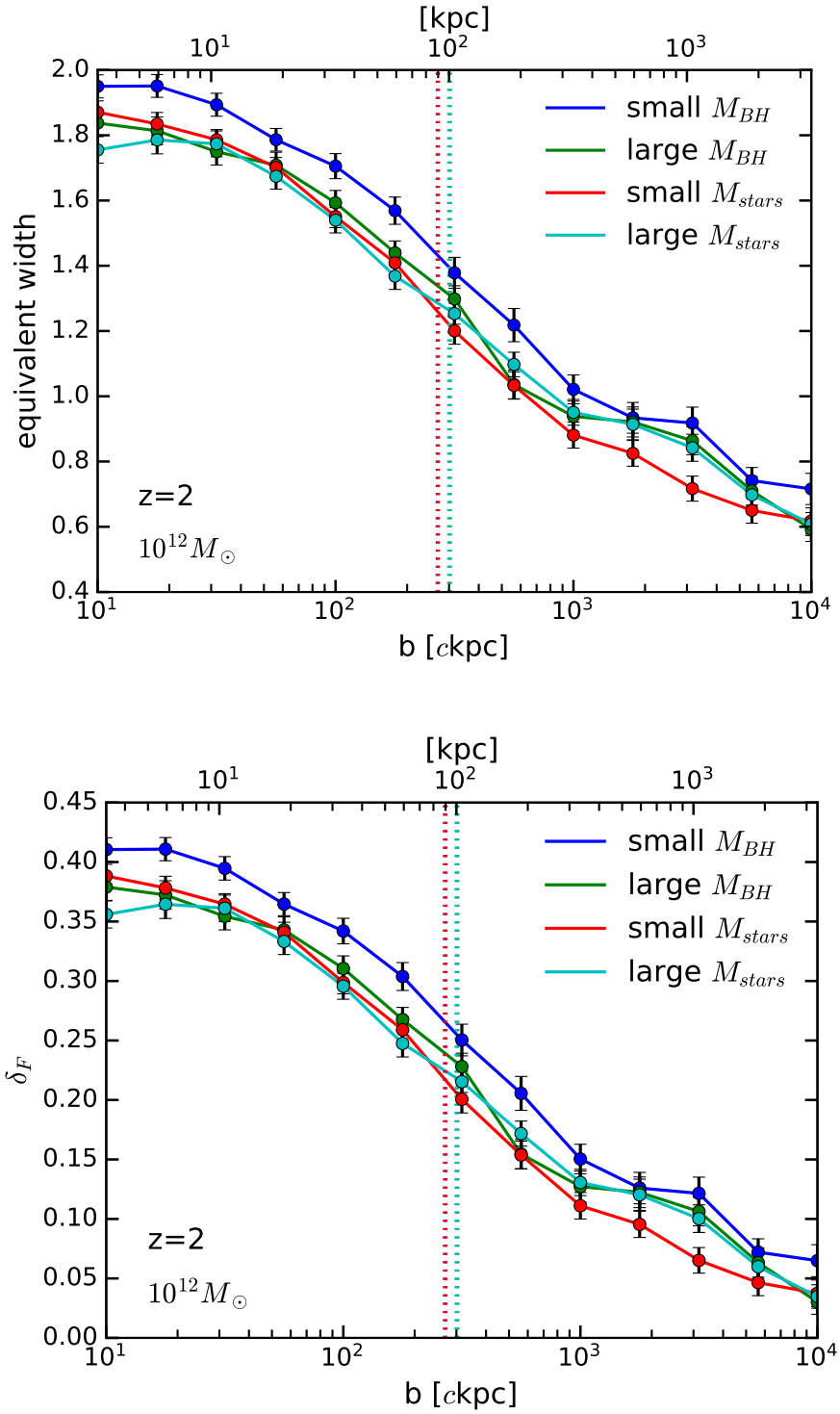


Figure 4.29: Lyman-$\alpha$ absorption equivalent width (*top panel*) and excess absorption (*bottom panel*) as a function of impact parameter $b$ for haloes of $10^{12}\mathrm{M}_\odot$ at $z = 2$ split into exhibiting strong (cyan) and weak (red) supernovae driven winds, and strong (green) and weak (blue) AGN feedback driven outflows. Error bars correspond to the standard error derived from 120 independent Lyman-$\alpha$ spectra contributing to each measurement. Dashed lines correspond to the mean virial radii of each halo sample, colour-coded correspondingly.

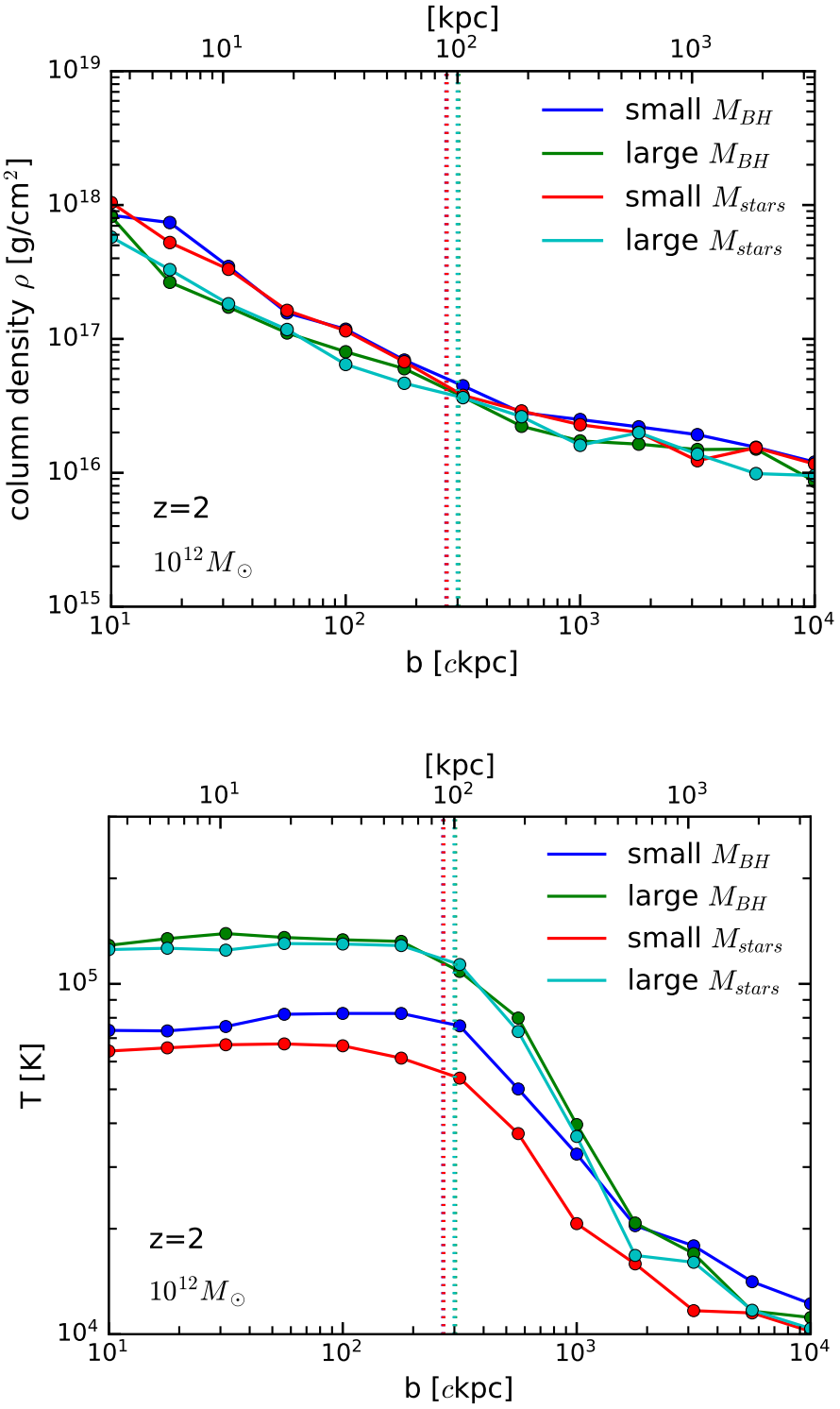


Figure 4.30: Integrated total column density (*top panel*) and median temperature (*bottom panel*) of the gas leading to the previously shown excess Lyman-$\alpha$ absorption as a function of impact parameter $b$ for haloes of $10^{12}\mathrm{M}_\odot$ at $z = 2$ split into exhibiting strong (cyan) and weak (red) supernovae driven winds, and strong (green) and weak (blue) AGN feedback driven outflows. Dashed lines correspond to the mean virial radii of each halo sample, colour-coded correspondingly.

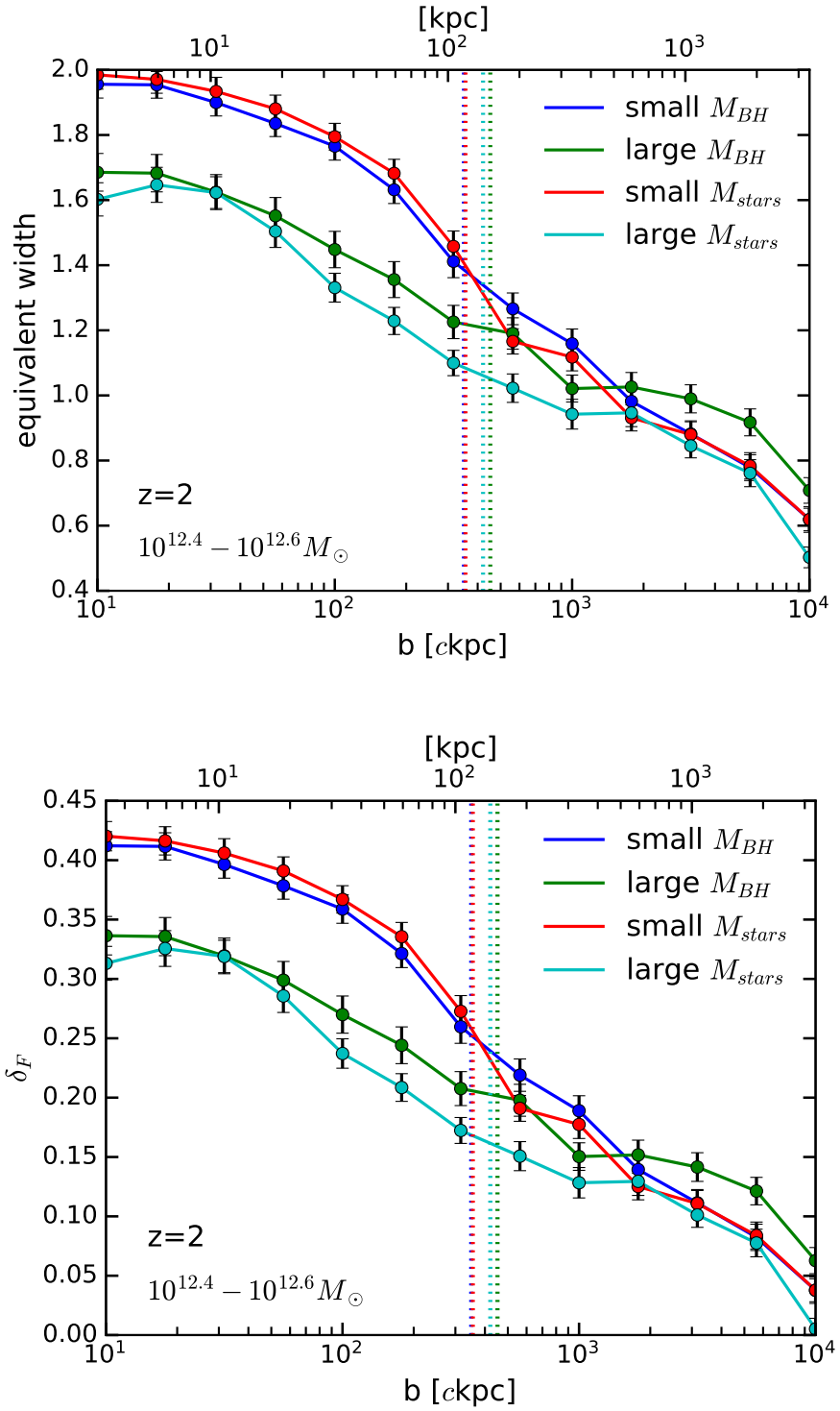


Figure 4.31: Lyman-$\alpha$ absorption equivalent width (*top panel*) and excess absorption (*bottom panel*) as a function of impact parameter $b$ for haloes of $10^{12.5}\mathrm{M}_\odot$ at $z = 2$ split into exhibiting strong (cyan) and weak (red) supernovae driven winds, and strong (green) and weak (blue) AGN feedback driven outflows. Error bars correspond to the standard error derived from 120 independent Lyman-$\alpha$ spectra contributing to each measurement. Dashed lines correspond to the mean virial radii of each halo sample, colour-coded correspondingly.

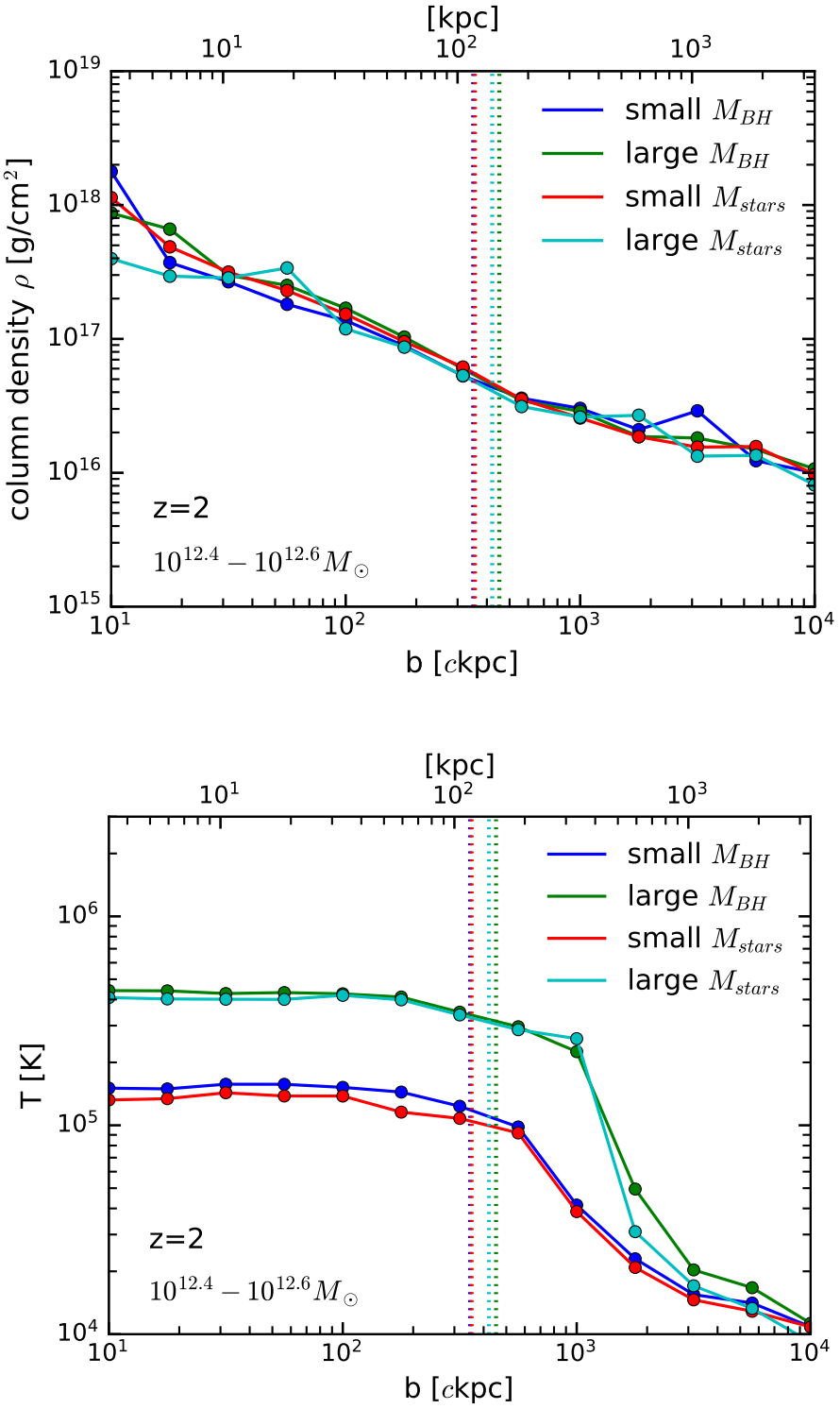


Figure 4.32: Integrated total column density (*top panel*) and median temperature (*bottom panel*) of the gas leading to the previously shown excess Lyman-$\alpha$ absorption as a function of impact parameter $b$ for haloes of $10^{12.5}$M$_\odot$ at $z = 2$ split into exhibiting strong (cyan) and weak (red) supernovae driven winds, and strong (green) and weak (blue) AGN feedback driven outflows. Dashed lines correspond to the mean virial radii of each halo sample, colour-coded correspondingly.

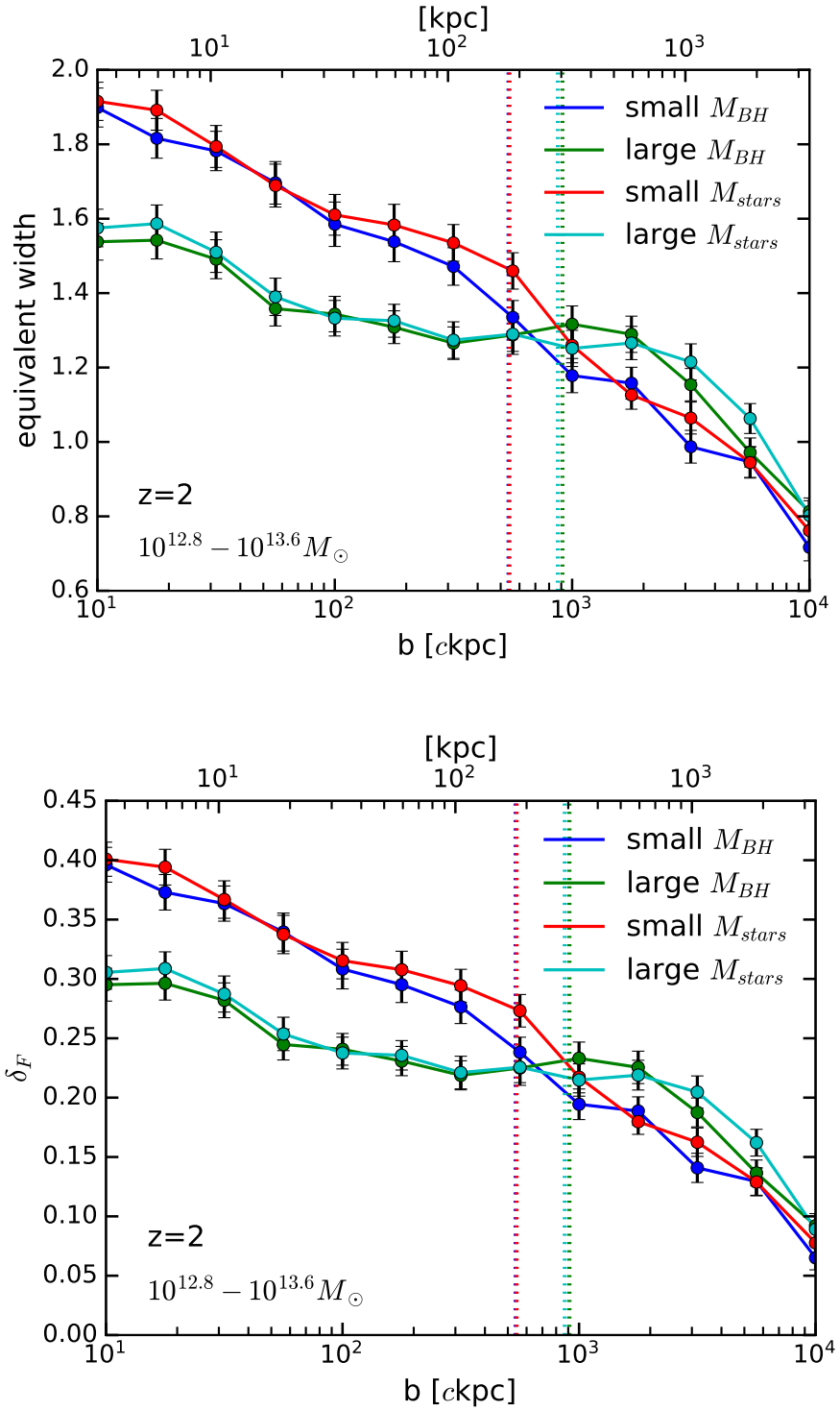


Figure 4.33: Lyman-$\alpha$ absorption equivalent width (*top panel*) and excess absorption (*bottom panel*) as a function of impact parameter $b$ for haloes of $10^{13}\mathrm{M}_\odot$ at $z = 2$ split into exhibiting strong (cyan) and weak (red) supernovae driven winds, and strong (green) and weak (blue) AGN feedback driven outflows. Error bars correspond to the standard error derived from 120 independent Lyman-$\alpha$ spectra contributing to each measurement. Dashed lines correspond to the mean virial radii of each halo sample, colour-coded correspondingly.

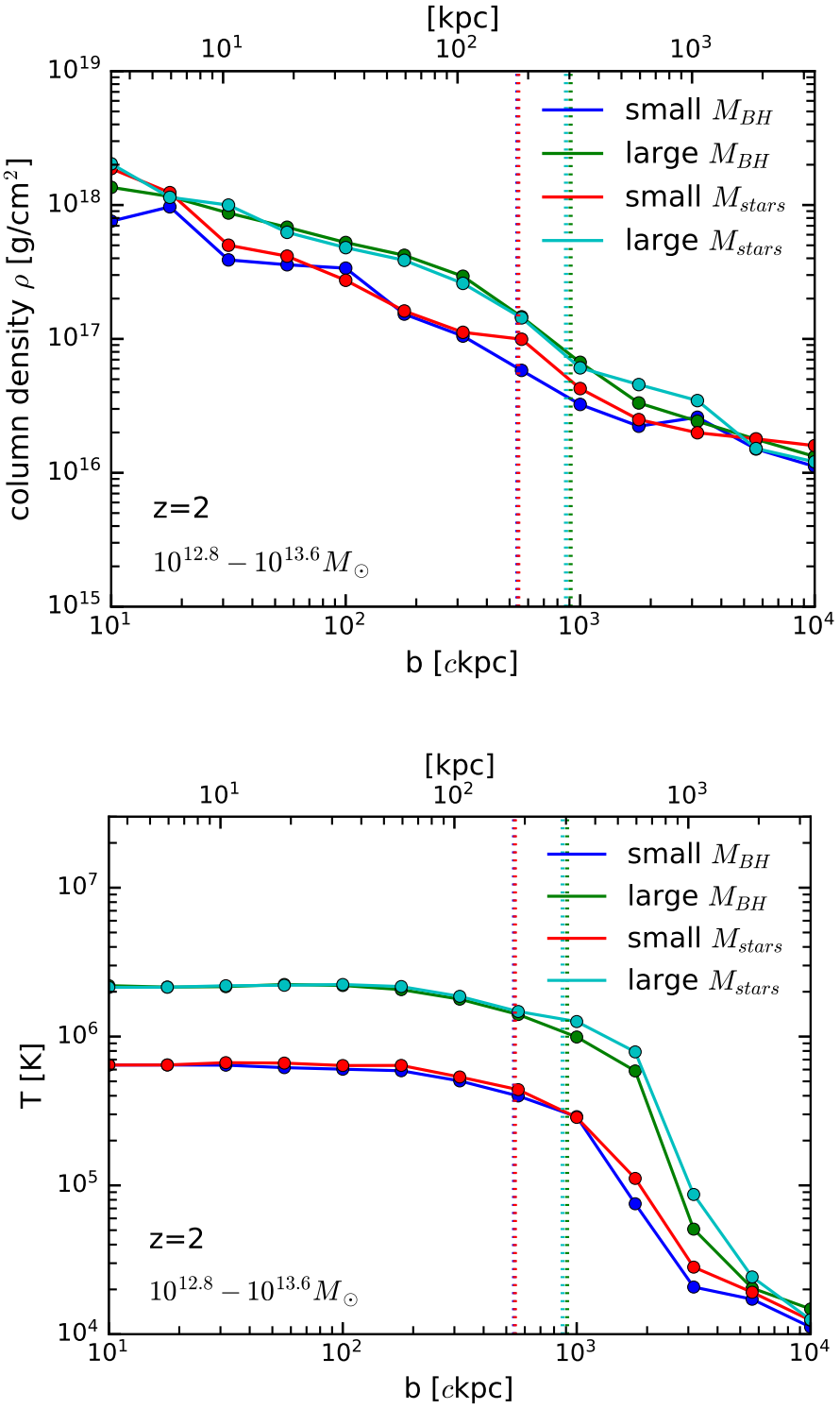


Figure 4.34: Integrated total column density (*top panel*) and median temperature (*bottom panel*) of the gas leading to the previously shown excess Lyman-$\alpha$ absorption as a function of impact parameter $b$ for haloes of $10^{13}\mathrm{M}_\odot$ at $z = 2$ split into exhibiting strong (cyan) and weak (red) supernovae driven winds, and strong (green) and weak (blue) AGN feedback driven outflows. Dashed lines correspond to the mean virial radii of each halo sample, colour-coded correspondingly.

star formation that leaves less gas in the halo for Lyman-$\alpha$ absorption. However, why this is not reflected in the integrated gas column density and what mechanisms exactly impact the Lyman-$\alpha$ absorption in the gas around low mass haloes is an open question for future investigation.

## 4.5 Summary and conclusions

In this study, we have investigated the impact of feedback driven galactic outflows on the statistical properties of the IGM as well as the role of haloes hosting galaxies with strong and weak supernovae winds and AGN feedback in changing the state of the diffuse gas in both the circum-galactic medium (CGM) and inter-galactic medium (IGM) as a function of distance from the halo centre. To investigate the impact of outflows on the state of the IGM in the most clean way, we have run a suite of simulations of varying boxsize with both the up to date most complete set of galaxy formation physics as encompassed in the IllustrisTNG (TNG) model, as well as the Quick Lyman-$\alpha$ (QLA) technique yielding an unperturbed IGM, that we have implemented in the moving-mesh code AREPO. For the first time, we thus employ a simulation suite that takes into account the two major known feedback mechanisms yielding realistic galaxies across the full mass range to study the state of the IGM as probed by the Lyman-$\alpha$ forest. This provides a substantial step forward with respect to previous computational studies which either took into account only heating by a time-varying spatially constant UV background omitting any form of galactic feedback (Lukić et al., 2015), or have included only supernovae driven winds (Bolton et al., 2017). Furthermore, complementing our simulation suite with the TNG100 simulation (Pillepich et al., 2018) that covers a cosmological volume of $75\,h^{-1}$Mpc providing good statistics also for large halo masses, we are able to extend our analysis up to halo masses of $\sim 10^{13.5}\,\mathrm{M}_{\odot}$. Previous studies (e.g. Meiksin et al., 2017) were limited to halo masses of $\sim 10^{12}\,\mathrm{M}_{\odot}$ due to the smaller boxsizes employed. However, the lack of a model for AGN feedback would have limited the insight that could be gained from a extension of those studies to higher halo masses. Haloes above a mass of $\sim 10^{12}\,\mathrm{M}_{\odot}$ host AGNs at their centres that can drive large scale outflows and quench their host galaxies, such that covering the halo mass range above this characterise halo mass for the onset of AGN feedback proves to be of crucial importance for the emerging state of the cosmic gas.

Furthermore, at each boxsize we have run the two physics models with identical initial conditions. This allows us to compare the outflow induced changes not only statistically but also on a line by line basis, as the Lyman-$\alpha$ absorption spectra derived at the same coordinates probe the same large scale structure in the two different physics models. Inspecting individual

Lyman-$\alpha$ forest spectra we find distinct regions with significantly more Lyman-$\alpha$ absorption and thus less transmitted flux in the presence of outflows compared to an unperturbed IGM. The excess Lyman-$\alpha$ absorption in the otherwise cold diffuse gas can only be due to additional matter expelled from galaxies and transported to large scales by feedback driven outflows that increases the gas density in areas that have been penetrated by those outflows. Surprisingly, these differences do not result in a visible change in the flux probability distribution function (PDF) which we derive from 1000 randomly selected lines of sight. The more sensitive Lyman-$\alpha$ flux power spectrum again derived from 1000 randomly selected spectra, however, shows clear signatures of galactic outflows. Compared to the unperturbed gas, we find the flux power spectrum derived from inter-galactic gas that was affected by outflows to robustly exhibit less power at small scales (large $k$) and correspondingly more power at large scales (small $k$) with a characteristic transition scale. The relative difference in power measured from the Lyman-$\alpha$ flux grows with time from up to $\sim 10\%$ at $z = 3$ to $\sim 20\%$ at $z = 2$. This can be understood through outflows transporting increasing amounts of matter from galaxies to large scales. The higher gas density in selected patches of the inter-galactic gas thus leads to more observed Lyman-$\alpha$ absorption at large scales, and the lack of the same matter in the vicinity of galaxies from where it has been expelled leads to the corresponding drop of power in the Lyman-$\alpha$ forest at small scales. Finally, we investigate the effect of outflows on the temperature-density distribution of diffuse gas. We find a larger volume fraction of the IGM at densities around the cosmic mean to be at temperatures of $10^{4.5} - 10^{5.5} K$. A higher mean temperature leads to a higher ionisation fraction and thus reduces the amount of neutral hydrogen available for Lyman-$\alpha$ absorption. As the above temperature range overlaps with the characteristic temperature of $T_{\mathrm{Ly}\alpha} \approx 1.18 \cdot 10^5\ K$ associated with the Lyman-$\alpha$ transition, the fraction of neutral hydrogen in its ground state is further reduced compared to the unperturbed gas leading to less observed Lyman-$\alpha$ absorption. Furthermore, we find that in the presence of galactic outflows the IGM equation of state exhibits a slightly higher offset reflecting the majority of the diffuse gas being heated to slightly higher temperatures.

In the second part of our study, we investigate the role of haloes hosting galaxies exhibiting strong and weak feedback in changing the state and thus absorption properties of their gaseous surrounding. This gives us insight on which galaxies and processes have the strongest impact also on the statistical changes introduced in the otherwise unperturbed inter-galactic gas when galaxy formation physics is taken into account. In a first step, we investigate the Lyman-$\alpha$ equivalent width and excess absorption as a function of distance from the halo centre as a function of halo mass at five target halo masses between $10^{11}\mathrm{M}_\odot$ and $10^{13}\mathrm{M}_\odot$ and redshifts $z = 3$, $z = 2.4$, and $z = 2$. We find significant excess in Lyman-$\alpha$ absorption in the vicinity of haloes compared to the mean IGM, that drops with increasing distance from the halo centre

and reaches average IGM values only beyond several Mpc away from the halo centre. The excess Lyman-$\alpha$ absorption is larger as a function of increasing halo mass due to the higher densities reached in more massive haloes. However, in the most massive haloes, we find a characteristic depletion of the excess Lyman-$\alpha$ absorption within the virial radius that grows and extends to lower halo masses with time that is caused by AGN feedback.

To better understand how the different types of feedback driven outflows impact the state of the diffuse gas and the resulting Lyman-$\alpha$ absorption, we further select haloes with large and small stellar and black hole masses tracing haloes with a history of strong and weak supernovae and AGN feedback, respectively, driving hot outflows into the IGM. For the such selected haloes at four halo masses between $10^{11}\mathrm{M}_{\odot}$ and $10^{13}\mathrm{M}_{\odot}$ and redshifts of $z = 3$, $z = 2.4$, and $z = 2$, we derive in addition to their excess Lyman-$\alpha$ absorption properties as a function of distance from the halo centre also the corresponding gas column densities and mean temperatures of the diffuse gas, which give us insight on what causes changes in the Lyman-$\alpha$ absorption. Interestingly, we find negligible changes in the gas column density in presence of strong or weak feedback driven outflows as a function of impact parameter across all halo masses and redshifts. The gas temperature on the other hand is raised to substantially higher values by strong feedback mechanisms, with a single exception for the lowest mass haloes. Low mass haloes of $\sim 10^{11}\mathrm{M}_{\odot}$ are dominated by supernovae feedback that initiates galactic outflows predominately at the peak of the cosmic star formation rate at $z = 3-2$, which reach the diffuse gas at large scales only with considerable delay time. For haloes of this mass we furthermore find less excess Lyman-$\alpha$ absorption with decreasing redshift in case of a large stellar mass, which is likely not caused by the impact of supernovae winds but rather the consumption of gas for star formation, though this is poorly reflected in the integrated gas column density. For haloes above a mass of $10^{12.5}\mathrm{M}_{\odot}$ the higher temperature caused by feedback from AGN leads to a higher ionisation fraction and thus lower neutral hydrogen fraction in the gas. This causes less observed Lyman-$\alpha$ absorption and a prominent depletion of excess Lyman-$\alpha$ absorption within the virial radius of haloes that exhibit strong AGN feedback compared to haloes with weak AGNs. Beyond the virial radius the excess Lyman-$\alpha$ absorption again converges to the same values determined by the halo mass independent of the feedback strength. This highlights the importance of AGN feedback driven outflows for the thermal state of the inter-galactic gas and the resulting Lyman-$\alpha$ forest absorption properties.

## 4.6 Convergence and resolution tests

In this section, we investigate the convergence of the Lyman-$\alpha$ statistics discussed in Chapter 4 with the number of used spectra, the resolution of the individual spectra, and the mass resolution of the employed simulation.

First, in addition to our main sample of 1000 randomly selected lines of sight from the TNG100 simulations, we derive two further samples with 2000 and 3000 random lines of sight at $z = 2$, resolved by 1024 pixel. We chose to investigate the convergence properties at the lowest redshift used for our study, as we expect any differences to show up stronger the more substructure has developed in the diffuse gas. In Fig. 4.35 we show the Lyman-$\alpha$ flux probability distribution function (PDF) derived from these three samples and find it to be perfectly converged with the number of used spectra. In the top panel of Fig. 4.36 we show the more sensitive Lyman-$\alpha$ flux power spectrum derived from the three samples, and for clearer display we show in the bottom panel of Fig. 4.36 the ratio of the flux power spectra derived from 1000 lines of sight (blue line) and 2000 lines of sight (red line) with respect to the power spectrum derived from the largest set of 3000 lines of sight, shown as back dashed line for reference. The ratios exhibit some uncorrelated noise at a few percent level. Except for this statistical fluctuations, the Lyman-$\alpha$ flux power spectra derived from the three sets of spectra are very well converged. This leads us to conclude, that a sample size of 1000 randomly selected Lyman-$\alpha$ absorption spectra is sufficient to faithfully probe the statistical properties of the IGM.

Next, we investigate the convergence of the Lyman-$\alpha$ forest statistics with the resolution of the derived spectra. To this end, we rederive the Lyman-$\alpha$ spectra from our main sample of 1000 randomly selected lines of sight from the TNG100 simulations that have a default of 1024 pixel per spectrum, with a resolution of 2048 and 3072 pixel per spectrum. We show the flux PDF derived at these three spectral resolutions in Fig. 4.37 and find very good convergence with the number of employed pixel per spectrum. In the top panel of Fig. 4.38 we show Lyman-$\alpha$ flux power spectrum derived from the three sets of spectra with different pixel resolution, and in the bottom panel of Fig. 4.38 we show the ratio of the flux power spectra derived from spectra with 1024 pixel per spectrum (blue line) and 2048 pixel per spectrum (red line) with respect to the power spectrum derived from the best resolved spectra with 3072 pixel per spectrum, shown as back dashed line for reference. Inspecting the power ratio, we find the power spectra derived with a resolution of 2048 and 3072 pixel per spectrum to be converged. However, the power spectrum derived from Lyman-$\alpha$ spectra with 1024 pixel per spectrum exhibits systematically less power at large scales (small $k$) then its higher resolved counterparts. To gain more insight on this systematic deviation we show in Fig. 4.39 the bottom panel of Fig. 4.38 extended to smaller physical scales (large $k$)

typically not displayed due to the lack of observational data for comparison at those scales. Fig. 4.39 reveals characteristic oscillations in the ratio of the flux power spectrum derived from spectra with 1024 pixel with respect to the power spectrum derived from spectra with 3072 pixel. Those oscillations are caused by the inability of Lyman-$\alpha$ spectra with 1024 pixel to resolve the small scale properties of the diffuse gas that are, however, resolved in the TNG100 simulation with 1820 gas cells per dimension. The fact, that the spectra are not able to resolve the Nyquist frequency of the simulation leads to a mapping of small scale power to larger scales, which manifests itself in the observed oscillations and as a systematic offset at large scales (here to a lower power). To avoid this phenomenon also known as aliasing, the Nyquist-Shannon sampling theorem requires Lyman-$\alpha$ spectra to be resolved by at least as many pixel as corresponds to the one-dimensional resolution of the employed hydrodynamical simulation. Furthermore, also the flux power spectrum derived from spectra with 2048 pixel exhibits some deviations at small physical scales (large $k$) with respect to the power spectrum derived from spectra with 3072 pixel. These deviations are likely caused by overdense regions in the simulation box that are covered by a larger number of gas particles/cells per volume than the average in the employed hydrodynamical simulation. Therefore, these regions will be better resolved and more faithfully covered by spectra with a larger number of pixel. However, these minor fluctuations appear at small scales that are not considered for any physical analysis. Therefore, we conclude that when deriving Lyman-$\alpha$ forest spectra, it is necessary to always use at least as many pixel per spectrum as corresponds to the one-dimensional resolution of the corresponding hydrodynamical simulation.

Finally, we investigate the convergence of the Lyman-$\alpha$ forest statistics with the mass resolution of the employed hydrodynamical simulation. To do so, we derive the Lyman-$\alpha$ spectra at the exact same positions as in our main sample of 1000 randomly selected lines of sight from the TNG100 simulation at $z = 2$, resolved by 1024 pixel per spectrum, from the TNG100-2 and TNG100-3 simulations that have a reduced mass resolution in one dimension by a factor of 2 and 4, respectively. In Fig. 4.40 we show flux PDF derived from the three simulations with different mass resolution. Minor deviations of the flux PDF derived from TNG100-3 having the lowest resolution are visible at the highest transmitted flux values and around a flux of $\sim 0.2$ with respect to the flux PDF obtained from TNG100-2 and TNG100. In the top panel of Fig. 4.41 we show the Lyman-$\alpha$ flux power spectrum derived from the three simulation levels, and in the bottom panel of Fig. 4.41 we show the ratio of the flux power spectra derived from TNG100-3 (blue line) and TNG100-2 (red line) with respect to the power spectrum derived from the TNG100 simulation that has the highest mass resolution, shown as back dashed line for reference. The power spectra derived from all three simulations exhibit significant deviations from each other at small scales (large $k$) as

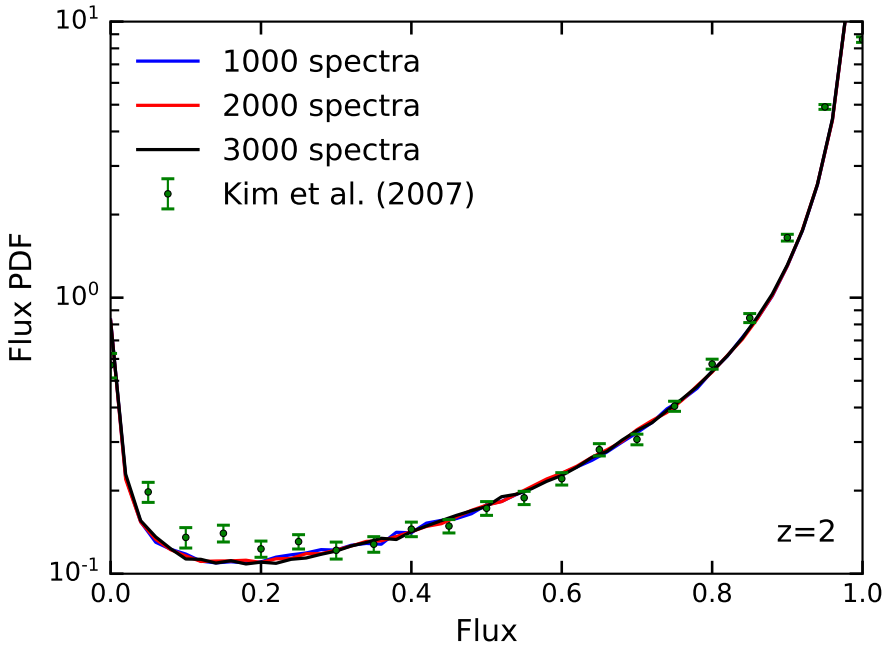


Figure 4.35: Lyman-$\alpha$ flux probability distribution function (PDF) derived from the TNG100 simulation at $z = 2$ employing three independent sets of Lyman-$\alpha$ forest spectra comprising 1000, 2000, and 3000 random lines of sight resolved by 1024 pixel. For comparison we show observational data from Kim et al. (2007). The flux PDF is perfectly converged with the number of employed spectra.

those scales are mostly affected by the lower mass resolution employed in TNG100-3 and TNG100-2. Furthermore, the power spectra from both TNG100-3 and TNG100-2 exhibit a similar offset to lower power at large scales (small $k$) compared to TNG100. Likely, this is due to different calibration factors derived for each mass resolution, that are employed to adjusts the mean flux to observational measurements from Kim et al. (2007). Applying the same calibration factor derived from the best resolved simulation to all simulations should restore the same large scale power in all three runs. Taking this correction into account, the three resolution levels converge to the same Lyman-$\alpha$ flux power at scales below $k \sim 10^{-1}$ within $\sim 5\%$. In order to establish the reliability of the best resolved TNG100 simulation, a comparison simulation with increased resolution (by a factor of 2) that can be performed in an substantially smaller volume, would be very insightful.

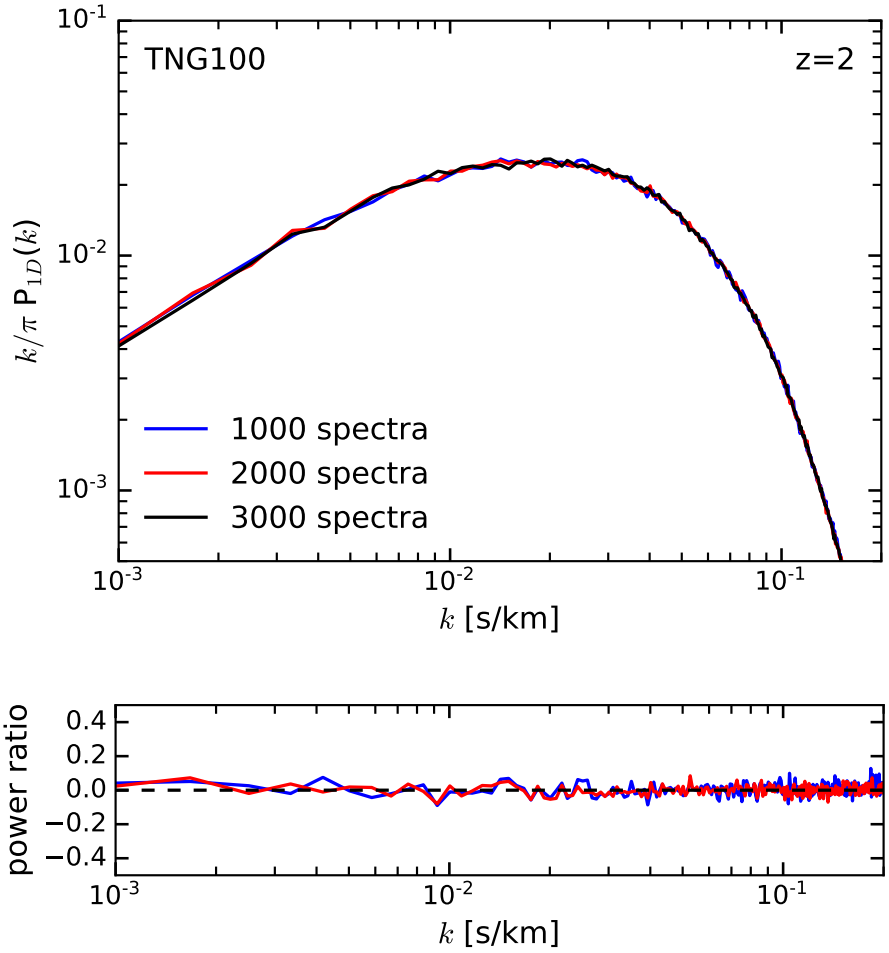


Figure 4.36: *Top panel* : Lyman-$\alpha$ flux power spectrum derived from the TNG100 simulation at $z = 2$ employing three independent sets of Lyman-$\alpha$ forest spectra comprising 1000, 2000, and 3000 random lines of sight resolved by 1024 pixel. *Bottom panel* : Ratio of flux power spectra derived from 1000 lines of sight (blue line) and 2000 lines of sight (red line) with respect to the power spectrum derived from the largest set of 3000 lines of sight, shown as back dashed line for reference. The ratios exhibit uncorrelated statistical noise at a few percent level, with the Lyman-$\alpha$ flux power spectra derived from the three sets of spectra being very well converged.

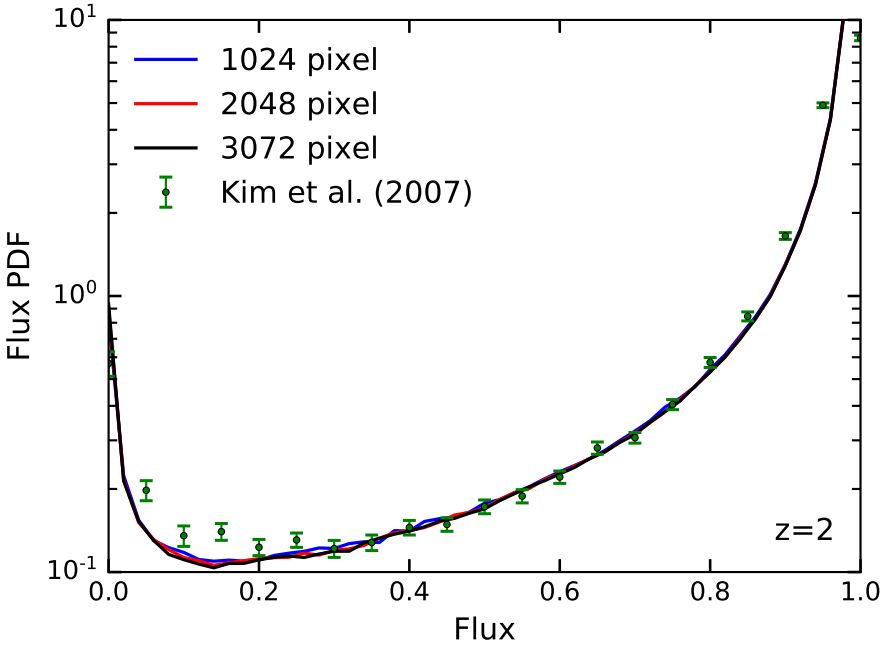


Figure 4.37: Lyman-$\alpha$ flux probability distribution function (PDF) derived from 1000 randomly selected lines of sight from the TNG100 simulation at $z = 2$ at three different spectral resolutions, including 1024, 2048, and 3072 pixel per spectrum. For comparison we show observational data from Kim et al. (2007). The flux PDF is perfectly converged with the number of pixel per spectrum.

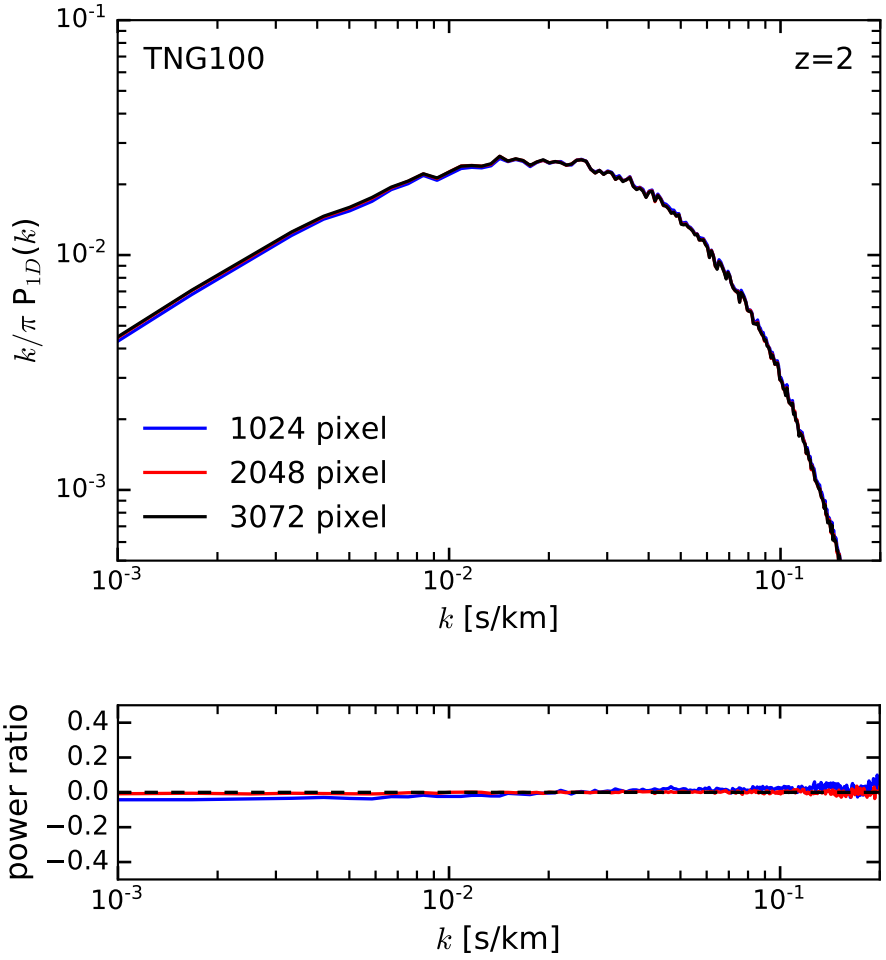


Figure 4.38: *Top panel* : Lyman-$\alpha$ flux power spectrum derived from 1000 randomly selected lines of sight from the TNG100 simulation at $z = 2$ at three different spectral resolutions, including 1024, 2048, and 3072 pixel per spectrum. *Bottom panel* : Ratio of flux power spectra derived at a resolution of 1024 pixel per spectrum (blue line) and 2048 pixel per spectrum (red line) with respect to the power spectrum derived at the highest resolution of 3072 pixel per spectrum, shown as back dashed line for reference. The flux power spectra derived at the two higher pixel resolutions show perfect convergence, whereas the flux power spectrum derived at a resolution of 1024 pixel per spectrum shows systematic deviations from the higher resolved default. The least resolved spectra yield a flux power spectrum that exhibits systematically less power at large scales (small $k$) and more power at small scales (large $k$) caused by aliasing effects.

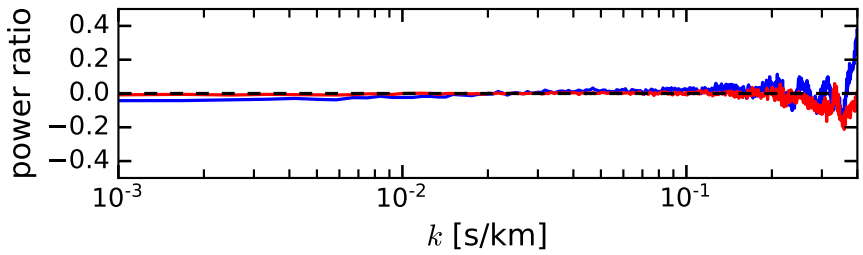


Figure 4.39: Same as bottom panel of Fig. 4.38, however extended to smaller scales (large $k$) that can still be resolved in our simulations but are typically not shown as they correspond to a regime for which no observational data is available up to date. For the lowest resolved spectra, characteristic oscillations at small scales becomes visible that are caused by aliasing effects.

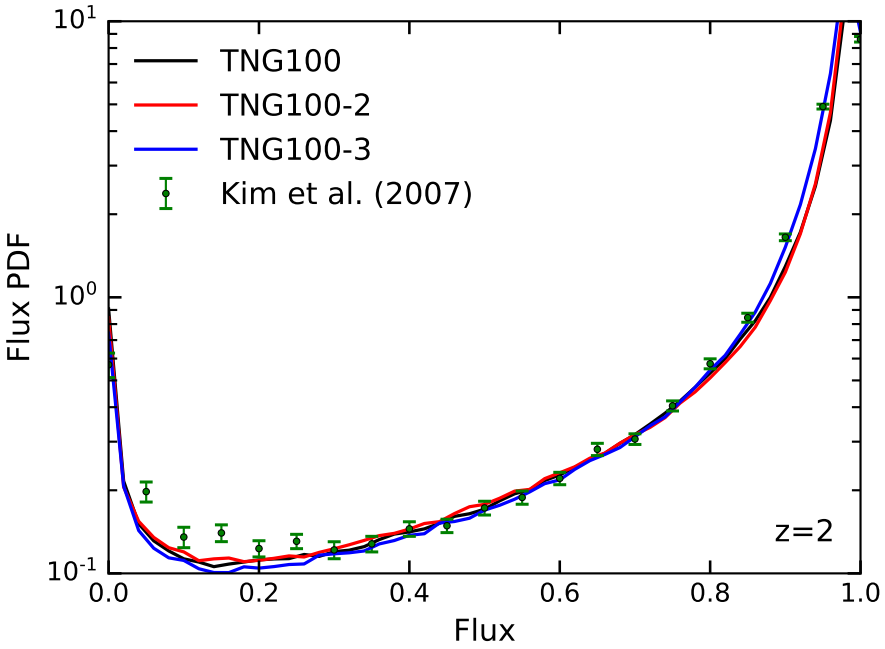


Figure 4.40: Lyman-$\alpha$ flux probability distribution function (PDF) derived from 1000 randomly selected lines of sight from the three resolution levels of the TNG100 simulation at $z = 2$, resolved by 1024 pixel per spectrum. For comparison we show observational data from Kim et al. (2007). Minor deviation of the flux PDF derived from TNG100-3 having the lowest resolution are visible at the highest transmitted flux values and around a flux of $\sim 0.2$ with respect to the flux PDF obtained from TNG100-2 and TNG100.

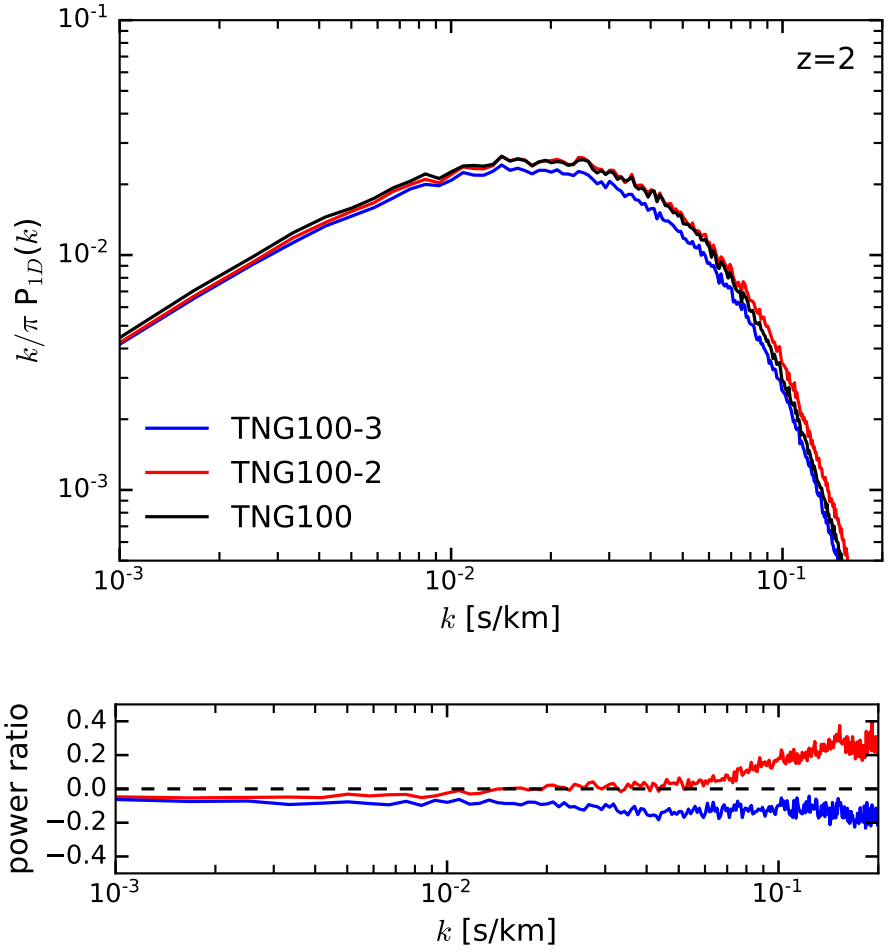


Figure 4.41: *Top panel* : Lyman-$\alpha$ flux power spectrum derived from 1000 randomly selected lines of sight from the three resolution levels of the TNG100 simulation at $z = 2$, resolved by 1024 pixel per spectrum. *Bottom panel* : Ratio of flux power spectra derived at a resolution of 1024 pixel per spectrum from the TNG100-3 simulation (blue line) and from the TNG100-2 simulation (red line) with respect to the power spectrum derived from TNG100, shown as back dashed line for reference. The displayed power spectra exhibit significant deviations from each other at small scales (large $k$) which are mostly affected by the different mass resolutions of the three simulations. The systematic offset at large scales (small $k$) is likely a spurious effect from the calibration of the mean flux to the observational data. Correcting for this effect, the three resolution levels converge to the same Lyman-$\alpha$ flux power at scales below $k \sim 10^{-1}$ within $\sim 5\%$.

# Chapter 5

# Summary and Outlook

Recent cosmological hydrodynamical simulations were for the first time able to produce galaxy populations with realistic sizes and morphologies in large cosmological volumes. This success can be attributed to the inclusion of subgrid models for unresolved galaxy evolution physics, and particularly to models for supernovae winds and active galactic nuclei (AGN) feedback which drive galactic outflows. Feedback driven outflows are crucial for regulating the gas distribution, the state and the properties of the gas both on galactic, as well as on extra-galactic scales. Outflows expel a significant fraction of a galaxy's gas, driving the baryon cycle in the circum-galactic medium (CGM) and partially reaching and perturbing the inter-galactic medium (IGM). In this thesis we have investigated two major implications of feedback driven outflows on galactic and extra-galactic scales.

In chapter 2, we employ the state-of-the-art hydrodynamical simulation suite Illustris, that produces a realistic galaxy population in a representative volume of the universe, to first characterise the amount of specific angular momentum in the baryonic component of haloes. To this end, we have extended the group finders FOF and SUBFIND (Springel et al., 2001) employed in the moving-mesh code AREPO (Springel, 2010a) to calculate in addition the angular momentum vectors of galaxies and their haloes, in their different definitions. This includes the total angular momentum vectors, as well as the angular momentum vectors of the different components, including the stellar component, the gas, and dark matter, and multiple related quantities. This group finder extension allows us to calculate the baryonic spin of an unprecedented number of more than 300.000 haloes from both in non-radiative Illustris simulation that follow the gas flow as prescribed by the Euler equations without including any star formation or galaxy evolution physics, as well as from the full-physics Illustris simulation. In the non-radiative case, were we would have expected the gas component to preserve its initial spin that is equal to the dark matter spin caused by the purely gravitational interaction with the primordial gravitational tidal field, we find the gas spin to grow with

time and yield a ratio of $\lambda_{\rm gas}/\lambda_{\rm dm} \sim 1.3$ across the whole halo population at $z = 0$. In the presence of galaxy evolution and feedback physics the baryonic spin is further enhanced yielding an overall ratio of $\lambda_{\rm gas}/\lambda_{\rm dm} \sim 1.8$. Assuming that both supernovae driven winds and AGN feedback expel strictly the gas with lowest angular momentum from galaxies, we can calculate the expected baryonic spin enhancement from the universal angular momentum profile (Bullock et al., 2001) if a given fraction of halo gas is expelled by outflows, and find this mechanism to be sufficient to explain the enhancement we measure from Illustris.

In chapter 3, we extend our analysis based on the Illustris simulation suite to the IllustrisTNG simulation suite with (amongst others) updated and improved models for supernovae driven winds (Pillepich et al., 2018) and AGN feedback (Weinberger et al., 2017), and refine our understanding of the role of feedback driven outflows in shaping the halo spin. In a first step, employing the non-radiative hydrodynamical counterpart of the Illustris simulation, we find that even in absence of any galaxy evolution and feedback physics the spin of the gas component in gravitationally self-bound haloes grows with time with respect to the dark matter spin. This growth is consistent with the transfer of a constant spin of $\Delta\lambda = 0.0013$ with a scatter of $\sim 0.12$ dex from dark matter onto the halo gas, accumulated across the whole halo evolution until $z = 0$. Applying our further improved extension of the group finders FOF and SUBFIND to IllustrisTNG we find a similar enhancement of the baryonic spin with respect to dark matter spin with a scatter of $\sim 0.17$ dex as already measured in the Illustris simulation. We confirm the correlation between spin enhancement and the expelled gas fraction due to supernovae winds and AGN feedback. However, this correlation turns out to be weak for halo masses mostly affected by supernovae feedback. This suggests that supernovae driven winds mix the initially ejected low specific angular momentum gas with higher specific angular momentum gas in the course of the baryon cycle, finally expelling a gas with mixed specific angular momentum content from the halo. AGN feedback on the contrary is found to expel gas with preferentially the lowest specific angular momentum. In order to better understand the propagation of feedback driven outflows through the CGM and the induced mixing of gas resulting in certain properties of the ultimately expelled gas, it is necessary to employ high-resolution simulations of the CGM around galaxies. In particular, to advance our understanding of the redistribution and expulsion of gas with certain specific angular momentum, both the use of tracers for gas flows as well as a high time resolution in the output data resolving the timescales on which supernovae winds are active will be required in future studies.

In chapter 4, we investigate the impact of expelled gas on the gas around haloes hosting galaxies with strong and weak feedback, as well as on the diffuse cosmic gas. In this study, we employ the Lyman-$\alpha$ forest as a probe for the state of the diffuse gas. In order to compare

the properties of the cosmic gas in presence of galactic outflows to its unperturbed state in the most clean way, we have implemented the Quick Lyman-$\alpha$ (QLA) technique in the moving-mesh code AREPO that yields an unperturbed IGM. We have run a suite of simulations of varying boxsize both with Quick Lyman-$\alpha$ technique, as well as the presently most complete set of galaxy formation physics as realised in the IllustrisTNG (TNG) model, which we use alongside the TNG100 simulation to investigate changes in the statistical properties of the IGM introduced by galactic outflows. In the presence of outflows, we find a larger volume fraction of the IGM at densities around the cosmic mean to be in the temperature range of $10^{4.5} - 10^{5.5} K$ which covers the temperature necessary to ionise neutral hydrogen, $T_{\rm ion} \approx 1.57 \cdot 10^5\ K$. Therefore, the higher mean temperature leads to a smaller neutral hydrogen fraction and less Lyman-$\alpha$ absorption. Though we detect no significant difference between the flux probability distribution function (PDF) of perturbed and unperturbed gas, we find the Lyman-$\alpha$ flux power spectrum of the perturbed gas to exhibit $\sim 10\%$ more power at large scales at $z = 3$, and up to $\sim 20\%$ more at $z = 2$, relative to the unperturbed power spectrum. A corresponding amount of power is lacking at small scales below a characteristic transition scale, which can be explained by feedback driven outflows transporting increasing amounts of matter from small, galactic scales to large scales.

Furthermore, we investigate the role of quasar-hosting and star-forming galaxies at centres of haloes in changing the state of their gaseous surrounding out to $\sim 3$ Mpc in the redshift range $3 \leqslant z \leqslant 2$, thus also being responsible for the changes in the statistical properties of the IGM observed when galaxy evolution physics is taken into account. We find significant excess in Lyman-$\alpha$ absorption in the vicinity of haloes compared to the mean IGM, that drops with increasing distance from the halo centre and reached average IGM values only beyond several Mpc away from the halo centre. The excess in Lyman-$\alpha$ absorption is higher around more massive haloes, whereas with decreasing redshift haloes above the threshold mass of $10^{12} \mathrm{M}_\odot$ develop a characteristic depletion of excess Lyman-$\alpha$ absorption within their virial radius caused by AGN feedback. In order to investigate the mechanism for this depletion as well as the role of strong and weak feedback in shaping the Lyman-$\alpha$ absorption properties of the adjacent gas, we derive the excess Lyman-$\alpha$ absorption as well as integrated gas column densities and mean temperatures of haloes with strong and weak feedback as a function of impact parameter. Interestingly, we find negligible changes in the gas column density induced by strong feedback relative to weak feedback driven outflows across all halo masses and examined redshifts. However, stronger AGN feedback heats the surrounding gas to substantially higher temperatures, raising the ionisation fraction and thus lowering the neutral hydrogen fraction in the gas. This causes less observed Lyman-$\alpha$ absorption and a prominent depletion of excess Lyman-$\alpha$ absorption within the virial radius of haloes

that exhibit strong AGN feedback compared to haloes with weak AGNs. Beyond the virial radius the excess Lyman-$\alpha$ absorption again converges to the same values determined by the halo mass. AGN feedback therefore proves to be of crucial importance for the thermal state and the Lyman-$\alpha$ absorption properties of the circum-galactic and inter-galactic gas. Future detailed comparison to observational results will provide further insight and help to put constraints on the strength of the employed feedback mechanisms, which in return will constrain the deviations of the true Lyman-$\alpha$ flux power spectrum from its default value derived from an unperturbed IGM. Precise knowledge of the amplitude of these deviations is crucial for SDSS/eBOSS to derive the baryonic acoustic oscillation (BAO) scale to the claimed precision and put constrains on the Dark Energy equation of state.

# List of publications

**1.* J. Zjupa** and V. Springel
*Angular momentum properties of haloes and their baryon content in the Illustris simulation*
MNRAS, 466:1625-1647, April 2017, doi: 10.1093/mnras/stw2945

**2.** V. Rodriguez-Gomez, L. V. Sales, S. Genel, A. Pillepich, **J. Zjupa**, D. Nelson, B. Griffen, P. Torrey, G. F. Snyder, M. Vogelsberger, V. Springel, C.-P. Ma, L. Hernquist
*The role of mergers and halo spin in shaping galaxy morphology*
MNRAS, 467:3083-3098, May 2017, doi: 10.1093/mnras/stx305

**3.** Q. Zhu, D. Xu, M. Gaspari, V. Rodriguez-Gomez; D. Nelson, M. Vogelsberger, P. Torrey, A. Pillepich, **J. Zjupa**; R. Weinberger, F. Marinacci, R. Pakmor, S. Genel, Y. Li, V. Springel, L, Hernquist
*Formation of a Malin 1 analogue in IllustrisTNG by stimulated accretion*
MNRAS, 480:L18-L22, October 2018, doi: 10.1093/mnrasl/sly111

* part of this thesis

# Bibliography

V. Avila-Reese, P. Colín, S. Gottlöber, C. Firmani, and C. Maulbetsch. The Dependence on Environment of Cold Dark Matter Halo Properties. *ApJ*, 634:51–69, November 2005. doi: 10.1086/491726.

A. S. Baldi, M. De Petris, F. Sembolini, G. Yepes, L. Lamagna, and E. Rasia. On the coherent rotation of diffuse matter in numerical simulations of galaxy clusters. *ArXiv e-prints*, June 2016.

M. L. Balogh, F. R. Pearce, R. G. Bower, and S. T. Kay. Revisiting the cosmic cooling crisis. *MNRAS*, 326:1228–1234, October 2001. doi: 10.1111/j.1365-8711.2001.04667.x.

J. Barnes and G. Efstathiou. Angular momentum from tidal torques. *ApJ*, 319:575–600, August 1987. doi: 10.1086/165480.

M. Bartelmann. *Lecture Notes: Cosmology*. 2009.

G. D. Becker and J. S. Bolton. New measurements of the ionizing ultraviolet background over $2 < z < 5$ and implications for hydrogen reionization. *MNRAS*, 436:1023–1039, December 2013. doi: 10.1093/mnras/stt1610.

G. D. Becker, J. S. Bolton, M. G. Haehnelt, and W. L. W. Sargent. Detection of extended He II reionization in the temperature evolution of the intergalactic medium. *MNRAS*, 410: 1096–1112, January 2011. doi: 10.1111/j.1365-2966.2010.17507.x.

G. D. Becker, P. C. Hewett, G. Worseck, and J. X. Prochaska. A refined measurement of the mean transmitted flux in the Ly$\alpha$ forest over $2 < z < 5$ using composite quasar spectra. *MNRAS*, 430:2067–2081, April 2013. doi: 10.1093/mnras/stt031.

M. J. Berger and P. Colella. Local adaptive mesh refinement for shock hydrodynamics. *Journal of Computational Physics*, 82:64–84, May 1989. doi: 10.1016/0021-9991(89)90035-1.

M. J. Berger and J. Oliger. Adaptive Mesh Refinement for Hyperbolic Partial Differential Equations. *Journal of Computational Physics*, 53:484–512, March 1984. doi: 10.1016/0021-9991(84)90073-1.

P. Bett, V. Eke, C. S. Frenk, A. Jenkins, J. Helly, and J. Navarro. The spin and shape of dark matter haloes in the Millennium simulation of a Λ cold dark matter universe. *MNRAS*, 376:215–232, March 2007. doi: 10.1111/j.1365-2966.2007.11432.x.

P. Bett, V. Eke, C. S. Frenk, A. Jenkins, and T. Okamoto. The angular momentum of cold dark matter haloes with and without baryons. *MNRAS*, 404:1137–1156, May 2010. doi: 10.1111/j.1365-2966.2010.16368.x.

J. Binney and M. Merrifield. *Galactic Astronomy*. Princeton University Press, 1998.

J. Binney and S. Tremaine. *Galactic Dynamics*. Princeton University Press, 2008.

G. R. Blumenthal, S. M. Faber, J. R. Primack, and M. J. Rees. Formation of galaxies and large-scale structure with cold dark matter. *Nature*, 311:517–525, October 1984. doi: 10.1038/311517a0.

J. S. Bolton, E. Puchwein, D. Sijacki, M. G. Haehnelt, T.-S. Kim, A. Meiksin, J. A. Regan, and M. Viel. The Sherwood simulation suite: overview and data comparisons with the Lyman $\alpha$ forest at redshifts $2 < z < 5$. *MNRAS*, 464:897–914, January 2017. doi: 10.1093/mnras/stw2397.

G. L. Bryan and M. L. Norman. Statistical Properties of X-Ray Clusters: Analytic and Numerical Comparisons. *ApJ*, 495:80–99, March 1998. doi: 10.1086/305262.

G. L. Bryan, M. L. Norman, B. W. O'Shea, T. Abel, J. H. Wise, M. J. Turk, D. R. Reynolds, D. C. Collins, P. Wang, S. W. Skillman, B. Smith, R. P. Harkness, J. Bordner, J.-h. Kim, M. Kuhlen, H. Xu, N. Goldbaum, C. Hummels, A. G. Kritsuk, E. Tasker, S. Skory, C. M. Simpson, O. Hahn, J. S. Oishi, G. C. So, F. Zhao, R. Cen, Y. Li, and Enzo Collaboration. ENZO: An Adaptive Mesh Refinement Code for Astrophysics. *ApJS*, 211:19, April 2014. doi: 10.1088/0067-0049/211/2/19.

S. E. Bryan, S. T. Kay, A. R. Duffy, J. Schaye, C. Dalla Vecchia, and C. M. Booth. The impact of baryons on the spins and shapes of dark matter haloes. *MNRAS*, 429:3316–3329, March 2013. doi: 10.1093/mnras/sts587.

J. S. Bullock, A. Dekel, T. S. Kolatt, A. V. Kravtsov, A. A. Klypin, C. Porciani, and J. R. Primack. A Universal Angular Momentum Profile for Galactic Halos. *ApJ*, 555:240–257, July 2001. doi: 10.1086/321477.

F. Calura, E. Tescari, V. D'Odorico, M. Viel, S. Cristiani, T.-S. Kim, and J. S. Bolton. The Lyman $\alpha$ forest flux probability distribution at z > 3. *MNRAS*, 422:3019–3036, June 2012. doi: 10.1111/j.1365-2966.2012.20811.x.

S. M. Carroll. *Spacetime and Geometry*. Addison Wesley, 2004.

G. Chabrier. Galactic Stellar and Substellar Initial Mass Function. *PASP*, 115:763–795, July 2003. doi: 10.1086/376392.

D. N. Chen, Y. P. Jing, and K. Yoshikaw. Angular Momentum Distribution of Hot Gas and Implications for Disk Galaxy Formation. *ApJ*, 597:35–47, November 2003. doi: 10.1086/378379.

S. Cole. Modeling galaxy formation in evolving dark matter halos. *ApJ*, 367:45–53, January 1991. doi: 10.1086/169600.

S. Cole and C. Lacey. The structure of dark matter haloes in hierarchical clustering models. *MNRAS*, 281:716, July 1996. doi: 10.1093/mnras/281.2.716.

L. Cortese, L. M. R. Fogarty, K. Bekki, J. van de Sande, W. Couch, B. Catinella, M. Colless, D. Obreschkow, D. Taranu, E. Tescari, D. Barat, J. Bland-Hawthorn, J. Bloom, J. J. Bryant, M. Cluver, S. M. Croom, M. J. Drinkwater, F. d'Eugenio, I. S. Konstantopoulos, A. Lopez-Sanchez, S. Mahajan, N. Scott, C. Tonini, O. I. Wong, J. T. Allen, S. Brough, M. Goodwin, A. W. Green, I.-T. Ho, L. S. Kelvin, J. S. Lawrence, N. P. F. Lorente, A. M. Medling, M. S. Owers, S. Richards, R. Sharp, and S. M. Sweet. The SAMI Galaxy Survey: the link between angular momentum and optical morphology. *MNRAS*, 463:170–184, November 2016. doi: 10.1093/mnras/stw1891.

R. A. C. Croft, D. H. Weinberg, M. Pettini, L. Hernquist, and N. Katz. The Power Spectrum of Mass Fluctuations Measured from the Ly$\alpha$ Forest at Redshift z = 2.5. *ApJ*, 520:1–23, July 1999. doi: 10.1086/307438.

R. A. C. Croft, D. H. Weinberg, M. Bolte, S. Burles, L. Hernquist, N. Katz, D. Kirkman, and D. Tytler. Toward a Precise Measurement of Matter Clustering: Ly$\alpha$ Forest Data at Redshifts 2-4. *ApJ*, 581:20–52, December 2002. doi: 10.1086/344099.

M. Danovich, A. Dekel, O. Hahn, D. Ceverino, and J. Primack. Four phases of angular-momentum buildup in high-z galaxies: from cosmic-web streams through an extended ring to disc and bulge. *MNRAS*, 449:2087–2111, May 2015. doi: 10.1093/mnras/stv270.

M. Davis, G. Efstathiou, C. S. Frenk, and S. D. M. White. The evolution of large-scale structure in a universe dominated by cold dark matter. *ApJ*, 292:371–394, May 1985. doi: 10.1086/163168.

A. G. Doroshkevich. The space structure of perturbations and the origin of rotation of galaxies in the theory of fluctuation. *Astrofizika*, 6:581–600, 1970.

Y. Dubois, S. Peirani, C. Pichon, J. Devriendt, R. Gavazzi, C. Welker, and M. Volonteri. The Horizon-AGN Simulation: Morphological Diversity of Galaxies Promoted by AGN feedback. *ArXiv e-prints*, June 2016.

C. Eckart. *Physics of Fluids*, 3:421–427, 1960.

K. El-Badry, E. Quataert, A. Wetzel, P. F. Hopkins, D. R. Weisz, T. K. Chan, A. Fitts, M. Boylan-Kolchin, D. Kereš, C.-A. Faucher-Giguère, and S. Garrison-Kimmel. Gas kinematics, morphology and angular momentum in the FIRE simulations. *MNRAS*, 473: 1930–1955, January 2018. doi: 10.1093/mnras/stx2482.

E. C. Elson. The relation between specific baryon angular momentum and mass for a sample of nearby low-mass galaxies with resolved H I kinematics. *MNRAS*, 472:4551–4562, December 2017. doi: 10.1093/mnras/stx2313.

E. Emsellem, M. Cappellari, D. Krajnović, K. Alatalo, L. Blitz, M. Bois, F. Bournaud, M. Bureau, R. L. Davies, T. A. Davis, P. T. de Zeeuw, S. Khochfar, H. Kuntschner, P.-Y. Lablanche, R. M. McDermid, R. Morganti, T. Naab, T. Oosterloo, M. Sarzi, N. Scott, P. Serra, G. van de Ven, A.-M. Weijmans, and L. M. Young. The ATLAS$^{3D}$ project - III. A census of the stellar angular momentum within the effective radius of early-type galaxies: unveiling the distribution of fast and slow rotators. *MNRAS*, 414:888–912, June 2011. doi: 10.1111/j.1365-2966.2011.18496.x.

S. M. Fall. Galaxy formation - Some comparisons between theory and observation. In E. Athanassoula, editor, *Internal Kinematics and Dynamics of Galaxies*, volume 100 of *IAU Symposium*, pages 391–398, 1983.

S. M. Fall and G. Efstathiou. Formation and rotation of disc galaxies with haloes. *MNRAS*, 193:189–206, October 1980. doi: 10.1093/mnras/193.2.189.

S. M. Fall and A. J. Romanowsky. Angular Momentum and Galaxy Formation Revisited: Effects of Variable Mass-to-light Ratios. *ApJ*, 769:L26, June 2013. doi: 10.1088/2041-8205/769/2/L26.

C.-A. Faucher-Giguère, J. X. Prochaska, A. Lidz, L. Hernquist, and M. Zaldarriaga. A Direct Precision Measurement of the Intergalactic Ly$\alpha$ Opacity at $2 < z < 4.2$. *ApJ*, 681:831–855, July 2008. doi: 10.1086/588648.

C.-A. Faucher-Giguère, A. Lidz, M. Zaldarriaga, and L. Hernquist. A New Calculation of the Ionizing Background Spectrum and the Effects of He II Reionization. *ApJ*, 703: 1416–1443, October 2009. doi: 10.1088/0004-637X/703/2/1416.

S. Genel, M. Vogelsberger, V. Springel, D. Sijacki, D. Nelson, G. Snyder, V. Rodriguez-Gomez, P. Torrey, and L. Hernquist. Introducing the Illustris project: the evolution of galaxy populations across cosmic time. *MNRAS*, 445:175–200, November 2014. doi: 10.1093/mnras/stu1654.

S. Genel, S. M. Fall, L. Hernquist, M. Vogelsberger, G. F. Snyder, V. Rodriguez-Gomez, D. Sijacki, and V. Springel. Galactic Angular Momentum in the Illustris Simulation: Feedback and the Hubble Sequence. *ApJ*, 804:L40, May 2015. doi: 10.1088/2041-8205/804/2/L40.

R. A. Gingold and J. J. Monaghan. Kernel estimates as a basis for general particle methods in hydrodynamics. *Journal of Computational Physics*, 46:429–453, June 1982. doi: 10.1016/0021-9991(82)90025-0.

F. A. Gómez, S. D. M. White, R. J. J. Grand, F. Marinacci, V. Springel, and R. Pakmor. Warps and waves in the stellar discs of the Auriga cosmological simulations. *MNRAS*, 465: 3446–3460, March 2017. doi: 10.1093/mnras/stw2957.

S. Gottlöber and G. Yepes. Shape, Spin, and Baryon Fraction of Clusters in the MareNostrum Universe. *ApJ*, 664:117–122, July 2007. doi: 10.1086/517907.

M. T. Graham, M. Cappellari, H. Li, S. Mao, M. Bershady, D. Bizyaev, J. Brinkmann, J. R. Brownstein, K. Bundy, N. Drory, D. R. Law, K. Pan, D. Thomas, D. A. Wake, A.-M. Weijmans, K. B. Westfall, and R. Yan. SDSS-IV MaNGA: Stellar angular momentum of about 2300 galaxies: unveiling the bimodality of massive galaxy properties. *MNRAS*, March 2018. doi: 10.1093/mnras/sty504.

R. J. J. Grand, F. A. Gómez, F. Marinacci, R. Pakmor, V. Springel, D. J. R. Campbell, C. S. Frenk, A. Jenkins, and S. D. M. White. The Auriga Project: the properties and formation mechanisms of disc galaxies across cosmic time. *MNRAS*, 467:179–207, May 2017. doi: 10.1093/mnras/stx071.

F. Haardt and P. Madau. Radiative Transfer in a Clumpy Universe. II. The Ultraviolet Extragalactic Background. *ApJ*, 461:20, April 1996. doi: 10.1086/177035.

O. Hahn, R. Teyssier, and C. M. Carollo. The large-scale orientations of disc galaxies. *MNRAS*, 405:274–290, June 2010. doi: 10.1111/j.1365-2966.2010.16494.x.

A. Heavens and J. Peacock. Tidal torques and local density maxima. *MNRAS*, 232:339–360, May 1988. doi: 10.1093/mnras/232.2.339.

J. F. Hennawi, J. X. Prochaska, S. Burles, M. A. Strauss, G. T. Richards, D. J. Schlegel, X. Fan, D. P. Schneider, N. L. Zakamska, M. Oguri, J. E. Gunn, R. H. Lupton, and J. Brinkmann. Quasars Probing Quasars. I. Optically Thick Absorbers near Luminous Quasars. *ApJ*, 651:61–83, November 2006. doi: 10.1086/507069.

F. Hoyle. The Origin of the Rotations of the Galaxies. In *Problems of Cosmical Aerodynamics*, page 195, 1949.

L. Hui and N. Y. Gnedin. Equation of state of the photoionized intergalactic medium. *MNRAS*, 292:27, November 1997. doi: 10.1093/mnras/292.1.27.

E. Janknecht, D. Reimers, S. Lopez, and D. Tytler. The evolution of Lyman $\alpha$ absorbers in the redshift range $0.5 < z < 1.9$. *A&A*, 458:427–439, November 2006. doi: 10.1051/0004-6361:20065372.

N. Katz, D. H. Weinberg, and L. Hernquist. Cosmological Simulations with TreeSPH. *ApJS*, 105:19, July 1996. doi: 10.1086/192305.

R. C. Kennicutt, Jr. Star Formation in Galaxies Along the Hubble Sequence. *ARA&A*, 36: 189–232, 1998. doi: 10.1146/annurev.astro.36.1.189.

A. Khokhlov. Fully Threaded Tree Algorithms for Adaptive Refinement Fluid Dynamics Simulations. *Journal of Computational Physics*, 143:519–543, July 1998. doi: 10.1006/jcph.1998.9998.

T.-S. Kim, M. Viel, M. G. Haehnelt, R. F. Carswell, and S. Cristiani. The power spectrum of the flux distribution in the Lyman $\alpha$ forest of a large sample of UVES QSO absorption spectra (LUQAS). *MNRAS*, 347:355–366, January 2004. doi: 10.1111/j.1365-2966.2004.07221.x.

T.-S. Kim, J. S. Bolton, M. Viel, M. G. Haehnelt, and R. F. Carswell. An improved measurement of the flux distribution of the Ly$\alpha$ forest in QSO absorption spectra: the

effect of continuum fitting, metal contamination and noise properties. *MNRAS*, 382: 1657–1674, December 2007. doi: 10.1111/j.1365-2966.2007.12406.x.

D. Kirkman, D. Tytler, N. Suzuki, C. Melis, S. Hollywood, K. James, G. So, D. Lubin, T. Jena, M. L. Norman, and P. Paschos. The HI opacity of the intergalactic medium at redshifts 1.6 < z < 3.2. *MNRAS*, 360:1373–1380, July 2005. doi: 10.1111/j.1365-2966.2005.09126.x.

E. Komatsu, K. M. Smith, J. Dunkley, C. L. Bennett, B. Gold, G. Hinshaw, N. Jarosik, D. Larson, M. R. Nolta, L. Page, D. N. Spergel, M. Halpern, R. S. Hill, A. Kogut, M. Limon, S. S. Meyer, N. Odegard, G. S. Tucker, J. L. Weiland, E. Wollack, and E. L. Wright. Seven-year Wilkinson Microwave Anisotropy Probe (WMAP) Observations: Cosmological Interpretation. *ApJS*, 192:18, February 2011. doi: 10.1088/0067-0049/192/2/18.

J. Kormendy and D. Richstone. Inward Bound—The Search For Supermassive Black Holes In Galactic Nuclei. *ARA&A*, 33:581, 1995. doi: 10.1146/annurev.aa.33.090195.003053.

C. d. P. Lagos, T. Theuns, A. R. H. Stevens, L. Cortese, N. D. Padilla, T. A. Davis, S. Contreras, and D. Croton. Angular momentum evolution of galaxies in EAGLE. *MNRAS*, 464: 3850–3870, February 2017. doi: 10.1093/mnras/stw2610.

C. d. P. Lagos, A. R. H. Stevens, R. G. Bower, T. A. Davis, S. Contreras, N. D. Padilla, D. Obreschkow, D. Croton, J. W. Trayford, C. Welker, and T. Theuns. Quantifying the impact of mergers on the angular momentum of simulated galaxies. *MNRAS*, 473: 4956–4974, February 2018. doi: 10.1093/mnras/stx2667.

S. Liao, L. Gao, C. S. Frenk, Q. Guo, and J. Wang. The segregation of baryons and dark matter during halo assembly. *MNRAS*, 470:2262–2269, September 2017. doi: 10.1093/mnras/stx1391.

Z. Lukić, C. W. Stark, P. Nugent, M. White, A. A. Meiksin, and A. Almgren. The Lyman $\alpha$ forest in optically thin hydrodynamical simulations. *MNRAS*, 446:3697–3724, February 2015. doi: 10.1093/mnras/stu2377.

M.-M. Mac Low and R. S. Klessen. Control of star formation by supersonic turbulence. *Reviews of Modern Physics*, 76:125–194, January 2004. doi: 10.1103/RevModPhys.76.125.

A. V. Macciò, A. A. Dutton, F. C. van den Bosch, B. Moore, D. Potter, and J. Stadel. Concentration, spin and shape of dark matter haloes: scatter and the dependence on mass and environment. *MNRAS*, 378:55–71, June 2007. doi: 10.1111/j.1365-2966.2007.11720.x.

A. V. Macciò, A. A. Dutton, and F. C. van den Bosch. Concentration, spin and shape of dark matter haloes as a function of the cosmological model: WMAP1, WMAP3 and WMAP5 results. *MNRAS*, 391:1940–1954, December 2008. doi: 10.1111/j.1365-2966.2008.14029.x.

A. H. Maller and A. Dekel. Towards a resolution of the galactic spin crisis: mergers, feedback and spin segregation. *MNRAS*, 335:487–498, September 2002. doi: 10.1046/j.1365-8711.2002.05646.x.

A. H. Maller, A. Dekel, and R. Somerville. Modelling angular-momentum history in dark-matter haloes. *MNRAS*, 329:423–430, January 2002. doi: 10.1046/j.1365-8711.2002.04983.x.

P. McDonald, J. Miralda-Escudé, M. Rauch, W. L. W. Sargent, T. A. Barlow, R. Cen, and J. P. Ostriker. The Observed Probability Distribution Function, Power Spectrum, and Correlation Function of the Transmitted Flux in the Ly$\alpha$ Forest. *ApJ*, 543:1–23, November 2000. doi: 10.1086/317079.

P. McDonald, U. Seljak, S. Burles, D. J. Schlegel, D. H. Weinberg, R. Cen, D. Shih, J. Schaye, D. P. Schneider, N. A. Bahcall, J. W. Briggs, J. Brinkmann, R. J. Brunner, M. Fukugita, J. E. Gunn, Ž. Ivezić, S. Kent, R. H. Lupton, and D. E. Vanden Berk. The Ly$\alpha$ Forest Power Spectrum from the Sloan Digital Sky Survey. *ApJS*, 163:80–109, March 2006. doi: 10.1086/444361.

A. Meiksin, J. S. Bolton, and E. Puchwein. Gas around galaxy haloes - III: hydrogen absorption signatures around galaxies and QSOs in the Sherwood simulation suite. *MNRAS*, 468:1893–1901, June 2017. doi: 10.1093/mnras/stx191.

J. Miralda-Escude and M. J. Rees. Tests for the minihalo model of the Lyman-alpha forest. *MNRAS*, 260:617–624, February 1993. doi: 10.1093/mnras/260.3.617.

H. Mo, F. van den Bosch, and S. White. *Galaxy Formation and Evolution*. Cambridge University Press, 2010.

H. J. Mo, S. Mao, and S. D. M. White. The formation of galactic discs. *MNRAS*, 295:319–336, April 1998. doi: 10.1046/j.1365-8711.1998.01227.x.

S. More, B. Diemer, and A. V. Kravtsov. The Splashback Radius as a Physical Halo Boundary and the Growth of Halo Mass. *ApJ*, 810:36, September 2015. doi: 10.1088/0004-637X/810/1/36.

J. F. Navarro and M. Steinmetz. Dark Halo and Disk Galaxy Scaling Laws in Hierarchical Universes. *ApJ*, 538:477–488, August 2000. doi: 10.1086/309175.

J. F. Navarro, C. S. Frenk, and S. D. M. White. A Universal Density Profile from Hierarchical Clustering. *ApJ*, 490:493–508, December 1997.

D. Nelson, A. Pillepich, S. Genel, M. Vogelsberger, V. Springel, P. Torrey, V. Rodriguez-Gomez, D. Sijacki, G. F. Snyder, B. Griffen, F. Marinacci, L. Blecha, L. Sales, D. Xu, and L. Hernquist. The illustris simulation: Public data release. *Astronomy and Computing*, 13: 12–37, November 2015. doi: 10.1016/j.ascom.2015.09.003.

A. F. Neto, L. Gao, P. Bett, S. Cole, J. F. Navarro, C. S. Frenk, S. D. M. White, V. Springel, and A. Jenkins. The statistics of $\Lambda$ CDM halo concentrations. *MNRAS*, 381:1450–1462, November 2007. doi: 10.1111/j.1365-2966.2007.12381.x.

D. Obreschkow and K. Glazebrook. Fundamental Mass-Spin-Morphology Relation Of Spiral Galaxies. *ApJ*, 784:26, March 2014. doi: 10.1088/0004-637X/784/1/26.

T. Okamoto, C. S. Frenk, A. Jenkins, and T. Theuns. The properties of satellite galaxies in simulations of galaxy formation. *MNRAS*, 406:208–222, July 2010. doi: 10.1111/j.1365-2966.2010.16690.x.

R. Pakmor and V. Springel. Simulations of magnetic fields in isolated disc galaxies. *MNRAS*, 432:176–193, June 2013. doi: 10.1093/mnras/stt428.

R. Pakmor, F. Marinacci, and V. Springel. Magnetic Fields in Cosmological Simulations of Disk Galaxies. *ApJ*, 783:L20, March 2014. doi: 10.1088/2041-8205/783/1/L20.

R. Pakmor, V. Springel, A. Bauer, P. Mocz, D. J. Munoz, S. T. Ohlmann, K. Schaal, and C. Zhu. Improving the convergence properties of the moving-mesh code AREPO. *MNRAS*, 455:1134–1143, January 2016. doi: 10.1093/mnras/stv2380.

N. Palanque-Delabrouille, C. Yèche, A. Borde, J.-M. Le Goff, G. Rossi, M. Viel, É. Aubourg, S. Bailey, J. Bautista, M. Blomqvist, A. Bolton, J. S. Bolton, N. G. Busca, B. Carithers, R. A. C. Croft, K. S. Dawson, T. Delubac, A. Font-Ribera, S. Ho, D. Kirkby, K.-G. Lee, D. Margala, J. Miralda-Escudé, D. Muna, A. D. Myers, P. Noterdaeme, I. Pâris, P. Petitjean, M. M. Pieri, J. Rich, E. Rollinde, N. P. Ross, D. J. Schlegel, D. P. Schneider, A. Slosar, and D. H. Weinberg. The one-dimensional Ly$\alpha$ forest power spectrum from BOSS. *A&A*, 559:A85, November 2013. doi: 10.1051/0004-6361/201322130.

J. A. Peacock. *Cosmological Physics*. Cambridge University Press, 1999.

P. J. E. Peebles. Origin of the Angular Momentum of Galaxies. *ApJ*, 155:393, February 1969. doi: 10.1086/149876.

P.J.E. Peebles. *Principles of Physical Cosmology*. Princeton University Press, 1993.

A. Pillepich, V. Springel, D. Nelson, S. Genel, J. Naiman, R. Pakmor, L. Hernquist, P. Torrey, M. Vogelsberger, R. Weinberger, and F. Marinacci. Simulating galaxy formation with the IllustrisTNG model. *MNRAS*, 473:4077–4106, January 2018. doi: 10.1093/mnras/stx2656.

Planck Collaboration, R. Adam, P. A. R. Ade, N. Aghanim, Y. Akrami, M. I. R. Alves, F. Argüeso, M. Arnaud, F. Arroja, M. Ashdown, and et al. Planck 2015 results. I. Overview of products and scientific results. *A&A*, 594:A1, September 2016a. doi: 10.1051/0004-6361/201527101.

Planck Collaboration, P. A. R. Ade, N. Aghanim, M. Arnaud, M. Ashdown, J. Aumont, C. Baccigalupi, A. J. Banday, R. B. Barreiro, J. G. Bartlett, and et al. Planck 2015 results. XIII. Cosmological parameters. *A&A*, 594:A13, September 2016b. doi: 10.1051/0004-6361/201525830.

J. X. Prochaska and J. F. Hennawi. Quasars Probing Quasars. III. New Clues to Feedback, Quenching, and the Physics of Massive Galaxy Formation. *ApJ*, 690:1558–1584, January 2009. doi: 10.1088/0004-637X/690/2/1558.

J. X. Prochaska, J. F. Hennawi, K.-G. Lee, S. Cantalupo, J. Bovy, S. G. Djorgovski, S. L. Ellison, M. W. Lau, C. L. Martin, A. Myers, K. H. R. Rubin, and R. A. Simcoe. Quasars Probing Quasars. VI. Excess H I Absorption within One Proper Mpc of z ˜ 2 Quasars. *ApJ*, 776:136, October 2013a. doi: 10.1088/0004-637X/776/2/136.

J. X. Prochaska, J. F. Hennawi, and R. A. Simcoe. A Substantial Mass of Cool, Metal-enriched Gas Surrounding the Progenitors of Modern-day Ellipticals. *ApJ*, 762:L19, January 2013b. doi: 10.1088/2041-8205/762/2/L19.

E. Puchwein. *Lecture Notes: Advanced Cosmology*. 2013.

E. Puchwein and V. Springel. Shaping the galaxy stellar mass function with supernova- and AGN-driven winds. *MNRAS*, 428:2966–2979, February 2013. doi: 10.1093/mnras/sts243.

O. Rakic, J. Schaye, C. C. Steidel, and G. C. Rudie. Neutral Hydrogen Optical Depth near Star-forming Galaxies at z = 2.4 in the Keck Baryonic Structure Survey. *ApJ*, 751:94, June 2012. doi: 10.1088/0004-637X/751/2/94.

M. Rauch, J. Miralda-Escudé, W. L. W. Sargent, T. A. Barlow, D. H. Weinberg, L. Hernquist, N. Katz, R. Cen, and J. P. Ostriker. The Opacity of the Ly$\alpha$ Forest and Implications for $\Omega_b$ and the Ionizing Background. *ApJ*, 489:7–20, November 1997. doi: 10.1086/304765.

M. J. Rees and J. P. Ostriker. Cooling, dynamics and fragmentation of massive gas clouds - Clues to the masses and radii of galaxies and clusters. *MNRAS*, 179:541–559, June 1977.

V. Rodriguez-Gomez, L. V. Sales, S. Genel, A. Pillepich, J. Zjupa, D. Nelson, B. Griffen, P. Torrey, G. F. Snyder, M. Vogelsberger, V. Springel, C.-P. Ma, and L. Hernquist. The role of mergers and halo spin in shaping galaxy morphology. *MNRAS*, 467:3083–3098, May 2017. doi: 10.1093/mnras/stx305.

A. J. Romanowsky and S. M. Fall. Angular Momentum and Galaxy Formation Revisited. *ApJS*, 203:17, December 2012. doi: 10.1088/0067-0049/203/2/17.

V. C. Rubin and W. K. Ford, Jr. Rotation of the Andromeda Nebula from a Spectroscopic Survey of Emission Regions. *ApJ*, 159:379, February 1970. doi: 10.1086/150317.

G. C. Rudie, C. C. Steidel, R. F. Trainor, O. Rakic, M. Bogosavljević, M. Pettini, N. Reddy, A. E. Shapley, D. K. Erb, and D. R. Law. The Gaseous Environment of High-z Galaxies: Precision Measurements of Neutral Hydrogen in the Circumgalactic Medium of z ˜ 2-3 Galaxies in the Keck Baryonic Structure Survey. *ApJ*, 750:67, May 2012. doi: 10.1088/0004-637X/750/1/67.

B. Ryden. *Introduction to Cosmology*. Addison Wesley, 2002.

B. S. Ryden. Galaxy formation - The role of tidal torques and dissipational infall. *ApJ*, 329: 589–611, June 1988. doi: 10.1086/166406.

L. V. Sales, J. F. Navarro, T. Theuns, J. Schaye, S. D. M. White, C. S. Frenk, R. A. Crain, and C. Dalla Vecchia. The origin of discs and spheroids in simulated galaxies. *MNRAS*, 423:1544–1555, June 2012. doi: 10.1111/j.1365-2966.2012.20975.x.

B. M. Schäfer and P. M. Merkel. Galactic angular momenta and angular momentum couplings in the large-scale structure. *MNRAS*, 421:2751–2762, April 2012. doi: 10.1111/j.1365-2966.2011.20224.x.

J. Schaye, T. Theuns, M. Rauch, G. Efstathiou, and W. L. W. Sargent. The thermal history of the intergalactic medium*. *MNRAS*, 318:817–826, November 2000. doi: 10.1046/j.1365-8711.2000.03815.x.

J. Schaye, A. Aguirre, T.-S. Kim, T. Theuns, M. Rauch, and W. L. W. Sargent. Metallicity of the Intergalactic Medium Using Pixel Statistics. II. The Distribution of Metals as Traced by C IV. *ApJ*, 596:768–796, October 2003. doi: 10.1086/378044.

J. Schaye, R. A. Crain, R. G. Bower, M. Furlong, M. Schaller, T. Theuns, C. Dalla Vecchia, C. S. Frenk, I. G. McCarthy, J. C. Helly, A. Jenkins, Y. M. Rosas-Guevara, S. D. M. White, M. Baes, C. M. Booth, P. Camps, J. F. Navarro, Y. Qu, A. Rahmati, T. Sawala, P. A. Thomas, and J. Trayford. The EAGLE project: simulating the evolution and assembly of galaxies and their environments. *MNRAS*, 446:521–554, January 2015. doi: 10.1093/mnras/stu2058.

D. Schlegel, I. Sloan Digital Sky Survey-eBOSS Collaboration, and Dark Energy Spectroscopic Survey (DESI) Collaboration. Next-Generation Baryon Acoustic Oscillations with eBOSS and DESI. In *APS April Meeting Abstracts*, page Z2.006, April 2015.

N. I. Shakura and R. A. Sunyaev. Black holes in binary systems. Observational appearance. *A&A*, 24:337–355, 1973.

P. R. Shapiro, I. T. Iliev, H. Martel, K. Ahn, and M. A. Alvarez. The Equilibrium Structure of CDM Halos. *ArXiv Astrophysics e-prints*, September 2004.

S. Sharma and M. Steinmetz. The Angular Momentum Distribution of Gas and Dark Matter in Galactic Halos. *ApJ*, 628:21–44, July 2005. doi: 10.1086/430660.

S. Sharma, M. Steinmetz, and J. Bland-Hawthorn. On the Origin of the Angular Momentum Properties of Gas and Dark Matter in Galactic Halos and Its Implications. *ApJ*, 750:107, May 2012. doi: 10.1088/0004-637X/750/2/107.

D. Sijacki, V. Springel, T. Di Matteo, and L. Hernquist. A unified model for AGN feedback in cosmological simulations of structure formation. *MNRAS*, 380:877–900, September 2007. doi: 10.1111/j.1365-2966.2007.12153.x.

C. M. Simpson, R. J. J. Grand, F. A. Gómez, F. Marinacci, R. Pakmor, V. Springel, D. J. R. Campbell, and C. S. Frenk. Quenching and ram pressure stripping of simulated Milky Way satellite galaxies. *MNRAS*, 478:548–567, July 2018. doi: 10.1093/mnras/sty774.

V. Springel. The cosmological simulation code GADGET-2. *MNRAS*, 364:1105–1134, December 2005. doi: 10.1111/j.1365-2966.2005.09655.x.

V. Springel. E pur si muove: Galilean-invariant cosmological hydrodynamical simulations on a moving mesh. *MNRAS*, 401:791–851, January 2010a. doi: 10.1111/j.1365-2966.2009.15715.x.

V. Springel. Smoothed Particle Hydrodynamics in Astrophysics. *ARA&A*, 48:391–430, September 2010b. doi: 10.1146/annurev-astro-081309-130914.

V. Springel. Fundamentals of simulation methods. 2016.

V. Springel and L. Hernquist. Cosmological smoothed particle hydrodynamics simulations: the entropy equation. *MNRAS*, 333:649–664, July 2002. doi: 10.1046/j.1365-8711.2002.05445.x.

V. Springel and L. Hernquist. Cosmological smoothed particle hydrodynamics simulations: a hybrid multiphase model for star formation. *MNRAS*, 339:289–311, February 2003. doi: 10.1046/j.1365-8711.2003.06206.x.

V. Springel, S. D. M. White, G. Tormen, and G. Kauffmann. Populating a cluster of galaxies - I. Results at [formmu2]z=0. *MNRAS*, 328:726–750, December 2001. doi: 10.1046/j.1365-8711.2001.04912.x.

V. Springel, S. D. M. White, A. Jenkins, C. S. Frenk, N. Yoshida, L. Gao, J. Navarro, R. Thacker, D. Croton, J. Helly, J. A. Peacock, S. Cole, P. Thomas, H. Couchman, A. Evrard, J. Colberg, and F. Pearce. Simulations of the formation, evolution and clustering of galaxies and quasars. *Nature*, 435:629–636, June 2005. doi: 10.1038/nature03597.

V. Springel, C. S. Frenk, and S. D. M. White. The large-scale structure of the Universe. *Nature*, 440:1137–1144, April 2006. doi: 10.1038/nature04805.

V. Springel, R. Pakmor, A. Pillepich, R. Weinberger, D. Nelson, L. Hernquist, M. Vogelsberger, S. Genel, P. Torrey, F. Marinacci, and J. Naiman. First results from the IllustrisTNG simulations: matter and galaxy clustering. *MNRAS*, 475:676–698, March 2018. doi: 10.1093/mnras/stx3304.

C. C. Steidel, D. K. Erb, A. E. Shapley, M. Pettini, N. Reddy, M. Bogosavljević, G. C. Rudie, and O. Rakic. The Structure and Kinematics of the Circumgalactic Medium from Far-ultraviolet Spectra of z ˜= 2-3 Galaxies. *ApJ*, 717:289–322, July 2010. doi: 10.1088/0004-637X/717/1/289.

M. Steinmetz and M. Bartelmann. On the spin parameter of dark-matter haloes. *MNRAS*, 272:570–578, February 1995. doi: 10.1093/mnras/272.3.570.

K. R. Stewart, A. H. Maller, J. Oñorbe, J. S. Bullock, M. R. Joung, J. Devriendt, D. Ceverino, D. Kereš, P. F. Hopkins, and C.-A. Faucher-Giguère. High Angular Momentum Halo Gas:

A Feedback and Code-independent Prediction of LCDM. *ApJ*, 843:47, July 2017. doi: 10.3847/1538-4357/aa6dff.

J. M. Stone, T. A. Gardiner, P. Teuben, J. F. Hawley, and J. B. Simon. Athena: A New Code for Astrophysical MHD. *ApJS*, 178:137–177, September 2008. doi: 10.1086/588755.

A. M. Swinbank, C. M. Harrison, J. Trayford, M. Schaller, I. Smail, J. Schaye, T. Theuns, R. Smit, D. M. Alexander, R. Bacon, R. G. Bower, T. Contini, R. A. Crain, C. de Breuck, R. Decarli, B. Epinat, M. Fumagalli, M. Furlong, A. Galametz, H. L. Johnson, C. Lagos, J. Richard, J. Vernet, R. M. Sharples, D. Sobral, and J. P. Stott. Angular momentum evolution of galaxies over the past 10 Gyr: a MUSE and KMOS dynamical survey of 400 star-forming galaxies from z = 0.3 to 1.7. *MNRAS*, 467:3140–3159, May 2017. doi: 10.1093/mnras/stx201.

A. F. Teklu, R.-S. Remus, K. Dolag, A. M. Beck, A. Burkert, A. S. Schmidt, F. Schulze, and L. K. Steinborn. Connecting Angular Momentum and Galactic Dynamics: The Complex Interplay between Spin, Mass, and Morphology. *ApJ*, 812:29, October 2015. doi: 10.1088/0004-637X/812/1/29.

R. Teyssier. Cosmological hydrodynamics with adaptive mesh refinement. A new high resolution code called RAMSES. *A&A*, 385:337–364, April 2002. doi: 10.1051/0004-6361:20011817.

D. Tytler, D. Kirkman, J. M. O'Meara, N. Suzuki, A. Orin, D. Lubin, P. Paschos, T. Jena, W.-C. Lin, M. L. Norman, and A. Meiksin. Cosmological Parameters $\sigma_8$, the Baryon Density $\Omega_b$, the Vacuum Energy Density $\Omega_\Lambda$, the Hubble Constant and the UV Background Intensity from a Calibrated Measurement of H I Ly$\alpha$ Absorption at z=1.9. *ApJ*, 617:1–28, December 2004. doi: 10.1086/425226.

P. Valageas, R. Schaeffer, and J. Silk. The phase-diagram of cosmological baryons. *A&A*, 388:741–757, June 2002. doi: 10.1051/0004-6361:20020548.

F. C. van den Bosch. The Formation of Disk-Bulge-Halo Systems and the Origin of the Hubble Sequence. *ApJ*, 507:601–614, November 1998. doi: 10.1086/306354.

F. C. van den Bosch, T. Abel, R. A. C. Croft, L. Hernquist, and S. D. M. White. The Angular Momentum of Gas in Protogalaxies. I. Implications for the Formation of Disk Galaxies. *ApJ*, 576:21–35, September 2002. doi: 10.1086/341619.

M. Veale, C.-P. Ma, J. E. Greene, J. Thomas, J. P. Blakeslee, N. McConnell, J. L. Walsh, and J. Ito. The MASSIVE Survey - VII. The relationship of angular momentum, stellar

mass and environment of early-type galaxies. *MNRAS*, 471:1428–1445, October 2017. doi: 10.1093/mnras/stx1639.

M. Viel, M. G. Haehnelt, and V. Springel. Inferring the dark matter power spectrum from the Lyman $\alpha$ forest in high-resolution QSO absorption spectra. *MNRAS*, 354:684–694, November 2004. doi: 10.1111/j.1365-2966.2004.08224.x.

M. Vitvitska, A. A. Klypin, A. V. Kravtsov, R. H. Wechsler, J. R. Primack, and J. S. Bullock. The Origin of Angular Momentum in Dark Matter Halos. *ApJ*, 581:799–809, December 2002. doi: 10.1086/344361.

M. Vogelsberger, S. Genel, D. Sijacki, P. Torrey, V. Springel, and L. Hernquist. A model for cosmological simulations of galaxy formation physics. *MNRAS*, 436:3031–3067, December 2013. doi: 10.1093/mnras/stt1789.

M. Vogelsberger, S. Genel, V. Springel, P. Torrey, D. Sijacki, D. Xu, G. Snyder, S. Bird, D. Nelson, and L. Hernquist. Properties of galaxies reproduced by a hydrodynamic simulation. *Nature*, 509:177–182, May 2014a. doi: 10.1038/nature13316.

M. Vogelsberger, S. Genel, V. Springel, P. Torrey, D. Sijacki, D. Xu, G. Snyder, D. Nelson, and L. Hernquist. Introducing the Illustris Project: simulating the coevolution of dark and visible matter in the Universe. *MNRAS*, 444:1518–1547, October 2014b. doi: 10.1093/mnras/stu1536.

M. S. Warren, P. J. Quinn, J. K. Salmon, and W. H. Zurek. Dark halos formed via dissipationless collapse. I - Shapes and alignment of angular momentum. *ApJ*, 399:405–425, November 1992. doi: 10.1086/171937.

R. Weinberger, V. Springel, L. Hernquist, A. Pillepich, F. Marinacci, R. Pakmor, D. Nelson, S. Genel, M. Vogelsberger, J. Naiman, and P. Torrey. Simulating galaxy formation with black hole driven thermal and kinetic feedback. *MNRAS*, 465:3291–3308, March 2017. doi: 10.1093/mnras/stw2944.

S. D. M. White. Angular momentum growth in protogalaxies. *ApJ*, 286:38–41, November 1984. doi: 10.1086/162573.

S. D. M. White and M. J. Rees. Core condensation in heavy halos - A two-stage theory for galaxy formation and clustering. *MNRAS*, 183:341–358, May 1978.

J. Zavala, T. Okamoto, and C. S. Frenk. Bulges versus discs: the evolution of angular momentum in cosmological simulations of galaxy formation. *MNRAS*, 387:364–370, June 2008. doi: 10.1111/j.1365-2966.2008.13243.x.

J. Zavala, C. S. Frenk, R. Bower, J. Schaye, T. Theuns, R. A. Crain, J. W. Trayford, M. Schaller, and M. Furlong. The link between the assembly of the inner dark matter halo and the angular momentum evolution of galaxies in the EAGLE simulation. *MNRAS*, 460:4466–4482, August 2016. doi: 10.1093/mnras/stw1286.

J. Zjupa and V. Springel. Angular momentum properties of haloes and their baryon content in the Illustris simulation. *MNRAS*, 466:1625–1647, April 2017. doi: 10.1093/mnras/stw2945.

Ich schaffe, was ihr wollt, und schaffe mehr;
Zwar ist es leicht, doch ist das Leichte schwer;
Es liegt schon da, doch um es zu erlangen,
Das ist die Kunst, wer weißes anzufangen?

- *Mephistopheles*

Faust, Der Tragödie zweiter Teil

*Johann Wolfgang von Goethe*

# Acknowledgements

I would like to deeply thank Volker Springel for providing the opportunity to work on the most challenging, relevant, but also rewarding topics in computational galaxy formation, as well as for his excellent technical and scientific advise. I am very grateful to Ruediger Pakmor for his support in all types of arising difficulties. Finally, I would like to thank all current and former members of the theoretical astrophysics group at the Heidelberg Institute for Theoretical Studies for the various enlightening discussions on all kinds of scientific and non-scientific topics, amongst others Ewald Puchwein, Federico Marinacci, Christoph Pfrommer, Martin Sparre, Kevin Schaal, Robert Grand, Christine Simpson, Christian Arnold, Rainer Weinberger, Freeke van de Voort, Thomas Guillet, Svenja Jacob, Felipe Goicovic, Sebastian Bustamante, and Dandan Xu.